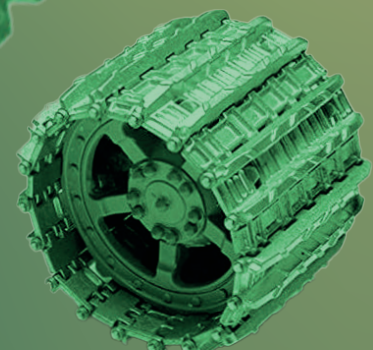
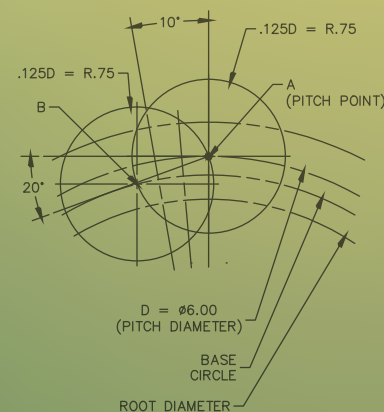
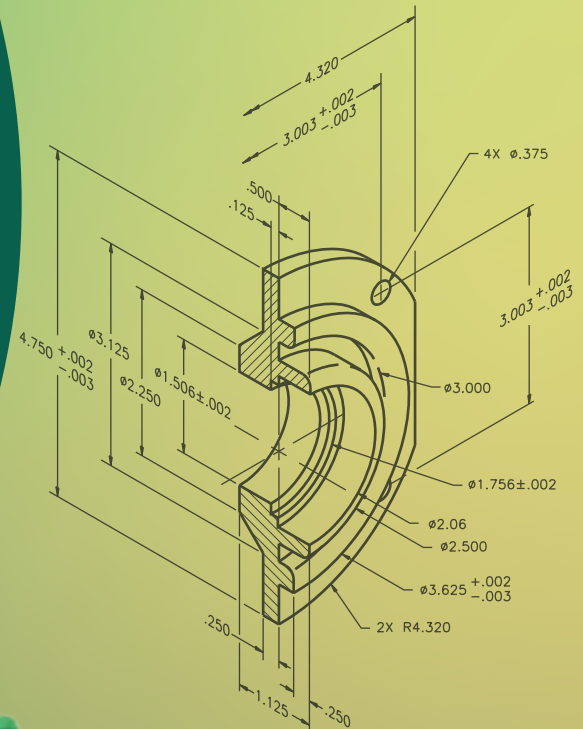




March 2025
Volume 9 · Issue 1

Exploring Innovations in Mechanical Science and Engineering

- Electrospun biopolymer blends of poly(lactic acid) and poly(hydroxybutyrate) reinforced with biochar derived from kitchen waste
- 2. Effect of annealing on tensile properties of carbon fiber reinforced PA 6 manufactured by fused deposition modeling 3.
- Experimental study on the thermal conductivity of a water-based ternary hybrid nanofluid incorporating MWCNTs-COOH-Fe₃O₄-rGO
- 4. Nanoindentation evaluation of mechanical and wear properties of Zn-3% Cu-9% Al alloy processed via ECAP



Editor in Chief**Mustafa Ozcanli**

Department of Automotive Engineering, Cukurova University, Türkiye
Email: ozcanli@cu.edu.tr, Orcid: <https://orcid.org/0000-0001-6088-2912>

Editors**Erdogan Madenci**

The University of Arizona College of Engineering, United States
<https://orcid.org/0000-0003-2895-6111>

Sandra Paszkiewicz

West Pomeranian University of Technology, Poland
Email: spaszkievicz@zut.edu.pl, Orcid: <https://orcid.org/0000-0001-7487-9220>

Raul Campilho

Instituto Superior de Engenharia do Porto, Portugal

Iulian Antoniac

Materials Science and Engineering, University Politecnica de Bucharest, Romania
Email: antoniac.iulian@gmail.com, <https://orcid.org/0000-0003-0112-3494>

Ana Pilipović

University of Zagreb Faculty of Mechanical

Ahmet Çalik

Mechanical Engineering, Burdur Mehmet Akif Ersoy University, Türkiye
Email: acalik@merhmetakif.edu.tr, Orcid: <https://orcid.org/0000-0001-7425-4546>

Murat Demiral

College of Engineering and Technology, American University of the Middle East, Kuwait,
Email: murat.demiral@aum.edu.kw, <https://orcid.org/0000-0002-7206-1713>

Tomasz Garbowski

Poznań University of Life Sciences

Mohd Ezree Abdullah

Universiti Tun Hussein Onn Malaysia, Malaysia

Nadir YILMAZ

Howard University, United States

Technical Editors**Ali Cem Yakaryılmaz**

Automotive Engineering, Cukurova University, Türkiye
Email: acyakaryilmaz@cu.edu.tr

Berkay Karaçor

Automotive Engineering, Cukurova University, Türkiye
Email: bkaracor@cu.edu.tr

Language Editorial Board**Umut Kumlu**

SAutomotive Engineering, Cukurova University, Türkiye, Email: ukumlu@cu.edu.tr

Ayşe Tırat Dalak Ataözü

School of Foreign Languages, Cukurova University, Turkey, Email: aataozu@cu.edu.tr

Indexed / Abstracted in:

TR-Dizin, EBSCO, Scilit, Index Copernicus, The Open Ukrainian Citation Index (OUCI), Paperity Open Science, Asian Science Citation Index

Aims and Scopes

European Mechanical Science (EMS) is an international, peer-reviewed journal that publishes full-length original research papers, and reviews related to all areas of Mechanical Engineering such as Solid Mechanics, Material, Automotive, Fluid Mechanics, Thermal, Engine and Power, Dynamics and Control, Robotics and Mechatronics, Transportation, Computational Mechanics, Design, Systems, Manufacturing, Biomedical, Process, and Aerospace published four times a year in March, June, September, and December. This is an open-access journal which means that all content is freely available without charge to the user or author's institution. EMS is a quarterly published journal operating an online submission and peer review system. It allows authors to submit articles online and track their progress via its web interface. This journal is a peer-reviewed open-access engineering journal published four times a year.

For inquiries and communication, please contact us at: emsjournal01@gmail.com

<https://dergipark.org.tr/ems>

Contents

– Research Articles

Electrospun biopolymer blends of poly(lactic acid) and poly(hydroxybutyrate) reinforced with biochar derived from kitchen waste

Alena Opálková Šišková, Tomáš Dvůrák, Andrej Opálek, Katarína Mosnáčková, Viera Dujnič, Nad'a Beronská.....

Effect of annealing on tensile properties of carbon fiber reinforced PA 6 manufactured by fused deposition modeling

Mislav Tujmer, Ana Pilipović 8

Experimental study on the thermal conductivity of a water-based ternary hybrid nanofluid incorporating MWCNTs-COOH-Fe₃O₄-rGO

Neşe Keklikcioğlu Çakmak 6

Nanoindentation evaluation of mechanical and wear properties of Zn-3% Cu-9% Al alloy processed via ECAP

Serkan Ateş 5

Investigation of micro-perforated plate structure and cavity used as Helmholtz resonator in wheel arch liner

Yasemin Gultekin, Thomas Jean, Mustafa Atakan Akar, Umut Kumlu 8

Thermal and electrical analysis of 26650 li-ion batteries in series connection using the NTGK model and virtual simulations

Metin Uzun 46

Failure Mode and effects analysis of selected weaving defects in viscose/linen fabrics using the fuzzy TOPSIS method

Çiğdem Sarpkaya 59

Mechanical and tribological investigation of jute fiber reinforcement in organic automotive brake pads and water repellency gain in natural fiber reinforced pads

Benek Hamamcı, Merve Sali 66

Structural analysis of a rope slewing system for loads with a variable center of gravity

Sinan Duzenli, Tolga Guney, Mucahit Soyaslan 78

Analysis of the pressure resistance of mini valve used in drip irrigation with finite elements

Yavuz Turan, Murat Kuru, Beyza Gizem Duman, Hülya Alaca, İbrahim Keleş 87

Electrospun biopolymer blends of poly(lactic acid) and poly(hydroxybutyrate) reinforced with biochar derived from kitchen waste

Alena Opálková Šišková^{1,2} , Tomáš Dvorák¹ , Andrej Opálek¹ , Katarína Mosnáčková² ,
Viera Dujnič³ , Nad'a Beronská^{1*} 

¹Institute of Materials and Machine Mechanics, Slovak Academy of Sciences, Dúbravská 9, 845 13 Bratislava, Slovakia.

²Polymer Institute of Slovak Academy of Sciences, Dúbravská cesta 9, 845 41 Bratislava, Slovakia.

³Institute of Chemistry, Slovak Academy of Sciences, Dúbravská cesta 9, 845 38, Bratislava, Slovakia.

Abstract: Biodegradable composites reinforced with natural fillers are exciting alternatives to expensive biodegradable polymers. This study aimed to investigate the effect of kitchen waste-derived biochar on the morphological, chemical, thermal, and mechanical properties of electrospun fibrous mats from a blend of biodegradable polymers poly(lactic acid) and poly(hydroxybutyrate). The electrospun neat PLA/PHB mats and mats with 5, 10, 15, 20, and 30 wt.% content of kitchen waste-derived biochar were produced. The techniques of scanning electron microscopy, Fourier transform infrared spectrometry analysis, thermogravimetric analysis, and different scanning calorimetry and tensile tests were used for the fundamental characterization of the produced electrospun mats. The results indicate that adding biochar to PLA/PHB does not significantly affect the properties of electrospun materials. This may be advantageous for packaging, filtration, or agriculture applications.

Keywords: biochar, biodegradable composites, electrospinning, material characterization, environmentally friendly polymers.

1. Introduction

The increasing global concern for environmental sustainability has driven the demand for natural, biodegradable, and biocompatible materials. Biopolymers, derived from renewable sources, offer an alternative to traditional petroleum-based plastics [1]. Among these, poly(lactic acid) (PLA) and poly(hydroxybutyrate) (PHB) have emerged as two of the most promising biopolymers due to their excellent biodegradability and biocompatibility. Blending PLA and PHB offers several advantages. The combination of PLA's ductility and PHB's crystallinity can enhance mechanical properties; the synergistic effect of the two polymers can improve the thermal stability of the blend. Adjusting the blend ratio allows the material's properties to be fine-tuned to meet specific applications [2, 3].

Electrospinning is a versatile technique that enables the fabrication of nanofibers with exceptional properties, such as high surface area, porosity, and tunable mechanical properties [4]. By combining electrospinning with biodegradable biopolymers like PLA and PHB,

innovative materials with potential applications in various fields, including tissue engineering, filtration, drug delivery, and packaging, can be created [5-7]. However, the global market for biodegradable polymers is still young and struggling with problems resulting from the high prices of its products and the limited infrastructure enabling its organic recycling. The material advantages of applying this type of polymer are undeniable but expensive; therefore, price reduction opportunities may be crucial. An enjoyable alternative in this field is the use of fillers, which, together with the polymer, form a composite; this leads to a reduction in price and modifies the material's properties [8].

Biochar, a carbon-rich material derived from biomass pyrolysis, offers a promising solution as a filler due to its unique properties, such as high surface area, porosity, and excellent thermal and electrical conductivity. Kitchen waste, such as vegetable scraps, fruit peels, and coffee grounds, is an excellent source of biomass for biochar production. By converting such organic waste into biochar, landfill waste can be reduced, and a valuable resource for sustainable industry can be created.

*Corresponding author:

Email: nada.beronska@savba.sk

Cite this article as:

Šišková, A.O., et.al. (2025). Electrospun biopolymer blends of poly(lactic acid) and poly(hydroxybutyrate) reinforced with biochar derived from kitchen waste. *European Mechanical Science*, 9(1): 1-7. <https://doi.org/10.26701/ems.1590916>

History dates:

Received: 25.11.2024, Revision Request: 23.12.2024, Last Revision Received: 31.12.2024, Accepted: 06.01.2025



© Author(s) 2025. This work is distributed under <https://creativecommons.org/licenses/by/4.0/>



Another benefit of using kitchen waste is the reduction of greenhouse gases in landfills produced when kitchen waste decomposes [9-12].

The current work aims to design fibrous composites with kitchen waste-derived biochar as filler for a sustainable way to manage kitchen waste. In the study, the electrospun mats PLA/PHB and fibrous composites PLA/PHB with different biochar content were prepared. The biochar used in this study was prepared from the peelings of root vegetable and potatoes contained in the of kitchen waste. The original combination of biodegradable polymers blend PLA/PHB, the kitchen waste derived biochar as filler of fibrous composites and electrospinning technology brings novelty to the study, as the authors have no knowledge of a similar combination of materials and their study from the literature. Due to this specific combination of materials it was necessary to determine the properties of these prepared fibrous composites and on the basic characteristics. The morphology of electrospun mats, chemical changes, and thermal and mechanical properties were investigated by SEM, FTIR, and RAMAN, TGA/DSC, and Instron, respectively. The effects of biochar as fillers on the mechanical, morphological, and thermal properties of electrospun poly(lactic acid) and poly(hydroxybutyrate) blends were characterized.

2. Materials

Commercial poly(lactic acid) pellets of PLA 4042 D with a density of 1.25 g.cm^{-3} were purchased from Resinex (Bratislava, Slovakia). Poly(3-hydroxybutyrate) PHB Biomer® powder with a density of 1.20 g.cm^{-3} was supplied by Biomer (Krailling, Germany). The acetyl tributyl citrate (ATBC) 98 % was used as a plasticizer and was purchased from Sigma Aldrich (Saint Luis, MO, USA). 1,1,1,3,3,3-hexafluoro-isopropanol (HFIP, >99.0% purity) was purchased from TCI Tokyo Kasei (Tokyo Japan); dichloromethane p.a. (DCM, 99.8% purity) from Lach-Ner (Bratislava, Slovakia).

3. Methods

The PLA/PHB/ATBC blend (85:15:15) was prepared by melt mixing in Plasti-Corder Brabender at 175°C at 40 rpm for 10 minutes. The molar mass of the PLA/PHB/ATBC has been estimated on $M_w = 74.5 \text{ kg.mol}^{-1}$. Then, PLA/PHB/ATBC solution was prepared in concentrations of 10 % (w/v) in the blend of 1,1,1,3,3,3-hexafluoro-isopropanol (HFIP) and dichloromethane (DCM). The solution was stirred intensively up to wholly dissolved. 60 mL of the solution was prepared.

The kitchen waste, consisting primarily of dried peelings from potatoes and root vegetables such as carrots, celery, and kohlrabi, was used to prepare biochar. The kitchen waste was stabilized in a conventional laboratory oven (Memmert GmbH, Germany). The tempera-

ture increased every 24 h, from 50°C to 250°C in this oven. Thus, stabilized waste was carbonized at 800°C in a tube electric resistance furnace (Clasic.cz, Řevnice, Czech Republic) under a vacuum of $\sim 10 \text{ Pa}$, with a heating rate of 2°C.min^{-1} , and a dwell time of 30 min in the targeted temperature. The cooling was carried out in the oven until room temperature was reached.

The PLA/PHB/ATBC solution was divided into six parts of 10mL each, and biochar was added to five of them to reach concentrations of 5, 10, 15, 20, and 30 wt.%. The samples were thoroughly homogenized to obtain solutions with finely distributed biochar particles with a size D50 of about $50 \mu\text{m}$, and 90 % of the powder was smaller than $100 \mu\text{m}$. The procedure of carbonization was adopted from [13]. Then, the electrospun mats without and with the different percentages of biochar were prepared by electrospinning under ambient temperature ($23 \pm 1^\circ\text{C}$, $H = 57\%$) in a horizontal spinning configuration with a flat-end needle with a 21 G inner diameter. The working distance was 12 cm. The applied voltage was between 15 kV, and the voltage was driven by a high-voltage power supply (Spellman SL-150W, Germany). A syringe pump fed the solutions with the feeding rate of 0.5 mL.h^{-1} . The electrospun mats were formed on collectors covered by aluminum foil.

The morphology of electrospun mats was observed by scanning electron microscopy (SEM) using a JSM Jeol 6610 microscope (Jeol, Japan) at an accelerated voltage of 15 kV. Before observing, the samples were sputtered with a thin layer of gold by the sputter coater Balzers SCD 040 (Balzers Union Limited, Lichtenstein). The average diameters of the samples in the mats were measured using ImageJ software. RAMAN spectroscopy was used to characterize the biochar. The DXR Raman Microscope (Thermo Electron Scientific Instruments LLC, Madison, WI USA) was used. The measurements were performed at room temperature in the range $50 - 3500 \text{ cm}^{-1}$. The Raman spectra were excited using the 532 nm laser, with the maximal laser power of 10 mW. The peak position was calibrated with a polystyrene standard. Power 0.5 - 5 mW was used to examine the samples. Fourier-transform infrared (FTIR) spectra were measured with spectrometer iS50 (Thermo Fisher Scientific, USA) equipped with DTGS detector and Omnic 9.0 software. The spectra were collected in the middle region from $4,000$ to 400 cm^{-1} at a resolution of 4 cm^{-1} ; the number of scans was 128. Diamond ATR was applied for measurement in solid/liquid state. Thermal analysis was carried out by the combined analyzer Netzsch STA 449 F1 Jupiter. Twenty milligrams of the samples in the Al_2O_3 crucible pans with a diameter of 6 mm were heated from 20 to 500°C at a $10^\circ\text{C.min}^{-1}$ heating rate under an argon atmosphere. The weight loss of the samples was recorded as a function of temperature with the help of the Netzsch Proteus software. The tensile tests of the electrospun samples were performed using a Dynamometer Instron 4301 (Instron Corporation, Norwood, MA, USA) following standard ASTM D638. Five testing strips for each formulation

were cut from the electrospun mats with the dimensions of the tested strip area of 15×50 mm with a thickness of approximately 0.1 mm. The initial length of the tested strips was 120 mm because of better handling, and the gripping distance was 50 mm. A $1 \text{ mm} \cdot \text{min}^{-1}$ testing rate was applied until 0.5 % deformation was reached, and then the rates were increased to $20 \text{ mm} \cdot \text{min}^{-1}$. Average values of the tensile strength, elongation at break, and Young's modulus were determined from the stress-strain curves.

4. Results and Discussions

PLA/PHB/ATBC solutions with 5, 10, 15, 20, and 30 wt.% biochar content were electrospun in the conditions mentioned above in 2. Methods. The color of the electrospun mats reflected the biochar content, as shown in ►Figure 1. The higher the biochar content, the darker the mats. Such electrospun mats were prepared for subsequent characterization, and their morphology, thermal, and mechanical properties were evaluated.

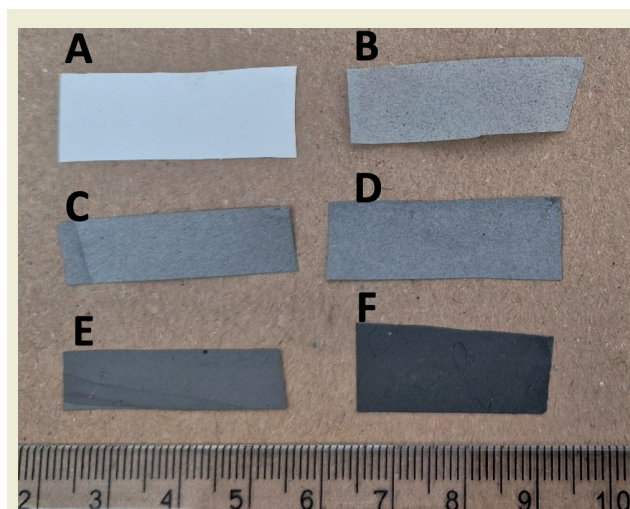


Figure 1. Evidence of color change of the electrospun mats with increasing biochar content in the solution. A – neat PLA/PHB (reference, sample without biochar), B – PLA/PHB + 5% biochar, C – PLA/PHB + 10% biochar, D – PLA/PHB + 15% biochar, E – PLA/PHB + 20% biochar, and F – PLA/PHB + 30% biochar.

4.1. Scanning electron microscopy

►Figure 2 shows the scanning electron microscopy images of the investigated samples. The investigation was carried out to check the fibrous structure and determine the fiber diameter depending on the increasing contents of biochar in the polymer solution used for electrospinning.

►Figure 2A presents the morphology of neat PLA/PHB fibers, demonstrating an average diameter of 460 ± 380 nm. While incorporating biochar did not significantly impact the average fiber diameter, it notably reduced the standard deviation (SD) from 380 nm (►Figure 2A) to 190 nm (►Figure 2F). This decrease suggests enhanced fiber uniformity, potentially attributed to increased solution conductivity during electrospinning by

adding the higher content of biochar.

While ►Figure 2B-2F shows the complete integration of biochar particles into the fiber structure, it is evident that the distribution of these particles within the mats is uneven. This uneven distribution may impact the overall properties of the material, especially the mechanical ones.

4.2. FTIR and RAMAN spectroscopy

The Raman spectra in ►Figure 3A confirmed the formation of the stable C–C bonds, indicating D- and G-bands formation.

These two prominent bands are observed at 1576 and 1355 cm^{-1} . The peak at 1576 cm^{-1} (G-band) is attributed to the vibration of sp^2 hybridized carbon atoms in a 2D hexagonal lattice, the peak at 1355 cm^{-1} (D-band) is associated with the vibrations of carbon atoms with dangling bonds inplane terminations of the disordered graphite from the defects and disorders of structures in carbon materials [14]. The D-band intensity ratio (148,076) to G-band (134,147) peaks depend on the type of graphitic materials and reflect the graphitization degree; in this case, the ratio of intensities (ID/IG) is 1,104.

FTIR analysis was carried out to determine the composites' chemical structure change. The FTIR spectra of the neat polymer blend and composite are presented in ►Figure 3B. The spectra were typical for PLA/PHB. The 753 and 871 cm^{-1} peaks indicate that plasticized PLA possesses a semicrystalline morphology.

The three absorption bands centered at 970 cm^{-1} , 868 cm^{-1} , and 1450 cm^{-1} correspond to the motions of the plasticizer's C–O and C–C stretching vibrations and the $-\text{CH}_3$ stretching vibration of PLA, PHB, and citrate ester molecules and reduced as their contents increased. The FTIR spectra of plasticized PLA/PHB indicate molecular interactions between PLA/PHB and citrate esters. The interaction between PLA and citrate esters may be attributed to the possible hydrogen bonding between the C=O group and the small number of terminal hydroxyl groups in the PLA main chain. The band supports this claim at 1757 cm^{-1} and shows peaks between 2941 cm^{-1} and 2996 cm^{-1} , corresponding to hydroxyl group stretching. The peaks at about $1100 - 1380 \text{ cm}^{-1}$ correspond to the C–O–C, C–O stretching, and CH_3 wagging of PHB [14].

No difference in the infrared pattern was revealed when the biochar was incorporated into the composite composition. The reason may be that biochar is almost completely integrated into the structure of PLA/PHB polymer fibers, supported by SEM images. Still, biochar has similar groups to PLA or PHB (►Figure 3A, FTIR of biochar), and the bands overlap, or there are no interactions between the biochar and polymer.

4.3. Thermal analysis

TGA analysis was used to determine the thermal stability of the neat PLA/PHB and composites PLA/PHB-biochar with various biochar contents. The neat PLA/PHB TGA shown in ►Figures 4A and 4B has multiple mass loss steps corresponding to the blend's single materials. The temperature of the maximum decomposition peak, around 272 °C, was assigned to PHB, and the second one was around 350 °C for PLA. These values are in agreement with the results reported in [15]. ►Figures 4A and 4B also show that the increasing content of biochar slightly increases the decomposition temperature of PHB from 272 to 282 °C. Still, the maximum decomposition temperature of PLA decreased from 352 to 330 °C. This situation can result from in-

creased biochar and better heat transfer, which for PLA increases with increased orientation and crystallization of the molecular chains and stronger molecular chain interactions [7].

DSC analysis was used to follow changes caused by cold crystallization characterized by temperature (T_{CC}) and enthalpy (ΔH_{CC}) and the melting process represented by melting temperature (T_m) and enthalpy (ΔH_m). As previously described [16], T_{CC} and T_m of neat PLA are at 60.3 °C and 150 °C, respectively. Likewise, the neat PHB shows T_{CC} and T_m at 90 °C and 180 °C, respectively. The PLA/PHB blend containing plasticizer was exhibited; therefore, only one T_{CC} was observed, indicating good system miscibility. In addition, two melting peaks at

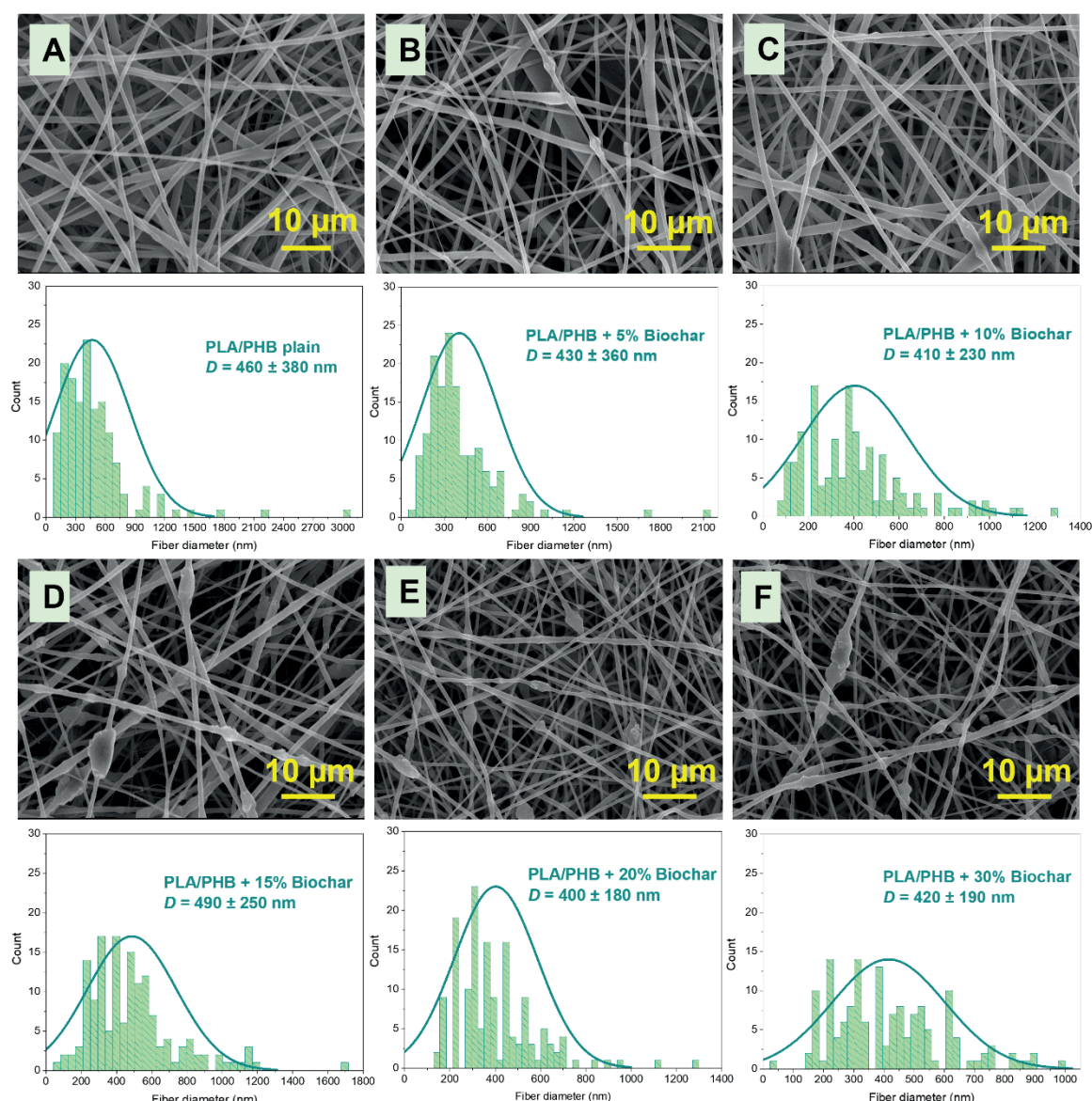


Figure 2. SEM images and histograms of fiber diameters. The image A – neat PLA/PHB (reference sample, without biochar), B – PLA/PHB + 5% biochar, C – PLA/PHB + 10% biochar, D – PLA/PHB + 15% biochar, E – PLA/PHB + 20% biochar, and F – PLA/PHB + 30% biochar. The images were taken at x2000 magnification. Below each image is a corresponding histogram of fiber diameters.

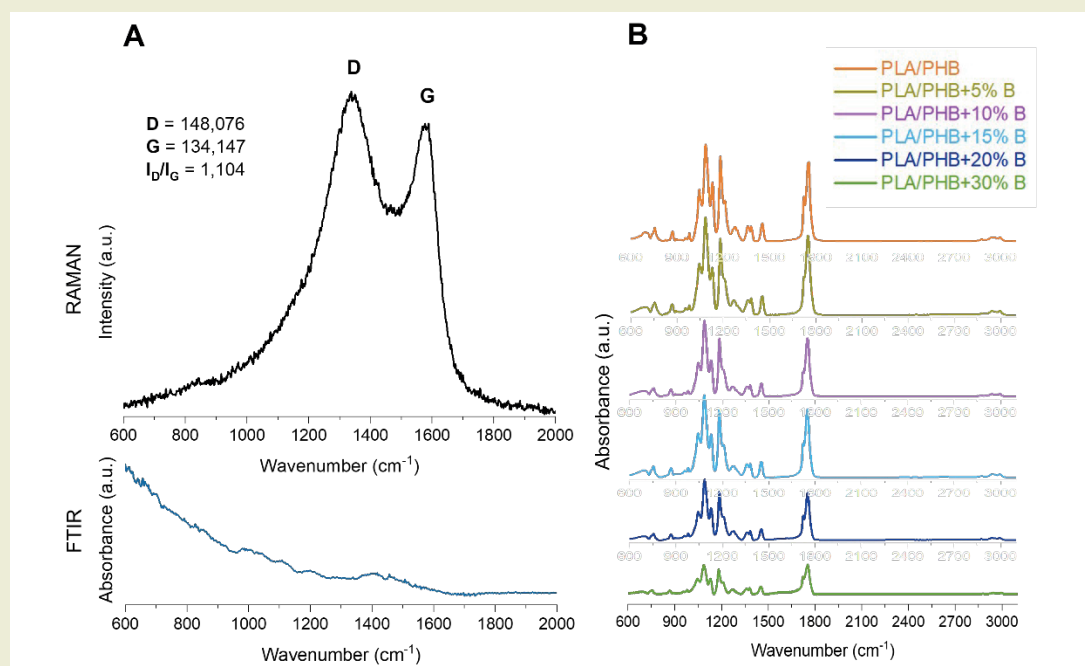


Figure 3. RAMAN and FTIR spectra of biochar (A) and PLA/PHB-biochar composites (B).

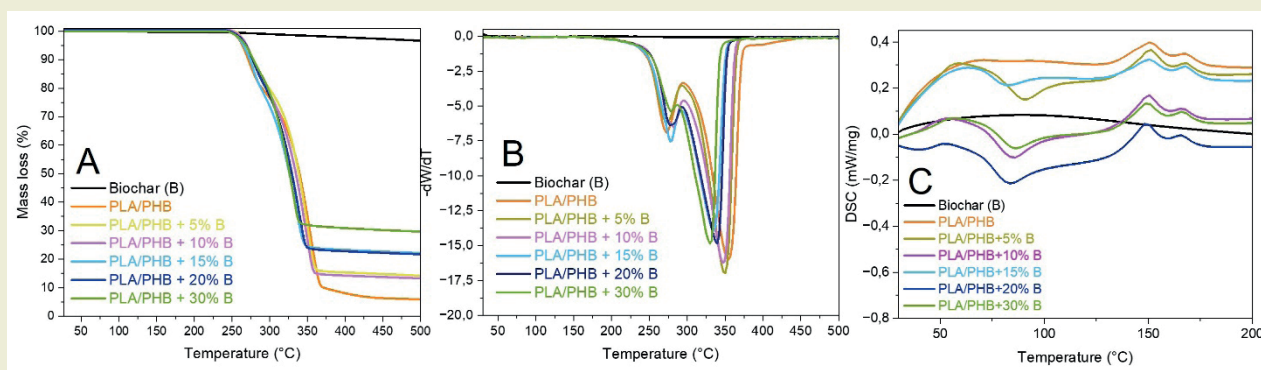


Figure 4. TGA (A), DTGA (B), and DSC (C) spectra of biochar, neat PLA/PHB, and PLA/PHB-biochar fibrous composites.

150 and 170 °C for PLA and PHB crystals, respectively, were observed during the first heating cycle, how as shown in ►Figure 4C.

The loadings of the biochar changed the T_{CC} , which decreased with adding biochar. The values are summarized in ►Table 2. The lowest T_{CC} was measured in PLA/PHB+15%B. The changes of T_{m1} and T_{m2} were less significant. However, there was not a clear trend, and the T_{CC} , T_{m1} , and T_{m2} fluctuated with the increasing content of biochar, possibly due to the uneven distribution of biochar in electrospun fibers. Despite that, it can be said that adding biochar does not significantly impact the thermal stability of the polymer blends, which may be advantageous in subsequent applications.

4.4. Mechanical properties

The tensile properties of the polymer blends and composites are significantly affected by compatibilizers and filler particles. The results of mechanical testing

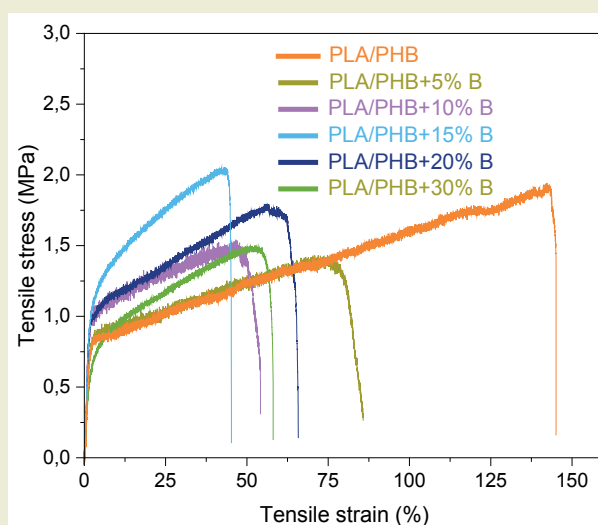


Figure 5. Stress - strain curves of electrospun PLA/PHB and bio-composites PLA/PHB with various biochar content.

Table 1. Summarized results of mechanical testing of plasticized PLA/PHB blend and composites differ in biochar loading.

Description	Tensile stress at tensile strength (MPa)	Tensile strain at break (%)	Young's modulus (MPa)
PLA/PHB	2.31 ± 0.22	161 ± 22.8	55.7 ± 11.3
PLA/PHB + 5% Biochar	1.37 ± 0.13	101 ± 29.2	64.3 ± 11.9
PLA/PHB+10% Biochar	1.54 ± 0.15	53.8 ± 12.9	81.7 ± 15.7
PLA/PHB+15% Biochar	1.90 ± 0.15	37.8 ± 11.3	79.1 ± 12.3
PLA/PHB+20% Biochar	1.81 ± 0.21	63.2 ± 6.83	77.5 ± 10.7
PLA/PHB+30% Biochar	1.40 ± 0.17	59.7 ± 10.9	39.1 ± 8.56

Table 2. DSC analysis of PLA/PHB and PLA/PHB+B mats.

Code	T _{cc} [°C]	T _{m1} (PLA) [°C]	T _{m2} (PHB) [°C]	ΔH _{cc} [J.g ⁻¹]	ΔH _{m1} [J.g ⁻¹]	ΔH _{m2} [J.g ⁻¹]
PLA/PHB	103.8	150.1	171.4	-0.1	6.8	0.4
PLA/PHB+5%B	89.8	150.1	168.5	-10.0	7.9	0.8
PLA/PHB+10%B	85.2	149.7	168.3	-7.7	8.6	0.7
PLA/PHB+15%B	79.8	149.2	166.9	-3.1	4.9	1.0
PLA/PHB+20%B	83.4	148.9	168.3	-4.6	6.2	0.7
PLA/PHB+30%B	82.5	148.1	167.2	-3.9	4.4	1.1

of plasticized PLA/PHB blend and composites differ in biochar loading are summarized in ►Table 1. The stress-strain curves for plasticized PLA/PHB blend and PLA/PHB reinforced with 5, 10, 15, 20, and 30 wt.% are shown in ►Figure 5. As is seen, adding 5 wt.% of biochar leads to a significant decline of elongation at break. It reaches half value compared to the unfilled blend due to the unequal distribution of filler particles in the composite volume. In addition, with increasing biochar loading, the reinforcing effect was manifested by tensile strength increase with a simultaneous drop in percentage elongation up to 15 wt.% biochar content. The decrease in tensile strength was also detected at higher biochar loading due to higher interfacial tension within multiphase composites, leading to the deterioration of mechanical properties.

The uneven distribution of biochar may cause values to fluctuate, in this case, also due to the thickness of the mats. Since it is impossible to control the thickness of the sample fully in a single-needle electrospinning device, the high standard deviation of tensile test results. The influence of biochar content on mechanical properties needs a more profound study in the future.

5. Conclusion

The study aims to design fibrous composites with kitchen waste-derived biochar as filler to biodegradable polymers for a sustainable way to manage kitchen waste. Such composites are an exciting alternative to expensive biodegradable polymers and could reduce the price of biodegradable polymers. In the study, the fibrous composites PLA/PHB + biochar were prepared using the electrospinning method and elementary characterization of such composites were carried out. The mor-

phology of electrospun mats was studied by SEM. The fibers with an average diameter of 400 – 500 nm were received, and there was not observed a significant effect of the percentual content of biochar in the solutions. All the biochar particles were capsulated into the structure of the fibers, which was observed in SEM images but also confirmed with spectroscopy; only the polymers left traces in the spectroscopic spectra. The thermal analysis revealed that biochar addition does not significantly impact the thermal stability of the polymer blends. The mechanical properties were most affected as both tensile strength and strain to stress were reduced, which may limit the practical use of these fiber mats. In the future, it is necessary to pay more attention to the compatibility of individual components in the composite, including validating the sustainability of waste utilization for biochar production, or the usability and feasibility of the composite in the individual applications such as the packaging industry, filtration, or as agrotexile.

Acknowledgements

None

Research ethics

Not applicable.

Author contributions

Conceptualization: [Alena Opálková Šišková, Naďa Beronská], Methodology: [Alena Opálková Šišková, Tomáš Dvůrák, Andrej Opálek, Katarína Mosnáčková, Viera Dujnič], Formal Analysis: [Tomáš Dvůrák, Andrej Opálek, Katarína Mosnáčková, Viera Dujnič], Investigation: [Alena Opálková Šišková, Katarína Mosnáčková], Resources: [Alena Opálková Šišková, Naďa Beronská],

Data Curation: [Alena Opálková Šišková, Tomáš Dvorák, Naďa Beronská], Writing - Original Draft Preparation: [Alena Opálková Šišková, Katarína Mosnáčková], Writing - Review & Editing: [Alena Opálková Šišková, Katarína Mosnáčková, Naďa Beronská], Visualization: [Tomáš Dvorák, Andrej Opálek, Katarína Mosnáčková, Viera Dujnič], Supervision: [Alena Opálková Šišková, Naďa Beronská], Project Administration: [Alena Opálková Šišková, Naďa Beronská], Funding Acquisition: [Alena Opálková Šišková, Naďa Beronská]

Competing interests

The author(s) declare(s) no conflict of interest.

Research funding

This work was supported by the Scientific Grant Agency of the Ministry of Education, Research, Development and Youth of the Slovak Republic and the Slovak Academy of Sciences with project VEGA 2/0136/24. Work is based upon work from COST Action (CA20133), FULLRE-CO4US-Cross-border transfer and development of sus-

tainable resource recovery strategies towards zero waste, supported by COST (European Cooperation in Science and Technology), a funding agency for research and innovation networks.

Data availability

The raw data can be obtained on request from the corresponding author.

Peer-review

Externally peer-reviewed.


Orcid

Alena Opálková Šišková  <https://orcid.org/0000-0003-4582-9114>

Tomáš Dvorák  <https://orcid.org/0009-0005-7080-3567>

Andrej Opálek  <https://orcid.org/0000-0001-8311-254X>

Katarína Mosnáčková  <https://orcid.org/0000-0003-1325-7449>

Viera Dujnič  <https://orcid.org/0000-0001-8647-7165>

Naďa Beronská  <https://orcid.org/0000-0003-1527-922X>

References

- [1] Zhao, X., Wang, Y., Chen, X., Yu, X., Li, W., Zhang, S., Meng, X., Zhao, Z. M., Dong, T., Andreson, A., Aiyedun, A., Li, Y., Webb, E., Wu, Z., Kunc, V., Ragauskas, A., Ozcan, S., Hogli, & Zhu. (2023). Sustainable bioplastics derived from renewable natural resources for food packaging. *Matter*, 6(1), 97-127. <https://doi.org/10.1016/j.matt.2022.11.006>
- [2] Rosenboom, J. G., Langer, R., & Traverso, G. (2022). Bioplastics for a circular economy. *Nature Reviews Materials*, 7, 117-137. <https://doi.org/10.1038/s41578-021-00407-8>
- [3] Popa, M. S., Frone, A. N., & Panaitescu, D. M. (2022). Polyhydroxybutyrate blends: A solution for biodegradable packaging? *International Journal of Biological Macromolecules*, 207, 263-277. <https://doi.org/10.1016/j.ijbiomac.2022.02.185>
- [4] Balakrishnan, S., Atayo, A., & Asmatulu, E. (2024). Machine learning applications for electrospun nanofibers: A review. *Journal of Materials Science*, 59, 14095-15140. <https://doi.org/10.1007/s10853-024-09994-7>
- [5] Arrieta, M. P., Perdiguer, M., Fiori, S., Kenny, J. M., & Peponi, L. (2020). Biodegradable electrospun PLA-PHB fibers plasticized with oligomeric lactic acid. *Polymer Degradation and Stability*, 179, 109226. <https://doi.org/10.1016/j.polymdegradstab.2020.109226>
- [6] Arrieta, M. P., Díez García, A., López, D., Fiori, S., & Peponi, L. (2019). Antioxidant bilayers based on PHBV and plasticized electrospun PLA-PHB fibers encapsulating catechin. *Nanomaterials*, 9(3), 346. <https://doi.org/10.3390/nano9030346>
- [7] Aydemir, D., & Gardner, D. J. (2020). Biopolymer blends of polyhydroxybutyrate and polylactic acid reinforced with cellulose nanofibers. *Carbohydrate Polymers*, 250, 116867. <https://doi.org/10.1016/j.carbpol.2020.116867>
- [8] Musioł, M., Rydz, J., Janeczek, H., Andrzejewski, J., Cristea, M., Musioł, K., Kampik, M., & Kowalczyk, M. (2024). (Bio)degradable biochar composites of PLA/P(3HB-co-4HB) commercial blend for sustainable future—Study on degradation and electrostatic properties. *Polymers*, 16(16), 2331. <https://doi.org/10.3390/polym16162331>
- [9] Selvarajoo, A., Wong, Y. L., Khoo, K. S., Chen, W. H., & Show, P. L. (2022). Biochar production via pyrolysis of citrus peel fruit waste as a potential usage as solid biofuel. *Chemosphere*, 294, 133671. <https://doi.org/10.1016/j.chemosphere.2022.133671>
- [10] Hu, L., Qin, R., Zhou, L., Hua, D., Li, K., & He, X. (2023). Effects of orange peel biochar and cipangopaludina chinensis shell powder on soil organic carbon transformation in citrus orchards. *Agronomy*, 13(7), 1801. <https://doi.org/10.3390/agronomy13071801>
- [11] Andrade, T. S., Vakros, J., Mantzavinos, D., & Lianos, P. (2020). Biochar obtained by carbonization of spent coffee grounds and its applications in the construction of an energy storage device. *Chemical Engineering Journal Advances*, 4, 100061. <https://doi.org/10.1016/j.cej.2020.100061>
- [12] World Wide Fund for Nature. (Erişim tarihi: 24.11.2024). Fight climate change by preventing food waste. WWF Stories.
- [13] Opálková Šišková, A., Dvorák, T., Šimonová Baranyaiová, T., Šimon, E., Eckstein Andicsová, A., Švajdlenková, H., Opálek, A., Krížik, P., & Nosko, M. (2020). Simple and eco-friendly route from agro-food waste to water pollutants removal. *Materials*, 13(23), 5424. <https://doi.org/10.3390/ma13235424>
- [14] Maiza, M., Benaniba, M. T., & Massardier-Nageotte, V. (2015). Plasticizing effects of citrate esters on properties of poly(lactic acid). *Journal of Polymer Engineering*, 36(4), 371-380. <https://doi.org/10.1515/polyeng-2015-0140>
- [15] Radu, E. R., Panaitescu, D. M., Nicolae, C. A., Gabor, R. A., Raditoiu, V., Stoian, S., Alexandrescu, E., Frierascu, R., Ioana, C., & Radu, F. (2021). The soil biodegradability of structured composites based on cellulose cardboard and blends of polylactic acid and polyhydroxybutyrate. *Journal of Polymers and the Environment*, 29, 2310-2320. <https://doi.org/10.1007/s10924-020-02017-x>
- [16] Mosnáčková, K., Danko, M., Šišková, A., Falco, L. M., Janigová, I., Chmela, Š., Vanovčanová, Z., Omaničková, L., Chodák, I., & Mosnáček, J. (2017). Complex study of the physical properties of a poly(lactic acid)/poly(3-hydroxybutyrate) blend and its carbon black composite during various outdoor and laboratory aging conditions. *RSC Advances*, 7(74), 47132-47142. <https://doi.org/10.1039/C7RA08869H>

Effect of annealing on tensile properties of carbon fiber reinforced PA 6 manufactured by fused deposition modeling

Mislav Tujmer^{1*} , Ana Pilipović¹ 

¹ University of Zagreb, Faculty of Mechanical Engineering and Naval Architecture, Ivana Lučića 5, 10000 Zagreb, Croatia

Abstract: Development of fiber reinforced filaments for fused deposition modeling - FDM shifted this technology application towards load carrying applications. For polymer materials reinforced with carbon fibers, it is important to carry out annealing of printed products to improve the mechanical properties. In this paper ANOVA approach was used to evaluate the effect of temperature and time of the annealing treatment of PA 6 filament reinforced with short carbon fibers (PA 6 - CF). Results indicate that higher temperatures (between 110 °C – 170 °C) result in better effects on tensile properties while duration of the annealing effect was negligible in most cases. An increase of up to 16.7% in tensile strength and up to 35% in tensile modulus can be achieved with proper annealing parameters. In some cases, annealing results in a decrease in tensile strain at break up to 35%. The p-values for tensile strength, strain and modulus are 0.0038, 0.0054, 0.0168, respectively, which indicates that the selected model of the influence of annealing parameters is significant because the p-value must be less than 0.05. The highest improvement in tensile strength and modulus was observed at a temperature of 170 °C, but this temperature is close to the softening temperature of PA 6 - CF, which is approximately 180 °C before annealing, which risks deformation of products.

Keywords: annealing; carbon fiber; fused deposition modeling - FDM; poly(amide) 6 - PA6; tensile properties.

1. Introduction

Additive technology opens the possibilities of design and functionality due to its material adding working principle. Until recently its application was common in areas where mechanical performance of printed parts was secondary or irrelevant such as visualization models, everyday usage products, customized parts or art pieces. Development of fiber reinforced polymer filament in fused deposition modeling enhances the load carrying capabilities of printed products. A better understanding of the impact of process parameters on mechanical properties has led to an optimized printing of various polymer materials [1]. One of the main setbacks of printed products is bad interlayer adhesion caused by rapid temperature crystallization and cooling of the previously printed layers. [2] This effect is enhanced in fiber reinforced polymers since the conductivity of fibers results in heat dissipation through the layer in longitudinal direction, rather through the thickness of the layer and reaching the layer underneath. Thus, poor adhesion is result of insufficient heating of the previously laid material. [3] Annealing at

temperatures higher than glass transition temperature increases the interfacial bond contact which strengthens the material. [4] The influence of annealing has been research for commonly used printing materials such as PLA [5], ABS [3] and PETG [6]. In most cases annealing increased mechanical properties of materials and reinforcement made them more suitable for annealing. The influence of annealing parameters (pressure and temperature) [7] on the mechanical properties is most often observed in the papers, but in this paper the influence of temperature and time on the tensile properties will be observed. This selection of input parameters is because most 3D printers already have only time and temperature included in their program, and these two parameters can be easily checked and compared because it is possible to do it in ordinary ovens as well. Furthermore, this selection of parameters was chosen primarily due to the industrial application itself, because time is economically important for the product to reach the market as soon as possible, accordingly, it is necessary to determine whether time has an impact on the improvement of mechanical properties through post-processing heat

*Corresponding author:

Email: mislav.tujmer@fsb.unizg.hr

Cite this article as:

Tujmer, M., Pilipović, A. (2025). Electrospun biopolymer blends of poly(lactic acid) and poly(hydroxybutyrate) reinforced with biochar derived from kitchen waste. *European Mechanical Science*, 9(1): 8-15. <https://doi.org/10.26701/ems.1595060>

History dates:

Received: 03.12.2024, Revision Request: 21.01.2025, Last Revision Received: 26.01.2025, Accepted: 26.01.2025



© Author(s) 2025. This work is distributed under <https://creativecommons.org/licenses/by/4.0/>



treatment. Furthermore, it is important to mention that all tests were carried out on a *Makerbot* 3D printer, on which the manufacturer recommends annealing PA6 reinforced with carbon fibers for 5 hours at a temperature of 80 °C. [8] In previous literature, authors examined the effect of annealing at different temperatures, and some of the most commonly used materials in fused deposition modeling, such as PLA and PET-G, were tested at a temperature of 90 °C, or according to the material manufacturer, PA-CF at 80 °C. [9-14] However, preliminary tests have shown that such a temperature does not have much effect on the mechanical properties, primarily strength and modulus, and that it is necessary to conduct tests at higher temperatures.

2. Materials and Methods

The manufacturing method for test specimens was fused deposition modeling - FDM. Tensile test specimens were printed on a *Makerbot Method X* 3D printer using original *Makerbot* PA6-CF material. Material was dried for 24 hours in 60 °C in oven (manufacturer *Falc*) before printing of test specimens. Test specimens dimension was 75 × 5 × 2 mm in accordance with standard HRN EN ISO 527:2019 type 1BA for tensile testing of plastics (ISO 527 Plastics — Determination of tensile properties). Printing parameters are set up in *Makerbot Print* slicer and shown in ►Table 1. The choice of processing parameters in fused deposition modeling plays a major role in mechanical properties, but as the paper aimed to show the influence of post-processing heat treatment, all parameters were taken according to the default printer parameters for this material.

Table 1. Printing parameters

Printing parameter	Value
Layer height [mm]	0.2
Number of shells	3
Infill density	30%
Infill pattern	Rectilinear
Nozzle temperature [°C]	250
Chamber temperature [°C]	80
Nozzle diameter [mm]	0.4
Raft	none

Statistical analysis was used for designing the parameters of annealing by Design Expert software (manufacturer *Stat Ease*). A central composite design of experiment was used where tensile strength, tensile strain and modulus were set up as response. Temperature and time were chosen as variables for the annealing treatment as those are the most influential parameters according to the literature review. Glass transition temperature of polyamide is between 45 °C – 70 °C [9] and common annealing times are from 6 up to 8 hours. Variables with 2

and 3 hours for the duration of the treatment are chosen to see how a shorter period in a combination with higher temperatures compares to other conditions. Instead of melt transition temperature, Vicat softening temperature according to standard HRN EN ISO 306:2022 was used to make sure the shape and dimensions are constant during the annealing. Vicat testing method B120 served as the purpose of defining the top temperature limit of the material for the annealing experiment. The Vicat softening temperature was measured on a Frank device, with a Tinius Olsen displacement gauge with a measuring range from 0 mm to 1.2 mm in 0.01 mm increments. Vicat test shown in ►Figure 1. resulted in temperatures 179.23 ± 4.1. °C without annealing and 188.13 ± 0.4 °C after annealing according to manufacturers guidelines (80 °C, 5 hours). First, a preliminary annealing experiment was made where the limits of the input factors for the temperature was 50 °C to 110 °C and the annealing time is from 2 h to 8 h. At these temperatures, the properties did not change at all, and it was decided to increase the annealing temperatures to the temperature close to Vicat softening temperature and set up a new experiment with limits for temperature from 50 °C to 170 °C and time from 2 h to 8 h.

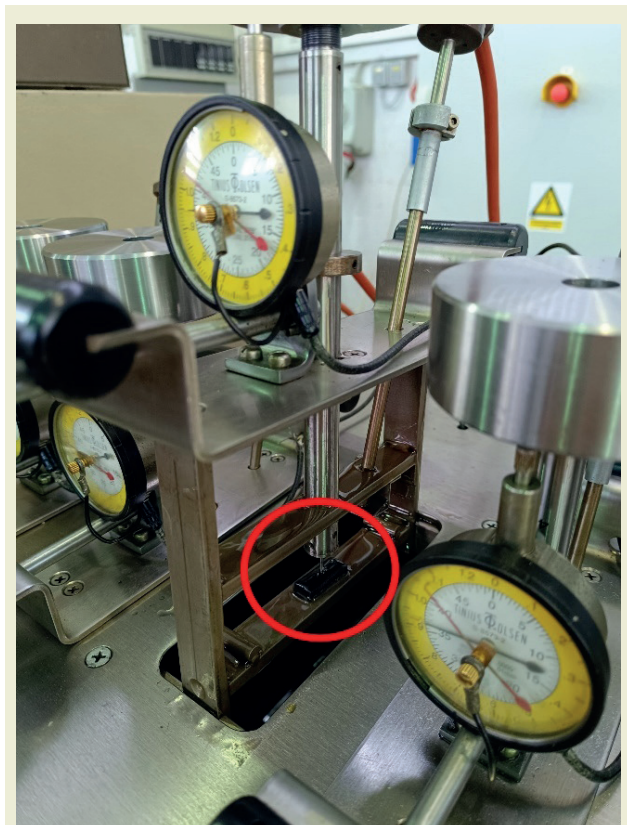


Figure 1. Vicat testing. The red circle in the figure shows the position of the test specimen during the Vicat softening temperature test. The test specimen is then lowered into the heated oil and when the test needle penetrates the specimen to a depth of 1 mm, the softening temperature value is recorded.

Test specimens for tensile properties were printed in plank face down position, so no support structures were

required. PVA glue was used to assure adhesion during printing, the residue of the glue was cleaned with a damp towel. Annealing treatment was done in *Falc* oven with closed air. The temperature range in the oven is up to a maximum of 300 °C, where air circulation can be turned on or off. The temperature can be adjusted in steps of 0.5 °C. Test specimens placed inside the oven chamber are shown in ►Figure 2.



Figure 2. Annealing of the tensile test specimens in the oven

A universal tensile testing machine was used for the test procedure (Shimadzu AGS-X max force 10 kN, manufacturer *Shimadzu*) with extensometer. The universal testing machine is in the measurement range from 10 N to 10 kN and is in the accuracy class of the measurement range 0.5 with an extensometer with a resolution of 0.003 mm, which meets all the requirements of the calibration standard HRN EN ISO 9513:2012. Testing was performed in accordance with standard HRN EN ISO 527:2019 at room temperature of 20 °C and 40% RH. The testing speed was 2 mm/min. Treated test specimens are compared to non-treated ones designated 0_1. The test was performed on 3 test specimens and

the mean value and standard deviation were then calculated.

3. Results and Discussions

Variables used in an annealing experiment with results are shown in ►Table 2. The effect of annealing procedure on the tensile properties of PA6-CF was tested according to the design of the experiment generated by software Design Expert, using response surface methodology. Data acquired by testing were processed by ANOVA (analysis of variance) linear modeling method with three center points.

►Figure 3 shows tensile stress and strain across all variables. Untreated test specimen (designation 0_1) has 28.4 N/mm² tensile strength and the highest result was 34.1 N/mm² in case of 9_1 test specimen. The average increase of tensile strength at break was 7.5%. Modulus has increased on average 14.8% while strain at break was decreased in cases with higher temperature treatment (above 150 °C) and on average was 21.7%.

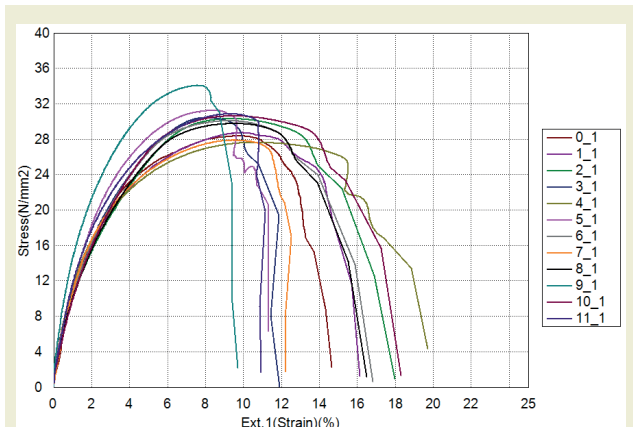


Figure 3. Diagram of tensile stress – strain for PA6-CF with different annealing factors. Each line represents the mean value obtained when measuring individual test specimens in each condition.

Table 2. Annealing factors (time and temperature) and results of the tensile testing

Run	Designation	Factor 1: Time t, h	Factor 2: Temperature θ, °C	Tensile strength σ_m [N/mm ²]	Tensile strain at break ϵ_b [mm/ mm]	Tensile modulus E [N/mm ²]
0	0_1	-	-	28.41 +/- 1.45	13.25 +/- 2.38	1060.82 +/- 545.32
1	1_1	5	50	28.78 +/- 1.59	14.71 +/- 2.82	1317.92 +/- 220.99
2	2_1	5	110	30.33 +/- 0.94	13.95 +/- 1.16	1007.68 +/- 170.73
3	3_1	7	150	30.74 +/- 0.63	10.13 +/- 1.66	1196.46 +/- 272.86
4	4_1	7	70	27.69 +/- 1.59	17.54 +/- 1.77	1270.22 +/- 184.78
5	5_1	3	150	31.53 +/- 1.58	11.24 +/- 0.68	1330.02 +/- 203.92
6	6_1	5	110	30.08 +/- 1.71	12.61 +/- 0.99	1096.69 +/- 249.68
7	7_1	3	70	27.92 +/- 0.97	11.9 +/- 0.77	1127.96 +/- 110.93
8	8_1	2	110	29.78 +/- 1.26	12.76 +/- 0.62	1106.7 +/- 124.4
9	9_1	5	170	34.1 +/- 1.82	8.32 +/- 0.78	1640.9 +/- 229.1
10	10_1	8	110	30.72 +/- 1.19	14.53 +/- 0.79	943.19 +/- 251.37
11	11_1	5	110	30.88 +/- 1.54	10.68 +/- 2.04	1283.07 +/- 75.29

Table 3. Analysis of variance – influence of annealing time and temperature on tensile strength

Source	Sum of Squares	df	Mean Square	F-value	p-value	
Model	25.24	2	12.62	13.65	0.0038	significant
A-Time	0.0179	1	0.0179	0.0194	0.8932	
B-Temperature	25.23	1	25.23	27.29	0.0012	
Residual	6.47	7	0.9245			
Lack of Fit	6.16	6	1.03	3.24	0.4011	not significant
Pure Error	0.3162	1	0.3162			
Cor Total	31.72	9				

3.1. Results for the tensile strength

ANOVA analysis of variance indicates that the linear interaction model best fits the influence of annealing procedures on the tensile strength. Tensile strength statistical results can be seen in ►Table 3 and ►Table 4.

The model F-value (variation between sample means) of 13.65 implies that the model is significant. There is only a 0.38% chance that an F-value this large could occur due to noise. p-values less than 0.05 indicate that model terms are significant. In this case, factor B, temperature shows a major role in the values of tensile strength. Factor A, time of annealing seems to have a negligible influence on tensile strength. The lack of fit F-value of 3.24 implies that the lack of fit is not significant relative to the pure error. There is a 40.11% chance that a lack of fit F-value this large could occur due to noise. Non-significant lack of fit is good because it means that the model fits.

Statistical data (mean value, standard deviation, and R^2) about the model are given in ►Table 4. The coefficient of determination R^2 is a measure of deviation from the arithmetic mean which is explained by the model. The closer R^2 is to 1, the better the model follows the data, that is, the phenomenon is better explained.

Table 4. Summary statistics about the model for tensile strength

Std. Dev.	0.9615	R^2	0.7960
Mean	30.22	Adjusted R^2	0.7377
C.V. %	3.18	Predicted R^2	0.5303
		Adeq Precision	9.8138

Tensile strength for PA6-CF can be described by Equation (1) in actual parameters:

$$\sigma_m = 25.36965 + 0.022956 \cdot t + 0.043069 \cdot \vartheta \quad (1)$$

where: σ_m (N/mm²) – tensile strength, ϑ (°C) – annealing temperature, t (h) – annealing time.

The obtained equation for tensile strength is determined by the annealing temperature and time in the range, which is shown in ►Table 1, i.e. for an annealing

temperature of 50 °C – 170 °C and for an annealing time of 2 h to 7 hours.

Figure 4 shows the tensile strength dependance on the annealing parameters. The diagram shows that the highest tensile strength is a result of a temperature of 150 °C in both cases of shorten or longest annealing time periods. The diagram shows the lowest values of tensile strength in blue, and the highest values in green lines. From ►Table 3 itself, and thus from the diagram in ►Figure 4, it can be seen that changing the annealing time has no effect on the tensile strength, but rather an increase occurs only when the annealing temperature is increased.

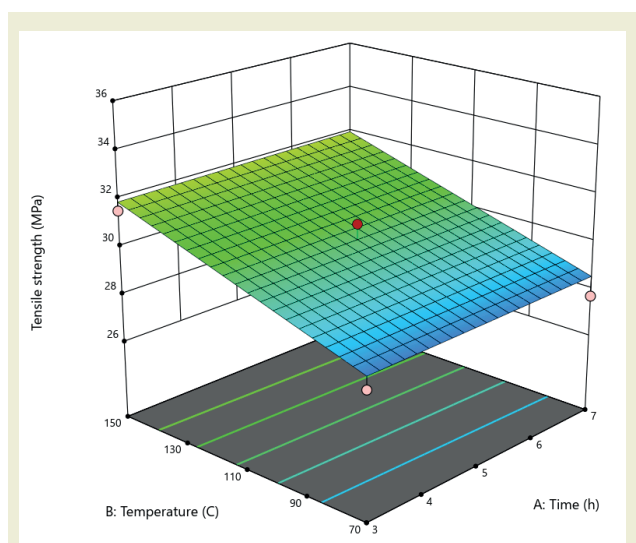


Figure 4. Dependence of annealing parameters (temperature and time) on the tensile strength. Blue fields show the lowest tensile strength values, and green and yellow fields show the highest values.

3.2. Results for the tensile strain at break

ANOVA analysis of variance indicates that the 2-factor interaction (2FI) model best fits the influence of annealing factors on the tensile strain at break. The details of analysis are shown in ►Table 5. The model F-value (variation between sample means) of 12.49 implies that the model is significant. There is only a 0.54% chance that an F-value this large could occur due to noise. P-values less than 0.05 suggest that temperature (factor

Table 5. Analysis of variance – influence of annealing time and temperature on tensile strain at break

Source	Sum of Squares	df	Mean Square	F-value	p-value	
Model	54.13	3	18.04	12.49	0.0054	significant
A-Time	6.04	1	6.04	4.18	0.0868	
B-Temperature	36.70	1	36.70	25.41	0.0024	
AB	11.38	1	11.38	7.88	0.0309	
Residual	8.67	6	1.44			
Lack of Fit	6.81	5	1.36	0.7354	0.7038	not significant
Pure Error	1.85	1	1.85			
Cor Total	62.79	9				

B) has a prevalent effect on tensile strain at break and also interaction of factors AB which can clearly be also seen on ►Table 5 and ►Figure 3. The lack of fit F-value of 0.7354 implies that the lack of fit is not significant relative to the pure error. There is a 70.38% chance that a lack of fit F-value this large could occur due to noise. Non-significant lack of fit is good because it means that the model fits which we want.

Table 6. Summary statistics about the model for tensile strain at break

Std. Dev.	1.20	R ²	0.8620
Mean	12.44	Adjusted R ²	0.7929
C.V. %	9.66	Predicted R ²	0.6873
		Adeq Precision	10.1619

From ►Table 6, it can be concluded that the model followed the data very well since the coefficient of determination is $R^2 = 0.8620$. The predicted R^2 of 0.6873 is in reasonable agreement with the adjusted R^2 of 0.7929; i.e., the difference is less than 0.2. Adequate precision measures the signal to noise ratio. A ratio greater than 4 is desirable. The ratio of 10.1619 indicates an adequate signal.

Tensile strain at break for PA6-CF can be described by Equation (2) in actual parameters:

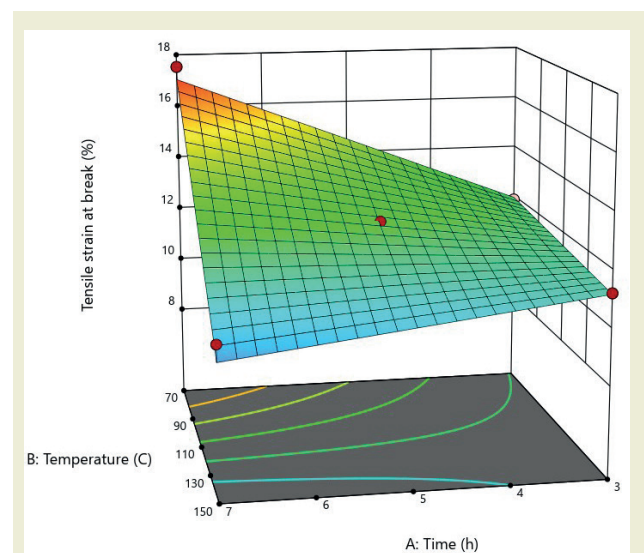
$$\varepsilon = 4.45197 + 2.7408 \cdot t + 0.053468 \cdot \vartheta \quad (2)$$

where: ε (mm/mm) – tensile strain, ϑ (°C) – annealing temperature, t (h) – annealing time.

The obtained equation for tensile strain at break is determined by the annealing temperature and time in the range, which is shown in ►Table 1, i.e. for an annealing temperature of 50 °C – 170 °C and for an annealing time of 2 h to 7 hours.

Figure 5. shows dependence of temperature and time on the tensile strain at break. The highest strain at break is measured in case of 7 hours of annealing time and 70 °C of annealing temperature. An increase in tensile strain

at break is observable with shorter annealing time in combination with lower annealing temperatures which can also be seen from ►Table 2.

**Figure 5.** Dependence of annealing parameters (temperature and time) on the tensile strain at break. Blue fields and contour lines show the lowest strain at break values, while the highest are shown in red.

3.3. Results for the tensile modulus

A quadratic model best fits statistical analysis of the tensile modulus. P-values less than 0.05 indicate model terms are significant. In this case B and B² are significant model terms (Table 7). The lack of fit F-value of 1.59 implies that the lack of fit is not significant relative to the pure error. There is a 51.42% chance that a lack of fit F-value this large could occur due to noise. Non-significant lack of fit is good because it means that the model fits which we want.

From ►Table 8, it can be concluded that the model followed the data very well since the coefficient of determination is $R^2 = 0.9360$.

Tensile modulus for PA6-CF can be described by Equation (3) in actual parameters:

Table 7. Analysis of variance – influence of annealing time and temperature on tensile modulus

Source	Sum of Squares	df	Mean Square	F-value	p-value	
Model	3.346E+05	5	66929.04	11.71	0.0168	significant
A-Time	6584.05	1	6584.05	1.15	0.3436	
B-Temperature	44174.95	1	44174.95	7.73	0.0498	
AB	19019.17	1	19019.17	3.33	0.1422	
A ²	764.90	1	764.90	0.1338	0.7330	
B ²	1.948E+05	1	1.948E+05	34.08	0.0043	
Residual	22865.89	4	5716.47			
Lack of Fit	18904.50	3	6301.50	1.59	0.5142	not significant
Pure Error	3961.39	1	3961.39			

$$E_t = 1812.6056 + 110.6715 \cdot t - 20.0234 \cdot \vartheta - 0.86194 \cdot \vartheta \cdot t - 2.9774 \cdot t^2 + 0.1188 \cdot \vartheta^2 \quad (3)$$

The obtained equation for tensile modulus is determined by the annealing temperature and time in the range, which is shown in ►Table 1, i.e. for an annealing temperature of 50 °C – 170 °C and for an annealing time of 2 h to 7 hours.

where: E_t (N/mm²) – tensile modulus, ϑ (°C) – annealing temperature, t (h) – annealing time.

Table 8. Summary statistics about the model for tensile modulus

Std. Dev.	75.61	R ²	0.9360
Mean	1203.77	Adjusted R ²	0.8561
C.V. %	6.28	Predicted R ²	0.5739
		Adeq Precision	10.3193

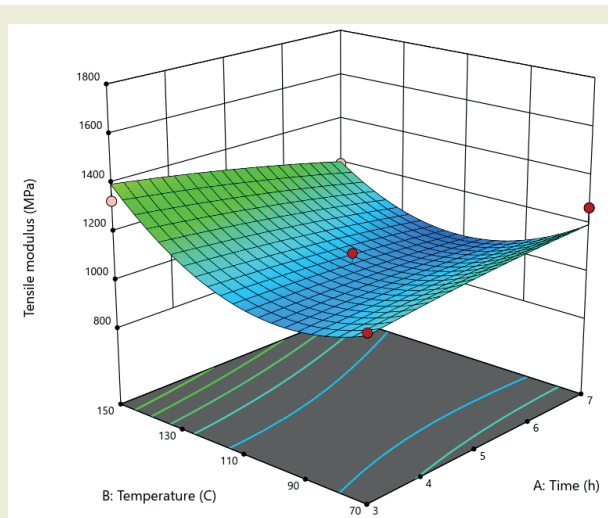


Figure 6. Dependence of annealing parameters (temperature and time) on the tensile modulus. Blue fields and contour lines show the lowest tensile modulus values, and green fields and contour lines show the highest values.

Results shown in ►Figure 6 show that there is a possibility in modifying the modulus of the material with the

combination of higher temperatures and longer duration or shorter duration and lower temperatures. Modulus results show that time does not significantly affect the modulus, but temperature has a range of effects. Or rather as the analysis showed in ►Table 7, the curve of the dependence of temperature and annealing time on the tensile modulus is quadratic and it can be seen that the higher the temperature, the greater the tensile modulus, but also at lower temperatures there is a smaller increase, while time has no effect.

4. Discussion

In previous research, the author Rhugdhriyva, R. attempted to determine the effect of annealing on reinforced ABS material, and result has shown improvement of tensile strength up to 12%. Combination of annealing and uniaxial pressure gives better results for tensile strength. [10]

In [11] author Sudin, M.N. tested ABS for the impact of annealing, and it was concluded that there is no linear relationship between annealing time and temperature for the best tensile strength results. Our results suggest that it does not seem to be the case with PA reinforced with carbon fibres since ►Figure 4 shows a strong linear dependence of temperature on tensile strength.

PA12 specimens reinforced with carbon fiber were annealed at a similar temperature range in [12] resulting in an increase of tensile strength (11%) and a decrease of tensile strain at break (29%) which is similar to our results. A trend of increased annealing temperatures towards higher tensile strength results is also observed in [13]. On the other hand, in [14] PLA, PLA-CF and PETG, PETG-CF were annealed at 90 °C and 120 °C for 6 and 8 hours. In the case of PETG and PETG-CF annealing did not result in any significant change in tensile strength. Annealing of PLA at 90 °C for 6 and 8 hours increased tensile strength for 13% and 17%. PLA-CF showed a decrease of interlayer tensile strength before annealing in comparison to PLA but after annealing at 90 °C for 6 and 8 hours a significant increase was recorded.

From the tests conducted it can be concluded that if one wants to increase the mechanical properties, primarily strength and modulus, it is necessary to go to much higher temperatures, and that temperatures of 80–120 °C as in these previous studies are not sufficient for improvement. The time of even 8 hours mentioned by the author Bhandari, S. et al. [14] is not necessary because time has no effect on the entire tensile properties what this research showed (all p-values > 0.5).

5. Conclusions

Bearing in mind the tensile strength results it can be said that higher temperatures and longer duration are both beneficial for tensile strength and modulus. Combination of temperature and duration of annealing gives various options for material modification in terms of desired modulus or strain at break. Results show that higher temperatures can increase tensile strength up to 16.7% and modulus up to 35%. Strain at break of the materials can be decreased up to 59%. Shorter periods of annealing can replace prolonged duration with the same or even better effect on tensile strength. As a dominant factor across all responses was temperature and we can say that higher temperature is in most cases the best way to modify PA6-CF properties by annealing. Depending on whether higher strength or higher flexibility is required, the appropriate annealing parameters can be selected from the results obtained or the balance between all mechanical properties can be determined.

The obtained equations (equations 1, 2 and 3) for calculating individual output values (strength, modulus and strain) can be of great help in industrial applications because in the mentioned temperature range (50 °C to 170 °C) and time (2 h to 7 h), the values can be calculated immediately and there is no need for individuals in the industry to perform the tests themselves.

This work can serve as a starting point for all other fiber/particle reinforced thermoplastic material where annealing is required, but for each material it is necessary to know the glass transition and melting temperatures in order to determine the limits that must not be exceeded during post-processing heat treatment.

Research ethics

Not applicable.

Author contributions

Conceptualization: [Mislav Tujmer], Methodology: [Mislav Tujmer and Ana Pilipović], Formal Analysis: [Mislav Tujmer and Ana Pilipović], Investigation: [Mislav Tujmer], Data Curation: [Mislav Tujmer], Writing - Original Draft Preparation: [Mislav Tujmer], Writing - Review & Editing: [Ana Pilipović], Visualization: [Ana Pilipović], Supervision: [Ana Pilipović], Funding Acquisition: [Ana Pilipović]

Competing interests

The authors state no conflict of interest.

Research funding

None declared.

Data availability

The raw data can be obtained on request from the corresponding author.

Peer-review

Externally peer-reviewed.

Orcid

Mislav Tujmer  <https://orcid.org/0000-0003-1060-6973>
Ana Pilipović  <https://orcid.org/0000-0003-1330-6458>

References

- [1] Mushtaq, R. T., Wang, Y., Rehman, M., Khan, A. M., Bao, C., Sharma, S., Eldin, S. M., & Abbas, M. (2023). Investigation of the mechanical properties, surface quality, and energy efficiency of a fused filament fabrication for PA6. *Reviews on Advanced Materials Science*, 62(1). doi: 10.1515/rams-2022-0332
- [2] Handwerker, M., Wellnitz, J., Marzbani, H., & Tetzlaff, U. (2021). Annealing of chopped and continuous fibre reinforced polyamide 6 produced by fused filament fabrication. *Composites Part B: Engineering*, 223. doi: 10.1016/j.compositesb.2021.109119
- [3] Seok, W., Jeon, E., & Kim, Y. (2023). Effects of annealing for strength enhancement of FDM 3D-printed ABS reinforced with recycled carbon fiber. *Polymers*, 15(14). doi: 10.3390/polym15143110
- [4] Yilmaz, M., Yilmaz, N. F., & Kalkan, M. F. (2022). Rheology, crystallinity, and mechanical investigation of interlayer adhesion strength by thermal annealing of polyetherimide (PEI/ULTEM 1010) parts produced by 3D printing. *Journal of Materials Engineering and Performance*, 31(12), 9900–9909. doi: 10.1007/s11665-022-07049-z
- [5] Dou, H., Cheng, Y., Ye, W., Zhang, D., Li, J., Miao, Z., & Rudykh, S. (2020). Effect of process parameters on tensile mechanical properties of 3D printing continuous carbon fiber-reinforced PLA composites. *Materials*, 13(17). doi: 10.3390/ma13173850
- [6] Valvez, S., Reis, P. N. B., & Ferreira, J. A. M. (2023). Effect of annealing treatment on mechanical properties of 3D-Printed composites. *Journal of Materials Research and Technology*, 23, 2101–2115. doi: 10.1016/j.jmrt.2023.01.097
- [7] Handwerker, M., Wellnitz, J., Marzbani, H., & Tetzlaff, U. (2023). Pressure and heat treatment of continuous fibre reinforced thermoplastics produced by fused filament fabrication. *Progress in Additive Manufacturing*, 8(2), 99–116. doi: 10.1007/s40964-022-00315-5
- [8] MakerBot Print software. (MakerBot).
- [9] Greco, R., & Nicolais, L. (1976). Glass transition temperature in nylons. *Polymer*, 17(12), 1049–1053. doi: 10.1016/0032-3861(76)90005-7
- [10] Rane, R. (2018). Enhancing tensile strength of FDM parts using thermal annealing and uniaxial pressure (Master's thesis). University of Texas at Arlington. https://mavmatrix.uta.edu/mechaerospace_the-

ses/930

- [11] Sudin, M. N. (2024). Effect of annealing parameters on surface roughness and tensile stress of 3D-printed ABS parts. *El-Cezeri Fen ve Mühendislik Dergisi*. doi: 10.31202/ecjse.1369831
- [12] Ferreira, I., Melo, C., Neto, R., Machado, M., Alves, J. L., & Mould, S. (2020). Study of the annealing influence on the mechanical performance of PA12 and PA12 fibre reinforced FFF printed specimens. *Rapid Prototyping Journal*, 26(10), 1761–1770. doi: 10.1108/RPJ-10-2019-0278
- [13] He, Y., Shen, M., Wang, Q., Wang, T., & Pei, X. (2023). Effects of FDM parameters and annealing on the mechanical and tribological properties of PEEK. *Composite Structures*, 313, 116901. doi: 10.1016/J.COMPSTRUCT.2023.116901
- [14] Bhandari, S., Lopez-Anido, R. A., & Gardner, D. J. (2019). Enhancing the interlayer tensile strength of 3D printed short carbon fiber reinforced PETG and PLA composites via annealing. *Additive Manufacturing*, 30. doi: 10.1016/j.addma.2019.100922

Experimental study on the thermal conductivity of a water-based ternary hybrid nanofluid incorporating MWCNTs-COOH-Fe₃O₄-rGO

Neşe Keklikcioğlu Çakmak^{1*} 

¹Department of Chemical Engineering, Faculty of Engineering, Sivas Cumhuriyet University, Sivas 58140, Türkiye

Abstract: This study explores the thermal conductivity characteristics of ternary nanofluids composed of water-based Fe₃O₄-decorated carboxylated multi-walled carbon nanotubes (MWCNT-COOH), reduced graphene oxide (rGO) and Fe₃O₄-MWCNT-COOH/rGO ternary hybrid nanoparticles. The investigation focuses on the influence of temperature and ternary hybrid nanoparticles concentration. Ultrasonic probes were employed to ensure the stability of the nanofluid and its structural properties were analyzed using scanning electron microscopy (SEM), energy dispersive X-ray spectroscopy (EDX), X-ray powder diffraction (XRD) and Fourier-transform infrared spectroscopy (FT-IR). The transient hot-wire technique was employed to measure the thermal conductivity of all nanofluids. Thermal conductivity measurements were conducted using a KD-2 Pro thermal analyzer across a temperature range of 25-60 °C and a ternary hybrid nanoparticles volume fraction range of 0.025-0.1%. Results demonstrated that the thermal conductivity ratio increased with higher solid volume fractions and elevated temperatures. Notably, the impact of temperature became more significant at higher ternary hybrid nanoparticles concentrations. The findings also revealed a maximum thermal conductivity enhancement of approximately 50%, achieved at a ternary hybrid nanoparticles fraction of 0.1% and a temperature of 60 °C.

Keywords: MWCNTsCOOH- Fe₃O₄-rGO, ultrasonification, thermal conductivity, ternary hybrid nanofluid.

1. Introduction

The main challenge for accelerating nanofluid studies is to enhance the performance of thermal systems such as radiators, heat exchangers, air conditioning devices and refrigerators by improving the thermophysical properties of nanofluids[1]. Choi [2] provided the emergence of the term nanofluid by using nanoparticle additives in the base fluid and in the continuation nanofluid studies, the particles and base fluids were diversified and used in many researches [3-8]. Although nanofluids are considered greatly attractive agents in heat transfer applications, it is not ensured that they have definite performance-enhancing effects [9]. In addition, nanofluids with insufficient stability cannot be applied in pumping systems due to aggregation and sedimentation complications. Problems caused by low stability lead to mechanical failure of thermal system equipment and trigger pollutants, negatively affecting heat transfer. In this concept, configurations have been created on the mono/multiple use of nanofluids and providing long-term stability and many researchers have examined and still

continue to study the positive and negative aspects of the use of designed configurations in heat transfer process [10-16]. The thermal conductivity of nanofluids used in thermal systems is great of importance [17]. The increase in thermal conductivity of nanofluids compared to conventional base fluids is due to the interaction of nanoparticles, which causes an increase in the kinetic motion of molecules at higher temperatures and therefore a higher rate of transfer of heat through the medium. The improvement of thermal conductivity varies depending on many parameters such as volume or weight fraction of the nanofluid, nanoparticle type and shape and nanofluid stability [18, 19]. To address the uncertainty in nanofluid thermal conductivity due to varying parameters, researchers have conducted several studies. For instance, Bakhtiari et al. [20] investigated the influence of temperature and volume fraction on the thermal conductivity of TiO₂-Graphene/Water hybrid nanofluids, concluding that volume fraction had a more significant impact than temperature. Similarly, Taherialekhouhi et al. [21] explored the thermal conductivity characteristics of water-graphene oxide/alumi-

*Corresponding author:

Email: nkeklikcioglu@cumhuriyet.edu.tr

Cite this article as:

Çakmak-Keklikcioğlu, N. (2025). Experimental study on the thermal conductivity of a water-based ternary hybrid nanofluid incorporating MWCNTs-COOH-Fe₃O₄-rGO. *European Mechanical Science*, 9(1): 16-24. <https://doi.org/10.26701/ems.1591623>

History dates:

Received: 26.11.2024, Revision Request: 08.01.2025, Last Revision Received: 22.01.2025, Accepted: 02.03.2025



© Author(s) 2025. This work is distributed under <https://creativecommons.org/licenses/by/4.0/>



num oxide nanoparticles as a potential cooling fluid. In this study, where the temperature and nanofluid volume fraction ranges were indicated as 25–50 °C and 0.1–1%, respectively, it was reported that the parameter of temperature was more triggering in promoting the thermal conductivity. The highest thermal conductivity enhancement of 33.9% was ensured at the configuration of the volume fraction of 1% and temperature of 50 °C. Akghar et al. [22] carried out an experimental investigation to evaluate the changes in thermal conductivity of water ethylene glycol/TiO₂-MWCNT nanofluid under varying temperatures and volume fractions. The results revealed that the volume fraction was increasingly dominant to improve thermal conductivity of hybrid nanofluid relative to temperature. A study by Kazemi et al. [23] investigated the variation of thermal conductivity using mono and hybrid Graphene/SiO₂ nanofluids at variety of volume fractions of 0.051% and temperature range between 25–50 °C. The study resulted with an improvement of 36.12% in thermal conductivity using Graphene-SiO₂/Water hybrid nanofluid. Due to high aspect ratio, superior thermal properties and synergistic relationships of nanoparticles with each other, the idea of producing hybrid nanofluids is triggered and initiated to achieve enhancement in heat transfer and pressure drop properties. In the last 3 years, a new research direction has emerged towards combining different nanoparticles to obtain nanofluids with optimum characteristics: this is the synthesis of three-particle or ternary nanofluids (THyNFs) [24]. Ternary hybrid nanofluids (THyNF) have garnered a lot of interest nowadays because of their exceptional capacity to enhance heat transfer efficiency in comparison to conventional fluids. These innovative nanofluids exhibit significantly higher convective heat transfer coefficients and thermal conductivity, which significantly increases total heat transfer efficiency in a variety of applications [24]. A base fluid is mixed with an exclusive combination of three different kinds of nanoparticles to create these ternary hybrid nanofluids. In order to improve fluid properties, especially thermal and transport ones, ternary hybrid nanofluids combine metallic, oxide, or carbon-based nanoparticles. As a basic fluid transport property, thermal conductivity aids in the comprehension of heat transfer mechanisms and the improvement of thermal management systems. Thermal conductivity affects the power cycle's efficiency and system dependability. Furthermore, accurate fluid thermal conductivity is necessary for the design and development of innovative technologies, including energy storage devices and cooling systems [18,19]. Fluid thermal conductivity has been measured using a variety of techniques. Widely applied and appropriate for fluids, the transient hot-wire (THW) approach has very low uncertainty [20, 21]. The benefits of THW approaches include lowering convective error during experimental data processing and avoiding the end effect by using two wires. Transient hot-wire (THW) approach, which has proven to be reliable, was used in this study.

In this study, an experimental study was conducted

on Fe₃O₄-decorated carboxylated multi-walled carbon nanotubes (MWCNT-COOH)/reduced graphene oxide (Fe₃O₄-MWCNT-COOH/rGO)/water ternary nanofluids to analyze the impact of temperature and ternary hybrid nanoparticles concentration on thermal conductivity.

2. Experimental Section

2.1. Materials

The chemicals utilized in this study included ferrous chloride tetrahydrate (FeCl₂·4H₂O), sodium hydroxide (NaOH), nitric acid (HNO₃, 70%), sulfuric acid (H₂SO₄, 96%) and ferric chloride hexahydrate (FeCl₃·6H₂O). All reagents were sourced from Sigma-Aldrich (Burlington, USA) and were used as received without further purification. Multi-walled carbon nanotubes (MWCNTs), with a purity of approximately 96%, an external diameter of 8–18 nm and lengths ranging from 10–30 μm, were synthesized using catalytic chemical vapor deposition. These were procured in their original form from Nanografi (Turkey).

2.2. Oxidation of MWCNTs

The oxidation of MWCNTs followed a previously established method [25]. A mixture containing 400 mg of MWCNTs and 100 mL of concentrated HNO₃ and H₂SO₄ (in a 1:3 ratio; 25 mL HNO₃ and 75 mL H₂SO₄) was subjected to ultrasonication for 140 minutes. This mixture was then transferred to a flask with a condenser and refluxed under vigorous agitation at 75 °C for six hours. Upon cooling to room temperature, the suspension was centrifuged at 18,000 rpm and the solid residue was washed multiple times with deionized water until the pH of the filtrate approached neutrality. The resulting solid was dried in a vacuum oven at 80 °C for two hours and designated as MWCNT-COOH.

The cutting of MWCNTs served two purposes: (i) to introduce functional –COOH groups and (ii) to enhance the solubility of the MWCNTs in various solvents.

2.3. Synthesis of MWCNT-COOH-Fe₃O₄ Hybrid Nanoparticles

The MWCNT-COOH-Fe₃O₄ hybrid nanoparticles were synthesized via in-situ growth and chemical coprecipitation methods [26, 27]. A solution of 0.35 g MWCNT-COOH in 100 mL of water was stirred for one hour, followed by the addition of FeCl₃ and FeCl₂ salts in a 2:1 molar ratio under continuous stirring. The reaction was performed under a nitrogen atmosphere. Once the iron salts dissolved, turning the solution light orange, water-diluted NaOH was gradually introduced. Within 10 minutes, black precipitates formed, indicating the completion of the reaction. The Fe₃O₄ nanoparticles attached are to the MWCNTs via the –COOH functional groups, which are thin enough to retain the fluid's heat

transfer characteristics when dispersed in water. The precipitates were repeatedly washed with water to eliminate chloride, sodium and hydrogen impurities before being dried at 80 °C for 24 hours. Pure Fe₃O₄ nanoparticles were also synthesized for comparison purposes using the same procedure, but without the addition of MWCNTs to the distilled water.

2.4. Synthesis of MWCNT-COOH-Fe₃O₄-rGO Ternary Hybrid Nanoparticles

The rGO was synthesized from natural graphite powder using a modified Hummers method, later employed to prepare the ternary hybrid nanoparticles [28–34]. Graphite oxide was dispersed in deionized (DI) water and exfoliation into individual sheets was achieved via ultrasonication at room temperature for 1 hour. To remove any unexfoliated graphite oxide, the suspension was centrifuged at 18,000 rpm for 30 minutes. The reduction and purification of rGO involved sonicating a mixture of 0.5 g graphite oxide (GO) and 5 g L-ascorbic acid in 500 mL of deoxygenated water for 30 minutes, followed by stirring at 60 °C for 36 hours. The resulting material was washed, filtered, dried and stored at room temperature. To form the hybrid material, carboxylated MWCNT-Fe₃O₄ was introduced into the rGO suspension. The mixture was vigorously stirred and ultrasonicated for 2 hours at room temperature to promote grafting and ensure the intercalation of MWCNT-COOH-Fe₃O₄ within the rGO nanosheets. The resulting MWCNT-COOH-Fe₃O₄-rGO composite was centrifuged at 18,000 rpm, thoroughly washed with DI water and dried at 80 °C for further characterization and experimentation.

2.5. Characterization

The synthesized ternary hybrid nanoparticles were structurally analyzed using X-ray diffraction (XRD) (Rigaku DMAX IIIC). Morphological features were assessed with a scanning electron microscope (SEM: TESCAN MIRA3 XMU) equipped with an energy-dispersive X-ray spectrometer (EDX). Functional groups were analyzed using Fourier-transform infrared spectroscopy (FTIR: Bruker Tensor II) within the range of 4000–500 cm⁻¹. Specimens were pressed into potassium bromide pellets for FTIR analysis.

2.6. Ultrasound application

The ternary hybrid nanoparticles were dispersed in water at concentrations ranging from 0.025% to 0.1% by volume and temperatures between 25 and 60 °C. Uniform dispersion and stability of the nanofluids were achieved using a 750-W ultrasonic liquid processor (Sonics & Materials Inc., USA, VCX750 sonicator). The nanofluids were under continuous and pulsed ultrasound treatment at 20 kHz for 60 minutes in an ultrasound device. To prevent overheating, a water bath was placed on the walls of the beaker holding the nanofluid.

The ultrasonic probe was positioned inside an acoustic foam sound-reduction enclosure. A cylindrical-diameter, cylindrical-shaped 13 mm tTi6Al4V titanium alloy probe was employed. In the continuous and pulsed processes, the probe was positioned 100 mm above the surface of the nanofluids, 10 mm below, with a frequency of 20 kHz and an amplitude level of 40%. Discrete nanoparticles or lower particle sizes were successfully produced by ultrasonication.

2.7. Thermal conductivity measurement

Nanofluids with varying MWCNT-COOH-Fe₃O₄-rGO ratios were prepared to evaluate their thermal conductivity. A KD2 Pro thermal properties analyzer (Decagon Devices, Inc., Pullman, WA, USA) employing the transient hot-wire technique was used for measurements. Synthesis of ternary hybrid nanoparticles and the thermal conductivity setup are illustrated in ►**Figure 1**. Thermal conductivity measurements were conducted at 25, 35, 45, 55 and 60 °C. Sensor accuracy was validated through repeated calibration with water. Measurements were performed 5 minutes after immersion in a water bath to stabilize temperature. Each test involved 20 readings taken at 15-minute intervals, with the average recorded. Thermal conductivity of the base fluid (water) was measured at the start and end of each experiment, aligning with reported literature values (Table 1, [42]) for verification.

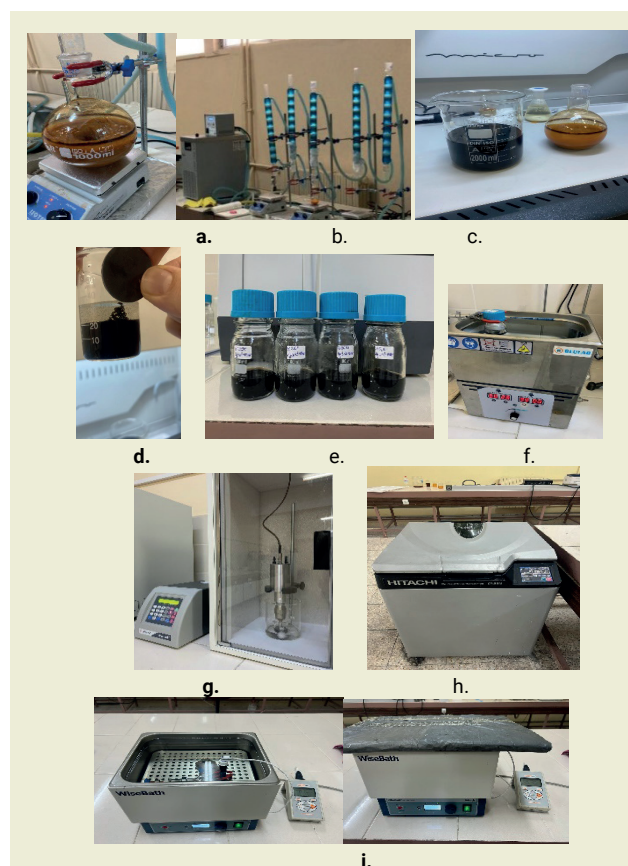


Figure 1. Figures of MWCNT-COOH-Fe₃O₄-rGO-water ternary hybrid nanofluid preparation process (a–e) f. bath sonicator g. probe sonicator h. high speed centrifuge i. thermal conductivity device and water bath.

Table 1. Experimental thermal conductivity (k) of base fluid water as a function of temperature (T)

	$k/(W\ m^{-1}\ K^{-1})$	$k/(W\ m^{-1}\ K^{-1})$
T/K	Measured data	Reference data
298	0.611 ± 0.002	0.6076 [42]
308	0.626 ± 0.002	0.6240 [42]
318	0.638 ± 0.003	0.6380 [42]
328	0.644 ± 0.002	0.6497 [42]
333	0.650 ± 0.004	0.6480 [42]

The “thermal conductivity ratio” is defined as follows to provide a clear investigation:

$$\text{thermal conductivity ratio} = \frac{k_{nf}}{k_{bf}}$$

3. Results and discussion

3.1. SEM Analysis

The particle size and surface morphology of the synthesized samples and hybrid material were analyzed using SEM, as shown in ►Figure 2. The SEM images reveal that carbon nanotubes grew on both sides of the rGO sheets, which exhibit ultrathin, wrinkled, wavy and fibrous structures. The MWCNT-COOH samples appear cylindrical, with curved and entangled morphologies. Furthermore, the Fe_3O_4 nanoparticles are nearly uniform in size and the SEM clearly shows their attachment to the surfaces of MWCNT-COOH.

3.2. SEM-EDX Analysis

SEM-EDX analysis was performed to determine the elemental composition of the samples. This technique provides precise identification and quantification of elements in small sample volumes. The EDX spectra of GO (►Figure 3a), MWCNT-COOH (►Figure 3b), MWCNT-COOH- Fe_3O_4 (Fig. 3c) and MWCNT-COOH- Fe_3O_4 -rGO (Fig. 3d) confirm the successful deposition

of Fe_3O_4 on MWCNT-COOH. The carbon (C) signal originates from the MWCNTs, while the oxygen (O) signal is attributed to functionalization with -COOH groups. The Fe signal confirms the presence of Fe_3O_4 . In the ternary hybrid nanoparticles, the composition by mass is C 46%, O 29.7% and Fe 24.3%, indicating a predominant presence of these elements.

3.3. XRD Analysis

The XRD patterns for GO, MWCNT-COOH and MWCNT-COOH- Fe_3O_4 -rGO are depicted in ►Figure 4. MWCNT-COOH exhibits peaks at 2θ values of 25.9° (002), 43.0° (100), and 44.0° (101) [36–38]. GO is characterized by a diffraction peak at $2\theta = 11.2^\circ$ [39], which disappears after reduction, with rGO showing a peak at 26.1° [40]. The overlap of MWCNT and rGO peaks at 26.1° increases intensity in this region. Fe_3O_4 diffraction peaks were observed at 2θ values of 18.5° , 30.3° , 35.7° , 43.5° , 53.4° , 57.2° , and 63.1° , corresponding to planes (111), (220), (311), (400), (422), (511) and (440), respectively, consistent with the cubic structure and JCPDS no. 65-3107 [41]. These results confirm that GO was fully reduced to rGO and Fe_3O_4 nanoparticles were successfully incorporated.

3.4. FTIR Analysis

Fourier-transform infrared spectroscopy (FTIR) (►Figure 5) was employed to examine functional groups in MWCNT-COOH- Fe_3O_4 -rGO. Peaks at $1550\ cm^{-1}$ and $1346\ cm^{-1}$ correspond to C=O and C=C groups, respectively, characteristic of carbon nanotube sidewalls. The broad peak at $3400\ cm^{-1}$ is attributed to O–H stretching in carboxylic acid groups, while the peak at $1044\ cm^{-1}$ is associated with C–O vibrations. A peak at $2800\ cm^{-1}$ indicates –CH stretching and the Fe–O vibration is observed at $561\ cm^{-1}$, confirming the presence of Fe_3O_4 . These findings demonstrate effective modification of nanotubes with –COOH groups and successful integration of Fe_3O_4 and rGO.

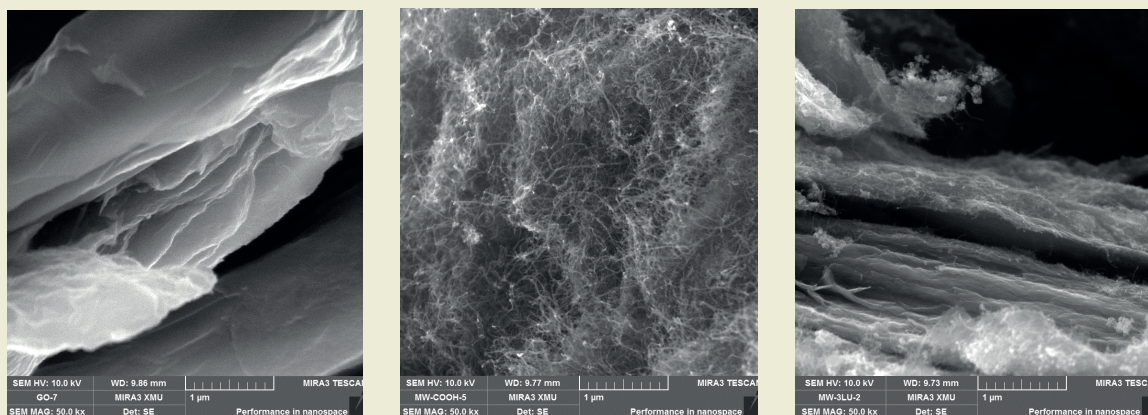


Figure 2. SEM images showing morphologies of GO, MWCNT-COOH and MWCNT-COOH- Fe_3O_4 -rGO.

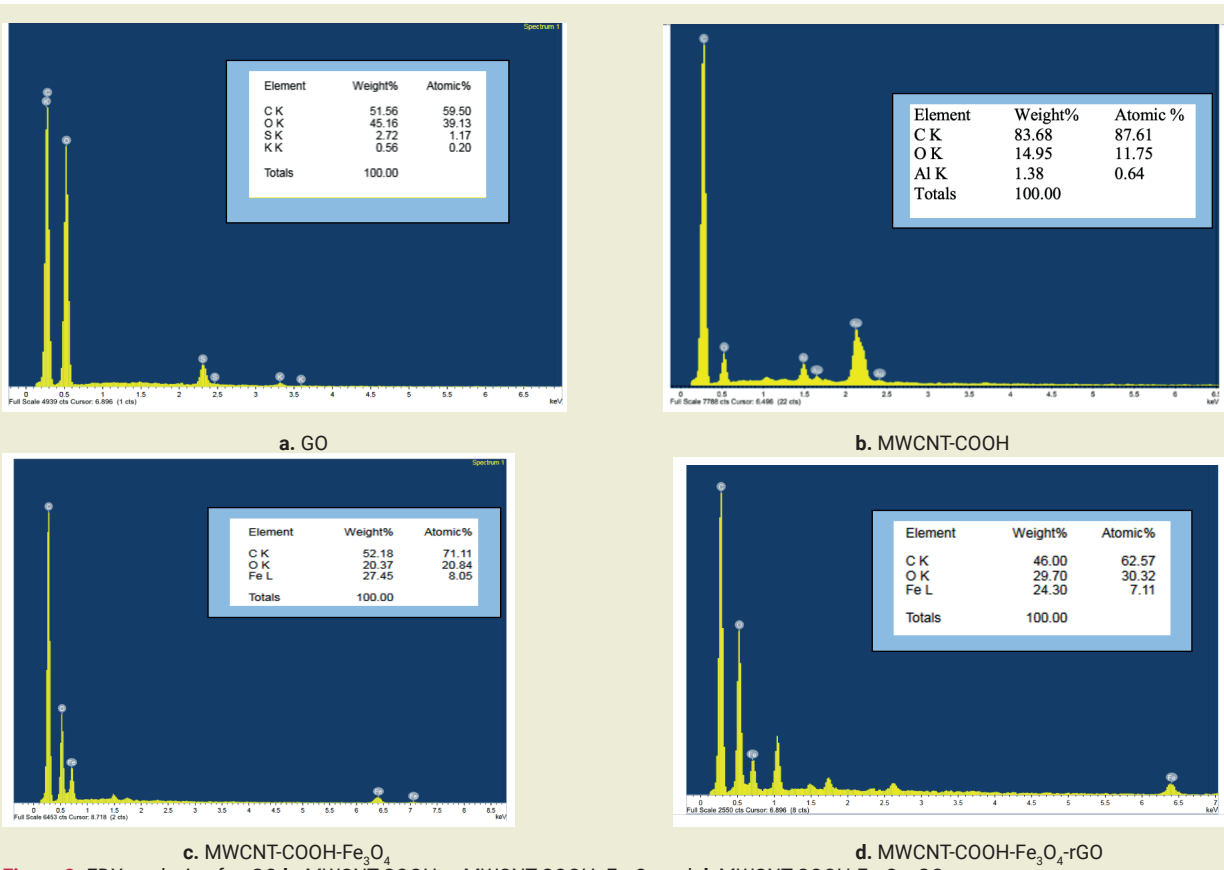


Figure 3. EDX analysis of **a.** GO **b.** MWCNT-COOH **c.** MWCNT-COOH-Fe₃O₄ and **d.** MWCNT-COOH-Fe₃O₄-rGO

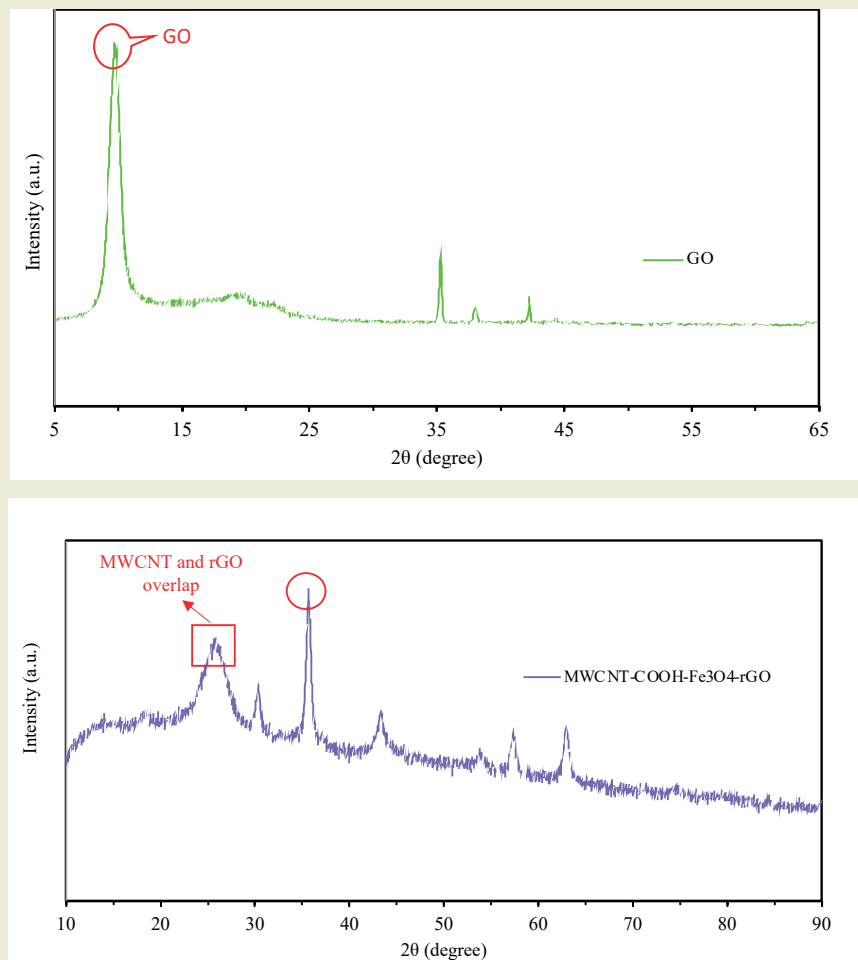


Figure 4. XRD patterns of GO, MWCNT-COOH and MWCNT-COOH-Fe₃O₄-rGO.

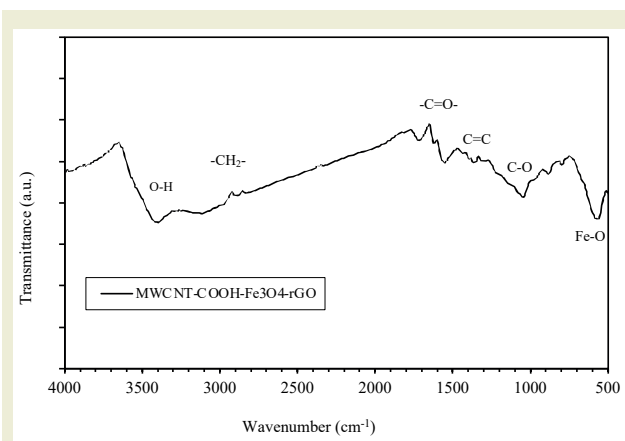


Figure 5. The FTIR spectra of MWCNT-COOH-Fe₃O₄-rGO

3.5. Thermal Conductivity Analysis

The experimental thermal conductivity of MWCNT-COOH-Fe₃O₄-rGO/water nanofluids was measured at temperatures ranging from 25 to 60 °C, with solid volume fractions of 0.025%, 0.05%, 0.075% and 0.1%, as shown in ►Figures 6 and 7. Thermal conductivity is influenced by nanoparticle concentration, temperature, and the thermal properties of both the base fluid and hybrid nanoparticles.

The data presented in ►Figures 6 and 7 illustrate a non-linear increase in thermal conductivity with temperature for all the studied nanofluids. At lower temperatures (25–30 °C), thermal conductivity values are modest, but a significant increase is observed at temperatures exceeding 30 °C, with notable enhancements compared to the base fluid. This behavior is attributed primarily to the intensified Brownian motion of nanoparticles at elevated temperatures, which outweighs the reduced thermal conductivity caused by thinner liquid layers surrounding the particles. Although Brownian motion is the primary driver of thermal conductivity variation, other factors, such as the high aspect ratio of the particles, nanoparticle agglomeration and the increased surface area of suspended nanostructures, also contribute to this trend. The concentration of the nanohybrid also plays a crucial role. Higher concentrations result in greater thermal conductivity due to the intrinsic high thermal transfer properties of nanoparticles. For instance, the highest thermal conductivity recorded was 0.988 W/mK at 60 °C for a 0.1% concentration of MWCNT-COOH-Fe₃O₄-rGO in water. Thermal conductivity generally exhibits a non-linear increase with rising nanohybrid concentrations, where low concentrations lead to slow increases due to thermal contact resistance. Additionally, overlapping or interacting liquid layers surrounding the nanoparticles can further enhance thermal conductivity.

Heat conduction is a microscopic phenomenon that is impossible to see or fully describe through experimentation. The ordered organization of liquid molecules on the surface of nanoparticles has been identified by sev-

eral studies as one of the main mechanisms displayed in relation to the abnormally high thermal conductivity of nanofluids. The interfacial layer, which was initially described and described by Choi et al. [2], is the term used to describe this organized layer structure that forms a shell at the surfaces of nanoparticles. It has been demonstrated that heat transfer from nanoparticles to the base liquid is interestingly influenced by the thickness of the interfacial layer. However, because of its incredibly small size, the interface layer remains exceedingly challenging to characterize experimentally. Some studies attempted to address this by examining and assessing the impact of the interfacial layer on the anomalous thermal conductivity using numerous simulations. The matter has been addressed in recent years by a number of simulated and experimental investigations that look at and assess how the interface layer affects thermal conductivity.

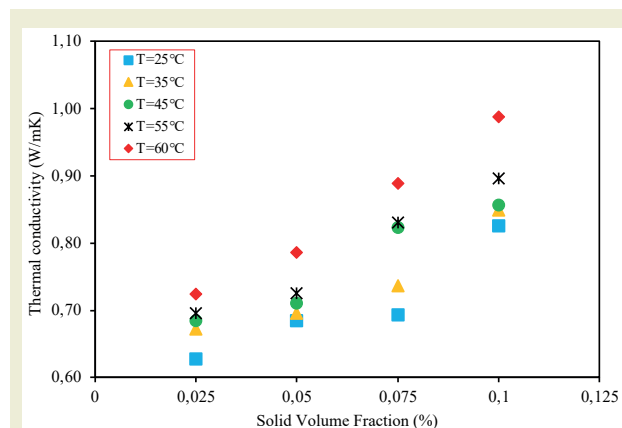


Figure 6. The ternary hybrid nanofluids' thermal conductivity in relation to the solid volume fraction at various temperatures.

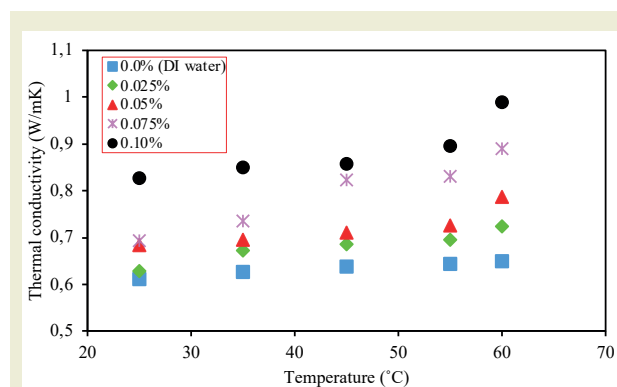


Figure 7. The ternary hybrid nanofluids' thermal conductivity in relation to temperature for different nanofluid samples.

3.6. Thermal Conductivity Ratio Analysis

Figures 8 and 9 provide a detailed depiction of the thermal conductivity ratio as a function of temperature and solid volume fraction. The variation in the thermal conductivity ratio with solid volume fraction becomes significantly more pronounced at higher temperatures than at lower ones. This can be attributed to the greater impact of temperature on the mobility of particles at higher concentrations. The data also demonstrate that

the influence of temperature on the thermal conductivity ratio becomes increasingly significant with larger solid volume fractions, where particle motion is more sensitive to temperature changes. A maximum thermal conductivity enhancement of approximately 50% was recorded at 60 °C with a solid volume fraction of 0.1%. These findings underscore the potential of hybrid nanofluids to significantly improve the heat transfer performance of base fluids under optimized conditions.

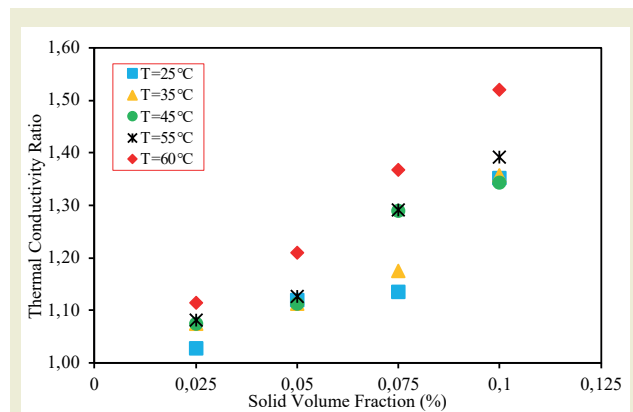


Figure 8. Change in the ternary hybrid nanofluid's thermal conductivity ratio with solid volume fraction

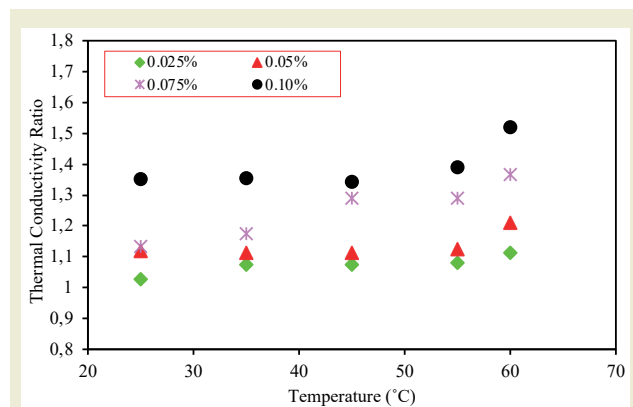


Figure 9. Change in the ternary hybrid nanofluid's thermal conductivity ratio with temperature.

4. Conclusion

This study investigated the thermal conductivity of MWCNT-COOH-Fe₃O₄-rGO hybrid nanofluids across temperatures ranging from 25 °C to 60 °C, with solid volume fractions of 0.025%, 0.05%, 0.075% and 0.1%. The experimental results demonstrated that both temperature and solid volume fraction significantly influence thermal conductivity. Specifically, thermal conductivity increased consistently with rising temperatures and solid volume fractions. Moreover, the findings revealed that at elevated temperatures, the influence of solid volume fraction on the thermal conductivity ratio was more pronounced compared to lower temperatures. Similarly, higher solid volume fractions

amplified the effect of temperature on the thermal conductivity ratio, emphasizing the synergistic relationship between these parameters. The study concluded that the maximum observed enhancement in thermal conductivity was approximately 50%, achieved at a temperature of 60 °C and a solid volume fraction of 0.1%. These findings demonstrate how hybrid nanofluids may improve heat transfer efficiency in particular circumstances. Nanofluids have proven to be highly suitable for a variety of heat transfer applications, including electronic cooling, refrigeration systems, heat exchangers, and solar thermal systems [43-46]. However, more research is required to determine whether nanofluids are appropriate for life cycle analysis of these physical systems. It is necessary to conduct thorough research on the economic implications of nanofluid. Long-term, very stable nanofluids, on the other hand, have superior thermophysical characteristics that enhance system performance and allow for several operating cycles, hence proving to be economically advantageous. The investigation indicates that, in comparison to the basic fluids (deionized water), hybrid nanofluids based on ternary hybrid nanoparticles have superior thermal properties. Consequently, these hybrid nanofluids are the nanofluids of the future for electronic cooling or heat exchange systems.

Research ethics

Not applicable.

Author contributions

The author solely conducted all stages of this research.

Competing interests

The author state no conflict of interest.

Research funding

None declared.

Data availability

The raw data can be obtained on request from the author.

Peer-review

Externally peer-reviewed.

Orcid

Neşe Keklikcioğlu Çakmak  <https://orcid.org/0000-0002-8634-9232>

References

- [1] Sarkar, J., Ghosh, P., & Adil, A. (2015). A review on hybrid nanofluids: recent research, development and applications. *Renewable and Sustainable Energy Reviews*, 43, 164-177.
- [2] Choi, S. U., & Eastman, J. A. (1995). Enhancing thermal conductivity of fluids with nanoparticles (No. ANL/MSD/CP-84938; CONF-951135-29). Argonne National Lab.(ANL), Argonne, IL (United States).
- [3] Gupta, M., Singh, V., & Said, Z. (2020). Heat transfer analysis using zinc Ferrite/water (Hybrid) nanofluids in a circular tube: An experimental investigation and development of new correlations for thermophysical and heat transfer properties. *Sustainable Energy Technologies and Assessments*, 39, 100720.
- [4] Sundar, L. S., Sintie, Y. T., Said, Z., Singh, M. K., Punnaiah, V., & Sousa, A. C. (2020). Energy, efficiency, economic impact, and heat transfer aspects of solar flat plate collector with Al₂O₃ nanofluids and wire coil with core rod inserts. *Sustainable Energy Technologies and Assessments*, 40, 100772.
- [5] Çakmak, N. K. (2019). Experimental Study of Thermal Conductivity of Boric Acid- Water Solutions. *Heat Transfer Research*, 50(17).
- [6] Keklikcioğlu, O., Dagdevir, T., & Özceyhan, V. (2019). Heat transfer and pressure drop investigation of graphene nanoplatelet-water and titanium dioxide-water nanofluids in a horizontal tube. *Applied Thermal Engineering*, 162, 114256.
- [7] Yarmand, H., Gharekhani, S., Shirazi, S. F. S., Amiri, A., Alehashem, M. S., Dahari, M., & Kazi, S. N. (2016). Experimental investigation of thermo-physical properties, convective heat transfer and pressure drop of functionalized graphene nanoplatelets aqueous nanofluid in a square heated pipe. *Energy Conversion and Management*, 114, 38-49.
- [8] Akdag, U., Akcay, S., & Demiral, D. (2014). Heat transfer enhancement with laminar pulsating nanofluid flow in a wavy channel. *International Communications in Heat and Mass Transfer*, 59, 17-23.
- [9] Sahoo, R. R. (2020). Thermo-hydraulic characteristics of radiator with various shape nanoparticle-based ternary hybrid nanofluid. *Powder technology*, 370, 19-28.
- [10] Urmi, W., Rahman, M. M., & Hamzah, W. A. W. (2020). An experimental investigation on the thermophysical properties of 40% ethylene glycol based TiO₂-Al₂O₃ hybrid nanofluids. *International Communications in Heat and Mass Transfer*, 116, 104663.
- [11] Akhavan-Behabadi, M. A., Shahidi, M., & Aligoodarz, M. R. (2015). An experimental study on heat transfer and pressure drop of MWCNT-water nano-fluid inside horizontal coiled wire inserted tube. *International Communications in Heat and Mass Transfer*, 63, 62-72.
- [12] Wusiman, K., Jeong, H., Tulugan, K., Afrianto, H., & Chung, H. (2013). Thermal performance of multi-walled carbon nanotubes (MWCNTs) in aqueous suspensions with surfactants SDBS and SDS. *International Communications in Heat and Mass Transfer*, 41, 28-33.
- [13] Sundar, L. S., Bhramara, P., Kumar, N. R., Singh, M. K., & Sousa, A. C. (2017). Experimental heat transfer, friction factor and effectiveness analysis of Fe₃O₄ nanofluid flow in a horizontal plain tube with return bend and wire coil inserts. *International Journal of Heat and Mass Transfer*, 109, 440-453.
- [14] Ghozatloo, A., Shariaty-Niasar, M., & Rashidi, A. M. (2013). Preparation of nanofluids from functionalized Graphene by new alkaline method and study on the thermal conductivity and stability. *International Communications in Heat and Mass Transfer*, 42, 89-94.
- [15] Chakraborty, S., & Panigrahi, P. K. (2020). Stability of nanofluid: A review. *Applied Thermal Engineering*, 174, 115259.
- [16] Das, P. K., Mallik, A. K., Ganguly, R., & Santra, A. K. (2016). Synthesis and characterization of TiO₂-water nanofluids with different surfactants. *International Communications in Heat and Mass Transfer*, 75, 341-348.
- [17] Esfe, M. H., & Hajmohammad, M. H. (2017). Thermal conductivity and viscosity optimization of nanodiamond-Co₃O₄/EG (40: 60) aqueous nanofluid using NSGA-II coupled with RSM. *Journal of Molecular Liquids*, 238, 545-552.
- [18] Sundar, L. S., Singh, M. K., & Sousa, A. C. (2013). Thermal conductivity of ethylene glycol and water mixture based Fe₃O₄ nanofluid. *International communications in heat and mass transfer*, 49, 17-24.
- [19] Javadi, F. S., Sadeghipour, S., Saidur, R., BoroumandJazi, G., Rahmati, B., Elias, M. M., & Sohel, M. R. (2013). The effects of nanofluid on thermophysical properties and heat transfer characteristics of a plate heat exchanger. *International Communications in Heat and Mass Transfer*, 44, 58-63.
- [20] Bakhtiari, R., Kamkari, B., Afrand, M., & Abdollahi, A. (2021). Preparation of stable TiO₂-Graphene/Water hybrid nanofluids and development of a new correlation for thermal conductivity. *Powder Technology*, 385, 466-477.
- [21] Taherialekouhi, R., Rasouli, S., & Khosravi, A. (2019). An experimental study on stability and thermal conductivity of water-graphene oxide/aluminum oxide nanoparticles as a cooling hybrid nanofluid. *International Journal of Heat and Mass Transfer*, 145, 118751.
- [22] Akhgar, A., & Toghraie, D. (2018). An experimental study on the stability and thermal conductivity of water-ethylene glycol/TiO₂-MW-CNTs hybrid nanofluid: developing a new correlation. *Powder Technology*, 338, 806-818.
- [23] Kazemi, I., Sefid, M., & Afrand, M. (2020). Improving the thermal conductivity of water by adding mono & hybrid nano-additives containing graphene and silica: A comparative experimental study. *International Communications in Heat and Mass Transfer*, 116, 104648.
- [24] Adun, H., Kavaz, D., & Dagbasi, M. (2021). Review of ternary hybrid nanofluid: Synthesis, stability, thermophysical properties, heat transfer applications, and environmental effects. *Journal of Cleaner Production*, 328, 129525.
- [25] Park, H. J., Kim, J., Chang, J. Y., & Theato, P. (2008). Preparation of transparent conductive multilayered films using active pentafluorophenyl ester modified multiwalled carbon nanotubes. *Langmuir*, 24(18), 10467-10473.
- [26] Şentürk, İ., & Keklikcioğlu Çakmak, N. (2025). Use of magnetic nanoparticle loaded functionalized multiwalled carbon nanotubes for effective removal of Maxilon red GRL from aqueous solutions. *Journal Of The Iranian Chemical Society*, vol.22, no.1, 141-159.
- [27] Hummers Jr, W. S., & Offeman, R. E. (1958). Preparation of graphitic oxide. *Journal of the american chemical society*, 80(6), 1339-1339.
- [28] Saleh, B., & Sundar, L. S. (2021). Thermal efficiency, heat transfer, and friction factor analyses of MWCNT+ Fe₃O₄/water hybrid nanofluids in a solar flat plate collector under thermosyphon condition. *Processes*, 9(1), 180.
- [29] Marcano, D. C., Kosynkin, D. V., Berlin, J. M., Sinitskii, A., Sun, Z., Slesarev, A., ... & Tour, J. M. (2010). Improved synthesis of graphene oxide. *ACS nano*, 4(8), 4806-4814.
- [30] Xiang, Q., Yu, J., & Jaroniec, M. (2011). Enhanced photocatalytic H₂-production activity of graphene-modified titania nanosheets. *Nanoscale*, 3(9), 3670-3678.
- [31] Said, Z., Çakmak, N. K., Sharma, P., Sundar, L. S., Inayat, A., Keklikcioğlu, O., & Li, C. (2022). Synthesis, stability, density, viscosity of ethylene glycol-based ternary hybrid nanofluids: Experimental investigations and model-prediction using modern machine learning techniques. *Powder Technology*, 400, 117190.
- [32] Keklikcioğlu Çakmak, N. (2020). The impact of surfactants on the stability and thermal conductivity of graphene oxide de-ionized water nanofluids. *Journal of Thermal Analysis and Calorimetry*, 139(3), 1895-1902.
- [33] Basu, A. K., Sah, A. N., Pradhan, A., & Bhattacharya, S. (2019). Poly-L-Lysine functionalised MWCNT-rGO nanosheets based 3-d hybrid structure for femtomolar level cholesterol detection using cantilever based sensing platform. *Scientific reports*, 9(1), 3686.
- [34] Han, C. L., Zou, A. L., Wang, G. D., Liu, Y., Li, N., Zhang, H. X., ... & Blackie, E. (2022). Study on 3D multi-performance composite films of Fe₃O₄ decorated CNTs/graphene oxide. *Diamond and Related Materials*, 124, 108953.
- [35] Zhou, J., Pan, K., Qu, G., Ji, W., Ning, P., Tang, H., & Xie, R. (2022).

- rGO/MWCNTs-COOH 3D hybrid network as a high-performance electrochemical sensing platform of screen-printed carbon electrodes with an ultra-wide detection range of Cd (II) and Pb (II). *Chemical Engineering Journal*, 449, 137853.
- [36] Das, R., Bee Abd Hamid, S., Eaqub Ali, M., Ramakrishna, S., & Yongzhi, W. (2015). Carbon nanotubes characterization by X-ray powder diffraction—a review. *Current Nanoscience*, 11(1), 23-35.
- [37] Salam, M. A., & Burk, R. (2017). Synthesis and characterization of multi-walled carbon nanotubes modified with octadecylamine and polyethylene glycol. *Arabian Journal of Chemistry*, 10, S921-S927.
- [38] Al-Jammal, N., Abdullah, T. A., Juzsakova, T., Zsirka, B., Cretescu, I., Vágvölggyi, V., ... & Domokos, E. (2020). Functionalized carbon nanotubes for hydrocarbon removal from water. *Journal of Environmental Chemical Engineering*, 8(2), 103570.
- [39] Zou, H., Li, X., Zhang, Y., Wang, Z., Zhuo, B., Ti, P., & Yuan, Q. (2021). Effects of different hot pressing processes and NFC/GO/CNT composite proportions on the performance of conductive membranes. *Materials & Design*, 198, 109334.
- [40] Siburian, R., Sihotang, H., Raja, S. L., Supeno, M., & Simanjuntak, C. (2018). New route to synthesise of graphene nano sheets. *Oriental Journal of Chemistry*, 34(1), 182.
- [41] Zeng, Y., Hao, R., Xing, B., Hou, Y., & Xu, Z. (2010). One-pot synthesis of Fe₃O₄ nanoprisms with controlled electrochemical properties. *Chemical communications*, 46(22), 3920-3922.
- [42] Kestin, J., Sengers, J. V., Kamgar-Parsi, B., & Sengers, J. L. (1984). Thermophysical properties of fluid H₂O. *Journal of Physical and Chemical Reference Data*, 13(1), 175-183.
- [43] Altun, A., Şara, O. N., & Şimşek, B. (2021). A comprehensive statistical approach for determining the effect of two non-ionic surfactants on thermal conductivity and density of Al₂O₃-water-based nanofluids. *Colloids and Surfaces A: Physicochemical and Engineering Aspects*, 626, 127099.
- [44] Altun, A., Şara, O., & Doruk, S. (2022). Sds Surfactant Effects On Stability and Thermophysical Properties Of Al₂O₃-Water Based Nanofluids. *Konya Journal of Engineering Sciences*, 10(3), 599-612.
- [45] Selimefendigil, F., Okulu, D., & Oztop, H. F. (2024). Application of ternary nanofluid and rotating cylinders in the cooling system of photovoltaic/thermoelectric generator coupled module and computational cost reduction. *Applied Thermal Engineering*, 250, 123436.
- [46] Sriharan, G., Harikrishnan, S., & Oztop, H. F. (2023). A review on thermophysical properties, preparation, and heat transfer enhancement of conventional and hybrid nanofluids utilized in micro and mini channel heat sink. *Sustainable Energy Technologies and Assessments*, 58, 103327.

Nanoindentation evaluation of mechanical and wear properties of Zn-3% Cu-9% Al alloy processed via ECAP

Serkan Ateş^{1*} 

¹Mechanical Engineering Department, Faculty of Engineering and Architecture, Burdur Mehmet Akif Ersoy University, Burdur, 15030, Türkiye

Abstract: This study utilizes equal channel angular pressing (ECAP), also known as equal channel angular extrusion (ECAE), to induce severe plastic deformation in Zn-3% Cu-9%Al (ZCA-9 Al) alloy, resulting in ultrafine-grained structures. ECAP is an unconventional technique used to impart severe plastic deformation to materials, producing ultrafine-grained (UFG) structures. To obtain UFG structures, two well-known Routes, A and Bc, as well as a newly proposed Route, D, were employed and evaluated. Following ECAP processing, the samples were subjected to various tests to assess their tensile properties, creep resistance, and wear track deformation behavior. The results demonstrated that all tested Routes significantly enhanced the tensile properties and creep resistance of ZCA-9 Al alloys. Routes A, Bc, and D increased the ultimate tensile strength (UTS) by 14.42%, 16.34%, and 12.82%, respectively, although they had minimal impact on wear track deformation. Overall, the findings indicate that Routes A, Bc, and D can improve the tensile and creep properties of ZCA-9 Al alloy, with Route Bc showing slightly superior results, though it required a higher extrusion force.

Keywords: ECAP, Nanoindentation, Ultrafine Grained Structures, Tensile Strength, Creep, Wear.

1. Introduction

ECAP, or ECAE is a method proposed by V. M. Segal that have garnered attention in recent years for producing UFG materials. UFG materials undergo severe plastic deformation (SPD), which results in superior mechanical and physical properties compared to their original state. These materials typically have grain sizes ranging between 1 μm and 2 μm in diameter. Additionally, UFG materials exhibit high electrical resistivity and diffusivity, making them suitable for a wide variety of applications [1].

There are numerous techniques for producing UFG materials, including plasma processing, chemical and physical vapor deposition, inert gas condensation, and milling. However, these methods are not suitable for mass production. To achieve significant changes in material properties, high-angle grain boundaries (HAGB) are necessary, as they possess misorientation angles greater than 15 degrees [2].

For this reason, it is imperative to investigate non-traditional SPD techniques, such as ECAP, to address the

shortcomings of conventional methods and to produce UFG materials with enhanced mechanical properties. UFG materials synthesized through SPD processes are typically characterized by granular HAGB. Grain boundaries play a pivotal role in grain size refinement by impeding dislocation motion within the material, which consequently improves both strength and hardness. The Hall-Petch relationship provides a robust explanation for the correlation between grain size, hardness, and strength. According to this principle, reducing the grain size brings the material closer to its theoretical strength limits, with maximum strength observed at approximately 20–30 nm [2-3].

If the UFG structure is preserved at elevated temperatures, where diffusion rates increase significantly, the material shows great potential for enabling superplastic forming at higher strain rates. For this reason, our focus is on ECAP as an SPD method for producing larger samples of UFG materials with low porosity. One of the key advantages of ECAP is that it strains the sample without causing dimensional changes. This is a significant benefit compared to other SPD methods, such as Accumulated Roll Bonding (ARB), which can induce

*Corresponding author:
Email: sates@mehmetakif.edu.tr

Cite this article as:

Ateş, S. (2025). Nanoindentation evaluation of mechanical and wear properties of Zn-3% Cu-9% Al alloy processed via ECAP. *European Mechanical Science*, 9(1): 25-37. <https://doi.org/10.26701/ems.1616622>

History dates:

Received: 10.01.2025, Revision Request: 26.02.2025, Last Revision Received: 28.02.2025, Accepted: 06.03.2025



© Author(s) 2025. This work is distributed under <https://creativecommons.org/licenses/by/4.0/>



dimensional changes and sometimes result in edge cracking or fracturing. ►Figure 1 provides a schematic illustration of the ECAP process.

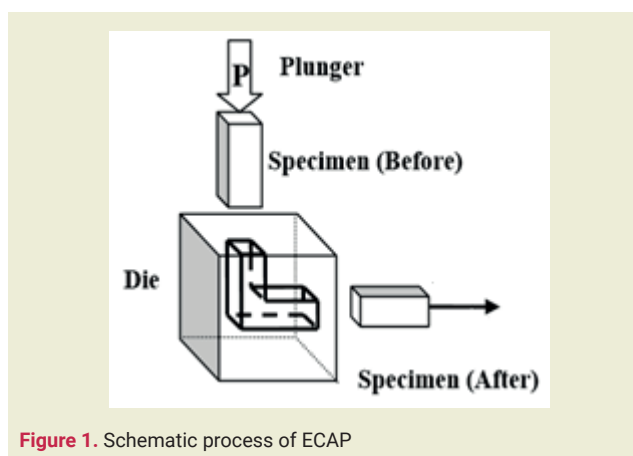


Figure 1. Schematic process of ECAP

Thus, ECAP is a widely used SPD method for achieving ultrafine-grained (UFG) structures by inducing large amounts of plastic deformation (with true strains greater than 10). A substantial body of evidence demonstrates that UFG structures processed through this method result in significant changes in the fundamental properties of the material [4–6]. ECAP also holds potential for large-scale production and commercial applications. Numerous studies have shown that the ECAP process improves the strength and ductility of materials in ways that may not be possible with conventional techniques.

For instance, Abioye et al. [7] found that subjecting AL 6063 alloys to ECAP enhanced their tensile properties. Similarly, Ding et al. [8] investigated three different processing Routes for Mg alloy and found that only Route A was effective in increasing strength. Jiang et al. [9] investigated how ECAP affects the room-temperature mechanical properties of cast Mg–9Al–Zn alloy, highlighting notable enhancements in yield strength, ultimate tensile strength, and elongation achieved through ECAP.

Martynenko et al. [10] studied the texture, microstructure, and mechanical behavior of magnesium alloy WE43 subjected to ECAP, concluding that the process improved both strength and ductility. Tolaminejad et al. [11] studied commercial purity aluminum subjected to ECAP using Route Bc. They found that the microstructure transitioned from elongated subgrains to ultrafine grains between passes 1 and 4, but no significant changes occurred between passes 4 and 8. They concluded that the first ECAP pass enhanced the mechanical properties by more than four times compared to the annealed condition.

Yang et al. [12] conducted a systematic analysis of the changes in microstructure, texture, and mechanical properties of extruded Mg-xY ($x = 1, 5$ wt.%) alloys during ECAP, utilizing optical microscopy, electron

backscatter diffraction (EBSD), and uniaxial tensile testing. Their findings revealed that the Mg-5Y alloy experienced notable improvements in strength and elongation post-ECAP, with yield strength, ultimate strength, and elongation increasing by 10%, 6%, and 72%, respectively.

A notable advantage of ECAP lies in its ability to deform materials without altering the sample's cross-sectional area. Furthermore, the same material can undergo repeated processing by varying its orientation, referred to as different Routes. With an increasing number of passes, the material experiences progressively higher levels of deformation. These varying orientations result in the development of distinct substructures. Among the available ECAP Routes, A and Bc have demonstrated exceptional efficacy in enhancing mechanical properties and exerting a profound influence on the microstructure. The shear plane and the sample's rotation after successive passes for Routes A and Bc are illustrated in ►Figure 2(a), ►Figure 2(b) and ►Figure 2(c), respectively.

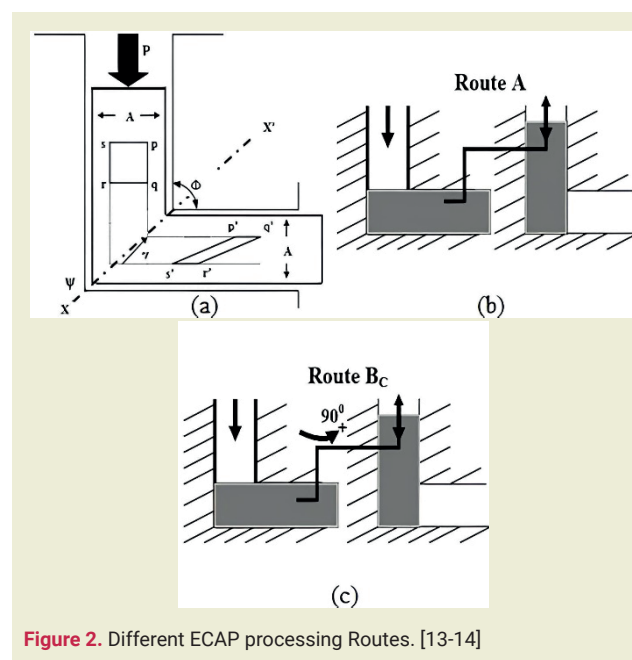


Figure 2. Different ECAP processing Routes. [13-14]

Route A produces elongated grains with a lamellar structure, formed by a gradual increase in the misorientation angle between adjacent grains. Conversely, Route Bc facilitates the development of a uniform microstructure comprising equiaxed grains, which are more rapidly delineated by high-angle grain boundaries (HAGB). Equiaxed grains are characterized by their nearly identical dimensions in all directions, providing a greater number of slip planes. This structural attribute significantly contributes to enhanced strength and ductility. In addition to Routes A and Bc, this study examines a new Route, named Route D, as shown in ►Figure 3.

In Route D, the sample is rotated along the X-axis after each consecutive pass, a strategy designed to more

efficiently produce a uniform microstructure with equiaxed grains separated by high-angle grain boundaries (HAGB). In addition to the chosen Routes, essential factors like die angle, extrusion temperature, and extrusion speed significantly influence the ECAP process. Thang et al. [15] determined that, among seven different Routes, a 90° die angle was the most effective for achieving significant grain size reduction. This finding reinforces the suitability of ECAP as a method for obtaining a refined equiaxed microstructure, with a range of Routes and extrusion angles available to customize the microstructure according to specific requirements.

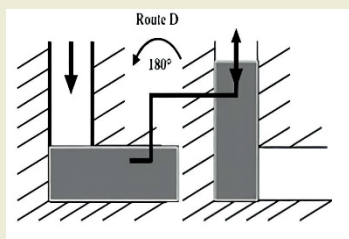


Figure 3. Route D

This study focused on Zn-Al alloys due to their widespread engineering applications. Savaskan et al. [16] noted that Zn alloys with 2–3% Cu offer high tensile strength, creep resistance, and wear resistance but become dimensionally unstable above 100°C . Zn-Al alloys are valued for their affordability, machinability, corrosion resistance, and superior surface finish compared to cast iron, with mechanical properties similar to low-carbon steel and aluminum. Their high damping capacity makes them suitable for noise and vibration reduction, though enhancing damping often compromises strength, posing a challenge in balancing both properties.

Zn-Al alloys with superior mechanical properties can be achieved through the addition of copper (Cu) or titanium (Ti), even without employing alternative forming techniques; however, this approach results in a reduction in ductility. Furthermore, the material's microstructure plays a pivotal role in determining its mechanical characteristics. ECAP, as an innovative and non-conventional processing method, holds significant potential for refining microstructures and generating ultrafine-grained (UFG) materials. Therefore, studying the impact of ECAP on the tribological and mechanical behaviors of Zn-Al alloys is crucial.

In this study, the tensile, creep, nanoindentation, scratch, and wear properties of cast and ECAP-processed Zn-9%Al-3%Cu alloys under various conditions were evaluated using nanoindentation instead of conventional testing methods. Additionally, the research analyzed the microstructural evolution of these alloys during ECAP, employing processing Routes A, Bc, and the newly proposed Route D.

2. Material and Methods

The ECAP process used a servo-hydraulic MTS machine with a 315 kN press to extrude samples through a die with two identical square channels, aided by a plunger. The system included a main block, center block, and supporting block, securely fastened with bolts.

Figure 4 shows the ECAP setup and a schematic of the die, featuring two channels intersecting at a 90° angle (Φ) with an outer arc angle (ψ) of 0° . Temperature was monitored using thermocouples placed 2 mm from the channel and within the environmental chamber enclosing the setup.

The extrusions were conducted at 650°C ($\pm 5^\circ\text{C}$), the minimum temperature to prevent shear cracks and control grain growth. Samples, made from as-cast ZCA-9 alloy (Zn-9%Al-3%Cu with trace Ti and Cr), were machined to dimensions of $6.35 \times 6.35 \times 35.75$ mm.

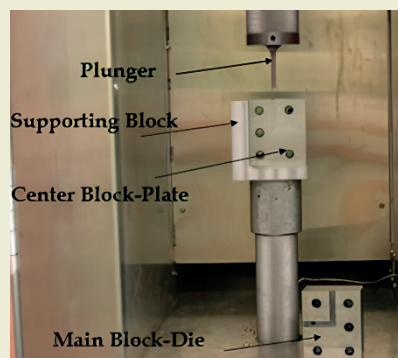


Figure 4. Photograph illustrating the ECAP setup

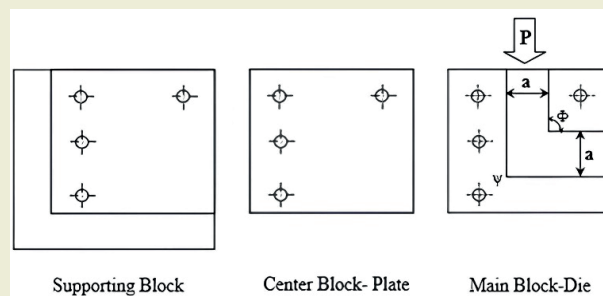


Figure 5. Schematic representation of the supporting block, center block, and main block of the ECAP die.

The sample was coated with molybdenum disulfide (MoS_2) paste, placed in the die's vertical channel, and heated for 15 minutes to reach the processing temperature before being extruded at a constant rate of 10 mm/min.

Following the initial extrusion, samples underwent processing via Routes A, BC, and D, with up to eight passes through the 90° die. The applied load was continuously monitored and recorded using a load cell.

2.1. Mechanical Testing

Tension Testing

A uniaxial tensile test was conducted at room temperature using an MTS machine with a 44 kN load cell on samples processed via Routes A, BC, and D. Tests followed ASTM E8 standards, with a strain rate of $1.74 \times 10^{-3} \text{ s}^{-1}$. Three samples per Route were tested, averaged, and prepared to dimensions of $30 \times 3 \times 2.1 \text{ mm}$.

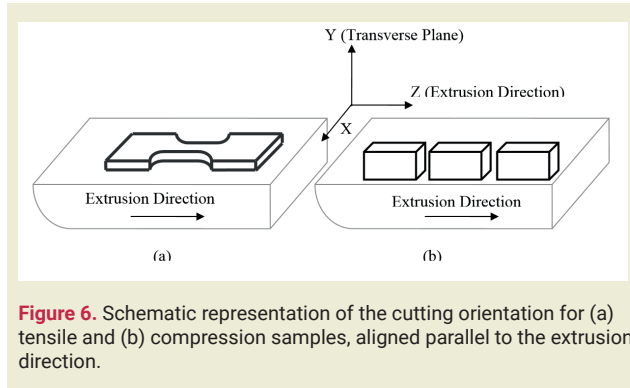


Figure 6. Schematic representation of the cutting orientation for (a) tensile and (b) compression samples, aligned parallel to the extrusion direction.

The samples were prepared in a dog bone shape with a rectangular cross-section, aligned parallel to the extrusion direction, and polished with $0.05 \mu\text{m}$ colloidal silica to eliminate surface imperfections. The gauge section was finalized at $10 \times 3 \times 2 \text{ mm}$. Strain gauges and a deflectometer were used to record strain and displacement during testing, with load-displacement data captured by a data acquisition system to calculate engineering stress (σ) and strain (ϵ):

$$\text{Engineering Stress, } \sigma = \frac{P}{A_0} \quad (1)$$

$$\text{Engineering Strain, } \epsilon = \frac{(L-L_0)}{L} \quad (2)$$

Elongation was determined as:

$$\text{Elongation} \quad (\%),$$

$$\% = \frac{L-L_0}{L_0} \times 100 \quad (3)$$

where L_0 is the gauge length before pulling depending on the size of the sample tested.

Nano hardness test

Nano hardness testing, also known as nanoindentation, involves measuring the depth of indentations on a nanometer scale. Nanoindentation tests using the MTS Nanoindenter XP were performed to assess the hardness and Young's modulus of the ZCA-9 alloy in its as-cast state and after ECAP processing. A Berkovich indenter created indentations at a depth of 1000–1500 nm with a strain rate of 0.05 s^{-1} . The schematic view of the ECAP-processed specimen is shown in ►Figure 7.

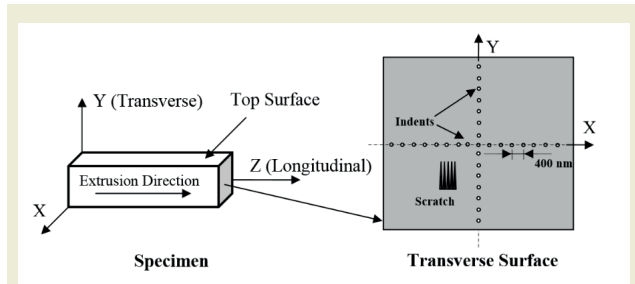


Figure 7. Schematic view of nanoindentation test on the transverse surface of the as-cast and ECAP processed alloy.

A series of fifteen nanoindents was conducted sequentially along the X and Y axes, with a spacing of 400 nm between each indent, to ensure that hardness remained consistent with depth along the axes. The indentation load and corresponding depths were recorded continuously during the tests, with a representative load-displacement curve shown in ►Figure 8.

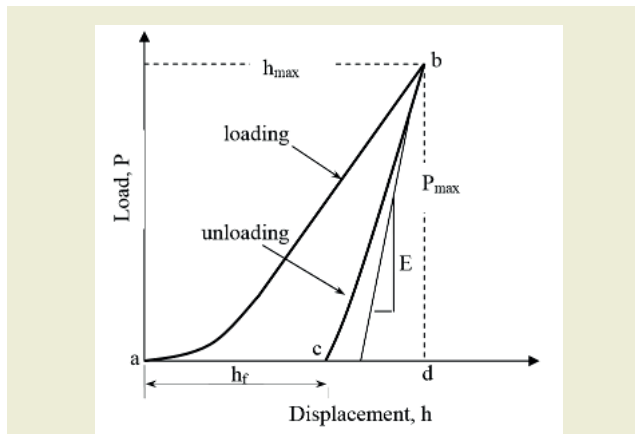


Figure 8. Schematic representation of a typical load-displacement curve generated during nanoindentation testing.

In nano hardness testing, the predetermined load is gradually and uniformly applied to the indenter, causing it to penetrate the sample (represented by curve AB in ►Figure 8). At point B, the material's resistance matches the applied load, halting further penetration. As the load is gradually reduced, the indentation undergoes elastic recovery, producing the unloading curve BC. The material's Young's modulus (E) is determined from the slope of the linear portion of the unloading curve and is calculated as:

$$E = \frac{dP}{dh} \quad (4)$$

The hardness of the material (H) can be determined as:

$$H = \frac{P_{max}}{A} \quad (5)$$

where P_{max} represents the maximum indentation load (point B), and A denotes the projected area of the indentation impression.

Nano scratch Testing

Nano scratch tests using the MTS Nano Indenter XP evaluated the scratch properties of as-cast and ECAP-processed materials. Five 500 μm -long scratches were made on longitudinal and transverse surfaces using a Berkovich indenter. The applied load increased linearly from 0 to 90 mN at 10 $\mu\text{m}/\text{s}$. Parameters such as load-displacement, lateral deflection, table position, and time were monitored, and friction coefficients were calculated as the lateral force to normal load ratio.

Creep Testing

Uniaxial tensile creep tests at room temperature assessed the creep strength of as-cast and ECAP-processed ZCA-9 samples under a constant 61 kg load (30 MPa stress). Samples, fabricated per ASTM E139 standards (5 mm diameter, 10 mm gauge length), were CNC machined for minimal heat and high surface quality. All but the as-cast samples were tested until failure. Displacement data were recorded using an extensometer and LVDT, with nominal strain (ϵ) calculated as the change in length (Δl) relative to the original length (l_0).

$$\epsilon = \frac{\Delta l}{l_0} \quad (6)$$

2.2. Microstructural Characterization

Optical Microscope and Scanning Electron Microscope

Metallurgical analysis of as-cast, ECAP-processed, and heat-treated ZCA-9 alloy was conducted using optical microscopy and Scanning Electron Microscope (SEM) for grain and particle size evaluation, while Environmental Scanning Electron Microscope (ESEM) analyzed alloy phases. Samples were sectioned transversely with a diamond blade, then ground with SiC paper (240–600 grit) and polished with alumina abrasives (5–0.05 μm).

OM and SEM Results

The microstructural changes in as-cast, as-ECAP, and post-ECAP alloys were analyzed using SEM. ► **Figures 9(a) and 9(b)** display Backscattered Electrons Mode (BSEM) images at low magnification and secondary images at higher magnification of the as-cast ZCA-9 alloy.

The as-cast ZCA-9 alloy exhibits randomly distributed grains with a three-phase eutectic structure, where dark, grey, and white regions correspond to Al-rich, Zn-rich, and Cu-rich phases, respectively. A tree-stem-like eutectic structure containing η , α , and ϵ phases was determined, with EDS analysis presented in ► **Figures 10–13**.

The η phase is dominant in Zn BSE images, the α phase in Al-scattered images, and the ϵ phase in Cu-scattered images. The as-cast ZCA-9 alloy also contains Al-rich dendrites and Zn-rich eutectic phases. Zhu et al. [17]

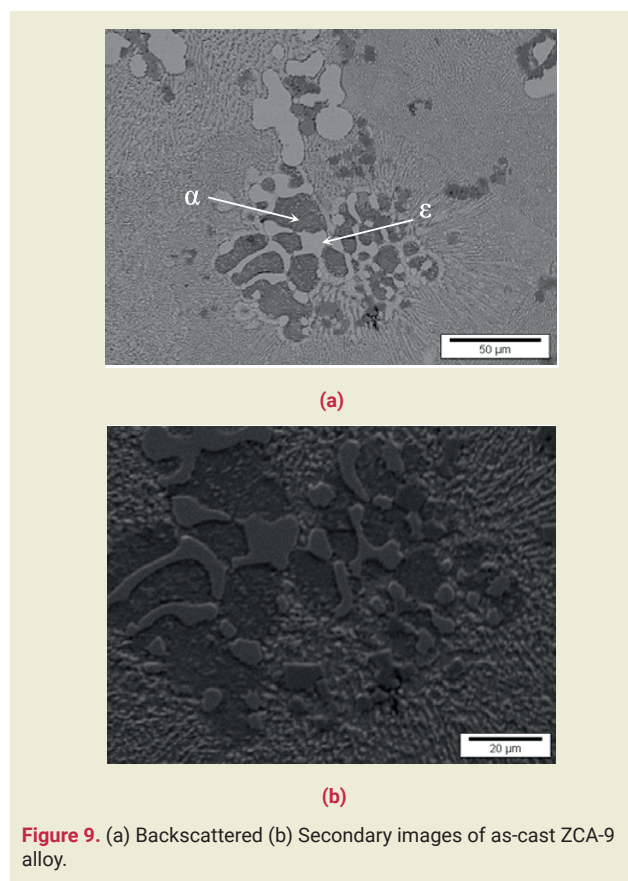


Figure 9. (a) Backscattered (b) Secondary images of as-cast ZCA-9 alloy.

reported similar dendritic structures in Zn-Al alloys, where reducing dendrite spacing enhances mechanical properties by minimizing microsegregation. Osorio et al. [18] and Turhal et al. [19] further confirmed that finer dendrite spacing improves tensile and yield strength while reducing porosity, particularly in Zn alloys with higher Al content.

ECAP-processed ZCA-9 alloys, contributing to improved mechanical properties, including increased strength and ductility. Optical micrographs (► **Figures 14(a)–(d)**) show that a single ECAP pass refined the microstructure into a uniform equiaxed grain structure (average grain size: 0.24 μm). Grain boundary sliding (GBS), crucial for structural superplasticity, was facilitated by equiaxed grains and the spherical distribution of Al-rich phases, enhancing GBS efficiency compared to laminar structures.

In Route A, grain structures become fibrous and elongated along the extrusion direction due to the lack of rotation during successive ECAP passes, leading to a mixture of coarse and fine grains with limited homogeneity. Deformation zones around hard particles and reduced deformation band spacing accelerate the formation of UFG structures [22]. As a directional strain process, Route A causes strain to accumulate consistently, subdividing grains into cell blocks with varying slip systems [23]. This process promotes grain rotation toward stable orientations, forming high-angle grain boundaries (HAGB).

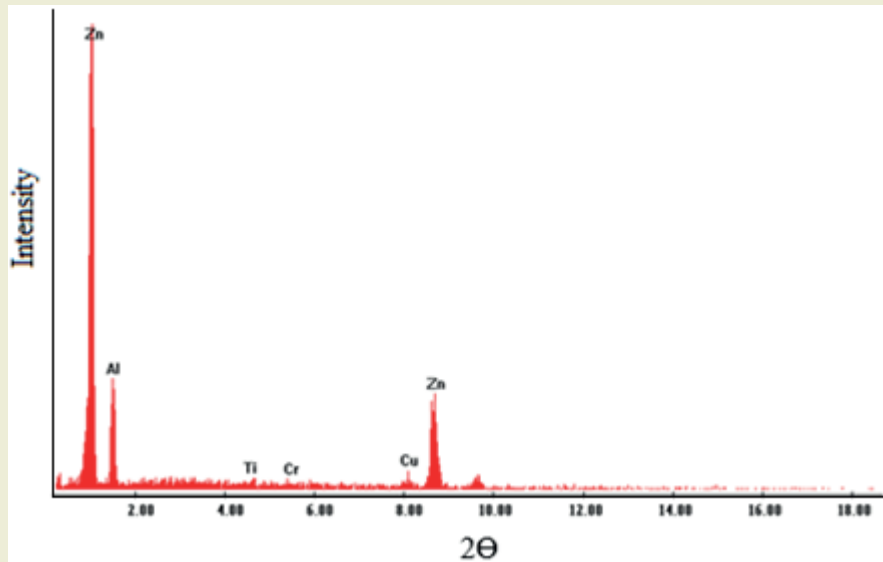


Figure 10. EDS spectrum of as-cast ZCA-9 alloy.

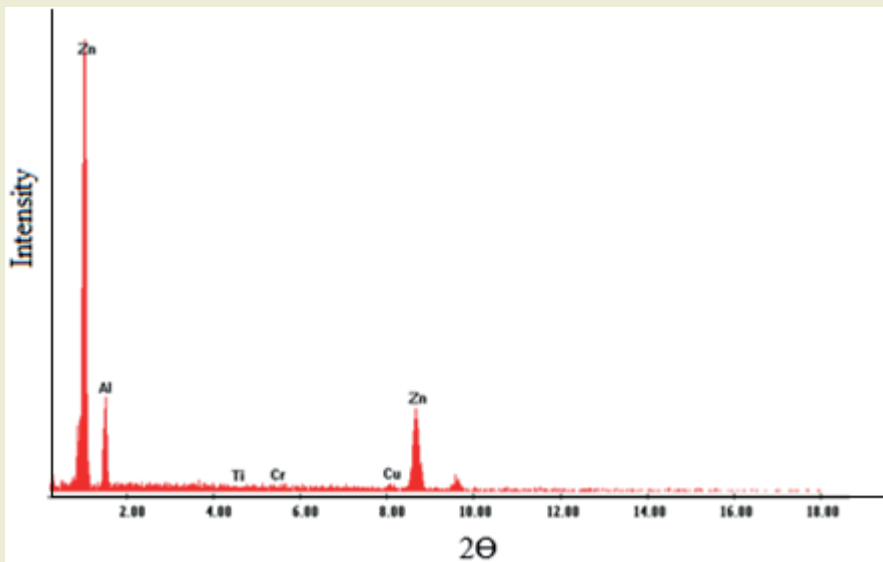


Figure 11. EDS spectrum of light phase of as-cast ZCA-9 alloy.

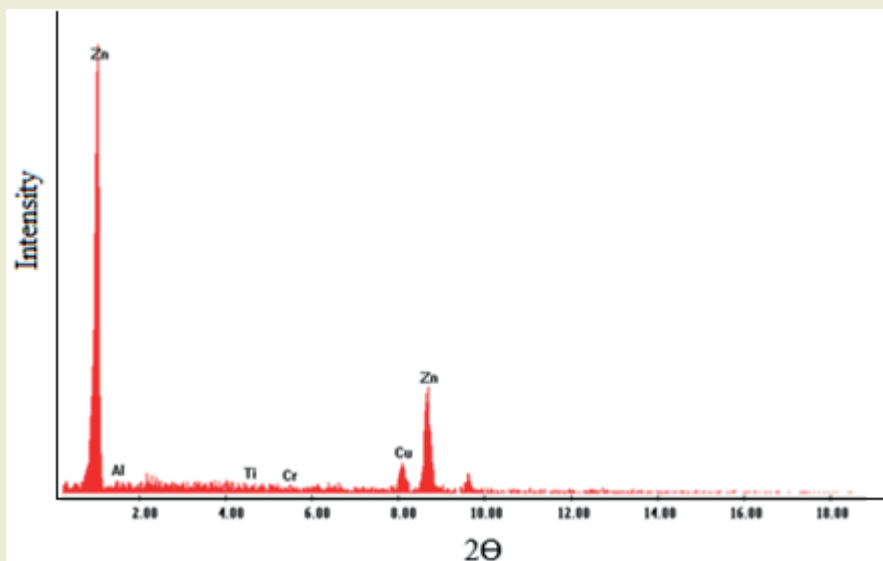


Figure 12. EDS spectrum of white phase of as-cast ZCA-9 alloy.

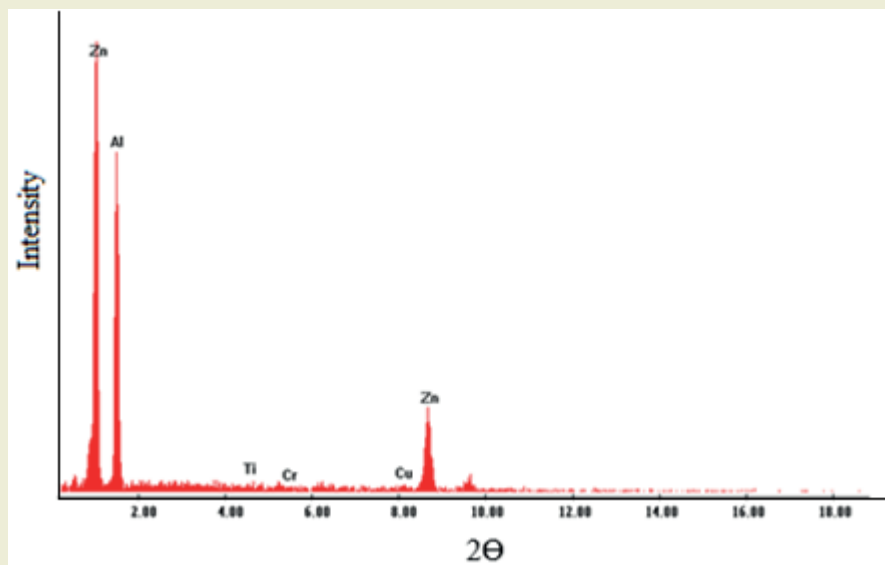


Figure 13. EDS spectrum of dark phase of as-cast ZCA-9 alloy.

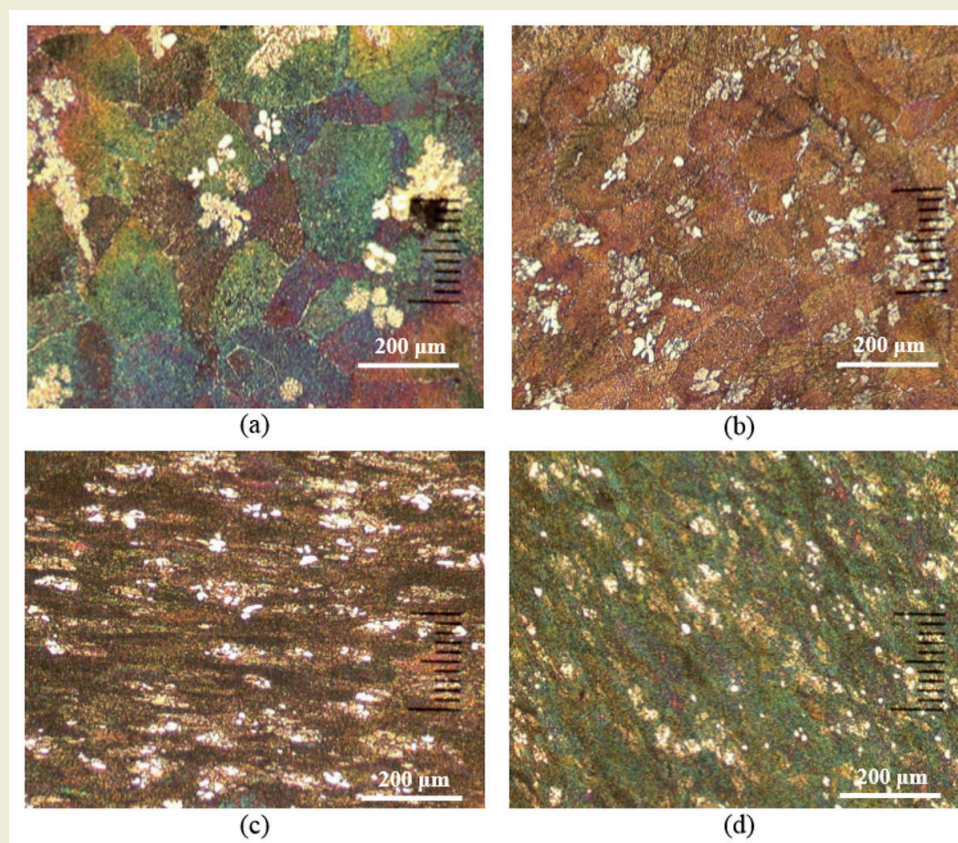


Figure 14. Optical micrographs illustrating typical microstructure of (a) as-cast, and ECAP processed sample up to (b) one pass, (c) Route A-two passes and (d) Route Bc-two passes.

3. Mechanical Results

3.1. ECAP Process

Figure 15(a) and (b) depict the variation in extrusion load as a function of displacement for the alloy during the ECAP process using Routes A and BC.

As shown in ►**Figures 15(a) and (b)**, at the start of the ECAP process, the extrusion force rises sharply as the plunger advances, but it quickly stabilizes due to the material's yield resistance. Once the yield resistance is overcome and the peak load is reached, the extrusion load decreases, then increases again to a level close to or exceeding the previous peak before dropping as the process concludes. In ►**Figure 15(a)**, the extrusion force remains constant for the first and second passes but

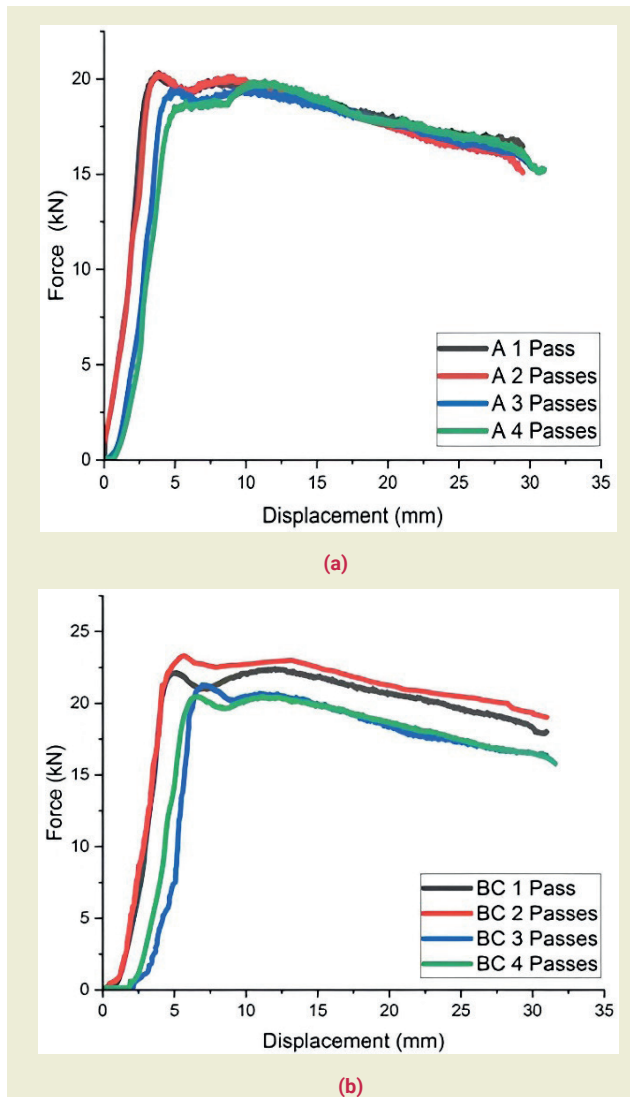


Figure 15. Force-displacement curves of the ZCA-9 samples from the ECAP process of different numbers of passes. (a) Route A, (b) Route Bc.

begins to decline thereafter. For Route Bc, the extrusion load increases from the first to the second pass and then follows a decreasing trend similar to Route A. Notably, the extrusion force required for the ECAP process is higher for Route Bc compared to Route A. This increased force requirement for Route Bc can be attributed to the presence of elongated grains and microbands aligned with the extrusion direction. Similar findings were reported by Purcek et al. [24] during high-temperature extrusion of Zn-27%Al alloy. It is also worth noting that the geometry of the die significantly influences the deformation process. The strain experienced by the material during ECAP is highly dependent on the channel angle (Φ) and the outer arc curvature angle (Ψ). The total strain intensity during the process can be determined using the following equation:

$$\epsilon_p = \frac{N}{\sqrt{3}} \left[2 \cot \left(\frac{\Phi + \Psi}{2} \right) + \cos \epsilon c \left(\frac{\Phi + \Psi}{2} \right) \right] \quad (7)$$

In the equation, N represents the number of passes, Ψ is the angle of the arc of curvature, and Φ is the angle

between the channels (refer to ►Figure 2). The equation indicates that the number of passes, N , is directly proportional to the efficiency of the ECAP process. According to Thang et al. [15], a channel angle Φ of 90° is the most effective for achieving significant grain size reduction. Nagasekhar et al. [25], through finite element analysis, studied the deformation behavior of extruded materials and determined that optimal strain homogeneity, minimal dead zone formation, and no adverse effects could be achieved with a Φ angle of 90° and a Ψ angle of 20° .

In this study, the die angles were set to $\Phi=90^\circ$ and $\Psi=20^\circ$ to examine the effects of ECAP on the mechanical and tribological properties of the Zn-3%Cu-9%Al alloy. Determining the optimal die angles is crucial for obtaining ultrafine-grained (UFG) materials with fewer ECAP passes, thereby making the process more time- and cost-efficient. The results indicate that Route Bc is the most effective in producing equiaxed fine-grained materials. However, this Route requires higher extrusion forces compared to Route A. Unfortunately, data on extrusion forces for Route D is unavailable, preventing any conclusions regarding its performance.

Tension Test Results

The tensile tests aimed to evaluate the mechanical properties of ECAP-processed samples, focusing on UTS and yield strength (YS). Engineering stress-strain curves for samples processed through Routes A, Bc, and D are shown in ►Figures 16(a)–(c).

All three engineering stress-strain diagrams reveal a substantial increase in ultimate tensile strength (UTS) following the first ECAP pass. Route A achieved its maximum UTS after the first pass, Route Bc reached its peak after the second pass, and Route D attained its highest UTS after the third pass. After reaching a peak UTS value, additional passes led to a reduction in both UTS and YS. The peak UTS values were similar among the Routes, with the highest observed for Route Bc. The UTS values increased by 14.42% for Route A, 16.34% for Route BC, and 12.82% for Route D. Additionally, each Route exhibited strain-softening behavior and improved ductility after successive passes, which is arguably the most noteworthy aspect of the engineering stress-strain diagrams. A substantial increase in ductility occurred without a significant decrease in tensile strength. These results suggest that Routes A, BC, and D can be used to enhance the tensile properties of ZCA-9 alloys.

The comparison with extrusion force data indicates that the force required for ECAP is influenced by the improved ductility in Route Bc, likely due to better grain refinement and reduced dislocation density from SPD. This effect is absent in Route A, where the lack of rotation between passes leads to repeated shear in the same direction, promoting a uniform microstructure and greater work-hardening. Extrusion data for Route

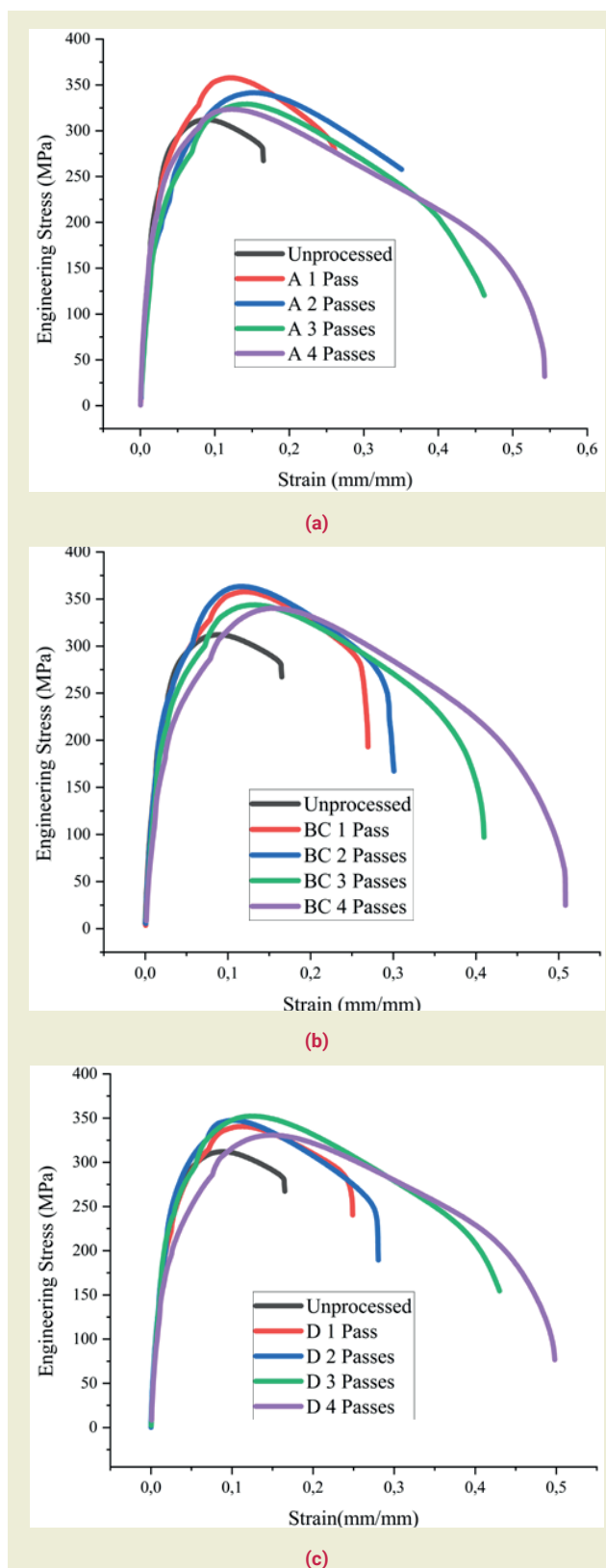


Figure 16. Engineering stress-strain curves for ZCA-9 samples processed through Route A (a), Route Bc (b), and Route D (c).

D are unavailable, preventing further analysis of its behavior.

Ramirez et al. [26] found that Route Bc significantly enhanced the tensile strength and ductility of Al-Si-Cu alloy by promoting a homogeneous and refined micro-

structure. Awasthi et al. [27] observed that Route BC enhanced tensile properties, including tensile strength and ductility, due to the development of refined grain structures. Similarly, Alateyah et al. [28] reported that Route A led to substantial grain refinement and the conversion of low-angle grain boundaries into high-angle grain boundaries, resulting in improved mechanical properties such as UTS and ductility. El-Shenawy et al. [38] found that ECAP processing using Route A for the AA2024 aluminum alloy significantly improved its tensile properties.

Creep Test Results

Figure 17 shows the displacement – time graph for the creep tests carried out on a single sample.

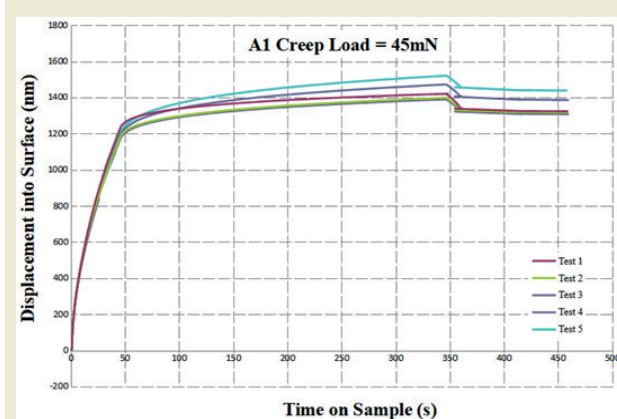


Figure 17. Displacement into surface – time graph for the 45 mN load test on Route A single pass sample.

Two phases typically observed in a creep test are clearly visible here. Displacement into the surface increases in the first region and continues to increase at a constant rate in the second region. After unloading, the displacement starts to decrease. Additionally, creep compliance graphs were obtained from the nanoindenter. Similar to the displacement versus time graph, creep compliance increases in the first and second phases. The creep compliance graph is shown in ►Figure 17.

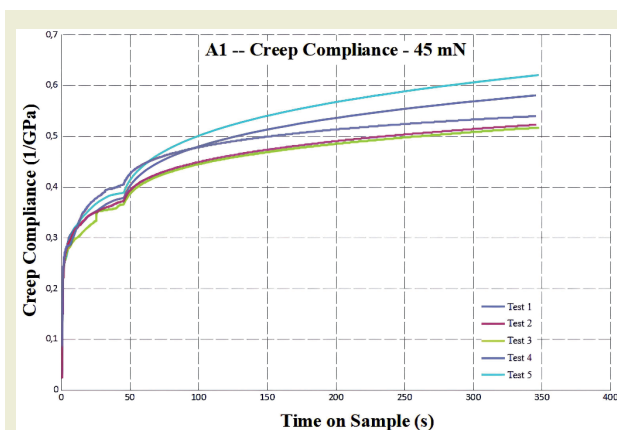


Figure 18. Creep compliance – time graph of Route A 1 pass sample.

As shown in ►Figure 18, variation in creep compliance is expected since the stress on the sample is constant and creep compliance is directly proportional to strain. The results for surface displacement and creep compliance were obtained from the nanoindenter for samples processed using Routes A, BC, and D. The stress exponent for the nanoindentation test was calculated by the software. ►Figure 19(a)–(c) illustrates the average stress exponent as a function of the number of passes for Routes A, BC, and D, respectively.

The stress exponent is an important parameter for predicting creep behavior. For the sample processed by Route A, as shown in ►Figure 19 (a), significant changes in the stress exponent were observed at different passes. Even after the first pass, a notable reduction in the stress exponent value was observed. The same trend was seen across different loading conditions. Another significant drop in the stress exponent occurred after the third pass. After the fourth pass, the stress exponent increased for lower loads but continued to decrease for higher loads. A similar pattern was observed for Route Bc; however, for Route D, all stress exponent values increased. Route Bc showed similarities to Route A. Stress exponent values were almost identical for some loads but began to vary with the number of passes. Another notable drop in the stress exponent value was seen after the second pass, while the fourth pass caused almost no change. For Route D, changes in the stress exponent values were more linear compared to Routes A and Bc. After the fourth pass, the stress exponent values increased for all loads. The lowest stress exponent values were observed in the sample processed using Route Bc. Maier et al. [30] have related strain rate sensitivity (m) to the stress exponent as:

$$m = \frac{1}{n} \quad (8)$$

Strain rate sensitivity can indicate resistance to necking. The earlier decrease in stress exponent values may suggest increased strain rate sensitivity. El-Shenawy et al. [29] reported that ECAP processing of AA2024 aluminum alloy resulted in improved tensile properties and strain rate sensitivity. The uniform plastic strain distribution and refined microstructure due to ECAP led to a reduction in the stress exponent, enhancing the material's ability to accommodate strain rate variations. Similarly, Zhao et al. [31] found that ECAP processing, followed by annealing at various temperatures, significantly improved the strain rate sensitivity and mechanical properties of TA15 titanium alloy. The ECAP-induced grain refinement contributed to the observed drop in the stress exponent, indicating enhanced strain rate sensitivity. A similar observation can be made for the ZCA-9 alloy, as the stress exponent values are lower for the ECAP-processed samples. While the stress exponent is not the only parameter for evaluating a material's creep behavior, it provides valuable insights.

Wear Test Results

For the wear tests, a 500 μm wear path length was used,

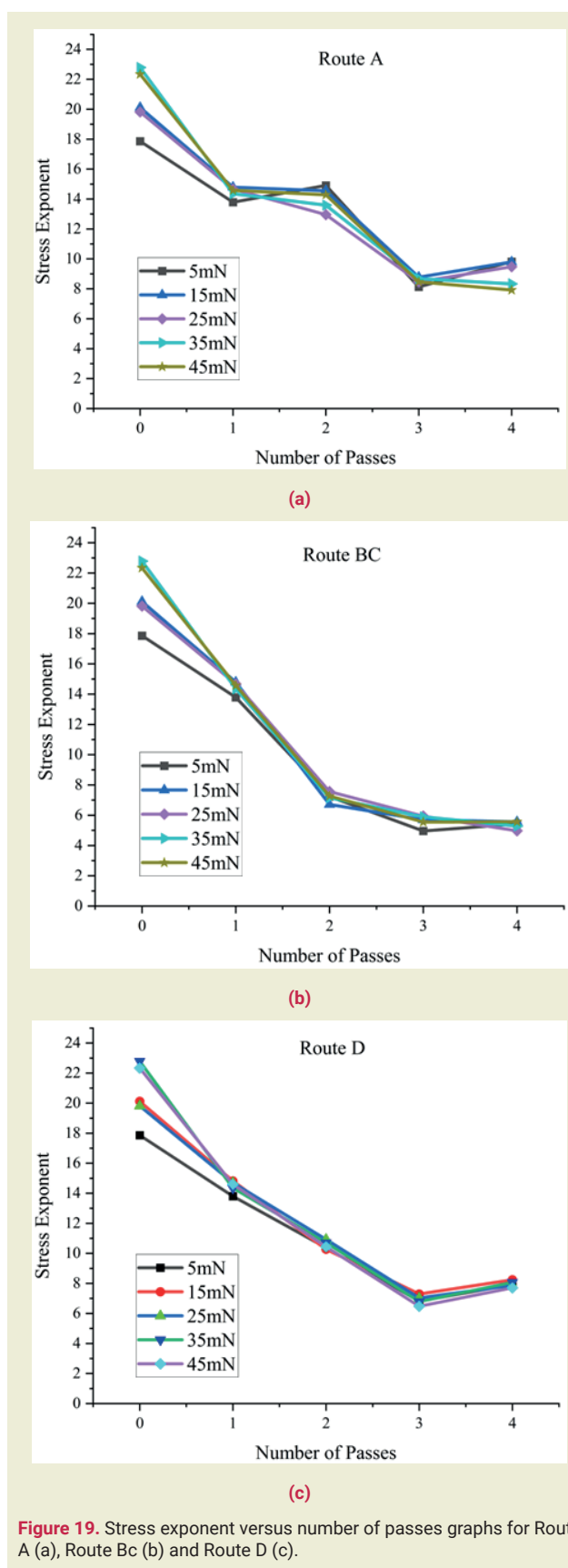


Figure 19. Stress exponent versus number of passes graphs for Route A (a), Route Bc (b) and Route D (c).

as previously mentioned. The values obtained are important for identifying the wear properties of the material. A higher wear track deformation value indicates lower wear resistance. ►Figure 20 shows the wear track deformation versus load on the sample and the number

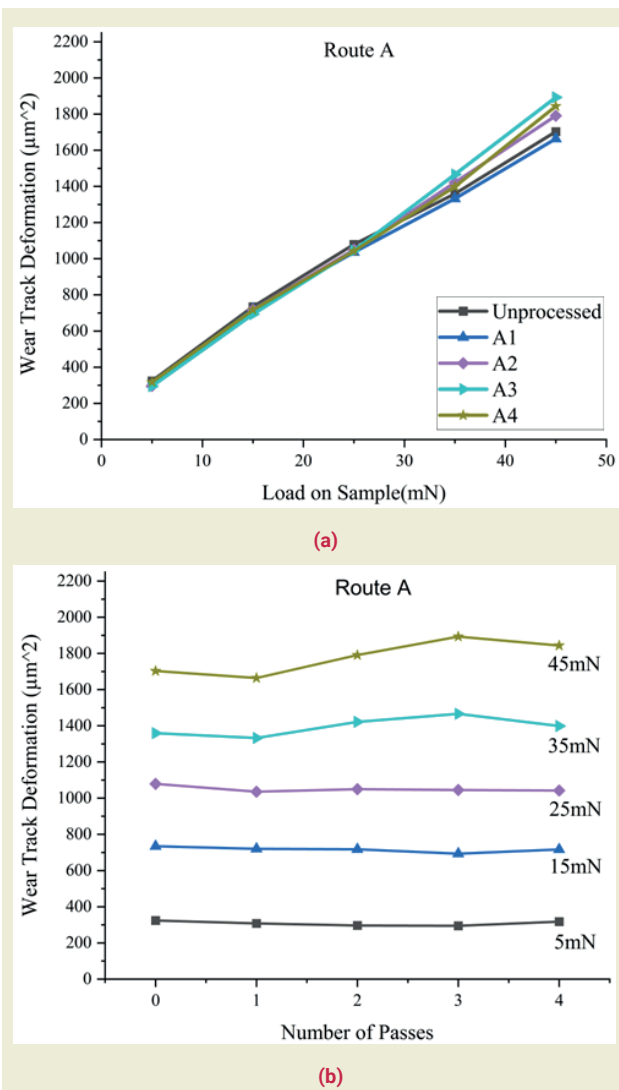


Figure 20. Wear track deformation versus load on sample and number of passing graphs for Route A.

of passes for Route A.

As shown in ►Figure 21 (a), wear track deformation increases as the applied force increases. ►Figure 21 (b) presents the wear track deformation versus the number of passes for Route A. As can be seen, the amount of material removed is almost linear, except for the 35 mN and 45 mN loads, where after the second pass, the amount of material removed increases. Yilmaz et al. [32] reported that wear track deformation was generally linear under various loads, except for specific intermediate loads like 35 mN and 45 mN, where an increase in wear was observed after subsequent ECAP passes. This was attributed to the complex interactions between the microstructure and applied loads during ECAP processing. ►Figure 21 shows the wear track deformation versus load on the sample and the number of passes for Route BC.

The wear track deformation for Route BC shows a similar linearity to that of Route A. However, unlike Route A, the wear track deformation for Route BC does not increase as much at the 35 and 45 mN loads. This sug-

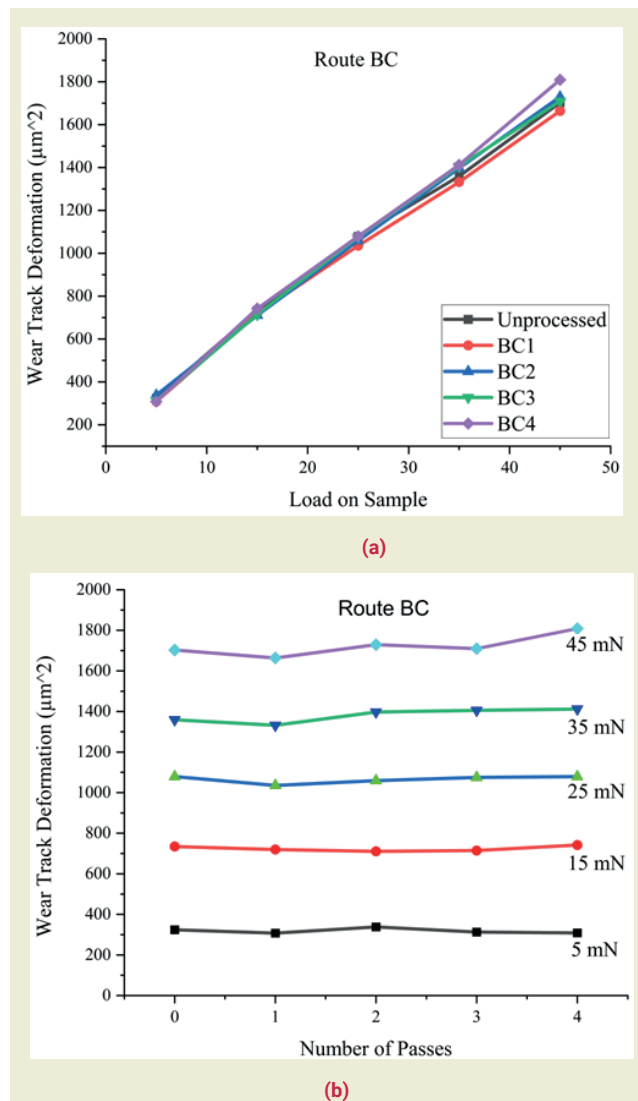


Figure 21. Wear track deformation versus load on sample and number of passing graphs for Route BC.

gests that samples processed by Route BC may be more suitable for such conditions, although the difference is not dramatic. Damavandi et al. [33] found that wear track deformation for samples processed by Route BC was more linear and exhibited less wear at higher loads compared to other Routes. This can be explained by the fact that Route BC produces a more uniform and homogeneous microstructure, which enhances wear resistance by providing a more uniform distribution of stress across the material. ►Figure 22 shows the wear track deformation versus load on the sample and the number of passes for Route D.

For Route D, the same linearity is observed. At the 35 mN load, wear track deformation starts to increase but remains more linear compared to Route A. However, at the 45 mN load, wear track deformation begins to resemble that of Route A. Therefore, it can be concluded that Route D falls somewhere between Routes A and Bc. Since the sample is rotated 180° after each pass, grain refinement is more homogeneous compared to Route A but less homogeneous than Route BC. Another reason could

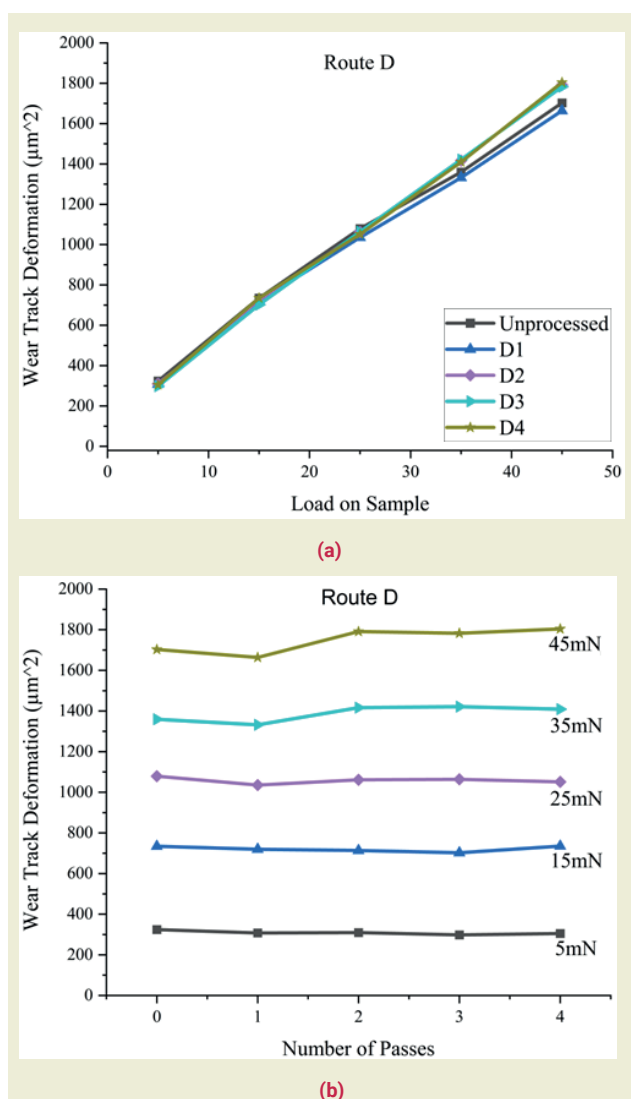


Figure 22. wear track deformation versus load on sample and number of passing graphs for Route D.

be that Route D generated more high-angle grain boundaries (HAGB) than Route A, which might have increased wear resistance by impeding dislocation movements.

4. Conclusion

The aim of this study was to investigate the tensile, creep, and wear properties of ECAP-processed ZCA-9

Al alloy and to test a newly proposed Route, referred to as Route D. The tension test results revealed that each Route can be used to improve the tensile strength of the ZCA-9 Al alloy. However, if optimal tensile strength is desired, Route BC is likely the best option. Additionally, the new Route, Route D, also shows promise for enhancing the tensile properties of the ZCA-9 Al alloy, but further studies are needed to fully understand its effects. For the creep tests, if only one or two passes are to be utilized, all tested Routes had significant effects on the stress exponent values. However, if higher creep resistance is desired, Route BC appears to be the best choice, as it exhibited the lowest stress exponent values for the third and fourth passes. Lastly, the wear test results indicate that ECAP processing did not have a significant effect on the wear resistance of the ZCA-9 Al alloy. If improved wear resistance is desired, other methods may need to be considered.

Research ethics

Not applicable.

Author contributions

The author solely conducted all stages of this research.

Competing interests

The author state no conflict of interest.

Research funding

None declared.

Data availability

The raw data can be obtained on request from the author.

Peer-review

Externally peer-reviewed.

Orcid

Serkan Ateş  <https://orcid.org/0000-0002-5858-5190>

References

- [1] Segal, V. M. (1999). Equal channel angular extrusion: From macro-mechanics to structure formation. *Materials Science and Engineering: A*, 271(1-2), 322–333.
- [2] Whang, S. H. (Ed.). (2011). *Nanostructured metals and alloys: Processing, microstructure, mechanical properties and applications*. Elsevier.
- [3] Naik, S. N., & Walley, S. M. (2020). The Hall–Petch and inverse Hall–Petch relations and the hardness of nanocrystalline metals. *Journal of Materials Science*, 55(7), 2661–2681.
- [4] Valiev, R. Z., Krasilnikov, N. A., & Tsenev, N. K. (1991). Plastic deformation of alloys with submicron-grained structure. *Materials Science and Engineering: A*, 137, 35–40.
- [5] Valiev, R. Z., Kozlov, E. V., Ivanov, Y. F., Lian, J., Nazarov, A. A., & Baudelet, B. (1994). Deformation behaviour of ultra-fine-grained copper. *Acta Metallurgica et Materialia*, 42(7), 2467–2475.
- [6] Alexandrov, I. V., & Valiev, R. Z. (1999). Nanostructures from severe plastic deformation and mechanisms of large-strain work hardening. *Nanostructured Materials*, 12(5-8), 709–712.
- [7] Abioye, O. P., Atanda, P. O., Osinkolu, G. A., Abioye, A. A., Olumori, I. D., Odunlami, O. A., & Afolalu, S. A. (2019). Influence of equal channel

- angular extrusion on the tensile behavior of Aluminum 6063 alloy. *Procedia Manufacturing*, 35, 1337–1343.
- [8] Ding, S. X., Lee, W. T., Chang, C. P., Chang, L. W., & Kao, P. W. (2008). Improvement of strength of magnesium alloy processed by equal channel angular extrusion. *Scripta Materialia*, 59(9), 1006–1009.
 - [9] Jiang, J., Wang, Y., Du, Z., Qu, J., Sun, Y., & Luo, S. (2010). Enhancing room temperature mechanical properties of Mg–9Al–Zn alloy by multi-pass equal channel angular extrusion. *Journal of Materials Processing Technology*, 210(5), 751–758.
 - [10] Martynenko, N. S., Lukyanova, E. A., Serebryany, V. N., Gorshenkov, M. V., Shchetinin, I. V., Raab, G. I., ... & Estrin, Y. (2018). Increasing strength and ductility of magnesium alloy WE43 by equal-channel angular pressing. *Materials Science and Engineering: A*, 712, 625–629.
 - [11] Tolaminejad, B., & Dehghani, K. (2012). Microstructural characterization and mechanical properties of nanostructured AA1070 aluminum after equal channel angular extrusion. *Materials & Design*, 34, 285–292.
 - [12] Yang, W., Quan, G. F., Ji, B., Wan, Y. F., Zhou, H., Zheng, J., & Yin, D. D. (2022). Effect of Y content and equal channel angular pressing on the microstructure, texture and mechanical property of extruded Mg–Y alloys. *Journal of Magnesium and Alloys*, 10(1), 195–208.
 - [13] Ferrasse, S., Hartwig, K. T., Goforth, R. E., & Segal, V. M. (1997). Microstructure and properties of copper and aluminum alloy 3003 heavily worked by equal channel angular extrusion. *Metallurgical and Materials Transactions A*, 28, 1047–1057.
 - [14] Langdon, T. G., Furukawa, M., Nemoto, M., & Horita, Z. (2000). Using equal-channel angular pressing for refining grain size. *JOM*, 52(4), 30–33.
 - [15] Tang, C. L., Hao, L. I., & Li, S. Y. (2016). Effect of processing route on grain refinement in pure copper processed by equal channel angular extrusion. *Transactions of Nonferrous Metals Society of China*, 26(7), 1736–1744.
 - [16] Savaskan, T., Pürçek, G., & Murphy, S. (2002). Sliding wear of cast zinc-based alloy bearings under static and dynamic loading conditions. *Wear*, 252(9–10), 693–703.
 - [17] Zhu, Y. H. (2001). Phase transformations of eutectoid Zn–Al alloys. *Journal of Materials Science*, 36(16), 3973–3980.
 - [18] Osório, W. R., & Garcia, A. (2002). Modeling dendritic structure and mechanical properties of Zn–Al alloys as a function of solidification conditions. *Materials Science and Engineering: A*, 325(1–2), 103–111.
 - [19] Turhal, M. Ş., & Savaşkan, T. (2003). Relationships between secondary dendrite arm spacing and mechanical properties of Zn–40Al–Cu alloys. *Journal of Materials Science*, 38, 2639–2646.
 - [20] Liu, Z., Li, P., Xiong, L., Liu, T., & He, L. (2017). High-temperature tensile deformation behavior and microstructure evolution of Ti55 titanium alloy. *Materials Science and Engineering: A*, 680, 259–269.
 - [21] Kumar, P., Xu, C., & Langdon, T. G. (2005). The significance of grain boundary sliding in the superplastic Zn–22% Al alloy after processing by ECAP. *Materials Science and Engineering: A*, 410, 447–450.
 - [22] Zhang, Y., Sao-Joao, S., Descartes, S., Kermouche, G., Montheillet, F., & Desrayaud, C. (2020). Microstructural evolution and mechanical properties of ultrafine-grained pure α -iron and Fe–0.02% C steel processed by high-pressure torsion: Influence of second-phase particles. *Materials Science and Engineering: A*, 795, 139915.
 - [23] Humphreys, F. J., & Hatherly, M. (2004). *Recrystallization and related annealing phenomena* (2nd ed.). Pergamon.
 - [24] Purcek, G., Altan, B. S., Miskioglu, I., & Patil, A. (2005). Mechanical properties of severely deformed ZA-27 alloy using equal channel angular extrusion. *Materials Science and Technology*, 21(9), 1044–1048.
 - [25] Nagasekhar, A. V., Tick-Hon, Y., Li, S., & Seow, H. P. (2006). Stress and strain histories in equal channel angular extrusion/pressing. *Materials Science and Engineering: A*, 423(1–2), 143–147.
 - [26] Ramirez, J. M. H., Bustamante, R. P., Merino, C. A. I., & Morquecho, A. M. A. (2020). *Unconventional techniques for the production of light alloys and composites*. Springer.
 - [27] Awasthi, A., Saxena, K. K., Dwivedi, R. K., Buddhi, D., & Mohammed, K. A. (2023). Design and analysis of ECAP processing for Al6061 alloy: A microstructure and mechanical property study. *International Journal on Interactive Design and Manufacturing (IJIDeM)*, 17(5), 2309–2321.
 - [28] Alateyah, A. I., Alawad, M. O., Aljohani, T. A., & El-Garaihy, W. H. (2022). Effect of ECAP route type on the microstructural evolution, crystallographic texture, electrochemical behavior and mechanical properties of ZK30 biodegradable magnesium alloy. *Materials*, 15(17), 6088.
 - [29] El-Shenawy, M., Ahmed, M. M., Nassef, A., El-Hadek, M., Alzahrani, B., Zedan, Y., & El-Garaihy, W. H. (2021). Effect of ECAP on the plastic strain homogeneity, microstructural evolution, crystallographic texture and mechanical properties of AA2xxx aluminum alloy. *Metals*, 11(6), 938.
 - [30] Maier, V., Merle, B., Göken, M., & Durst, K. (2013). An improved long-term nanoindentation creep testing approach for studying the local deformation processes in nanocrystalline metals at room and elevated temperatures. *Journal of Materials Research*, 28(9), 1177–1188.
 - [31] Zhao, Y., Guo, H., Shi, Z., Yao, Z., & Zhang, Y. (2011). Microstructure evolution of TA15 titanium alloy subjected to equal channel angular pressing and subsequent annealing at various temperatures. *Journal of Materials Processing Technology*, 211(8), 1364–1371.
 - [32] Yilmaz, T. A., Totik, Y., Senoz, G. M. L., & Bostan, B. (2022). Microstructure evolution and wear properties of ECAP-treated Al–Zn–Mg alloy: Effect of Route, temperature and number of passes. *Materials Today Communications*, 33, 104628.
 - [33] Damavandi, E., Nourouzi, S., Rabiee, S. M., Jamaati, R., & Szpunar, J. A. (2021). Effect of Route BC-ECAP on microstructural evolution and mechanical properties of Al–Si–Cu alloy. *Journal of Materials Science*, 56, 3535–3550.

Investigation of micro-perforated plate structure and cavity used as Helmholtz resonator in wheel arch liner

Yasemin Gultekin¹ , Thomas Jean² , Mustafa Atakan Akar³ , Umut Kumlu^{3*} 

¹NOVARES Turkey Otom. A.Ş. TOSB TAYSAD Org San Bölgesi 2. Cadde 11 Yol Şekerpınar, Kocaeli, Türkiye

²NOVARES GROUP, 9 Rue des Poissonniers, 62300, Lens, France

³Çukurova University, Department of Automotive Engineering, 01330, Adana, Türkiye

Abstract: Noise pollution, which is one of the pollutions in the developing world, affects human health and daily life. Cars make up a large part of this noise. This study focused on the transition noise reduction of automobiles by integrating the micro-perforated plate structure into the wheel arch liners. The noise absorption coefficients of the samples produced within the scope of the study were experimentally tested in Alpha Cabin and then validated with numerical simulations. When the results of the simulations were compared with the experimental test data, a compatible correlation was reached with the test data in terms of the reliability of the research. Finally, these structures were integrated and simulated in 4 different combinations on the wheel arch liners of a vehicle that is actively used in the market, and their noise absorption properties were compared with each other. As expected, while the noise absorption coefficients increased with the increase in perforated structures, combinations were obtained to meet the expectations of customers in the automotive industry. In addition, it is stated in the study results that the use of perforated structures in wheel arch liner (WAL) has the potential to reduce pass-by noise values.

Keywords: Wheel arch liner; acoustic; alpha cabin; micro-perforated plate; noise absorption; automotive.

1. Introduction

In today's world, pollution shows diversity. With the increase in the number of people and structures, one of the pollutions augmenting daily is noise pollution. Noise pollution negatively affects the lives of millions of people [1]. Noise-related problems include sleep disturbance, auditory loss, stress-regarding illnesses, slurred speech, high blood pressure, and loss of performance [2]. When it comes to the sources of the noise problem, traffic noise stands out. The noise emission created by vehicles in the daily distance they travel is an important problem [3]. Assorted tests are carried out for this problem, which is tried to be brought under control by administrative activities around the world [4]. In these tests, in which the pass-by noise is measured, the vehicles are operated at certain speeds and the noise produced by all their components is measured collectively [5]. For production conformity and type approval, automotive producers carry out pass-by noise measurement as mandatory [6]. From April 2014, 68 dB(A) is required as maximum noise in 2025 according to ISO

362, 51-03 noise test procedure. It is foreseen that the pass-by noise will be reduced by 2 dB every 2 years according to the regulations [7], [8].

Researchers actively seeking solutions to noise emissions try to prevent noise in certain parts of the vehicle. Along with alternative solutions such as the integration of noise absorber materials, there are studies on different acoustic absorber geometries. In a study, Bozca and Fietkau focused on reduce the noise produced by a gearbox using the empirical model approach. By considering various design parameters, the researchers optimized the number of teeth and the gaps in the gearbox in the design as geometrical, reducing the operating noise of the structure by 14% [9]. In another study, Nghiem and Wang, aimed to reduce vehicle engine noise and mainly focused on crankshaft strength and engine coatings. The researchers reduced the noise emission by 1 dB by rigidifying the crankshaft, and by using 3 different acoustic shields, a total of 3 dB noise emission [10]. There are also studies where researchers use Micro-perforated plates (MPP) structures to provide

*Corresponding author:

Email: ukumlu@cu.edu.tr

Cite this article as:

Gultekin, Y., et.al. (2025). Investigation of micro-perforated plate structure and cavity used as Helmholtz resonator in wheel arch liner. *European Mechanical Science*, 9(1): 38-43. <https://doi.org/10.26701/ems.1600309>

History dates:

Received: 12.12.2024, Revision Request: 28.01.2025, Last Revision Received: 01.02.2025, Accepted: 01.02.2025



© Author(s) 2025. This work is distributed under <https://creativecommons.org/licenses/by/4.0/>



acoustic absorption in vehicles. In a study, Zhu evaluated MPP structures for use in an automobile body. Focusing on hole diameters, cavities, and pores, they examined the acoustic performance of the structures and compared the structures, and presented the result [11]. Allam and Abom examined the feasibility of developing sound-absorbing mufflers for automotive ventilation and exhaust systems. Their research involved incorporating MPP absorbers into noise sources and conducting acoustic experiments. The findings indicated that MPP-based mufflers could serve as an effective solution for reducing noise in automotive applications [12].

The noise produced by vehicles comes from certain parts of the vehicle[13]. The noise made by moving parts in automobiles is the majority, and the part that produces the highest noise emission is the wheels where the vehicles meet the ground[10]. WALs around the wheels have no effect on reducing noise emissions, but the idea of integrating MPP structures into WALs is the motivation of this study. With this innovation, which has no examples in the literature, it is intended to reduce the pass-by noise of an automobile. In the study, first of all, experimental tests were carried out on real samples in the alpha cabin. These experimental tests were then simulated and validated numerically. Based on these results, these structures were simulated by integrating into the wheel arch liner models of a vehicle in the market with 4 different combinations. With the realization of this process, it is aimed to respond to the different option expectations of automobile customers. According to the results of the pass-by-noise tests, the highest noise levels are observed in the 630-2000 Hertz range. Hence, this study examined the sound emission levels in this range.

2. Materials and Methods

2.1. Materials

In the noise-absorbing structure studied in the previous study, polypropylene was used as the perforated plate material. Polypropylene is a thermoplastic polymer material that is often used in various fields from automotive to aviation, from building construction to shipping [14], [15]. The biggest reason why it is frequently used in these areas is that it can be easily shaped with the effect of heat and pressure. In addition to this feature, it is light and cheap, which makes it preferred by manufacturers [16], [17]. Many automobile manufacturers in the sector have this product in various parts of the vehicles. It is a material that is often used in WALs, which is the subject of the study. The properties of polypropylene, which is used as the raw material of the perforated plate, which is one of the main themes of the study, are given in ►Table 1.

WALs do not have noise absorbing properties on their own. For this reason, this feature is achieved by using

absorbent materials on the backside. The properties of the absorbent product used in the structure in the study are as in ►Table 2.

Table 1. Used Polypropylene's Properties for WALs[18]

Features	Values
Thickness (mm)	1.7
Density (g/cm ³)	0.90-0.95
Melt flow rate (230oC; 2,16 kg)(g/10min)	9-14
Flexural modulus (2mm/min)(MPa)	≥700
Notched impact strength (Izod) (23oC) kJ/m ²	≥8
Hardness (D-shore)	56-60
Tensile stress (50 mm/min)(MPa)	≥16
Tensile strain at break (50 mm/min)(%)	≥40
Tensile modulus (1mm/min) (MPa)	≥750

Table 2. Properties of acoustic absorbent[18]

Features	Values
Compression resistance (40%, 4th cycle) (kPa)	2.5 - 5
Flammability (thickness 13 mm) (mm/min)	≤80
Thickness(mm)	8
Net density(g/m ³)	400
Tensile strength (kPa)	120
Elongation at break (%)	200
Compression set (50% compression, 70°C, 22 h)(%)	3.1
Tear resistance (N/cm)	4.5
Odour (2 h, 80°C) (rate)	2.5
Acoustic on 10 mm (NRC value) (%)	30
Acoustic on 20 mm (NRC value) (%)	46
Fogging reflection (thickness 10 mm-3 h, 100°C)(%)	83
Fogging gravimetric (thickness 10 mm-16 h, 100°C)(mg)	0.7
Formaldehyde content(ppm)	2

2.2. Method

In this study, firstly, the plates to be tested in the Alpha cabin were prepared. The samples prepared to be tested in the Alpha cabin were prepared in 1x1.2m² dimensions by considering the studies in the literature. Based on the reference studies, the diameter of the holes was determined as 3 mm and the density was 7% on the plate[18]. In addition, the cavities behind the WAL were also applied to the test samples. The structure of the experimental test specimens is represented in ►Figure 1.

The output of the experimental studies is the sound absorption coefficient (Sa). This value is a result obtained by examining reverberation times in the Alpha Cabin. In the second part of the study, the validation process was carried out. In this part of the study, the sound absorption coefficients of the combinations were compared. First, the perforated plate, second the absorbent material, and finally the whole structure was validated.

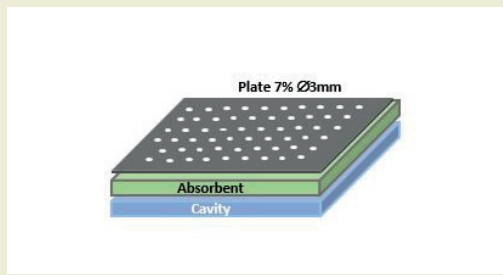


Figure 1. The structure of the experimental test specimens

ed with different cavity values. All this work was done with Matelys suite, based on the Transfer Matrix Method (TMM/FTMM) which predicts the vibro-acoustic

response of multi-layer systems [19]. In the last part of the study, the WALs of a vehicle model that is active in the sector are modeled by integrating these MPP structures. Simulations were carried out without ignoring the cavities behind the WALs on the vehicle. Models of WAL's in this reference vehicle, acoustic absorbers, and the the values of the cavities behind them are given in ►Figure 2.

In the study, instead of applying the integration of MPP structures to each wheel, it was applied in 4 different combinations. The aim here is to examine different scenarios on each wheel and to meet the option expectations of automobile drivers. The simulation combinations determined within the scope of the research are as in ►Figure 3.

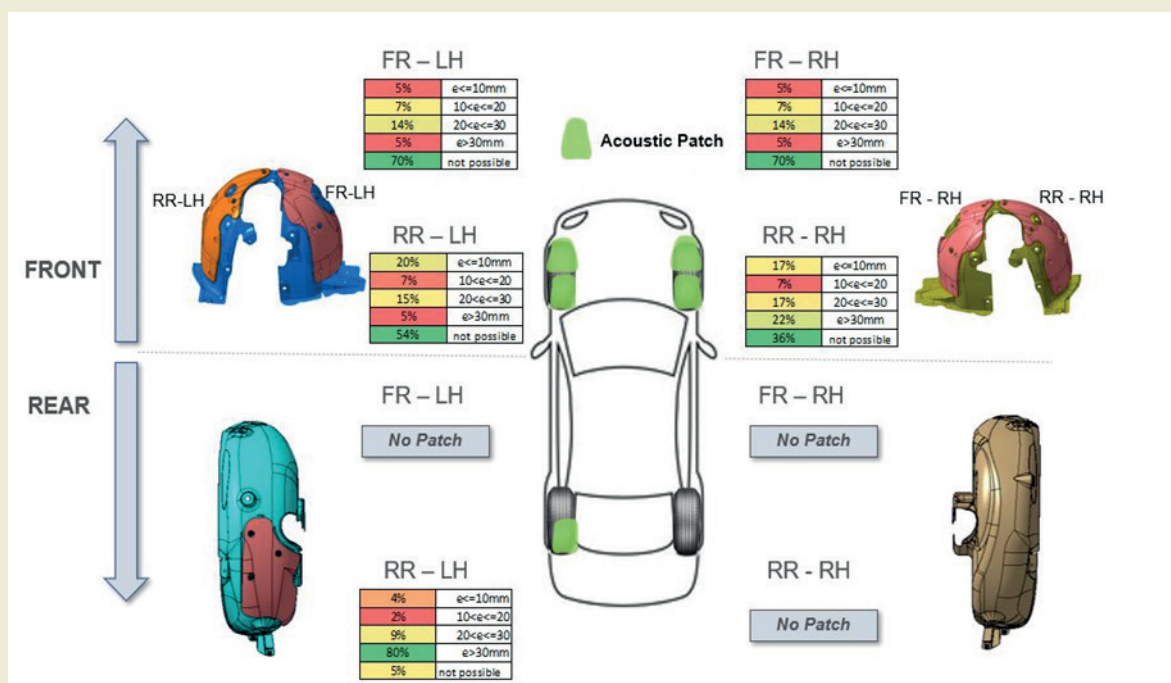


Figure 2. Models of WAL's in this reference vehicle, acoustic absorbers, and the values of the cavities behind WAL's

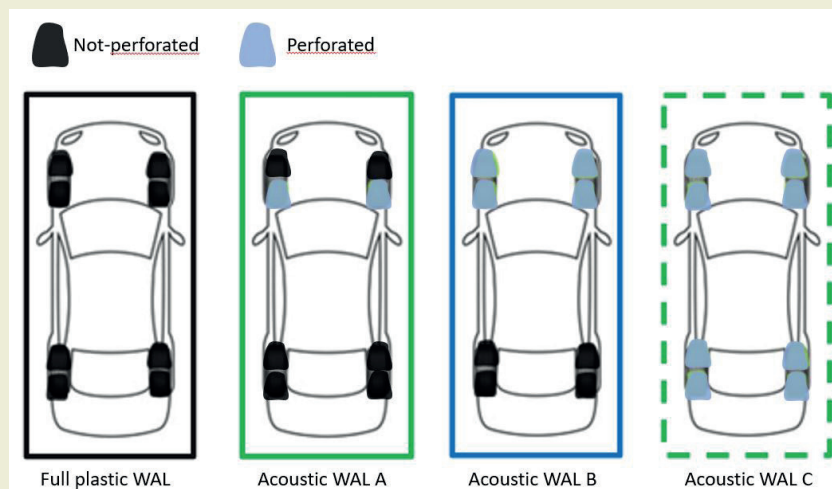


Figure 3. WAL combinations of simulations on current automobile in sector

2.3. Acoustic material model

According to studies in literature, acoustic behaviour of porous material can be defined with some parameters. The main parameters that we will consider are:

- the static air flow resistivity σ (N.s.m^{-4}),
- the open porosity ϕ ,
- the high frequency limit of the dynamic tortuosity ,
- the viscous characteristic length Λ (m),
- the thermal characteristic length Λ' (m).

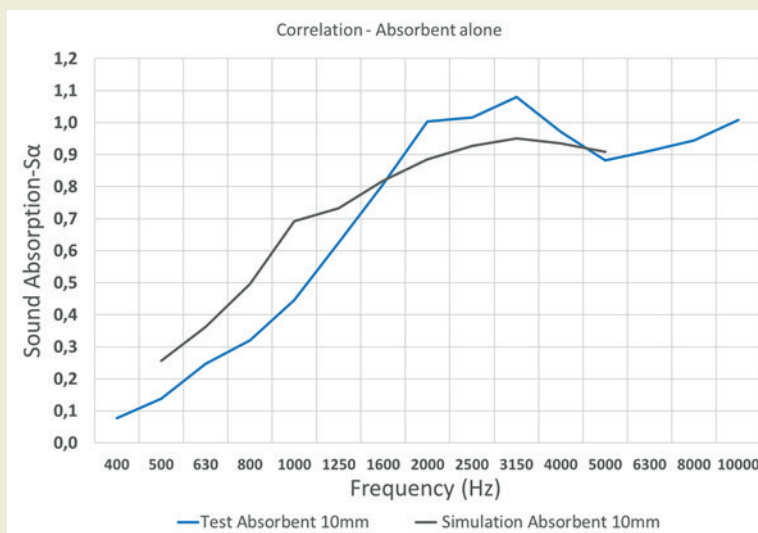
Static air flow resistivity σ and the open porosity ϕ of the material are the main parameters that should be measured with direct methods [20-21]. The other parameters are estimated from acoustic measurements in a stationary wave tube according to methods described in [22,23]. Parameters , (the high frequency limit of the dynamic tortuosity), Λ (the viscous characteristic length) and Λ' (the thermal characteristic length) are

then estimated from their analytical expressions deduced from the Johnson-Champoux-Allard (JCA) model and the Johnson-Champoux-Allard-Lafarge (JCAL) model [24-26]. All the work was done using MATELYS software.

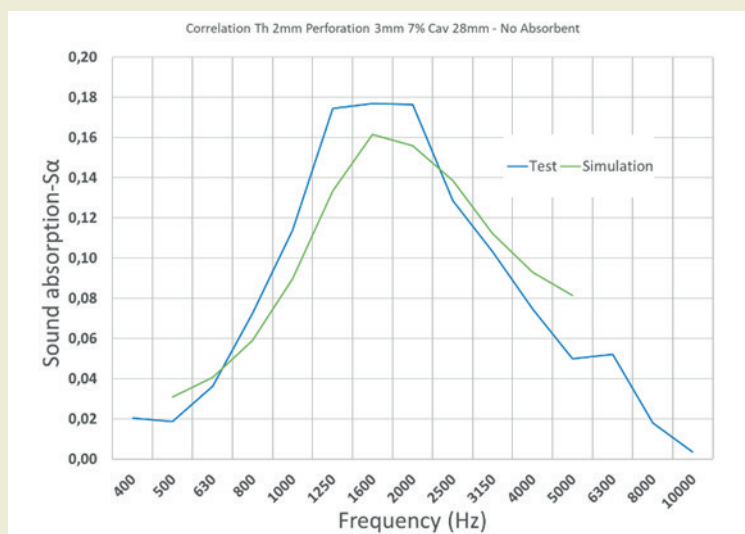
3. Results and Discussions

3.1. Comparison of Numerical and Experimental Results

In order to carry out the acoustic simulations of advanced WAL models in which WALs and MPP structures in a current car, which constitute the motivation of the study, are integrated, they must first be validated. Therefore, real plates and absorbents were modeled and simulated after being tested in the Alpha Cabin and the two types of results were compared with each other.

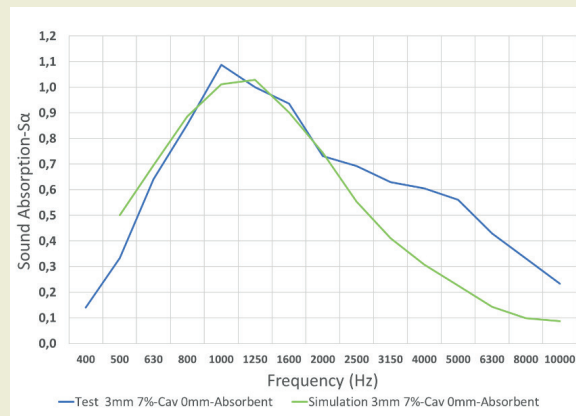


a)

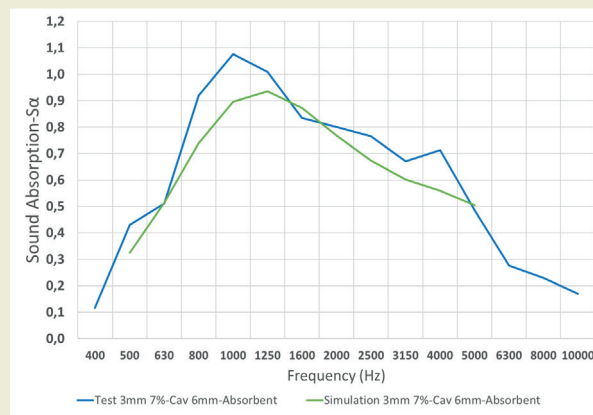


b)

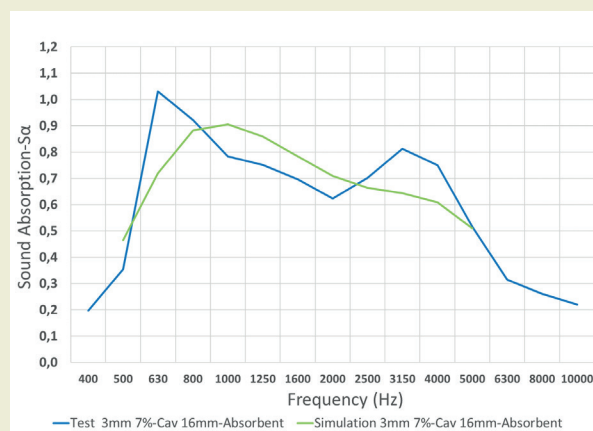
Figure 4. graphics experimental tests and simulation a) absorbent alone b) WAL alone



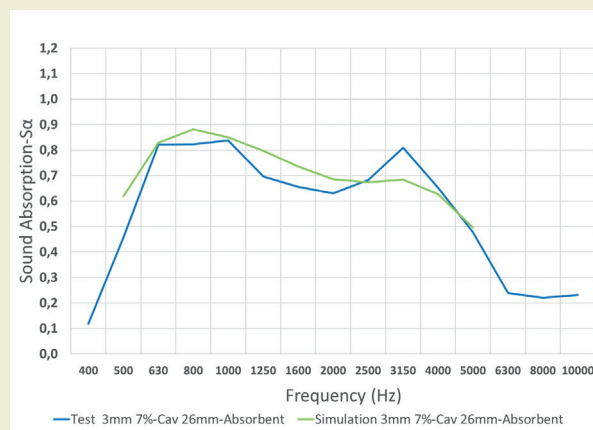
a)



b)



c)



d)

Figure 5. Comparison between test and simulation of Acoustic WAL for different cavity sizes a) 0 mm, b) 6 mm, c) 16 mm d) 26 mm

er. By going from the specific to the general, firstly the absorbent was tested and simulated alone. Then, the same process was applied only to the perforated plate without absorbent. While the diameter of the holes in the plate was 3 mm and the hole density was 7%, the cavity behind it was determined as 28 mm. The absorbent thickness used in the validation process was 10 mm. Experimental tests and simulation graphics of absorbent and WAL are shown in ►Figure 4.

As can be seen from the graphics, a good correlation was obtained between the experimental results and the simulations. Considering the absorbent, the highest sound absorption coefficient was 1.07 in the experimental test, while 0.96 was obtained in the simulation. The error rate was 10.3%. Considering only WAL, the sound absorption coefficient was found to be 0.16 in the simulation and 0.18 in the experimental test. The error rate was 9.04%. After the absorbent and WAL were validated alone, plates with both were produced and tested in the alpha cabinet to obtain sound absorption coefficients. Afterward, the models of these samples were created and examined in simulation and compared with the results obtained in experimental tests. The cavities behind the absorbents were determined as 0, 6, 16, and 26 mm, thus the effect of cavity increase was also examined. On the other hand, it is aimed to increase the reliability of the study by validating the results with 4 different cavity values. Experimental tests and simulation graphics of the plates according to the Cavity values are given in ►Figure 5.

Experimental test results and acoustic simulation results had the same tendency and gave close results in combinations of absorbent and WAL alone as well as in combinations. When the experimental test results of the plates are examined, the highest sound absorption values were obtained as 1.09 in 0 mm cavity, 1.08 in 6

mm cavity, 1.03 in 16 mm cavity and 0.84 in 26 mm cavity. In the simulations, the sound absorption values were found to be 1.03, in the 0 mm cavity, 0.94 in the 6 mm cavity, 0.91 in the 16 mm cavity, and 0.88 in the 26 mm cavity, respectively. When the results are examined according to these cavity values, the error rates are 5.5% in the 0 mm cavity, 13% in the 6 mm cavity, 11.6% in the 16 mm cavity, and 4.7% in the 26 mm cavity, respectively. By considering both experimental tests and simulation results, it is clearly observed that cavity values have a significant effect on acoustic absorption values. In addition, the overlapping of the experimental data with the simulation results also showed the way for the continuation of the study. The results validated with different cavity values showed that there is potential for improvement in acoustic absorption by examining these values in detail.

3.2. Comparison of WAL combinations on current automobile

After the validations have been made, perforated structures have been integrated into the WALs of a real vehicle for 4 different combinations that will meet the expectations of automobile customers. In the simulations, WALs with acoustic patches, the cavities behind the WALs, and the percentages of these cavities are as shown in ►Figure 2. Based on the automobiles on the market, the absorbent thickness was determined as 14 mm in this process. The sound absorption coefficient graphics obtained as a result of acoustic simulations of the combinations, one of which is a non-perforated full plastic structure and three of which are enhanced WALs, are shown in ►Figure 6.

As seen in ►Figure 6, the highest Sa value was seen in Acoustic WAL A with 1.11. The second highest val-

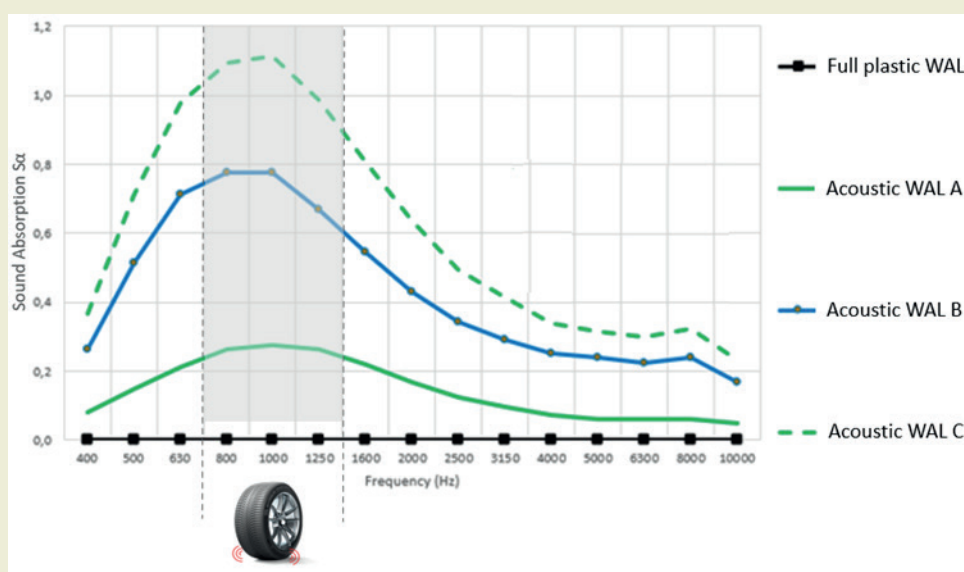


Figure 6. Results of numerical acoustic analysis of WAL combinations on current automobile

ue was found in Acoustic WAL B with 0.78, while the third highest value was in Acoustic WAL C with 0.28 Sa value. The acoustic absorption values of the non-perforated plate were close to zero. When the three acoustic WALs were compared to each other, Acoustic WAL A had 29.73% higher noise absorption values than Acoustic WAL B and 74.77% higher than Acoustic WAL C. When the acoustic absorption test results were evaluated, the increase in absorption values paralleled the increase in perforated structures. Considering consumer expectations, acoustic absorption values can be adjusted with various combinations. But it should not be forgotten that the strength of the WAL structure will decrease with the holes opened.

4. Conclusions

The effects of noise pollution on the environment and human health stand out as a fact of today's world. In this study, pass by noise in vehicles, which is one of the biggest sources of this problem in daily life, is discussed. The motivation of the research is to reduce the pass by noise by integrating the MPP structures into the wheel arch liners in the vehicles. First of all, the real samples created were tested in alpha cabin, then modeled and validated by performing numerical analysis. A very good correlation was reached between the numerical analyzes performed and the test results. In the continuation of the research, the wheel arch liners of a vehicle currently in the industry were modeled and the integration of MPP structures was made in 4 different combinations. Acoustic emission values increased as expected in regions where MPP structures are in the majority. As a result of this study, wheel arch liners developed with 4 different options were provided to the manufacturers. In the results, it was explained that the pass by noise can be reduced with improved WALs by integrating MPP structures. In the results, it has been stated that a good noise absorption performance can be achieved by

optimizing the spaces behind MPP structures.

Research ethics

Not applicable.

Author contributions

Conceptualization: [Yasemin Gultekin, Thomas Jean], Methodology: [Thomas Jean], Formal Analysis: [Thomas Jean], Investigation: [Yasemin Gultekin, Thomas Jean, Umut Kumlu], Resources: [Yasemin Gultekin, Thomas Jean], Data Curation: [Yasemin Gultekin, Thomas Jean], Writing - Original Draft Preparation: [Mustafa Atakan Akar, Umut Kumlu], Writing - Review & Editing: [Mustafa Atakan Akar, Umut Kumlu], Visualization: [Thomas Jean, Yasemin Gultekin, Umut Kumlu], Supervision: [Mustafa Atakan Akar, Umut Kumlu], Project Administration: [Thomas Jean, Yasemin Gultekin]

Competing interests

The authors states no conflict of interest.

Research funding

None declared.

Data availability


Not applicable.


Peer-review


Externally peer-reviewed.

Orcid

Yasemin Gultekin  <https://orcid.org/0000-0001-9967-8329>

Thomas Jean  <https://orcid.org/0009-0003-8097-5448>

M. Atakan Akar  <https://orcid.org/0000-0002-0192-0605>

Umut Kumlu  <https://orcid.org/0000-0001-7624-6240>

References

- [1] Chen, S., Wang, D., & Liu, B. (2013). Automotive Exterior Noise Optimization Using Grey Relational Analysis Coupled with Principal Component Analysis. *Fluctuation and Noise Letters*, 12(3), 1–22. <https://doi.org/10.1142/S021947751350017X>
- [2] U. S. Office of Noise Abatement Control & National Association of Noise Control Officials. (1981). *Noise Effects Handbooks: a Desk Reference to Health and Welfare Effects of Noise*. National Association of Noise Control Officials, Washington D. C.
- [3] Ibarra, D., Ramírez-Mendoza, R., & López, E. (2016). A New Approach for Estimating Noise Emission of Automotive Vehicles. *Acta Acustica United with Acustica*, 102(5), 930–937. <https://doi.org/10.3813/AAA.919007>
- [4] Baudson, R., Lafont, T., Balamraj, V.S., Ronzio, F., & Nieuwenhof, B. V. (2019). Parametric Analysis of an Automotive Wheel Arch Acoustic Treatment. In *Automotive Acoustics Conference 2019*. (pp. 185–199)
- [5] Huijssen, J., Hallez, R., Pluymers, B., & Desmet, W. (2013). A synthesis procedure for pass-by noise of automotive vehicles employing numerically evaluated source–receiver transfer functions. *Journal of Sound and Vibration*, 332(15), 3790–3802. <https://doi.org/10.1016/j.jsv.2013.01.042>
- [6] Yasuda, T., Wu, C., Nakagawa, N., & Nagamura, K. (2013). Studies on an automobile muffler with the acoustic characteristic of low-pass filter and Helmholtz resonator. *Applied Acoustics*, 74(1), 49–57. <https://doi.org/10.1016/j.apacoust.2012.06.007>
- [7] ISO 362-1: 2015., (2015). *Measurement of Noise Emitted by Accelerating Road Vehicles – Part 1: M and N Categories*.
- [8] Bertolini, C., Horak, J., & Lafont, T., (2020). Design of sound package for pass-by noise reduction: process and application. In *Automotive Acoustics Conference 2019* (pp.137–169).
- [9] Bozca, M., & Fietkau, P. (2010). Empirical model based optimization of gearbox geometric design parameters to reduce rattle noise in an automotive transmission. *Mechanism and Machine Theory*, 45(11), 1599–612. <https://doi.org/10.1016/j.mechmachtheory.2010.06.013>
- [10] Nghiem, G., & Wang, S. (2014). Improvement of engine sound radiation for the new pass-by noise regulation. *SAE Technical Paper Series*

- ries, 2014-01-2074, <https://doi.org/10.4271/2014-01-2074>
- [11] Zhu, C.Y. (2011). Research on the absorption characteristic of three-layer microperforate plate of the automotive body. *Advanced Materials Research*, 201–203, 2160–2166. <https://doi.org/10.4028/www.scientific.net/AMR.201-203.2160>
- [12] Allam, S., & Åbom, M. (2011). A new type of muffler based on microperforated tubes. *Journal of Vibration and Acoustics*, 133(3), 1–8. <https://doi.org/10.1115/1.4002956>
- [13] O'Boy, D.J. (2020). Automotive wheel and tyre design for suppression of acoustic cavity noise through the incorporation of passive resonators. *Journal of Sound and Vibration*, 467, 1–14. <https://doi.org/10.1016/j.jsv.2019.115037>
- [14] Park, J.-M., Kim, P.-G., Jang, J.-H., Wang, Z., Hwang, B.-S., & DeVries, K.L. (2008). Interfacial evaluation and durability of modified Jute fibers/polypropylene (PP) composites using micromechanical test and acoustic emission. *Composites Part B: Engineering*, 39(6), 1042–1061. <https://doi.org/10.1016/j.compositesb.2007.11.004>
- [15] Çolak, Ö.Ü., & Çakır, Y. (2019). Genetic algorithm optimization method for parameter estimation in the modeling of storage modulus of thermoplastics. *Sigma Journal of Engineering and Natural Sciences*, 37(3), 981–8.
- [16] Hariprasad, K., Ravichandran, K., Jayaseelan, V., & Muthuramalingam, T. (2020). Acoustic and mechanical characterisation of polypropylene composites reinforced by natural fibres for automotive applications. *Journal of Materials Research and Technology*, 9(6), 14029–14035. <https://doi.org/10.1016/j.jmrt.2020.09.112>
- [17] Cho, D., Seo, J.M., Lee, H.S., Cho, C.W., Han, S.O., & Park, W.H. (2007). Property improvement of natural fiber-reinforced green composites by water treatment. *Advanced Composite Materials: The Official Journal of the Japan Society of Composite Materials*, 16(4), 299–314. <https://doi.org/10.1163/156855107782325249>
- [18] Gültekin, Y., Jean, T., Akar, M.A., & Kumlu, U., (2024) Acoustic emission reduction in vehicles by using MPP structures in wheel ARCH liner structures. *Sigma Journal of Engineering and Natural Sciences*, 42(6), 1749–1755. <https://doi.org/10.14744/sigma.2024.00133>
- [19] Santoni, A., Bonfiglio, P., Fausti, P., & Pompoli, F. (2021). Computation of the alpha cabin sound absorption coefficient by using the finite transfer matrix method (FTMM): inter-laboratory test on porous media. *Journal of Vibration and Acoustics*, 143(2), <https://doi.org/10.1115/1.4048395>
- [20] Bertolini, C., & Guj, L. (2011). Numerical simulation of the measurement of the diffuse field absorption coefficient in small reverberation rooms. *SAE International Journal of Passenger Cars - Mechanical Systems*, 4(2), 1168–1194. <https://doi.org/10.4271/2011-01-1641>
- [21] Atalla, N., & Sgard, F. (2007). Modeling of perforated plates and screens using rigid frame porous models. *Journal of Sound and Vibration*, 303(1–2), 195–208. <https://doi.org/10.1016/j.jsv.2007.01.012>
- [22] Panneton, R., & Olny, X. (2006). Acoustical determination of the parameters governing viscous dissipation in porous media. *The Journal of the Acoustical Society of America*, 119(4), 2027–2040. <https://doi.org/10.1121/1.2169923>
- [23] Olny, X., & Panneton, R. (2008). Acoustical determination of the parameters governing thermal dissipation in porous media. *The Journal of the Acoustical Society of America*, 123(2), 814–824. <https://doi.org/10.1121/1.2828066>
- [24] Johnson, D.L., Koplik, J., & Dashen, R. (1987). Theory of dynamic permeability and tortuosity in fluid saturated porous media. *Journal of Fluid Mechanics*, 176, 379–402. <https://doi.org/10.1017/S0022112087000727>
- [25] Champoux, Y., & Allard, J.F. (1991). Dynamic tortuosity and bulk modulus in air-saturated porous media. *Journal of Applied Physics*, 70(4), 1975–1979. <https://doi.org/10.1063/1.349482>
- [26] Lafarge, D., Lemarinier, P., Allard, J.F., & Tarnow, V. (1997). Dynamic compressibility of air in porous structures at audible frequencies. *The Journal of the Acoustical Society of America*, 102(4), 1995–2006. <https://doi.org/10.1121/1.419690>

Thermal and electrical analysis of 26650 li-ion batteries in series connection using the NTGK model and virtual simulations

Metin Uzun^{1*} 

¹Department of Airframe and Powerplant Maintenance, Faculty of Aeronautics and Astronautics, Iskenderun Technical University, 31200 Hatay, Türkiye

Abstract: Lithium-ion batteries are extensively used in various renewable sources such as renewable energy storage systems, electric vehicles, and portable electric vehicles due to their storage properties. However, since they are significantly affected by ambient temperature, their lifetime and safety issues in general negatively affect their electrical performance. In order to ensure that batteries achieve their optimum potential, it is necessary to understand the interaction between charge and discharge rates and temperature changes very well. In this study, the electrical characteristics of 26650 lithium-ion batteries were analyzed in series under different environmental conditions and different discharge rates. To understand the relationship between environmental temperatures and battery performance, Newman, Tiedemann, Gu, and Kim (NTGK) evaluated the effectiveness of previously used models in predicting these effects. The Ansys Battery Ntgk model was used to predict the temperature behavior and voltage variations under different outdoor temperature conditions. In this study, four ambient temperatures (273 K, 283 K, 298 K, and 318 K) and four discharge rates (0.5C, 1C, 1.5C, and 2C) were investigated to study the thermal characteristics and voltage variations. The mesh independence study was carried out in detail at the beginning of the analysis to validate the simulation results. The results indicate that the discharge time decreases significantly due to increased internal resistance and electrochemical side reactions. The 1S1P battery design reaches a maximum internal temperature of 303.2 K at 273.15 K ambient temperature and 336.7 K at 318.15 K ambient temperature, while the 2S1P battery design exhibits an even higher maximum temperature of 341.3 K at an ambient temperature of 318.15 K, indicating that compound heat buildup occurs in series connections.

Keywords: 26650 lithium-ion battery; voltage output; thermal behavior; ambient temperature; NTGK model; ANSYS simulation; electric vehicles; thermal management systems.

1. Introduction

Because of its high energy density, extended cycle life, and low self-discharge rates, lithium-ion (Li-ion) batteries are at the forefront of energy storage technology and are extensively utilized in portable electronics, electric vehicles (EVs), and renewable energy systems. Lithium-ion batteries are critical for applications where high reliability and efficient operation are desired. Lithium-ion batteries are widely used in many areas today due to their high energy density, long life, and low maintenance requirements [1,2]. However, thermal management is crucial for batteries to operate efficiently and safely. Especially at high discharge rates and variable environmental conditions, the effects of internal heat generation and ambient temperature on the voltage

balance and thermal efficiency of batteries are examined in detail by researchers [3,4]. Therefore, Thermal Management Systems (TMS) are being developed to prevent overheating and keep temperature imbalances under control. An ineffective thermal management system shortens the life of the battery, while also causing energy losses and safety risks.

In this context, methods such as phase change materials (PCM), hybrid cooling systems, and numerical modeling techniques continue to be developed to increase the thermal performance of batteries [5,6]. PCMs can also maintain temperature balance by preventing overheating of batteries thanks to their high heat storage capacities. Studies have shown that metal fins integrated into PCM systems increase the heat conduction of

*Corresponding author:
Email: metin.uzun@iste.edu.tr

Cite this article as:

Uzun, M. (2025). Thermal and electrical analysis of 26650 li-ion batteries in series connection using the NTGK model and virtual simulations. *European Mechanical Science*, 9(1): 46-58. <https://doi.org/10.26701/ems.1600894>

History dates:

Received: 15.12.2024, Revision Request: 08.02.2025, Last Revision Received: 16.02.2025, Accepted: 06.03.2025



© Author(s) 2025. This work is distributed under <https://creativecommons.org/licenses/by/4.0/>



these materials and make the temperature distribution more balanced [3]. Especially in applications requiring high power such as electric vehicles, the use of PCMs with liquid cooling or thermoelectric modules ensures safe and efficient operation of batteries [6,7].

The Newman, Tiedemann, Gu, and Kim (NTGK) model, developed to understand the electrochemical and thermal behaviors of batteries, stands out with its ability to accurately predict temperature changes and voltage behaviors in different environmental conditions [8,9]. This model contributes to the optimization of battery management systems (BMS) and to ensuring battery safety. In addition, hybrid cooling systems combining active and passive cooling methods are also being investigated to improve thermal management [7]. It is stated in the literature that PCM-based thermal management systems provide effective temperature control at high discharge rates and balance heat dissipation [5,8]. In addition, finned systems have been shown to reduce temperature differences by increasing heat transfer in battery modules.

Numerical modeling and dynamic simulation techniques are widely used to better understand and improve the thermal and electrical performance of batteries [4,6]. These methods allow the development of new generation thermal management systems by examining how batteries respond to different discharge rates and environmental conditions. In addition, the mechanical and thermal interactions of batteries have been examined in detail and the effects of temperature changes on battery life and current characteristics have been revealed.

In order to further improve the thermal management performance of batteries, metallic PCM integration providing fast thermal response has been proposed, and new micro-fin designs have been developed to increase heat dissipation in high-density battery modules [10]. These innovations are considered as important steps to close the gap between battery technologies and industrial applications [10,11].

Despite all these developments, the relationship between internal heat generation, battery voltage and ambient temperature has not been fully answered in the literature.. Therefore, new studies based on advanced modeling approaches and experimental validations are needed to analyze the thermal and electrical behavior of batteries more comprehensively. In this study, the electrical and thermal behavior of 26650 lithium-ion batteries under different environmental conditions is investigated using the NTGK model. The simulation results combined with theoretical frameworks contribute to the development of effective thermal management systems for applications such as electric vehicles, renewable energy systems, and portable electronics [12,13].

Despite the large number of studies on the thermal and electrical behavior of lithium-ion batteries, research on the application of the NTGK model in series-connected configurations of type 26650 batteries under differ-

ent ambient temperatures has been limited. Previous studies have mostly focused on single-cell simulations or experimental verifications and do not fully integrate numerical modeling techniques to evaluate the voltage behavior and thermal variations in multicell systems. To address this gap, this research aims to perform detailed simulations of 26650 batteries using the NTGK model to evaluate their thermal and electrical performance under different environmental conditions and discharge rates. The findings will contribute to optimizing battery thermal management strategies for real-world applications.

Most previous studies have focused on single-cell lithium-ion battery simulations or performed analyses based on experimental data without integrating detailed electrochemical-thermal modeling techniques. However, this study presents a comprehensive approach by evaluating the thermal and electrical performance of series-connected 26650 cells through the NTGK model. The novelty of this study lies in the detailed numerical modeling approach and the examination of multi-cell configurations under varying environmental conditions, which have not been extensively studied in the literature. Furthermore, this study contributes to understanding the complex interactions between voltage behavior, heat accumulation, and discharge conditions, which are crucial for optimizing battery thermal management in practical applications such as electric vehicles and energy storage systems. A key innovative aspect of this study is the implementation of the use Virtual Battery Connection method, which eliminates the need for physical busbars in series-connected battery configurations. Traditional bus-bar connections introduce additional weight and resistive losses, which can negatively impact overall system efficiency, particularly in weight-sensitive applications such as electric vehicles (EVs) and aerospace battery systems. By utilizing a virtual connection approach, this study provides a lightweight and computationally efficient alternative, ensuring a more accurate representation of real-world battery pack behavior without the added complexity of physical interconnections. Furthermore, unlike previous research that primarily focuses on either experimental or simplified numerical modeling approaches, this study integrates the Newman, Tiedemann, Gu, and Kim (NTGK) model with advanced numerical simulations to offer a more precise analysis of the thermal and electrical performance of series-connected 26650 lithium-ion cells under various ambient temperature and discharge conditions. These findings contribute to the optimization of battery pack design, enhancing performance and safety in high-power applications such as electric vehicles, renewable energy storage, and aerospace systems.

2. Materials and Methods

The following table provides a list of symbols and their corresponding definitions used throughout the mathematical modeling and numerical analysis sections of

this study. This nomenclature ensures clarity in the interpretation of equations and parameters presented in the manuscript.

2.1. Battery Specification and Configuration

Commercially available 26650 lithium-ion (Li-ion) batteries with a 5000 mAh capacity and a nominal voltage of 3.7 V were used in this investigation. Unlike the traditional busbar connection method, the serial connection of battery packs is achieved using the virtual connection model in Ansys Fluent. By eliminating the resistance losses caused by hardwired busbar connections, this new technique has made it possible to accurately simulate the series or parallel connection behavior of batteries. In this study, the following assumptions were made in the numerical analysis:

Battery Materials and Homogeneity: The battery components (cathode, anode, separator) were assumed to be homogeneous and isotropic in terms of thermal and electrical properties.

Heat Generation and Dissipation: The heat generation was considered primarily due to Joule heating and electrochemical reactions, while radiation heat transfer was neglected.

Electrochemical Kinetics: The NTGK model parameters were derived from experimental discharge data, assuming uniform reaction kinetics within the battery structure.

No Aging Effects: Battery degradation effects such as capacity fade and resistance growth over repeated cycles were not included in the model.

Ambient Conditions: The ambient temperature was considered uniform, with no external forced convection applied unless explicitly stated in the simulation conditions.

These assumptions were necessary to ensure computational efficiency while maintaining accuracy in predicting thermal and voltage behavior.

2.1.1 Equations of the Battery Model Used in Numerical Analysis

In this work, the thermal and electric fields of the battery are solved in the CFD domain at the battery cell scale using the following differential equation

$$\partial(\rho C_p T)/\partial t - \nabla \cdot (k \nabla T) = \sigma_+ |\nabla \phi_+|^2 + \sigma_- |\nabla \phi_-|^2 + \dot{q}_{Ech} + \dot{q}_{SHORT} + \dot{q}_{abuse} \quad (1)$$

$$\nabla \cdot (\sigma_+ \nabla \phi_+) = -(j_{Ech} - j_{short}) \quad (2)$$

$$\nabla \cdot (\sigma_- \nabla \phi_-) = j_{Ech} - j_{short} \quad (3)$$

where σ_+ and σ_- are the effective electric conductivities for the positive and negative electrodes, ϕ_+ and ϕ_- are phase potentials for the positive and negative electrodes, j_{Ech} and \dot{q}_{Ech} are the volumetric current transfer rate and the electrochemical reaction heat due to electrochemical reactions, respectively, j_{short} and \dot{q}_{SHORT} are the current transfer rate and heat generation rate due to battery internal short-circuit, respectively, \dot{q}_{abuse} and is the heat generation due to the thermal runaway reactions under the thermal abuse condition [16].

NTGK is a simple semi-empirical electrochemical model. The volumetric current transfer rate is related to the potential field by:

$$j_{Ech} = \frac{Q_{nominal}}{Q_{ref} Vol} Y[U - V] \quad (4)$$

where denotes the active zone's volume of a single battery; V is the battery cell voltage, which is either obtained directly from the circuit network solution method or calculated as $\phi_+ - \phi_-$ from the MSMD solution method; $Q_{nominal}$ is the battery total electric capacity in Ampere hours; and Q_{ref} is the capacity of the battery that is used in experiments to obtain the model parameters Y and Y/U and U are functions of the battery depth of discharge (DoD):

$$DoD = \frac{Vol}{3600 Q_{nominal}} \int_0^t j dt \quad (5)$$

For a given battery, the voltage-current response curve can be obtained through experimentation. Then Y and U in Equations 6 and 7 can be fitted, in theory. There are two approaches to specifying functions [16]:

Y and U can be fitted from testing data as functions of DOD and temperature explicitly before simulations. The relationship between Y/U and DOD/temperature can be provided:

$$U = \left(\sum_{n=0}^5 a_n (DoD)^n \right) - C_2 (T - T_{ref}) \quad (6)$$

$$Y = \left(\sum_{n=0}^5 b_n (DoD)^n \right) \exp \left[-C_1 \left(\frac{1}{T} - \frac{1}{T_{ref}} \right) \right] \quad (7)$$

where C_1 and C_2 are the battery-specific NTGK model constants.

Y and U are not predetermined. Instead, the relationship between current and voltage from raw test data is stored, and Y and U are calculated dynamically during the simulation.

Model parameters are battery specific. You can use the Y and U parameters from a tested battery with a capacity Q_{ref} for a battery with a different capacity $Q_{nominal}$

as long as the battery's material is the same. If the model parameters are from the battery that is analogous to the one you are simulating, then capacities $Q_{nominal}$ and Q_{ref} will be the same.

The electrochemical reaction heat \dot{q}_{Ech} is calculated as

$$\dot{q}_{Ech} = j_{ECh} = \left[U - V - T \frac{dU}{dT} \right] \quad (8)$$

The Li-ion cell specifications, material properties for the NTGK model, U and Y coefficients, and material properties are listed [16] in ►Tables 1 to 3 respectively.

2.2. Simulation Model

For in-depth thermal and electrochemical simulations, the Newman, Tiedemann, Gu, and Kim (NTGK) model was used. The NTGK model offers a semi-empirical framework that can precisely forecast battery cell temperature rise, voltage behavior, and thermal distribution under a range of operating circumstances. To guarantee accurate findings, simulations were carried out using ANSYS Fluent, using the virtual connection and the NTGK modeling technique.

To ensure the accuracy of the numerical model, a mesh independence test was conducted by evaluating different element counts ranging from 20,000 to 50,000. As shown in ►Table 1, the maximum internal temperature and voltage results stabilize when the mesh size reaches 40,256 elements, with negligible variation observed in the 50,000-element case. Increasing the mesh density beyond this point resulted in only a 0.1 K difference in maximum temperature, which falls within an acceptable numerical error range. However, computational time increased significantly, from 2500 seconds for

Table 1. Effect of Mesh Density on Temperature and Voltage Predictions

Mesh Elements	Maximum Temperature (K)	Voltage (V)	Computational Time (s)
20,000	318.9	3.72	1800
30,000	316.1	3.74	2200
40,256	316.7	3.75	2500
50,000	316.6	3.75	3100

40,256 elements to 3100 seconds for 50,000 elements, without yielding substantial improvements in accuracy.

Previous studies have demonstrated that 20,000 mesh elements are sufficient for accurate thermal heat flux distribution prediction in an electric vehicle battery cell [18]. However, other works have shown that more refined mesh structures (38,777 to 45,604 elements) provide enhanced accuracy in complex battery thermal simulations [19]. Considering these findings, a 40,256-element mesh was selected as the optimal balance between computational efficiency and numerical precision in this study. Our results confirm that finer mesh sizes beyond this threshold contribute to excessive computational costs without a significant accuracy gain.

Therefore, the selection of a network with 40,256 mesh elements has provided an appropriate numerical model to ensure computational efficiency.

The mesh independence study, the thermal behavior study for a single battery were conducted with the NTGK model. In these tests, maximum temperature was chosen as the main evaluation criterion. As a result of the analysis, it was decided that a network structure

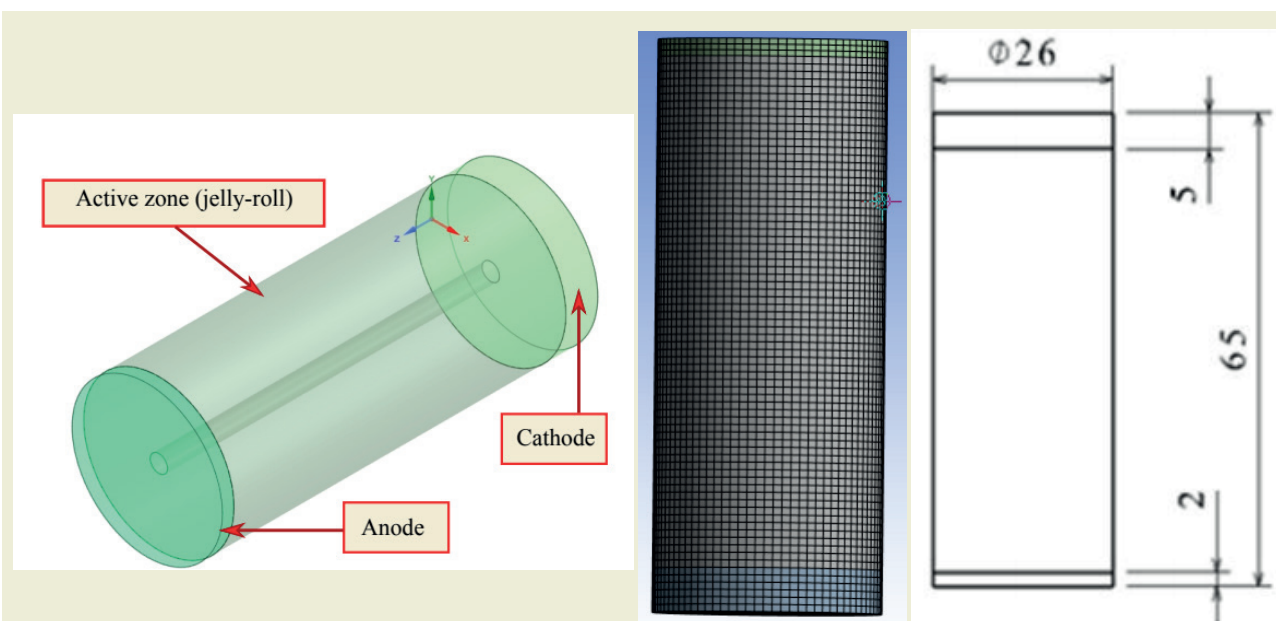


Figure 1. Battery details for Newman, Tiedemann, Gu, and Kim (NTGK) model

consisting of approximately 40256 elements is the optimal value in terms of both computational efficiency and accuracy of results in single-cell battery simulations. This network structure provided sufficient ktireter to model the thermal and electrical behavior of the battery with sufficient accuracy. A comprehensive diagram of the 26650 Li-ion battery used in the study is shown in detail in ►Figure 1 using the NTGK framework. The diameter of the battery used in this study was modeled as 26 mm and the height as 65 mm.”The mesh independence test indicated that a mesh size of 40,256 elements provided an optimal balance between computational efficiency and accuracy. This is in agreement with previous studies on battery thermal modeling, where similar element counts (ranging from 35,000 to 50,000 elements) were reported to achieve mesh-independent solutions [17].”

2.3. Virtual Simulation Setup

A virtual series connection of the batteries was modeled to replicate realistic operating conditions.

Table 1. 26650 Li-ion battery Specification [14]

Parameter	Specification
Nominal Voltage	3.7 V
Nominal Capacity	4 Ah
Maximum Discharge Rate	2C
Maximum Charge Rate	1C
Dimensions (Diameter × Height)	26 mm × 65 mm
Mass	88 g
Cathode Material	LiCoO ₂
Anode Material	Graphite
Charging Voltage Limit	4.2 V
Cut-off Voltage	2.75 V
Emissivity	0.8

Simulations incorporated ambient temperatures of 273.15 K, 283.15 K, 298.15 K, and 318.15 K, and discharge rates of 0.5C, 1C, 1.5C, and 2C. Key input parameters, such as heat generation rate and thermal conductivity of the battery components, were included to ensure accuracy.

The selected ambient temperature ranges correspond to real-world operating conditions that lithium-ion batteries frequently encounter in various applications. 273.15 K (0°C) represents cold winter conditions, particularly relevant for electric vehicles (EVs) operating in high-latitude regions or elevated terrains where low temperatures can significantly impact battery performance. 283.15 K (10°C) reflects mildly cold conditions, typical of early spring or late autumn, where battery efficiency starts to improve but remains affected by moderate temperature variations. 298.15 K (25°C) represents standard room temperature, a benchmark condition

widely used in laboratory settings and industrial applications to evaluate battery performance under ideal circumstances. 318.15 K (45°C) simulates high-temperature scenarios, such as summer conditions in warm climates or situations where EVs are exposed to prolonged sunlight, leading to increased heat accumulation within the battery pack. Understanding battery behavior across these temperature ranges is crucial for optimizing thermal management strategies and ensuring reliable performance under diverse environmental conditions.

2.4. Battery Specifications

The following table summarizes the key specifications of the 26650 Li-ion battery used in the study:

Table 2. Battery material properties[14]

Property	Jelly Roll (Active Zone)	Positive Tab (Aluminum)	Negative Tab (Steel)
Density (kg/m ³)	2226	2719	8030
Specific Heat (J/kg·K)	1197	871	502.48
Thermal Conductivity (W/m·K)	27	202.4	16.27
Electrical Conductivity (S/m)	1.19×10 ⁶ , 9.83×10 ⁵	3.54×10 ⁷	8.33×10 ⁶

Table 3. U and Y coefficients for the NTGK model [14]

U	a0: 4.0682, a1: -1.2669, a2: -0.9072, a3: 3.7550, a4: -2.3108, a5: -0.1701
Y	b0: 16.5066, b1: -27.0367, b2: 237.3297, b3: -632.603, b4: 725.0825, b5: -309.8760

The U and Y parameters used in the NTGK model were obtained from experimental discharge tests conducted under controlled environmental conditions. In order to investigate the behavior of the batteries depending on the temperature and discharge rate, numerical studies were performed at four different ambient temperatures (273 K, 283 K, 298 K, and 318 K) and four different discharge rates (0.5C, 1C, 1.5C, and 2C). The obtained numerical data were used to determine the parameters of the NTGK model. In this process, the Y(DOD, T) and U(DOD, T) functions, which explain the effects of deep discharge (DOD) and temperature (T) on the internal resistance and open circuit voltage of the battery, were optimized by the least squares method.

In order to test the accuracy of the model, a control study was performed for the battery data at temperatures of 288.15 K and 308.15 K and discharge rates of 0.75C and 1.25C. When the simulation results were compared with the experimental data, the root mean square error (RMSE) between the voltage and temperature values predicted by the model and the experimental results was found to be 0.678 V. These results showed that the NTGK model can successfully predict the thermal and electrical behavior of the battery over

a wide operating range.

Table 4. Use Virtual Battery Connection

mp 1
nS 2
tab_n_1 tab_p_1
tab_n_2 tab_p_2

Structural series and parallel connections without busbars involve connecting battery cells directly via their terminals or conductive surfaces, eliminating the need for additional busbar components. This approach reduces the overall weight and cost of the battery pack, resulting in a simpler and more compact design. However, varying current paths and connection interfaces can affect thermal dissipation and electrical resistance, and require careful optimization of connection geometry and materials. Tools such as Fluent simulate the thermal and electrical performance of such configurations, allowing the design to be evaluated and optimized for improved efficiency and reliability.

3. Results and Discussion

This chapter investigates the thermal and electrical performance of series-connected 26650 lithium-ion cells under different ambient temperatures and discharge rates. Using the NTGK model and advanced virtual simulation techniques, the analysis sheds light on critical performance metrics such as voltage stability, discharge time, heat dissipation, and maximum temperatures. The findings reveal the complex interactions between battery internal heat generation, environmental factors, and discharge rates, highlighting their combined impact on battery performance. The results are examined for different cell configurations, such as 1S1P and 2S1P, and the thermal and electrical behavior of these structures under realistic operating conditions are analyzed. Particular focus is placed on the identification of key performance thresholds such as critical temperatures and voltage drops, emphasizing the role of these parameters in the design of efficient thermal management systems (TMS). Furthermore, the decisive effects of ambient temperature variations on discharge efficiency, heat accumulation, and voltage stability over time are evaluated in detail.

► **Figure 2** verifies the accuracy of the NTGK model by comparing the simulated voltage outputs with reference values. The results obtained at 1C discharge rate show that the model is able to predict the voltage behavior with high accuracy under different operating conditions. The maximum deviation is within $\pm 0.5\%$, which supports the reliability and predictive power of the model. The strong agreement between simulation data and experimental results proves the robustness of the NTGK model and its ability to accurately represent re-

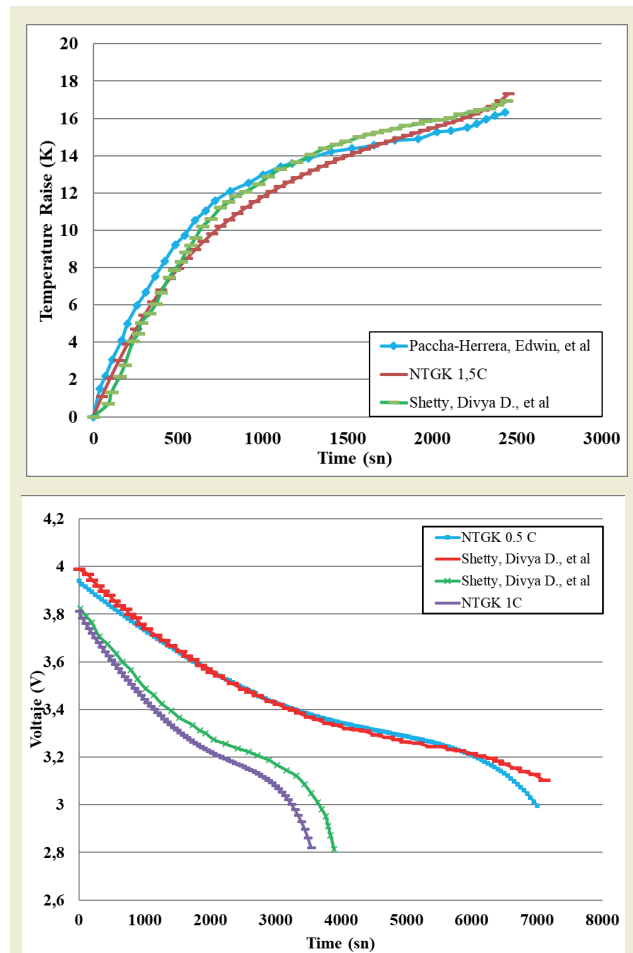


Figure 2. Validation with reference values

al-world thermal-electrical dynamics. Increasing voltage difference over time causes polarization increase and uneven charge distribution due to the increase in battery internal resistance and depletion of active lithium ions. This process directly affects the electrochemical balance of the battery, leading to voltage instability and performance losses.

To further evaluate the accuracy of the NTGK model, additional simulations were performed under different ambient temperatures (283.15 K and 318.15 K) and discharge rates (0.5C and 2C). These analyses were performed to verify how well the model can represent the thermal and electrical behavior of the batteries under different operating conditions. The additional tests provided a comprehensive comparison of the model's predictive capability in various scenarios and demonstrated the consistency of the NTGK model in voltage prediction. Furthermore, a cross-validation method was applied using an independent dataset, and discharge profiles that were not included in the original parameterizations were evaluated during this validation process. The findings demonstrate the complex interactions between internal heat generation, environmental factors, and discharge rates, emphasizing their combined impact on battery performance.

Although additional simulations at different temperatures and discharge rates were not performed within the scope of this study, the validation results presented in ►Figure 2 show that the NTGK model can accurately capture the correct operation of the system under the tested conditions. Future work will focus on improving the reliability of the model by covering a wider range of temperatures and discharge rates and testing the robustness of the system at higher battery temperatures.

3.1. 1S1P Battery Pack

This figure illustrates the discharge behavior of a 1S1P battery under various ambient temperatures. At a 2C discharge rate, the discharge time decreases significantly as the ambient temperature rises, dropping from approximately 3600 seconds at 273.15 K to around 2500 seconds at 318.15 K. Lower ambient temperatures provide greater voltage stability throughout the discharge process, while higher temperatures result in more rapid voltage drops. This behavior is attributed to increased internal resistance and thermal effects at elevated temperatures. These results underscore the necessity for

effective thermal management systems to minimize performance degradation and ensure voltage stability, especially in high-temperature environments.

At higher temperatures, the increased internal resistance restricts efficient charge transport, leading to enhanced voltage losses and reduced discharge efficiency. Additionally, the electrochemical reaction rate accelerates, intensifying undesired side reactions such as electrolyte decomposition and SEI layer breakdown. These processes further contribute to performance degradation, increasing resistive heat generation and hastening capacity fade. As a result, the sharp decrease in discharge time between 298.15 K and 318.15 K is primarily driven by these thermally induced changes, emphasizing the importance of optimized cooling strategies to mitigate excessive heat buildup and ensure prolonged battery lifespan.

►Figure 4 presents the maximum internal temperatures of the 1S1P battery setup across different ambient

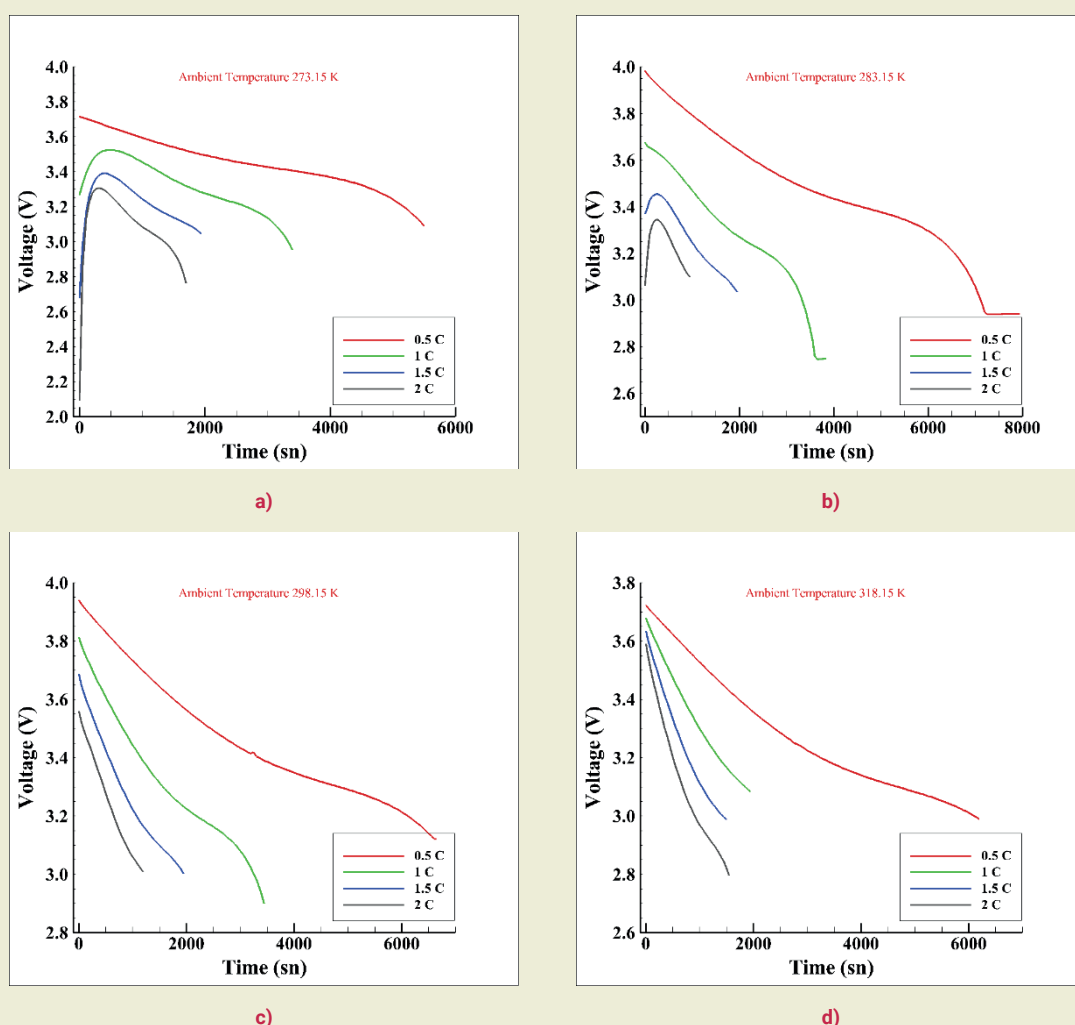


Figure 3. Discharge data of 1S1P battery for different ambient temperature (a-273.15 K b-283.15 K c-298.15K d- 318.15 K)

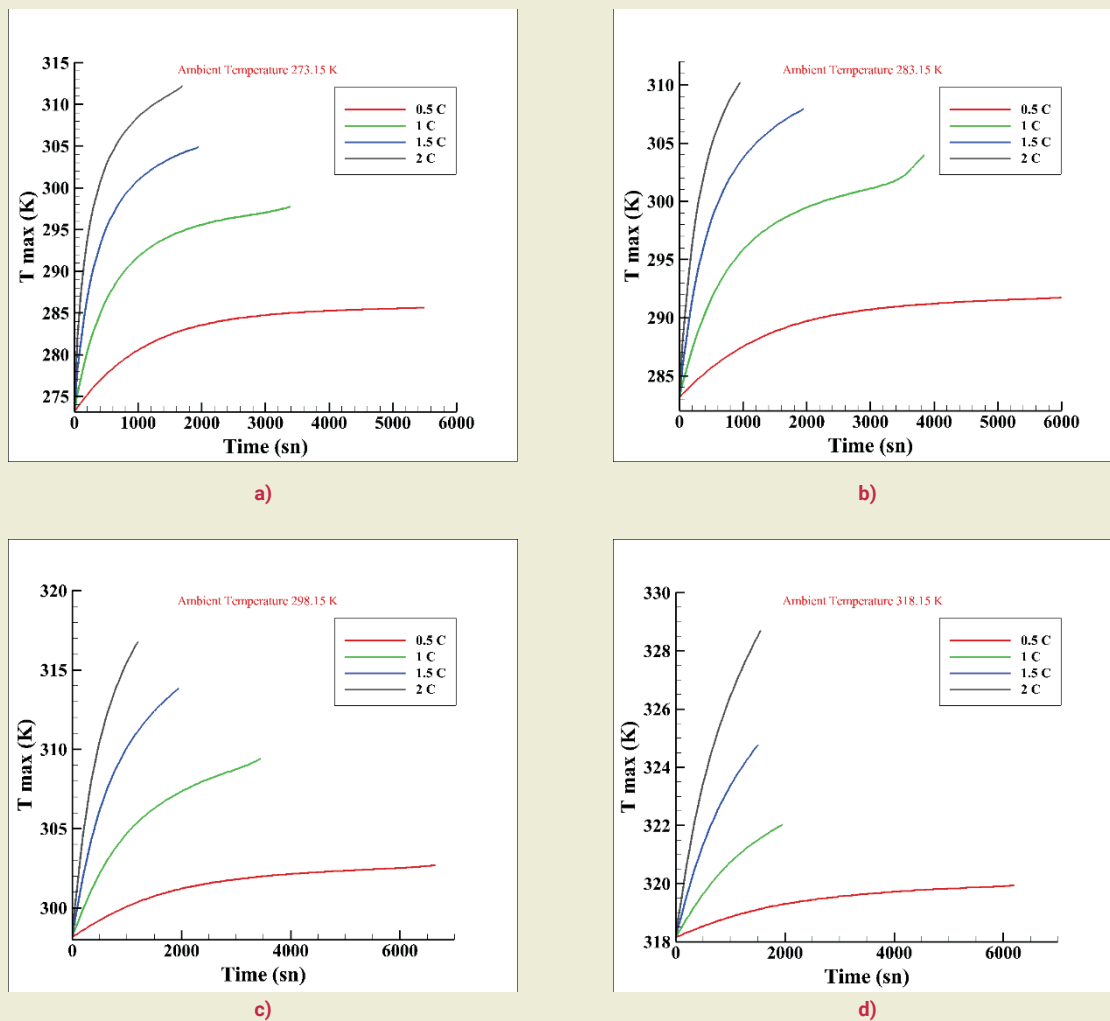


Figure 4. Maximum temperature information for 1S1P battery at different ambient temperature (a-273.15 K b-283.15 K c-298.15K d- 318.15 K)

temperatures and discharge rates. At a 0.5C discharge rate and 273.15 K, the peak temperature is recorded at 303.2 K. As the ambient temperature rises to 318.15 K with a 2C discharge rate, the maximum internal temperature increases significantly to 336.7 K. This stark rise in temperature highlights the compounding effect of higher discharge rates and elevated ambient conditions on thermal stress. The findings emphasize the importance of advanced cooling solutions to control the internal temperature and prevent thermal runaway in lithium-ion batteries operating under demanding conditions.

This figure provides a thermal map of the 1S1P battery configuration at an ambient temperature of 298.15 K and a 1.5C discharge rate. The distribution shows localized hotspots where heat accumulation is more pronounced, with temperatures peaking around the central regions of the battery.

These hotspots indicate uneven thermal dissipation, which can compromise battery performance and safety over time. The figure highlights the need for improved thermal uniformity and efficient heat dissipation mechanisms in battery designs.

The temperature distribution observed in ►**Figure 5** highlights localized heat accumulation in specific regions of the 1S1P battery configuration at an ambient temperature of 298.15 K and a discharge rate of 1.5C. The primary reason for these hotspots is the non-uniform distribution of cur-

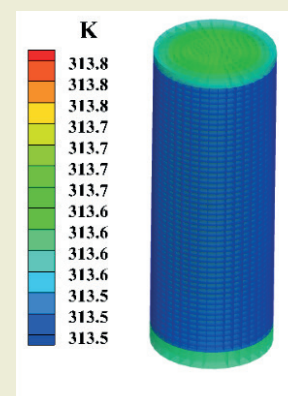


Figure 5. Maximum temperature distribution for 1S1P battery at 298.15 K ambient temperature and 1.5 C discharge information

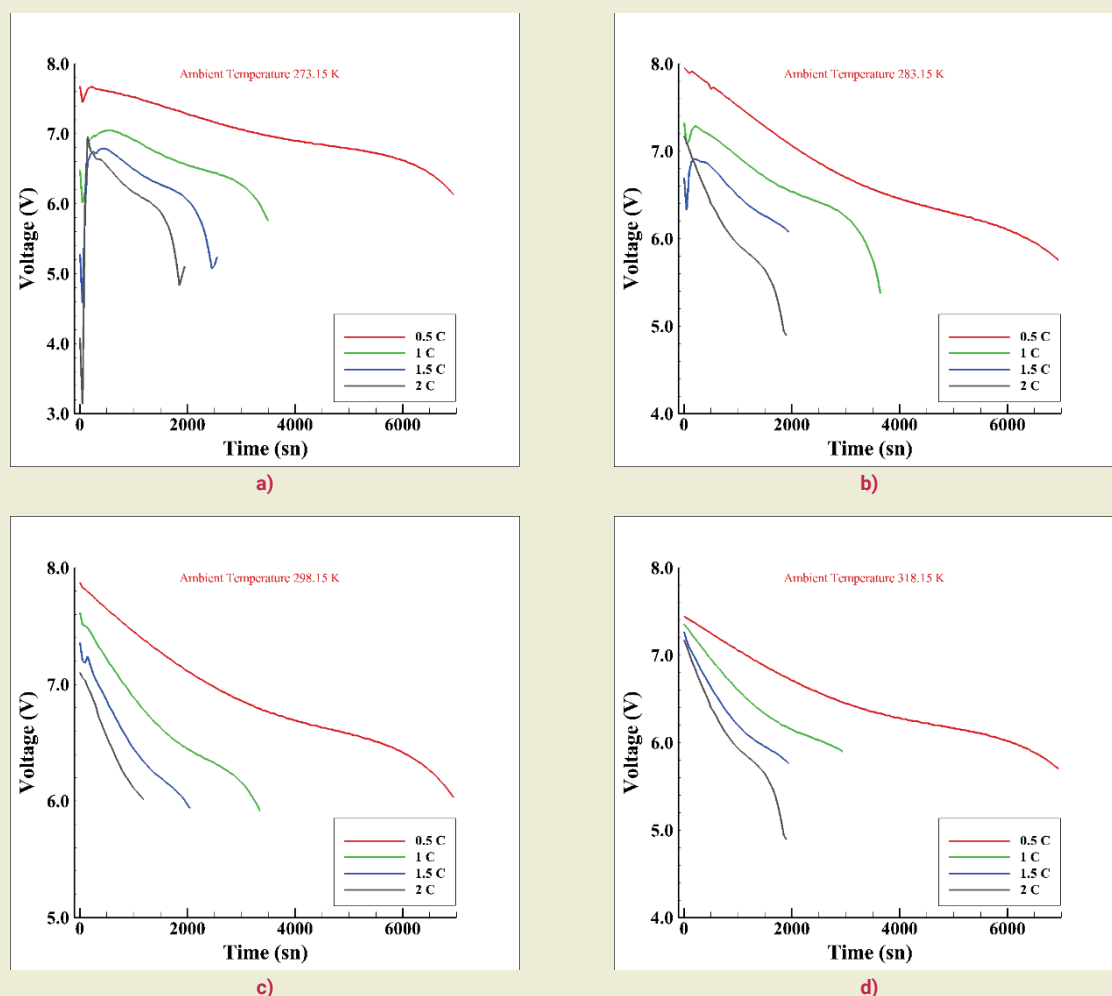


Figure 6. Discharge data of 2S1P battery packet for different ambient temperature (a-273.15 K b-283.15 K c-298.15K d- 318.15 K)

rent density within the battery. The positive and negative electrode tabs, where electrical connections are made, act as localized heat sources due to increased contact resistance and high current density in these areas. Furthermore, the anisotropic thermal conductivity of battery materials leads to uneven heat dissipation, with the electrode regions exhibiting higher thermal buildup than the separator and casing.

In a single-cell (1S1P) configuration, the overall heat dissipation is relatively more uniform compared to multi-cell arrangements. However, localized thermal buildup still occurs due to the non-homogeneous nature of electrical and thermal conductivity within the cell structure. The cylindrical battery geometry further exacerbates this issue, as heat tends to accumulate near the central core region, where thermal dissipation is more restricted. The results highlight the necessity for optimized cooling techniques, such as enhanced tab cooling, heat spreaders, or phase change materials, to mitigate hotspot formation and ensure uniform temperature distribution.

3.2. 2S1P Battery Pack

Figure 6 examines the discharge behavior of a 2S1P battery configuration under different ambient temperatures. Similar to the 1S1P setup, the discharge time decreases as ambient temperature increases, reducing from approximately 4200 seconds at 273.15 K to about 3100 seconds at 318.15 K for a 2C discharge rate. The voltage profile shows a more pronounced drop at the end of the discharge cycle under higher temperatures, highlighting the amplified impact of ambient conditions on series-connected batteries. These results point to the necessity of effective cooling systems for maintaining voltage stability and maximizing discharge duration in multi-cell configurations.

The significant reduction in discharge time between 298.15 K and 318.15 K can be attributed to the increased internal resistance, accelerated side reactions, and thermal effects on electrochemical processes. At moderate temperatures (273.15 K–298.15 K), ion transport and electrolyte viscosity gradually improve, leading to stable discharge performance. However, as the temperature rises beyond 318.15 K (45°C), the internal resistance increases due to accelerated electrolyte decomposition and degradation of the solid electrolyte interphase (SEI) layer. Additionally, excessive thermal

energy enhances parasitic reactions, leading to faster voltage drops and reduced available capacity. These factors collectively result in a steeper decline in discharge time at high temperatures, highlighting the need for effective cooling strategies to maintain battery stability in high-temperature environments.

This figure illustrates the maximum internal temperatures of the 2S1P battery configuration under varying ambient temperatures and discharge rates. At 0.5C and 273.15 K, the peak temperature is 304.7 K, while at 2C and 318.15 K, it rises sharply to 341.3 K. The higher temperatures in the 2S1P configuration compared to 1S1P demonstrate the compounded thermal challenges of series-connected batteries, where heat accumulation from multiple cells exacerbates thermal stress. These results underline the importance of implementing advanced cooling strategies, such as hybrid thermal management systems, to ensure operational safety and efficiency in high-capacity battery systems. A key factor in lithium-ion battery safety is the identification of critical temperature thresholds that may increase the risk of thermal runaway. While the highest ambient tempera-

ture examined in this study was 318.15 K, this research suggests that significant thermal instability begins at temperatures exceeding 333.15 K (60°C). At this point, electrolyte decomposition accelerates, leading to increased gas generation and internal pressure buildup within the battery cell. If the temperature continues to rise beyond 373.15 K (100°C), exothermic reactions between the electrolyte and electrode materials can trigger thermal runaway, a self-sustaining chain reaction that can result in catastrophic battery failure, including cell venting, fire, or explosion.

In the 2S1P configuration, where heat accumulates due to the series connection, localized hotspots may cause certain regions within the battery pack to exceed safe operating temperatures, leading to non-uniform degradation and increased thermal stress. To mitigate these risks, advanced cooling strategies such as liquid cooling, phase change materials (PCM), or thermally conductive coatings should be considered, particularly for applications exposed to high ambient temperatures. Furthermore, integrating early warning systems, such as thermal sensors and BMS algorithms, can help de-

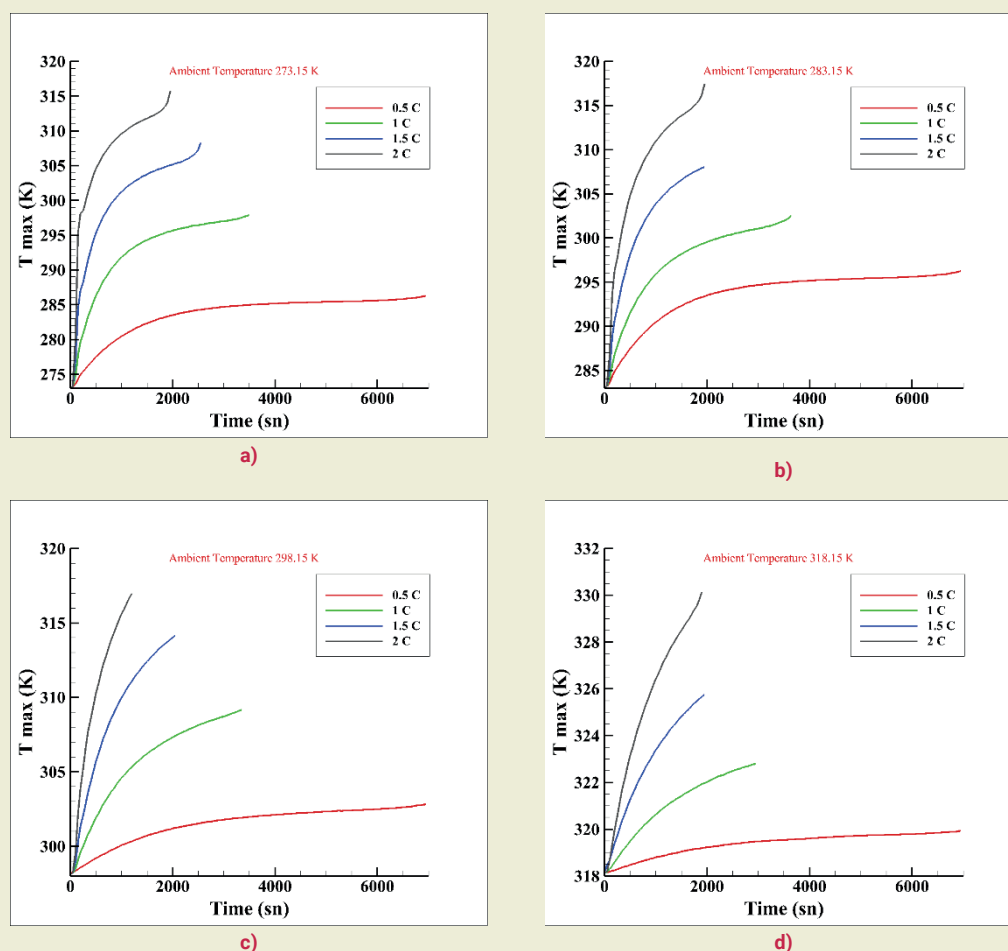


Figure 7. Maximum temperature information for 2S1P battery paket at different ambient temperature (a-273.15 K b-283.15 K c-298.15K d- 318.15 K)

tect temperature anomalies and prevent hazardous conditions before they escalate.

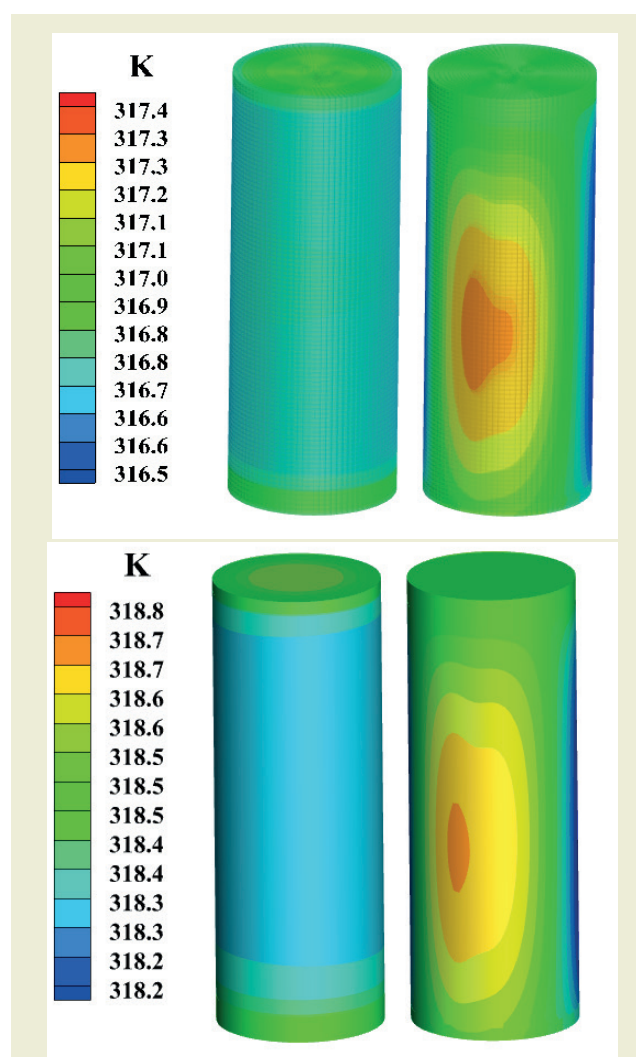


Figure 8. Maximum temperature distribution for 2S1P battery packet at 283.15 and 298.15 K ambient temperature and 2 C discharge information

For different external conditions, the heat distributions on the batteries are shown with thermal maps for 2S1P battery designs at ambient temperatures of 283.15 K and 298.15 K under a 2C discharge rate. The highest temperatures obtained as a result of numerical modeling are 317.4 K and 318.2 K, respectively. The hot spot formation in ►Figure 8 shows the thermal difficulties of a 2S1P battery pack operating at ambient temperatures of 283.15 K and 298.15 K with a 2C discharge rate. Compared to the 1S1P battery pack, the 2S1P pack is formed as a result of the combination of heat generated in each cell. By this logic, the difference will increase more at higher discharge rates (2C), where the need for more current demand will increase and the pack will be exposed to higher differential temperature.

Furthermore, the connection points between the cells serve as additional resistance sources, contributing to higher localized temperature spikes at the interconnection regions. The uneven heat dissipation observed in

the thermal map is due to the asymmetric positioning of electrode tabs and variations in thermal conductivity between different battery layers. The results highlight the importance of thermal management techniques such as improved interconnection materials, heat dissipation coatings, or active cooling methods (e.g., forced air or liquid cooling systems) to minimize thermal gradients and ensure uniform temperature distribution across the battery pack. Battery Management Systems (BMS) that integrate temperature-dependent control algorithms can significantly benefit from these findings. The results highlight the importance of adaptive thermal management techniques, such as variable coolant flow rates, active cooling mechanisms, and real-time temperature monitoring, to mitigate excessive heating in high-power applications. Furthermore, series-connected battery configurations can utilize these insights to optimize cell balancing algorithms, ensuring uniform charge distribution and preventing localized thermal stress. This study's findings can be directly applied to the development of next-generation BMS for electric vehicles, grid-scale energy storage, and aerospace propulsion systems, where precise thermal regulation is critical for operational efficiency and safety.

4. Conclusion

This study analyzed the thermal and electrical performance of 26650 Li-ion batteries in 1S1P and 2S1P configurations under different environmental temperatures and discharge rates using the NTGK model and virtual simulations. The batteries exhibited different thermal and electrical behaviors depending on the environmental conditions and load levels; in particular, temperature rise and high discharge rates caused the battery internal temperatures to reach critical levels and accelerated voltage drops. In the 1S1P configuration, at 0.5C at 273.15 K, the battery was stable for 5500 seconds to maintain its internal temperature at 285.6 K, whereas at 2C, this time was reduced to only 1700 seconds and the temperature increased up to 312.2 K. This indicates that at high discharge rates, electrochemical reactions inside the battery accelerate and energy losses are converted into heat. Similarly, at 283.15 K, the temperature remained at 294.2 K when the battery was operating at 0.5C for 7950 seconds, but at 2C it lasted only 1000 seconds to reach 310.2 K. This trend was also observed at 298.15 K, where the internal temperature of the battery operating at 0.5C for 6650 seconds was 302.7 K, while at 2C it increased to 316.8 K in 1200 seconds. The highest increase in the internal temperature of the battery occurred at an ambient temperature of 318.15 K, where the battery reached 319.9 K for 6200 seconds at 0.5C and 328.7 K for 1550 seconds at 2C.

When the 2S1P configuration was analyzed, it was observed that the series connection caused a compound heat accumulation inside the battery. At 273.15 K, the internal temperature reached 286.3 K in 6950 seconds at 0.5C, while at 2C the temperature increased to 315.7

K in 1950 seconds. The main difference observed here is that although the battery life is longer than that of 1S1P, the temperature increase becomes more pronounced. At 283.15 K, at 0.5C, the battery operated for 6950 seconds, raising its temperature to 317.6 K, while at 2C, it reached 317.4 K in 1950 seconds, showing that batteries reach a certain temperature threshold at high discharge rates. At 0.5C at 298.15 K, the battery only reached 302.8 K in 950 seconds, while at 2C it reached 316.9 K in 1200 seconds. The highest temperature was measured at 318.15 K, where at 0.5C the battery temperature was 319.9 K in 6950 seconds, while at 2C it rose to 330.1 K in only 1900 seconds. This shows that at high ambient temperatures, batteries heat up rapidly, and safe operating limits can be exceeded.

The voltage analysis clearly demonstrated the sensitivity of the batteries to temperature and discharge rates. In the 1S1P configuration, the voltage was found to be 3.087 V at 0.5C at 273.15 K and decreased to 2.760 V at 2C. This decrease is related to the increasing internal resistance and the temperature-dependent variation of ion motions inside the battery. At 283.15 K, the voltage at 0.5C remained at 2.941 V, while at 2C it was measured as 3.096 V. At 298.15 K, the voltage at 0.5C was 3.121 V, while at 2C it decreased to 3.007 V. The largest voltage loss was observed at 318.15 K, where the voltage at 0.5C was 2.988 V, while at 2C it decreased to 2.795 V.

In the 2S1P configuration, higher total voltage values were obtained, but the voltage drop was accelerated by the temperature effect. At 273.15 K, the battery reached 6.125 V at 0.5C and decreased to 5.098 V at 2C. At 283.15 K, the voltage was measured as 5.754 V at 0.5C and decreased to 5.089 V at 2C. At 298.15 K, the voltage was 6.026 V at 0.5C and 6.008 V at 2C. At 318.15 K, the voltage remained at 5.699 V at 0.5C, while it decreased to the lowest value of 4.894 V at 2C. This decrease indicates that at high temperatures, electrode materials lose performance, and side reactions inside the battery increase.

The findings show that at high temperatures and high discharge rates, the internal temperature of the batteries approaches critical thresholds, and heat accumulation increases, posing a risk to battery safety. In particular, the temperature reaching 330.1 K at a 2C discharge rate and 318.15 K ambient temperature highlights the need for an effective thermal management strategy. Therefore, the application of advanced thermal management solutions such as liquid cooling, phase change materials and hybrid cooling systems in battery packs can control the internal temperature of the battery to extend the life and maintain safe operating limits. Furthermore, the integration of temperature-oriented intelligent algorithms in BMS can play a critical role in preventing battery overheating by tracking instantaneous temperature changes. This study highlights the necessity of optimized cooling strategies to maintain thermal and electrical balance in battery packs and provides important guidance for future bat-

tery technologies.

Future research can expand on these findings by conducting experimental validation to further confirm the accuracy of the NTGK model under varying environmental conditions. Additionally, investigating the application of the Use Virtual Battery Connection method in larger-scale battery packs and multi-module configurations can provide deeper insights into its scalability and practical feasibility. Moreover, integrating machine learning-based thermal management algorithms into battery simulations could enable predictive control strategies that enhance overall system efficiency. Finally, exploring alternative cooling methods, such as PCM or immersion cooling, could further optimize temperature regulation in high-performance battery applications.

Nomenclature

Symbol	Definition	Unit
Q	Battery capacity	Ah
R _{int}	Internal resistance	Ω (Ohm)
T	Temperature	K
I	Discharge current	A
V	Terminal voltage	V
Y(DOD,T)	TGK model parameter function	-
U(DOD,T)	Open-circuit voltage function	V
SOC	State of charge	%
DOD	Depth of discharge	%
P	Power dissipation	W
C _p	Specific heat capacity	J/kg·K
k	Thermal conductivity	W/m·K

Research ethics

Not applicable.

Author contributions

The author solely conducted all stages of this research.

Competing interests

The author states no conflict of interest.

Research funding

None declared.

Data availability

Not applicable.

Orcid

Metin Uzun  <https://orcid.org/0000-0002-0744-3491>

References

- [1] Hussain, M., Khan, M. K., & Pathak, M. (2023). Thermal analysis of phase change material encapsulated li-ion battery pack using multi-scale multi-dimensional framework. *Journal of Energy Storage*, 65, 107290.
- [2] Khan, M. M., Alkhedher, M., Ramadan, M., & Ghazal, M. (2023). Hybrid PCM-based thermal management for lithium-ion batteries: Trends and challenges. *Journal of Energy Storage*, 73, 108775.
- [3] Khan, S. A., Xiangrong, L. I., Lau, K. T., Dong, K., He, S., Wabaidur, S. M., & Zhao, J. (2024). Metallic PCM-based battery thermal management system for fast charging/discharging applications. *International Communications in Heat and Mass Transfer*, 155, 107473.
- [4] Hemmerling, J., Fill, A., & Birke, K. P. (2024). Analysis of the age-, current- and temperature-dependent expansion of cylindrical NCM| Graphite Li-ion battery cells using strain gauges. *Journal of Energy Storage*, 99, 113177.
- [5] Dey, H., Pati, S., Randive, P. R., & Baranyi, L. (2024). Effect of finned networks on PCM based battery thermal management system for cylindrical Li-ion batteries. *Case Studies in Thermal Engineering*, 59, 104572.
- [6] Han, J., Seo, J., Kim, J., Koo, Y., Ryu, M., & Lee, B. J. (2024). Predicting temperature of a Li-ion battery under dynamic current using long short-term memory. *Case Studies in Thermal Engineering*, 63, 105246.
- [7] Murali, G., Sravya, G. S. N., Jaya, J., & Vamsi, V. N. (2021). A review on hybrid thermal management of battery packs and its cooling performance by enhanced PCM. *Renewable and Sustainable Energy Reviews*, 150, 111513.
- [8] Li, J., Jiaqiang, E., Ding, J., Cai, L., & Luo, B. (2024). Effect analysis on the low-temperature preheating performance of a novel micro-combustor air preheater for the cold start of the Li-ion battery packs. *Energy*, 312, 133606.
- [9] Han, J., Seo, J., Kim, J., Koo, Y., Ryu, M., & Lee, B. J. (2024). Predicting temperature of a Li-ion battery under dynamic current using long short-term memory. *Case Studies in Thermal Engineering*, 63, 105246.
- [10] Lin, X. W., Li, Y. B., Wu, W. T., Zhou, Z. F., & Chen, B. (2024). Advances on two-phase heat transfer for lithium-ion battery thermal management. *Renewable and Sustainable Energy Reviews*, 189, 114052.
- [11] Zhang, F., Wang, F., Zhu, Y., & He, Y. (2024). Structural optimization of thermal management system for bionic liquid cold battery based on fuzzy grey correlation analysis. *Applied Thermal Engineering*, 249, 123347.
- [12] Xu, G., Jiang, M., Li, J., Xuan, X., Li, J., Lu, T., & Pan, L. (2024). Machine learning-accelerated discovery and design of electrode materials and electrolytes for lithium ion batteries. *Energy Storage Materials*, 103710.
- [13] Li, Y., Li, B., Bei, S., Li, L., Zhang, L., & Hu, M. (2024). Thermal management of lithium-ion battery modules optimized based on the design of cold plate with convex pack structure. *Applied Thermal Engineering*, 257, 124186.
- [14] Shetty, D. D., Sulthan, M., Zuber, M., Badruddin, I. A., & Kini, C. R. (2022). Computational design and analysis of a novel battery thermal management system of a single 26650 Li-ion battery cell for electric vehicle application. *Journal of Advanced Research in Fluid Mechanics and Thermal Sciences*, 93(2), 61-75.
- [15] Paccha-Herrera, E., Calderón-Muñoz, W. R., Orchard, M., Jaramillo, F., & Medjaher, K. (2020). Thermal modeling approaches for a licoo2 lithium-ion battery—a comparative study with experimental validation. *Batteries*, 6(3), 40.
- [16] Fluent Ansys (2021), Ansys Fluent Theory Guide, ANSYS Inc., USA, vol. 15317, no. July, pp. 819-821
- [17] Torun, E., & Buyruk, E. (2024). Lityum İyon Pillerde Farklı Deşarj Hızlarında Oluşan Sıcaklık Profillerinin Deneysel ve Sayısal Olarak Karşılaştırılması. *Osmaniye Korkut Ata Üniversitesi Fen Bilimleri Enstitüsü Dergisi*, 7(2), 622-637.
- [18] Chavan, S., Venkateswarlu, B., Salman, M., Liu, J., Pawar, P., Joo, S. W., Choi, G. S. & Kim, S. C. (2024). Thermal management strategies for lithium-ion batteries in electric vehicles: Fundamentals, recent advances, thermal models, and cooling techniques. *International Journal of Heat and Mass Transfer*, 232, 125918.
- [19] Shelly, T. J., Weibel, J. A., Ziviani, D., & Groll, E. A. (2021). Comparative analysis of battery electric vehicle thermal management systems under long-range drive cycles. *Applied Thermal Engineering*, 198, 117506.

Failure Mode and effects analysis of selected weaving defects in viscose/linen fabrics using the fuzzy TOPSIS method

Çiğdem Sarpkaya^{1*} 

¹Safranbolu Şefik Yılmaz Dizdar Vocational School, Fashion Design, Karabuk University, 78600 Karabük, Türkiye

Abstract: Production-related weaving defects are a significant issue in the textile industry, directly impacting the material quality of products. These defects typically arise from mechanical, material, or operator-related problems during production processes, negatively affecting the durability, aesthetics, and functionality of the product. This study aims to identify the causes of weaving defects encountered in viscose/linen woven fabrics and determine the importance of these defects from the customer's perspective. Therefore, Failure Mode and Effects Analysis (FMEA) was conducted using the Fuzzy TOPSIS optimization technique to analyze selected weaving defects frequently encountered in viscose/linen woven fabric within a textile company. The analyzed woven fabric has a warp yarn count of Ne 16/1 Viscose/Linen and a weft yarn count of Ne 16/1 Viscose/Linen/Elastane. For the produced material, selected weaving defects were classified using linguistic variables by decision-making experts during the final fabric quality control process. This approach allowed the experts to prioritize weaving defects of greater importance to the customer by employing the Fuzzy TOPSIS optimization method. The study concluded that "Draft Defect" ranked first as the most critical defect, requiring immediate resolution.

Keywords: Viscose/Linen materials; Weaving Production Defects; Fuzzy TOPSIS; FMEA; Optimization.

1. Introduction

The rapid advancements in textile technology have accelerated the transformation of the industry from a labor-intensive structure to a capital-intensive one. Modern textile machines, with high production capacities and skilled personnel, are replacing traditional equipment. The widespread adoption of automation has increased both production efficiency and product quality. Quality control systems, along with efficient and hygienic distribution methods, not only enhance product quality but also facilitate the sale of more affordable raw materials and improve customer distribution processes. The quality of raw materials directly impacts the characteristics of the final product.

Faults encountered in woven fabrics, which are widely used in the textile sector, have been systematically classified. Based on this classification, faults are generally divided into four categories: yarn faults, faults in the weft direction, faults in the warp direction, and finishing faults [1]. Production faults occurring during material manufacturing are directly related to the proper-

ties and strength of the weft and warp yarns, as well as the efficiency of the weaving machine (e.g., number of stops and yarn breakage rates) [2]. Ensuring customer satisfaction requires identifying, eliminating, or minimizing faults during the production process. Failure Mode and Effects Analysis (FMEA) is recognized as an effective method in quality improvement processes [3]. Preventing faults before they occur is crucial for the efficient use of resources. As one of the fundamental tools of total quality management, FMEA is an effective method for identifying and prioritizing potential faults. It aims to eliminate errors and enhance quality levels by developing and implementing preventive measures for each type of fault [4].

In order to detect the errors encountered, analyze their risks and prioritize them, the Fuzzy TOPSIS method and Failure Mode and Effects Analysis (FMEA) can be used together as a new method in various fields. While the Fuzzy TOPSIS method allows errors to be evaluated through linguistic variables, preventive measures can be taken to reduce errors with severity, probability and detectability criteria [3,4]. TOPSIS (Technique for

*Corresponding author:

Email: csarpkaya@karabuk.edu.tr

Cite this article as:

Sarpkaya, Ç. (2025). Failure Mode and effects analysis of selected weaving defects in viscose/linen fabrics using the fuzzy TOPSIS method. *European Mechanical Science*, 9(1): 59-65. <https://doi.org/10.26701/ems.1602729>

History dates:

Received: 17.12.2024, Revision Request: 21.01.2024, Last Revision Received: 04.02.2025, Accepted: 09.03.2025



Order Preference by Similarity to Ideal Solution) method is a method used in multi-criteria decision-making processes developed by Hwang and Yoon (1981). This method aims to determine the alternative closest to the positive ideal solution and farthest from the negative ideal solution by considering the criteria weights. Due to the inadequacy of numerical expressions in measuring human judgments, the TOPSIS method has been extended with fuzzy numbers [5]. The fuzzy TOPSIS method is one of the multi-criteria decision-making techniques. This approach, first developed by Chen and Hwang (1992), utilized trapezoidal fuzzy numbers [6]. In later studies, methods using different types of fuzzy numbers such as triangular fuzzy numbers have also been developed. These developments have facilitated the modeling of uncertainty and subjective evaluations of the method [7]. When the areas of use of the fuzzy TOPSIS method are examined, it is seen that it is used in a wide range of sectors and application areas. It has been stated that it is widely used in main subjects such as supplier selection [8], performance evaluation processes [9], risk analysis and management [10] and personnel selection [11]. The fuzzy TOPSIS method allows the alternatives to be ranked in a way that they are closest to the positive ideal solution and farthest from the negative ideal solution. The positive ideal solution can be defined as the situation where the benefit criteria are optimized to the maximum level and the harm criteria are minimized. In contrast, the negative ideal solution refers to the situation where the harm criteria are maximized and the benefit criteria are minimized [8]. It basically solves the problem based on the TOPSIS method. Unlike this method, subjective evaluations about the criteria are evaluated using linguistic variables and the most appropriate alternative is determined. The fuzzy TOPSIS method provides more realistic solutions to problems by using verbal expressions instead of numerical values, allowing human judgments to be reflected more accurately in the model. In the method, decision criteria and their weights are evaluated with verbal expressions such as “low,” “very low,” “high.” The fuzzy TOPSIS method first begins with defining the alternatives to be evaluated, the decision criteria by which these alternatives will be measured, and the decision-making group. Decision makers evaluate the alternatives and criteria with the determined verbal expressions. Especially in cases where there is uncertainty and differences or variability arise in the evaluations of decision makers, the fuzzy TOPSIS method allows group decisions to be made more consistently and accurately. In addition, the fact that the decision criteria used in the evaluation of alternatives have different weights is one of the basic features of the method [12].

Tooranloo and Ayatollah (2016), Failure Mode and Effects Analysis (FMEA) is a powerful method in the field of risk management and is widely used to increase process reliability in the production and service sectors. In order to better manage uncertainties, the intuitive fuzzy approach-based FMEA model was used to evaluate error types for internet banking service quality [13].

Yılmaz and Şenol (2017) added the cost factor to the traditional risk analysis and determined the factor weights with Fuzzy AHP and prioritized the hazards and precautions with Fuzzy TOPSIS. In the application made in the metal industry, it was determined that the cost factor was more effective in the magnitude of the hazard, the most important risk sources were determined as the work environment, machine and employee-related hazards, and the priority precautions were determined as drill, training and machine renewal [14].

İşçi et al. (2024) applied Fuzzy AHP and Fuzzy TOPSIS methods in a company that produces parking equipment in order to evaluate risks in a more mathematical and objective way. In the sample including physical, chemical, ergonomic and psychological risks, the analysis results using probability and severity variables were compared and the hazards were ranked according to their importance [10]. Nadaban et al. (2016) conducted a compilation study describing the development of fuzzy TOPSIS methods [15]. Ünlükal and Yücel (2021) evaluated the risks in the production process of a company in the aviation sector with the FMEA and fuzzy TOPSIS approach; risk factors were weighted and prioritized by experts [16].

Günaydın (2022) used fuzzy multi-criteria decision-making techniques in a company operating in the fasteners sector to eliminate the disadvantages of the classical FMEA method. Potential errors were determined by the brainstorming method and divided into two groups as product and process-based, then weighted with the DEMATEL method and analyzed with fuzzy VIKOR, TOPSIS, MOORA and Gray Relational Analysis (GIA) methods. A model combining these methods was proposed to increase the consistency of the results obtained from different methods and to minimize errors [17].

In this study, it is aimed to determine the reasons for weaving defects encountered in viscose/linen blended woven fabrics as material and the importance level of these defects for the customer. Therefore, Failure Mode and Effects Analysis (FMEA) was performed using the fuzzy TOPSIS optimization technique for selected weaving defects frequently encountered in viscose/linen blended woven fabrics in a textile company.

2. Materials and Methods

2.1. Materials

The material used in this study is a woven fabric with a plain weave structure, featuring warp yarn of Ne 16/1 Viscose/Linen and weft yarn of Ne 16/1 Viscose/Linen/Elastane. After being woven on a weaving machine, the finished fabric undergoes quality control by an operator on fabric inspection tables. During this process, various defects, such as color and pattern irregularities, are identified on the fabric. Defects detected on the fabric

flowing over the inspection panel are recorded, and those that can be rectified are reprocessed for correction. Defects that cannot be remedied are categorized into different quality grades based on their severity. In this study, common weaving defects originating from the weaving department were selected for analysis. These include frequent-sparse density variations, weft skip, warp streak, lattice defect, and draft defect. ►**Table 1** presents the selected defects along with their definitions.

Table 1. Selected weaving defects, their definitions

Selected weaving defects	
Frequent-sparse density variations	Frequent refers to the placement of one or more weft yarns at intervals closer than the standard density. Sparse, on the other hand, refers to the placement of one or more weft yarns at intervals wider than the standard density.
Weft skip	It refers to the absence of one or more weft yarns in the weaving during the weaving process.
Warp streak	It is the difference in color tones that occurs because of the change in warp threads.
Lattice defect	It is a situation where the warp threads are not included in the weave and remain free, passing over the weft threads.
Draft defect	It is a fault that results from one or more of the warp threads being passed through the heddles incorrectly, causing the weave pattern to be disrupted throughout the fabric.

2.2. Methods

In this study, selected production-related defects of the produced material were detected, and these defects were analyzed using the Fuzzy TOPSIS method according to severity, probability and detectability criteria. The criteria were compared by three experts, their importance weights were determined and then the proximity coefficients for the alternatives were calculated using the Fuzzy TOPSIS method and a ranking was made. In the solution of the multi-criteria decision-making problem, the Fuzzy TOPSIS method developed by Chen (2000) was used and the triangular linguistic expressions in the evaluation of the alternatives and criteria are presented in ►**Table 2** [3, 4, 18].

The process steps of the fuzzy TOPSIS method and the equations used are shown in ►**Table 3** (3, 19, 20).

3. Results and Discussions

The Fuzzy TOPSIS method has been applied step by step according to ►**Table 3**, and the results are presented sequentially in the following tables (**Tables 4-10**). Initially, verbal expressions for the criteria and alternatives were converted into numerical values, and a fuzzy decision matrix was constructed. The normalized fuzzy decision matrix was then calculated, followed by the weighted normalized fuzzy decision matrix. Positive and negative ideal solutions were determined, and the closeness coefficients were obtained. Finally, the alter-

natives were ranked from highest to lowest based on their CC_i values, assigning rankings from 1 to 5.

Step 1: Assignment of judgment values to verbal expressions for the criteria and calculation of their importance weights.

In ►**Table 4**, the importance of weights for severity, probability and detectability criteria were calculated using formula 1. The importance weight for the severity criteria was found to be (0.03; 0.17; 0.37), the importance weight for the probability criteria was found to be (0.3; 0.5; 0.7) and the importance weight for the detectability criteria was found to be (0.57; 0.77; 0.93).

Step 2: Assignment of judgment values to verbal expressions for the alternatives and calculation of their importance weights.

In ►**Table 5**, the importance weights were calculated using Formula 2 by assigning judgment values to the verbal expressions of the alternatives (frequent-sparse density variations, weft skip, warp streak, lattice defect, draft defect). Accordingly, as an example, it can be observed that the importance weight of the judgment value for Decision Maker 1 (DM1) under the severity criterion for the frequent-sparse density variation alternative is (1; 3; 5).

Step 3: Creating the fuzzy decision matrix

In ►**Table 6**, the fuzzy decision matrix for the alternatives and criteria was created by applying Formula 3. As an example, in ►**Table 6**, the fuzzy decision matrix value for the weft skip alternative under the severity criterion was calculated as (0.33; 1.67; 3.67).

Step 4: Creation of normalized fuzzy decision matrix

The normalized fuzzy decision matrix for the alternatives and criteria was created using Formula 4 and is presented in ►**Table 7**. As an example, when examining ►**Table 7**, it can be observed that the normalized fuzzy decision matrix value calculated for the lattice defect alternative under the probability criterion is (0.13; 0.47; 0.87).

Step 5: Weighted normalized fuzzy decision matrix

The weighted normalized fuzzy decision matrix for the alternatives and criteria was created using Formula 5 and is presented in ►**Table 8**. As an example, when examining ►**Table 8**, it can be observed that the weighted normalized fuzzy decision matrix value calculated for the draft defect alternative under the severity criterion is (0.0143; 0.1190; 0.3667).

Step 6: Calculation of fuzzy positive ideal solutions (A^+) and negative ideal solutions (A^-)

In ►**Table 9**, the fuzzy positive ideal solutions (A^+) and negative ideal solutions (A^-) were calculated using For-

Table 2. Verbal expressions and their triangular fuzzy number equivalents in the evaluation of alternatives and criteria [18]

For alternatives		For criteria	
Verbal Expression	Triangular Fuzzy Number	Verbal Expression	Triangular Fuzzy Number
Very Bad (VB)	(0; 0; 1)	Very Weak (VW)	(0; 0; 0.1)
Bad (B)	(0; 1; 3)	Weak (W)	(0; 0.1; 0.3)
Medium Bad (MB)	(1; 3; 5)	Medium Weak (MW)	(0.1; 0.3; 0.5)
Medium (M)	(3; 5; 7)	Medium (M)	(0.3; 0.5; 0.7)
Medium Good (MG)	(5; 7; 9)	Medium Strong (MS)	(0.5; 0.7; 0.9)
Good (G)	(7; 9; 10)	Strong (S)	(0.7; 0.9; 1.0)
Very Good (VG)	(9; 10; 10)	Very Strong (VS)	(0.9; 1.0; 1.0)

Table 3. Process steps and equations of the fuzzy TOPSIS method

Steps	Formulas	Formula no
Step 1: Verbal expressions for the criteria are evaluated using triangular fuzzy numbers by decision-makers (DM1, DM2, DM3), and the importance weights of the criteria are calculated. \tilde{w}_{ij} : the weight of relation to jth criterion K: number of decision-makers	$\tilde{W}_{ij} = \frac{1}{K} [\tilde{w}_{ij}^1 + \tilde{w}_{ij}^2 + \dots + \tilde{w}_{ij}^K]$	(1)
Step 2: The alternatives are evaluated by the decision-makers using verbal expressions, which are represented by triangular fuzzy numbers. The importance weights of the alternatives are then calculated. \tilde{x}_{ij} : the weight of relation to ith alternative	$\tilde{X}_{ij} = \frac{1}{K} [\tilde{x}_{ij}^1 + \tilde{x}_{ij}^2 + \dots + \tilde{x}_{ij}^K]$	(2)
Step 3: For the Fuzzy TOPSIS method, the decision problem is formulated in the format of a fuzzy decision matrix. \tilde{D} : Fuzzy decision matrix \tilde{x}_{ij} : The criterion value of the alternative according to the decision criterion. \tilde{W}_{ij} : Fuzzy weight matrix	$\tilde{D} = \begin{bmatrix} \tilde{x}_{11} & \tilde{x}_{12} & \dots & \tilde{x}_{1n} \\ \tilde{x}_{21} & \tilde{x}_{22} & \dots & \tilde{x}_{2n} \\ \vdots & \vdots & \ddots & \vdots \\ \tilde{x}_{m1} & \tilde{x}_{m2} & \dots & \tilde{x}_{mn} \end{bmatrix} \quad \tilde{W} = [\tilde{w}_1, \tilde{w}_2, \dots, \tilde{w}_n]$	(3)
Step 4: The normalized fuzzy decision matrix is calculated considering the benefit criterion. \tilde{r}_{ij} : Normalized fuzzy decision matrix c_j^+ : In the case where the decision criterion is a benefit criterion, it is obtained by dividing each element in the column by the element with the largest third component within that column.	$\tilde{r}_{ij} = \left(\frac{a_{ij}}{c_j^+}, \frac{b_{ij}}{c_j^+}, \frac{c_{ij}}{c_j^+} \right), \quad j \in B$ $c_j^+ = \max c_{ij}, \quad \forall j \in B$	(4)
Step 5: The weighted normalized fuzzy decision matrix is calculated. \tilde{v}_{ij} : Weighted normalized fuzzy decision matrix	$\tilde{v}_{ij} = \tilde{r}_{ij} \cdot \tilde{W}_j$	(5)
Step 6: The fuzzy positive ideal solutions (A^+) and negative ideal solutions (A^-) are determined by identifying the maximum and minimum values for each criterion. A^+ : Fuzzy positive ideal solutions A^- : Fuzzy negative ideal solutions	$A^+ = \{v_1^+, v_2^+, \dots, v_n^+\}$ $A^- = \{v_1^-, v_2^-, \dots, v_n^-\}$ $\tilde{v}_j^+ = \max_i \{v_{ij3}\} \quad \text{ve} \quad \tilde{v}_j^- = \min_i \{v_{ij1}\}$	(6)
Step 7: In this step, the closeness of the alternatives to the ideal solutions (d_i^* and d_i^-) is calculated using the Vertex method. d_i^* and d_i^- : The closeness of the alternatives to the ideal solutions	$d_v(\tilde{a}, \tilde{b}) = \sqrt{\frac{1}{3} [(a_1 - b_1)^2 + (a_2 - b_2)^2 + (a_3 - b_3)^2]}$ $d_i^+ = \sum_{j=1}^n d(\tilde{v}_{ij}, \tilde{v}_j^+)$ $d_i^- = \sum_{j=1}^n d(\tilde{v}_{ij}, \tilde{v}_j^-)$	(7) (8) (9)
Step 8: The CCI values are calculated using the closeness coefficients of the alternatives to the ideal solution. The alternatives are then ranked from highest to lowest, and the most suitable alternative is determined. CCI: Closeness coefficient for alternatives	$CCI_i = \frac{d_i^-}{d_i^+ + d_i^-}$	(10)

Table 4. Evaluation of criteria using linguistic variables by decision-makers and calculation of importance weights

Criteria	DM1	DM2	DM3	Weights
Severity	(0; 0.1; 0.3)	(0.1; 0.3; 0.5)	(0; 0.1; 0.3)	(0.03; 0.17; 0.37)
Probability	0.3; 0.5; 0.7	(0.5; 0.7; 0.9)	(0.1; 0.3; 0.5)	(0.3; 0.5; 0.7)
Detectability	(0.7; 0.9; 1.0)	(0.5; 0.7; 0.9)	(0.5; 0.7; 0.9)	(0.57; 0.77; 0.93)

Table 5. Evaluation of alternatives using linguistic variables by decision-makers and calculation of importance weights.

Alternatives	Frequent-sparse density variations									Weft skip			Warp streak			Lattice defect			Draft defect		
Criteria	DM1	DM2	DM3	DM1	DM2	DM3	DM1	DM2	DM3	DM1	DM2	DM3	DM1	DM2	DM3	DM1	DM2	DM3	DM1	DM2	DM3
Severity	1	3	5	3	5	7	0	0	1	3	5	7	0	1	3	0	1	3	5	7	9
Probability	3	5	7	1	3	5	0	1	3	3	5	7	1	3	5	0	1	0	1	3	1
Detectability	3	5	7	5	7	9	0	1	3	3	5	7	3	5	7	9	1	3	5	0	1

Table 6. The fuzzy decision matrix

Alternatives	Criteria								
	Severity			Probability			Detectability		
Frequent-sparse density variations	1.33	2.67	4.33	1.33	3.00	5.00	2.67	4.00	6.33
Weft skip	0.33	1.67	3.67	1.33	2.67	4.33	3.67	5.67	7.67
Warp streak	0.33	1.33	3.00	0.33	1.67	3.67	0.67	2.33	4.33
Lattice defect	2.00	3.67	5.67	0.67	2.33	4.33	1.33	3.00	5.00
Draft defect	3.00	5.00	7.00	0.33	1.33	3.00	5.00	7.00	8.67

Table 7. Normalized fuzzy decision matrix

Alternatives	Criteria								
	Severity			Probability			Detectability		
Frequent-sparse density variations	0.19	0.38	0.62	0.27	0.60	1.00	0.31	0.46	0.73
Weft skip	0.05	0.24	0.52	0.27	0.53	0.87	0.42	0.65	0.88
Warp streak	0.05	0.19	0.43	0.07	0.33	0.73	0.08	0.27	0.50
Lattice defect	0.29	0.52	0.81	0.13	0.47	0.87	0.15	0.35	0.58
Draft defect	0.43	0.71	1.00	0.07	0.27	0.60	0.58	0.81	1.00

Table 8. Weighted normalized fuzzy decision matrix

Alternatives	Criteria								
	Severity			Probability			Detectability		
Frequent-sparse density variations	0.0063	0.0635	0.2270	0.0800	0.3000	0.7000	0.1744	0.3538	0.6821
Weft skip	0.0016	0.0397	0.1921	0.0800	0.2667	0.6067	0.2397	0.5013	0.8256
Warp streak	0.0016	0.0317	0.1571	0.0200	0.1667	0.5133	0.0436	0.2064	0.4667
Lattice defect	0.0095	0.0873	0.2968	0.0400	0.2333	0.6067	0.0872	0.2654	0.5385
Draft defect	0.0143	0.1190	0.3667	0.0200	0.1333	0.4200	0.3269	0.6192	0.9333

Table 9. Calculation of fuzzy positive and negative ideal solutions (A^+ , A^-)

Alternatives	Criteria								
	Severity			Probability			Detectability		
Frequent-sparse density variations	0.0063	0.0635	0.2270	0.0800	0.3000	0.7000	0.1744	0.3538	0.6821
Weft skip	0.0016	0.0397	0.1921	0.0800	0.2667	0.6067	0.2397	0.5013	0.8256
Warp streak	0.0016	0.0317	0.1571	0.0200	0.1667	0.5133	0.0436	0.2064	0.4667
Lattice defect	0.0095	0.0873	0.2968	0.0400	0.2333	0.6067	0.0872	0.2654	0.5385
Draft defect	0.0143	0.1190	0.3667	0.0200	0.1333	0.4200	0.3269	0.6192	0.9333
A^+		0.3667			0.7000			0.9333	
A^-		0.0016			0.0200			0.0436	

Table 10. Calculation of closeness coefficients (d_i and d_i^-) and ranking of alternatives (CC_i)

Alternatives	Severity		Probability		Detectability		Σd_i		CCi	Ranking
	d_i^*	d_i^-	d_i^*	d_i^-	d_i^*	d_i^-	Σd_i^*	Σd_i^-		
Frequent-sparse density variations	0.283581102	0.134979757	0.425989	0.425989	0.5701	0.4167	1.28	0.98	0.43	3
Weft skip	0.300381885	0.112149344	0.440034	0.369063	0.4759	0.5353	1.22	1.02	0.46	2
Warp streak	0.310566687	0.091482384	0.510454	0.297147	0.7160	0.2617	1.54	0.65	0.30	5
Lattice defect	0.264873348	0.177553241	0.469783	0.360596	0.6628	0.3141	1.40	0.85	0.38	4
Draft defect	0.248654733	0.221540906	0.536007	0.240031	0.3943	0.6333	1.18	1.09	0.48	1

mula 6. The highest and lowest values among the calculated results for the severity, probability, and detectability criteria are highlighted. Accordingly, the highest and lowest values are as follows: for the severity criterion, (0.3667 and 0.0016); for the probability criterion, (0.7000 and 0.0200); and for the detectability criterion, (0.9333 and 0.0436).

Step 7 and Step 8: Calculation of closeness coefficients (d_i and d_i^-) and ranking of alternatives (CC_i)

► **Table 10** was created by calculating the closeness coefficients (CC_i) and ranking values of the alternatives and criteria using Formulas 7–10. When the alternatives are ranked based on the obtained CC_i values, it is observed that the draft defect alternative has the highest CC_i value.

In the last step, according to ► **Table 10** of the severity, probability and detectability criteria with the fuzzy TOPSIS approach, it is seen that the drafting error ranked 1st has the highest CC_i value. Accordingly, it is seen that it is the most important production error that needs to be solved first by ranking 1st. By analyzing the error type and effects with the fuzzy TOPSIS method, it is possible to evaluate each error independently, and the priority order in solving the error types is determined by including the opinions of the decision makers in the process.

4. Conclusions

In this study, production-related selected defects were identified during the quality control process conducted on a woven fabric with a plain weave structure, featuring warp yarn of Ne 16/1 Viscose/Linen and weft yarn of Ne 16/1 Viscose/Linen/Elastane. The importance weights of the defects were determined based on the criteria of severity, probability, and detectability through evaluations by three experts. The defects were analyzed using the Fuzzy TOPSIS method within the framework of Failure Mode and Effects Analysis (FMEA). According to Step 8 outlined in ► **Table 3** of the Method section, the CC_i values were calculated and ranked from highest

to lowest. It was determined that “draft defect” with the highest closeness coefficient (CC_i) and were identified as the most critical production defect. Consequently, it was concluded that this defect should be prioritized for corrective actions. The other most important faults that need to be addressed are, in order of priority, “weft skip”, “frequent-sparse density variations”, “lattice defect”, and “warp streak”. Additionally, this study presents an innovative approach for the textile industry by prioritizing defects that cannot be corrected after weaving in viscose/linen blended fabrics, calculating their importance weights, and determining the top-ranking alternative using the fuzzy TOPSIS method.

Acknowledgments

We would like to thank the company employees who supported the realization of this study.

Research ethics

Not applicable.

Author contributions

The author solely conducted all stages of this research.

Competing interests

The author(s) state(s) no conflict of interest.

Research funding

None declared.


Data availability

Not applicable.

Peer-review

Externally peer-reviewed.

Orcid

Çiğdem Sarpkaya  <https://orcid.org/0000-0001-7710-1035>

References

- [1] Barış, B., & Özek, H. Z. (2019). Dokuma kumaş hatalarının sistematik sınıflandırılması üzerine bir çalışma. *Tekstil ve Mühendis*, 26(114), 156-167. <https://doi.org/10.7216/1300759920192611405>
- [2] Chen, C. T. (2000). Extensions of the TOPSIS for group decision-making under fuzzy environment. *Fuzzy Sets and Systems*, 114(1), 1-9.
- [3] Chen, S. J., & Hwang, C. L. (1992). Fuzzy multiple attribute decision making methods. Springer. https://doi.org/10.1007/978-3-642-46768-4_5
- [4] Değermenci, A., & Ayvaz, B. (2016). Bulanık ortamda TOPSIS yöntemi ile personel seçimi: Katılım bankacılığı sektöründe bir uygulama. *İstanbul Ticaret Üniversitesi Fen Bilimleri Dergisi*, 15(30), 77-93.
- [5] Günaydın, E. (2022). Bulanık çok kriterli karar verme teknikleri ile hata türü ve etkileri analizi: Bağlantı elemanları sektöründe bir uygulama [Yüksek lisans tezi]. İnönü Üniversitesi Sosyal Bilimler Enstitüsü.
- [6] Gülsün, B., & Erdoğan, K. N. (2021). Bankacılık sektöründe bulanık analitik hiyerarşi prosesi ve bulanık TOPSIS yöntemleri ile finansal performans değerlendirilmesi. *Süleyman Demirel Üniversitesi Fen Bilimleri Enstitüsü Dergisi*, 25(1), 1-15. <https://doi.org/10.19113/sdu-fenbed.639972>
- [7] Hwang, C. L., & Yoon, K. (1981). Methods for multiple attribute decision making. In *Multiple attribute decision making* (ss. 58-191). Springer. https://doi.org/10.1007/978-3-642-48318-9_3
- [8] İşçi, H., Baykara, Z., & Tülüce, B. (2024). Bulanık TOPSIS ve bulanık AHP yöntemleri ile risk analizi örneği. *ALKÜ Fen Bilimleri Dergisi*, 6(1), 28-45.
- [9] Karaatlı, M., Ömürbek, N., Işık, E., & Yılmaz, E. (2016). Performans

- değerlemesinde DEMATEL ve bulanık TOPSIS uygulaması. *Ege Academic Review*, 16(1), 49-64.
- [10] Karakış, E. (2019). Bulanık AHP ve bulanık TOPSIS ile bütünleşik karar destek modeli önerisi: Özel okullarda öğretmen seçimi. *Erciyes Üniversitesi İktisadi ve İdari Bilimler Fakültesi Dergisi*, 53, 112-137.
- [11] Nădăban, S., Dzitac, S., & Dzitac, I. (2016). Fuzzy TOPSIS: A general view. *Procedia Computer Science*, 91, 823-831. <https://doi.org/10.1016/j.procs.2016.07.088>
- [12] Özçakar, N., & Demir, H. (2011). Bulanık TOPSIS yöntemiyle tedarikçi seçimi. *İstanbul Üniversitesi İşletme Fakültesi İşletme İktisadi Enstitüsü Yönetim Dergisi*, 22(69), 25-44.
- [13] Öztürk, B. (2011). Çok kriterli karar verme tekniklerinden bulanık TOPSIS ve bulanık analitik hiyerarşi süreci [Doktora tezi]. Bursa Uludağ Üniversitesi Sosyal Bilimler Enstitüsü.
- [14] Pınar, Z., Gülağız, F. K., Altuncu, M. A., & Şahin, S. (2020). Denim kumaşlarda görüntü işleme ile hata tespiti. *Bitlis Eren Üniversitesi Fen Bilimleri Dergisi*, 9(4), 1609-1620.
- [15] Tekez, E. K. (2018). Failure modes and effects analysis using fuzzy TOPSIS in knitting process. *Tekstil ve Konfeksiyon*, 28(1), 21-26.
- [16] Tooranloo, H. S., & Ayatollah, A. S. (2016). A model for failure mode and effects analysis based on intuitionistic fuzzy approach. *Applied Soft Computing*, 49, 238-247. <https://doi.org/10.1016/j.asoc.2016.07.047>
- [17] Tayyar, N. (2012). Pet şişe tedarikçisi seçiminde bulanık AHP ve bulanık TOPSIS yaklaşımı. *Süleyman Demirel Üniversitesi İktisadi ve İdari Bilimler Fakültesi Dergisi*, 17(3), 351-371.
- [18] Ünlükal, C., & Yücel, M. (2021). Risk analysis application in aviation sector with intuitionistic fuzzy TOPSIS method. *Dumlupınar Üniversitesi Sosyal Bilimler Dergisi*, 70, 97-111. <https://doi.org/10.51290/dpusbe.956270>
- [19] Yılmaz, N., & Senol, M. (2017). A model and application of occupational health and safety risk assessment. *Journal of the Faculty of Engineering and Architecture of Gazi University*, 32(1). <https://doi.org/10.17341/gazimmfd.300597>
- [20] Yürek Eş, E. (2023). Kumaş boyama sürecinde bulanık TOPSIS ile hata türü ve etkileri analizi. *Uludağ Üniversitesi Mühendislik Fakültesi Dergisi*, 28(3), 915-926. <https://doi.org/10.17482/uumfd.1383914>

Mechanical and tribological investigation of jute fiber reinforcement in organic automotive brake pads and water repellency gain in natural fiber reinforced pads

Benek Hamamci^{1*} , Merve Sali² 

¹ Kafkas University, Faculty of Engineering & Architecture, 36200, Kars, Türkiye

² Alma Mater Studiorum University of Bologna Department of Industrial Engineering, I-40136 Bologna, Italy

Abstract: Many studies have shown that the materials used in the composition of brake pads are directly related to friction, wear mechanisms and tribological behavior. Heat-resistant jute fiber is an organic fiber that can be added to the composition of brake pads that can achieve good braking. In the study, pads were produced by adding different amounts of jute fiber using phenolic resin with powder metallurgy method and the results were compared with pads without jute fiber. It was observed that adding 5% jute fiber in addition to aramid fibers used in brake pad manufacturing had positive effects on friction coefficients, friction fluctuations and wear mechanism. At the same time, water absorption values of natural fibers were reduced by 30% and water repellency was provided to the pads. According to sample A, the density of JF3 decreased by 25.4% and shear strength by 39%. The hardness value is at the standard value used in the market.

Keywords: Pad, Friction, Wear, Jute Fiber, Silane, Water repellency

1. Introduction

The rapid advances of technological developments nowadays especially in the automotive field and consideration of an environmentalist approach in the existing situation have led to usage of some environment-friendly materials in the compositions of automobile brake pads [1–5]. This way, brake pads started to be produced by using organic fibers and without using asbestos. The friction materials that are used in brake systems should satisfy the following conditions: high and stable friction coefficient, low fading, better reclamation and low wear in highly variable working conditions [6–8].

Brake pad formulations are made up of five categories as: binders, fillers, fibers, abrasives and lubricants [6,9]. Generally, phenolic resins are used as binders, while barium sulphate, calcium carbonate and clays are used as filler. Fibers such as: organic (Kevlar, jute), inorganic (lapis), metallic (copper), ceramic (glass), natural (cellulose) and their various combinations are used in brake pads. Metal oxides and carbides are used as abrasives, whereas graphite and metal sulfides are common-

ly used as lubricants [10–12].

Nowadays, research is carried out on the effects of natural fibers as an alternative to synthetic fibers. Natural fibers have become a reason for choice instead of synthetic fibers as that have low density, low cost, high impact strength, easy production and no harm on the environment [9,13–15]. Likewise, with their biodegradability, they have found a prevalent usage area in several fields including the automotive, aviation and transportation industries. Components of natural fibers include cellulose, hemicelluloses, lignin, pectin, waxes and water-soluble substances [16,17].

Brake pads serve the function of reducing the velocity of or stopping a vehicle by converting the kinetic energy in the vehicle into heat energy [18–20]. For this reason, the properties and quantities of structures that will affect the friction performance of pads are a significant factor that will change the braking performance. Manufacturers have tried several different compositions to achieve properties such as increasing the high-temperature performance of the material under different

*Corresponding author:

Email: benekhamamci@kafkas.edu.tr

Cite this article as:

Harmanci, B., Sali, M. (2025). Mechanical and tribological investigation of jute fiber reinforcement in organic automotive brake pads and water repellency gain in natural fiber reinforced pads. *European Mechanical Science*, 9(1): 66-77. <https://doi.org/10.26701/ems.1620000>

History dates:

Received: 15.01.2025, Revision Request: 01.03.2025, Last Revision Received: 13.03.2025, Accepted: 13.03.2025



© Author(s) 2025. This work is distributed under <https://creativecommons.org/licenses/by/4.0/>



braking conditions, increasing material strength and wear strength and achieving a stable friction coefficient [21–23].

It is known that usage of asbestos fiber leads to cancer, lung tumors and other medical problems. As usage of asbestos fiber has been prohibited, it has been considered to utilize different friction materials such as Kevlar, fiberglass and graphite to be used in brake pads. Pads manufactured by using natural fibers have high water absorbency.

This feature is a problem for all composite material production. This problem limits the use of natural fibers. Studies should be carried out to give the fibers water-repellent properties [24]. Different types of chemicals can be used to add water repellency.

In this study, jute fiber, which is a natural fiber, was used in different ratios to produce brake pads and subjected to various tests. The goal was determined as that the produced pads would have a structure not harmful to human health, their tribological properties and metallographic structures were then examined and compared to those of commercial pads. At the same time, water repellency has been provided to the pads by using Silane Agent.

2. Materials and Method

2.1. Materials and type of manufacturing

Composite materials for brake pads included Novolak-type phenolic resin (Polikem), barite and mica (Başer Madencilik), aramid fiber (DuPont Türkiye), alumina (Esan-Eczacıbaşı), quartz and magnesite (Kale Maden), iron powder (Sintek Toz Metalurji), copper powder (Mayda Toz Metal), graphite (Karabacak Madencilik), power rubber (ÜN-SAL Danışmanlık Gıda Tekstil) and jute fiber (Aksa Tekstil). The pads were manufactured by using different ratios of jute fiber, binders, filling materials, reinforcement materials and friction regulators (abrasives and lubricants). The ratios of the components were kept constant by mass and jute fiber was added as filling material by reducing the ratio of barite. The powders used in the manufacture of brake pads generally have high densities. On the contrary, the density of natural fibers is very very low. In studies, natural fibers are generally used at a maximum of 10% [2,25]. The reason for this is that the natural fibers used more are too much for the mixture. In addition, it is difficult to ensure product integrity in brake pads produced with excess natural fibers. For this reason, in the study, brake pads were produced in 4 different compositions by adding 1%, 3%, 5% and 7% jute fiber to the brake pad composition by mass (Table 1). In addition, brake pads without jute fiber were also produced and comparisons were made with brake pads with jute fiber additives.

The pads that were reinforced with jute fiber were named as JF, while those they were produced only by aramid fiber without adding extra fiber reinforcement were called A.

Table 1. Ratios of Brake Pad Components by Weight

	A (%)	JF1 (%)	JF2 (%)	JF3 (%)	JF4 (%)	JF3-Silane (%)
Phenolic Resin	25	25	25	25	25	25
Powder Rubber	3	3	3	3	3	3
Barite	31	30	28	26	24	26
Mica	3	3	3	3	3	3
Aramid Fiber	5	5	5	5	5	5
Jute Fiber	-	1	3	5	7	5-S
Iron Powder	5	5	5	5	5	5
Copper Powder	7	7	7	7	7	7
Alumina	7	7	7	7	7	7
Quartz	3	3	3	3	3	3
Magnesite	1	1	1	1	1	1
Graphite	10	10	10	10	10	10

By using a KERN ACJ220-4M brand precision scale, the material components were weighted in the amounts specified in ►Table 1 and made ready for mixing. The materials were mixed for 40 minutes using an M-TOPE-MS3040D brand laboratory mixer until a homogeneous structure was formed. The mixer was operated at 2000 rpm. The mixture was made ready for compression. Three pieces of each sample were produced, so that the experiments would have 3 replications.

A Hidrokar brand hot press with a 20 ton capacity was used for compression. As seen in ►Figure 1, the compression process was carried out using 192x120 mm molds at 180°C temperature and 21.5 MPa pressure [26]. The lower plate of the hydraulic press was mobile and heated, while the upper plate was fixed. The mold included a back plate below it to be compressed with the pad material. A female plate was placed above it. The pad material was laid out by hand in batches inside the mold. After each process of laying out, 10 min of compression was applied. The purpose of the gradual form of the process was to aerate the mold for each batch, release the gasses inside and prevent the gaps that could be formed inside the pad material. The brake pad sample was produced with the help of the mold shown in ►Figure 1, with dimensions of 106.34x62.5 mm.

PROTHERM-PLF 120/10 brand industrial type furnace was used for sintering, which is the last stage of production. The samples were sintered at 180°C for 18 hours, allowed to cool at room temperature and the pad production process was completed [26].

2.2. Silane treatment of fibers

Karotect C1 type silane, used as a water-based and hy-

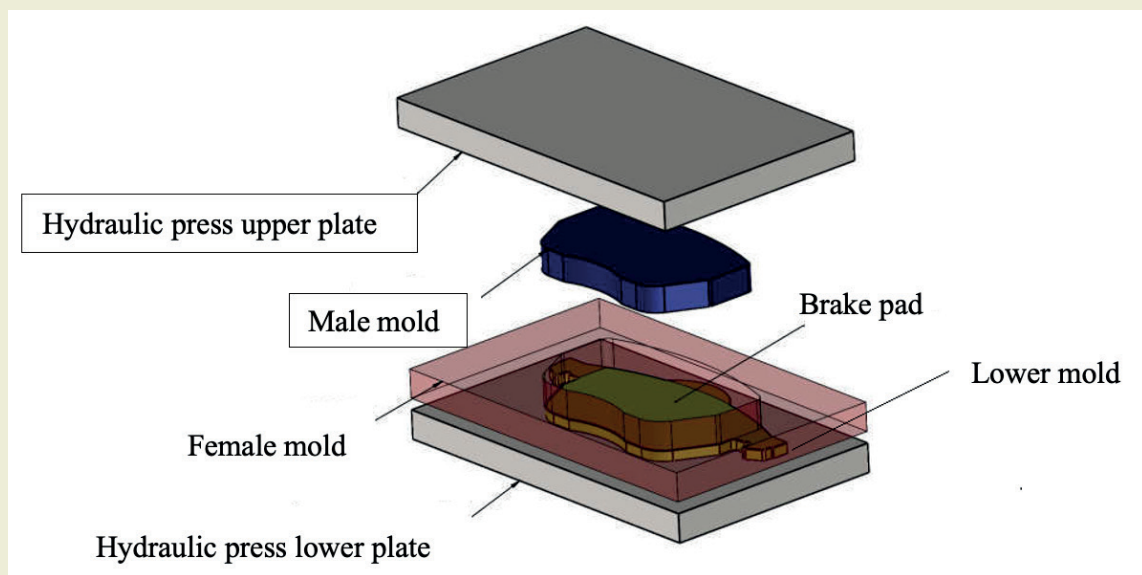


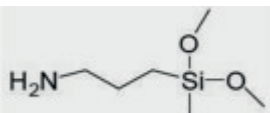
Figure 1. Schematic display of the brake pad production process



Figure 2. Jute fibers with and without silane-treated fibers.

drophobic agent, was obtained from Varkim Industrial Chemicals company. The technical properties of silane are shown in ►Table 2. When water-based silane is applied, it not only adds water repellency to the material, but is also environmentally friendly.

Table 2. Chemical structure and technical data sheet of Silane [24].

Appearance	
	Solid Content (%) 5 (±0,5)
	Density (25 °C) 0,80 g/cm ³
	Flash Point ~38 °C

After the jute fibers were immersed in silane, they were kept at room temperature for 24 hours, ensuring that the silane was absorbed by the fibers as much as possible. They were then removed and a stripping process was performed to remove excess silane from the fibers. The drying process of the jute fibers soaked in silane was carried out by keeping them in an oven at 80°C for

24 hours. With this process, the fibers gained water repellency instead of water absorption. A new brake pad powder mixture was prepared using silane-coated jute fibers and changes in water absorption values, which is one of the biggest problems of brake pads produced with natural fibers, were observed. JF3-Silane has the same mixture percentages as JF3, the only difference being that the fibers in the mixture are coated with silane.

2.3. Tribological properties

A block-on-disk device was used for wear test (►Figure 3). In the experimental setup, the sample with dimensions of 10x10x30 mm³ was placed onto a housing on the arm in a way that it would be over the disk rotating at a certain speed. The pressure between the disk and the sample was provided by the load connected to the arm. When the brake disk rotated, the sample was pressed onto the disk with the help of the load connected to the arm and wear was achieved with the movement of the disk. The block-on-disk device had an abrasive disk made out of 4140 steel with the diameter of 210 mm and hardness value of 54-56 HRC. To rotate this disk,

an electric motor with the properties of 1000 rpm and 2.2 kW was used. An inverter was used to set the rotation speed of the electric motor.

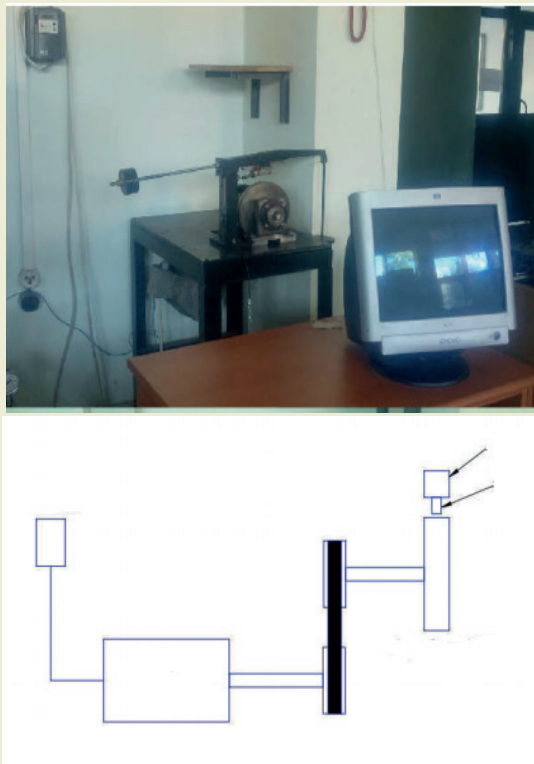


Figure 3. Block on Disk

The experiment was applied in a way that 50 minutes of friction test would be applied on each sample satisfying the TS 555 standards under a speed of 3.14m/s and at a sliding distance of 9420 m. The pad sample was placed into the housing on the load arm with a connected weight. Afterwards, when the arm was released, contact was achieved between the pad sample and the disk. The weight placed onto the load arm was set to provide a pressure of 3MPa. This way, friction was achieved between the pad and the disk as soon as the disk started rotating. To obtain wear rate values, the experiments were carried out with 3 repetitions and the final friction coefficients were reached by taking the arithmetic averages of the results.

Additionally, the wear rate amounts in the samples were determined. For these amounts, the masses of the samples were measured by a precision scale before and after the experiments and the specific wear rate amounts were determined with Equation 1 below.

$$Ws = \frac{\Delta m}{L \cdot \rho \cdot Fn} \quad (1)$$

In the formula, Ws (mm³/Nm) is the specific wear rate amount, Δm (gr) is the sample weight loss, L (m) is the total distance covered, ρ (gr/mm³) is the density of the sample and Fn (N) is the load of the sample (7). The force applied on the pad is 300N.

2.4. Mechanical, Physical and Chemical properties

Hardness tests were conducted at room temperature. Measurements were made from 5 different points on each sample. By taking the arithmetic average of the measured values, the hardness value for each sample was determined. The densities of the samples were determined by the Archimedes principle.

Water absorption experiments were conducted by using the ASTM D570-98 standards. The samples were kept in distilled water for 24h at 24°C. 3 pieces of each sample were freed of humidity by drying in an oven at 80°C for 24h. The dried samples were weighed by using a precision scale and then dipped in water. After 24h, the samples were taken out of the water, wiped and their dry weights were measured. The percentage water absorption ratios were calculated with equation 2 where m_{dry} is the weight dried in oven and m_{wet} is the weight kept in distilled water for 24h.

$$M(\%) = (m_{wet} - m_{dry}) / m_{dry} \times 100 \quad (2)$$

The shear tests of the samples were conducted with an MTS Systems Corporation-FXSA105A brand wedge device. An apparatus specifically prepared for the shear strength test was utilized (►Figure 4).

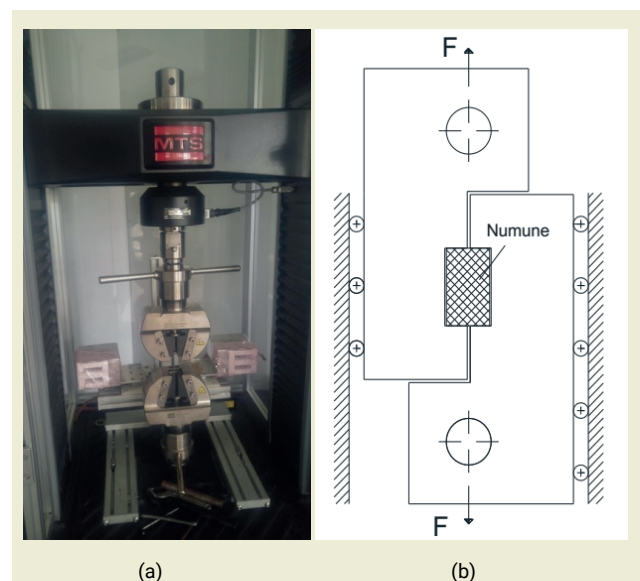


Figure 4. (a) Tensile Test Device, (b) Special Shear Test Apparatus

The samples were cut to 25x25x10 mm dimensions using a Yilmaz Brand Metal Cutting Machine (►Figure 5). During shearing, increased load was applied on the samples in parallel to the stress direction at a rate of 5 mm/min. The load was increased until the material broke. Using the measured shear forces of the samples, shear strength was calculated with the formula $\tau = F/A$.

3. Results and Discussion

This section presents the data obtained from the wear

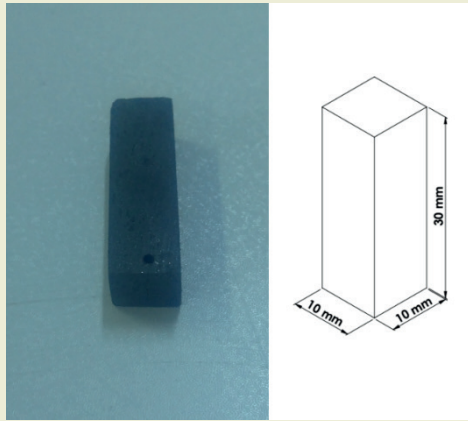


Figure 5. Pad test dimensions

test and the specific wear rates calculated with these data. In addition to these, hardness, shear test results and water absorption are also interpreted in this section.

3.1. Tribological Test Result

In the wear tests, the block-disc device broke the record. The graphical representation of the obtained test data is presented in ►**Figure 6**. Considering the friction-time graphs, it is reported that all the pads except the non-fiber reinforced pad (A) have a constant amount of sta-

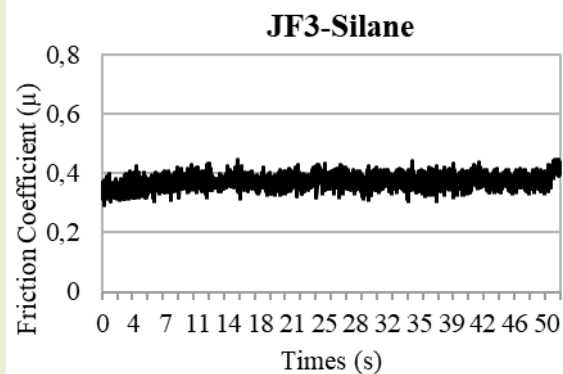
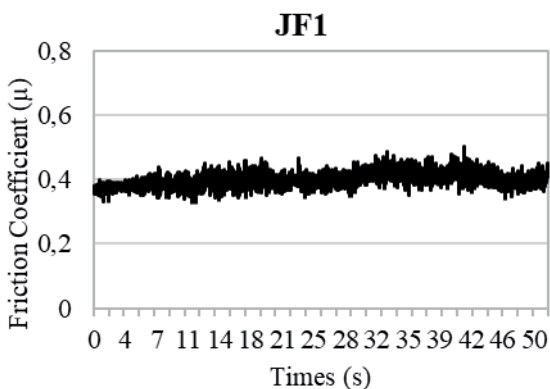
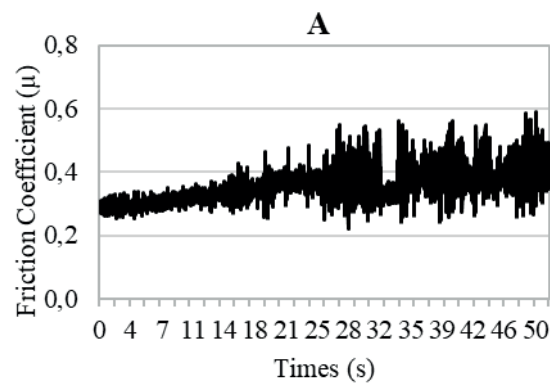
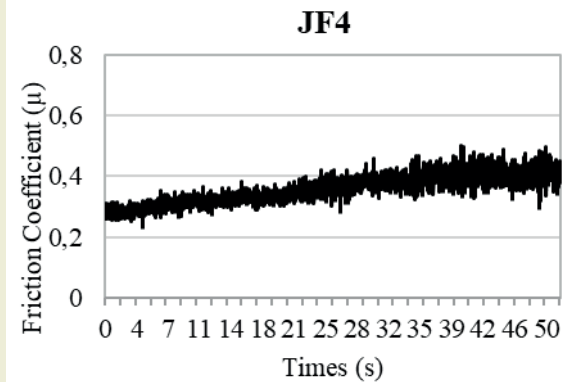
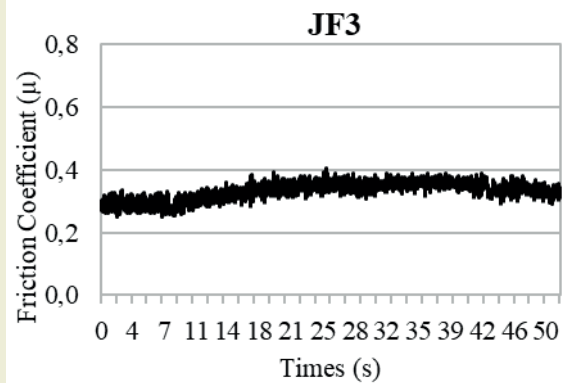
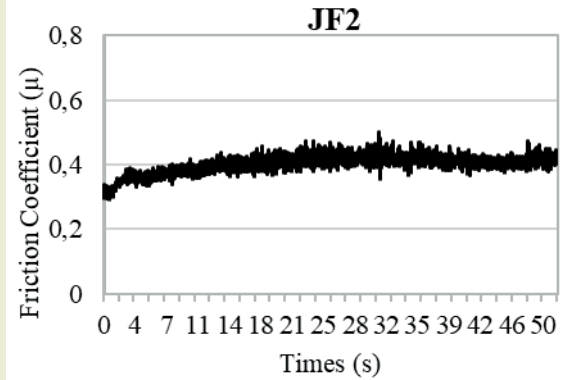


Figure 6. Friction coefficient plots of the A and JF1, JF2, JF3, JF4, JF4-Silane brake pads

bility. All other samples have changes in their stability. This is due to the increase in the brake pad components, which are stable at high speeds [27]. The lowest average change values were obtained as 0.37 in the JF3 sample and 0.386 in the JF3-Silane treated sample. It was concluded that the pads produced using natural fibers increased their friction coefficients similar to the study by Zhen-Yu et al [28] and Rajan et al [29].

The wear images of the pads are shown in ►Figure 7. The specific wear values of each brake pad were calculated by using the shear test data and the specific wear ratios and average friction coefficient values are shown together in ►Figure 8.

The average wear ratio values were in the range of $13.48\text{--}20.1 \times 10^{-6} \text{mm}^3/\text{Nm}$. The JF1 sample had the highest specific wear resistance. Increased ratios of jute fiber reduced the wear resistance and the JF3 sample had the minimum value.

The average friction coefficients were in the range of 0.368–0.487. The JF1 sample had the highest friction coefficient, as in the case of specific wear resistance, increased jute fiber ratios positively affected specific wear resistance and the lowest value was found in the JF3 sample. The reason for the increase in the friction coef-

ficient up to JF3 was thought to be that the insufficient jute fibers could not resist the temperature and friction that occurred with contact with the disk which had high hardness. It is considered that, after the jute ratio of 5%, the jute reduced the friction coefficient due to its heat-resistant property and this way, it could resist friction. It is seen that the friction coefficients of JF3-silane pad and JF3 pad are close to each other. It is seen that the friction coefficient values of JF3-silane pad and JF3 pad are close to each other. When silane was applied to the fibers of the pad sample with JF3 composition, it was observed that there was not much difference in the specific wear ratios and average friction coefficient values.

3.2. Physical, Chemical and Mechanical Test Result

►Figure 9 shows the density and water absorption results of the samples graphically. The average density of the samples is between 1.818 and 1.283 g/ml. The density decreased as the jute fiber ratio increased. The hardness values in the brake pad samples reinforced with jute fiber decreased by 13–17% compared to sample A. Silane increased the density of the fibers and thus increased the pad density. The hardness values were measured on the Rockwell R scale and it was seen that the material hardness was not directly proportional to the fiber ratio, but different rates of fiber reinforcement af-



Figure 7. Pad Wear images (Respectively A, JF1, JF2, JF3, JF4, JF3-Silane)

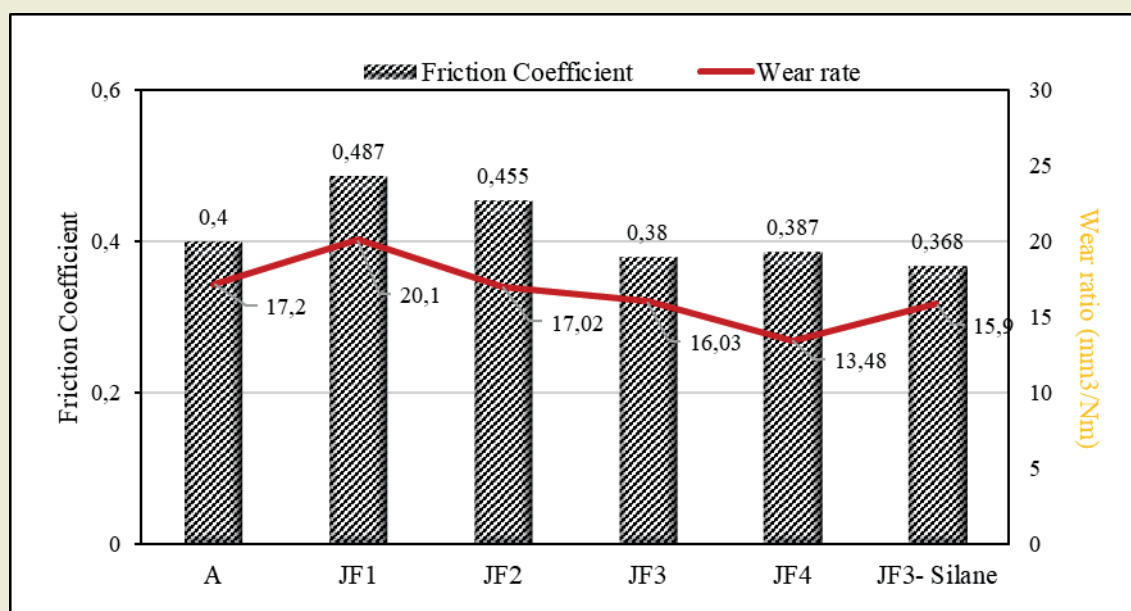


Figure 8. Average friction coefficient values and specific wear ratio for jute fiber reinforced brake pads

affected the hardness values at different rates (► **Figure 9**). The desired hardness value is 30-75 HRR. Lower pads cause rapid wear and higher hardness causes the disc to be damaged in a short time. All pads except A and JF4 pads comply with the standards. JF4 pad is 80.9HRR. It can be said that the reason for the high hardness of JF4 pad, which is expected to have lower hardness, is due to the fibers. The fiber ratio is high and there may not have been a homogeneous and complete mixture and the areas where the measurements were made may have misled us.

Considering the commercial brake pad values taken as reference, the shear stress of the pads should be higher than 2.3 MPa. Based on these values, considering the results listed in ► **Figure 6**, all pads were produced with

appropriate shear strength values higher than this reference value (► **Figure 10**). In addition, the shear stress values of samples A and JF1 are high, while JF2 is the lowest. The silane treatment of sample JF3 caused a 30% increase in shear strength.

3.3. Water absorption

Natural fibers can be preferred in pad manufacturing as they increase mechanical properties and are environmentally friendly. In recent years, in the production of composite materials used in different fields, the use of natural materials has been emphasized. This issue is very important in terms of the environment and the benefit of future generations. Especially composites containing natural fibers have attracted great interest

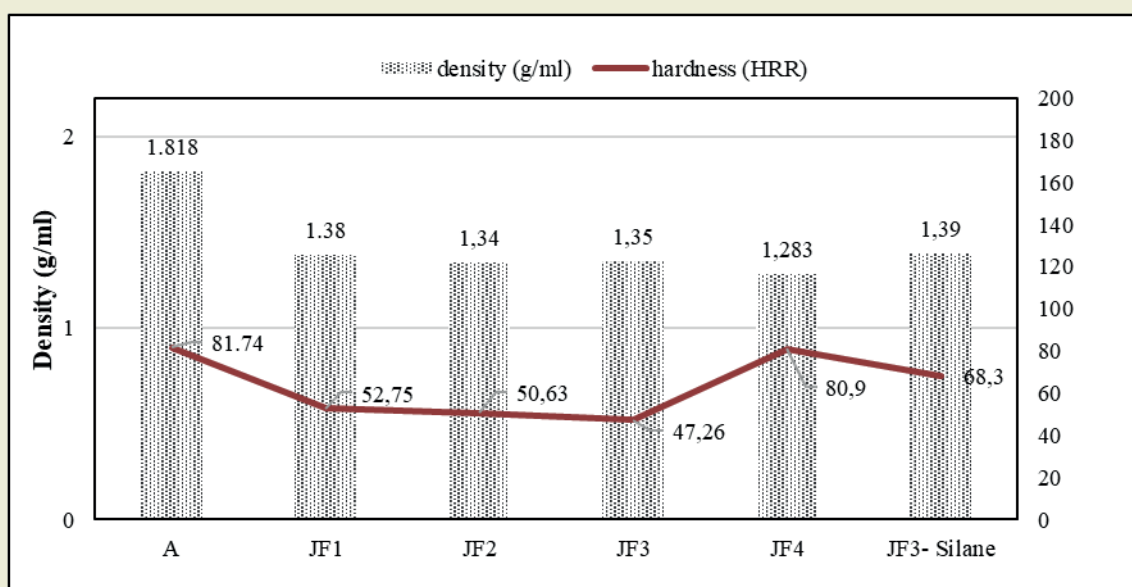


Figure 9. Density and hardness chart

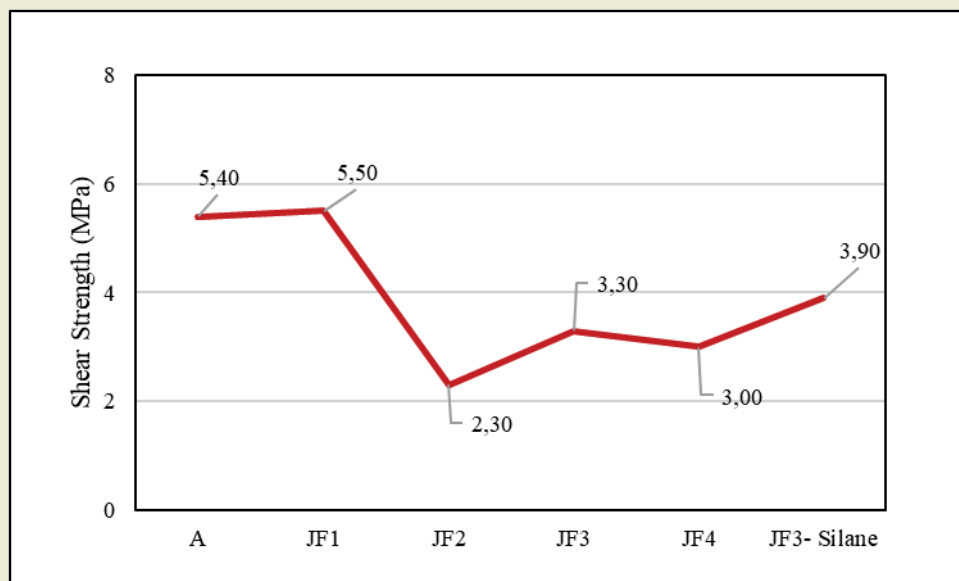


Figure 10. Maximum Shear Force Values of All Pad Samples

in the world. These materials are completely biodegradable and do not cause emissions of carbon-based organic compounds such as petrochemicals. However, the hydrophilic nature of the fibers can negatively affect both their mechanical and physical properties [24,30,31].

Hydrophilic fibers used in axe production can be made hydrophobic, i.e. water repellent, to provide water repellency. For this reason, Silane was applied to 5% jute fibers in the JF3 mixture, which has the best performance in terms of all mechanical and tribological properties. JF3-Silane brake pad samples were produced.

► **Figure 11** shows the graph of water absorption rates

of brake pads kept in water for 1, 2 and 24 hours. As the jute fiber percentage increased, the water absorption rate of the brake pads also increased. While the water absorption percentages of the brake pads were very close to each other in the first 1st hour, they increased rapidly towards the 2nd hour. Brake pads without jute fiber have low water absorbency. It is seen that the JF3-silane sample applied with silane prevents water absorption. It is very close to the values of the brake pad without jute fiber. Silane can provide water repellency to brake pads.

It is seen that the water absorption rate of the pads manufactured with jute fiber increases as the fiber ra-

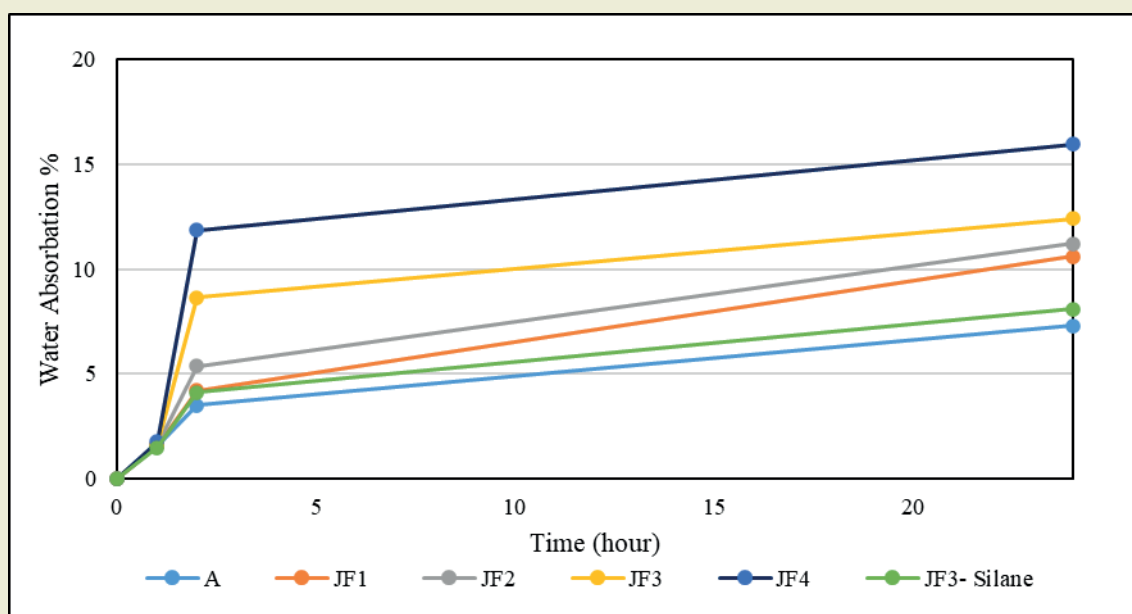


Figure 11. The graph of water absorption ratios in water for the all pads.

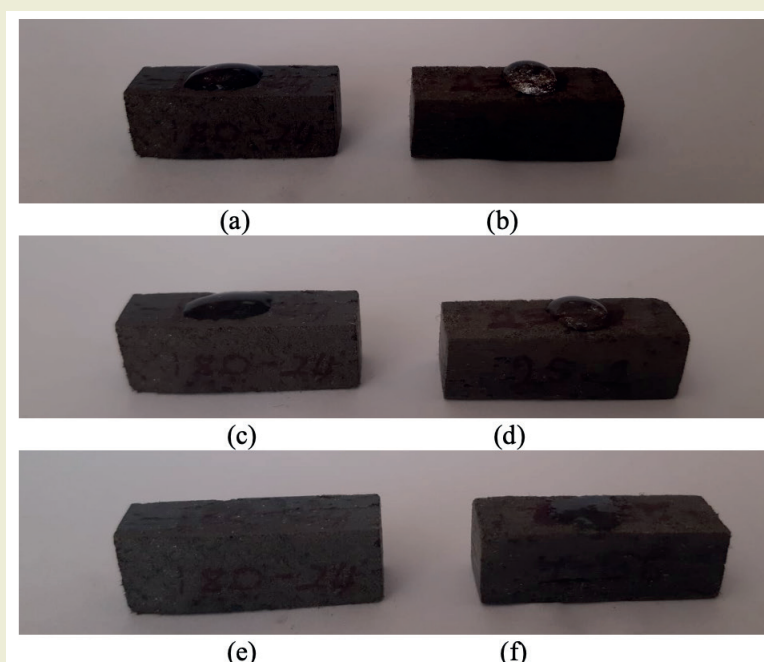


Figure 12. The contact appearance of JF3 and JF3-silane sample with water

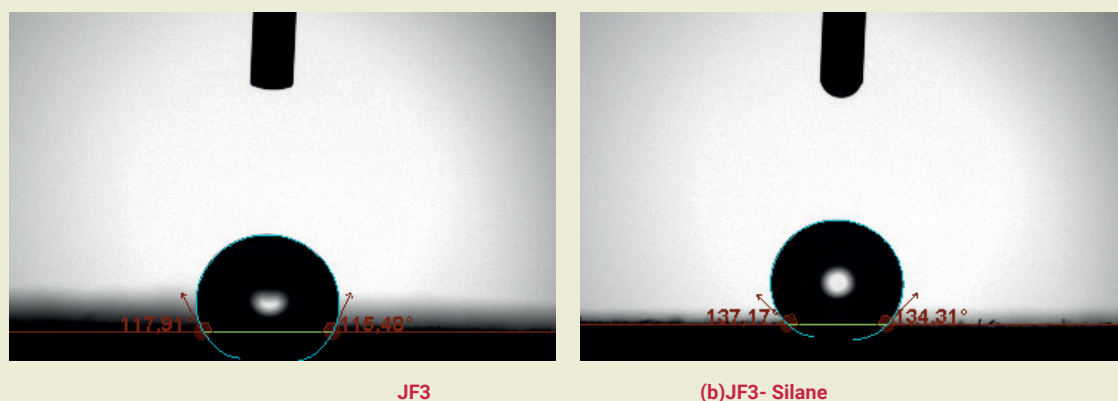


Figure 13. The contact angles of the samples with water (JF3, JF3-Silane, respectively).

tio increases (►Figure 12). At the same time, it is understood that the water absorption value of the sample with silane applied to the fibers is close to the values of the pad samples without fiber. The water repellency of the JF3- Silane sample increased by 10.32% compared to the JF3 sample.

Water drop moment (a) JF3 (b) JF3-Silane 20 seconds after adding water to the sample (c) JF3 (d) JF3-Silane 1 hour after adding water to the sample (e) JF3 (f) JF3-Silane

Figure 13 shows the contact angles of JF3 and JF3-Silane samples with water. It is seen from the study that the water repellency of the silane applied sample increased. As a result, it has been understood once again that agricultural fibers can be used in the production of composite pads. The fibers have been transformed into samples in a more hydrophobic form with the Silane agent and with this application, the water repellency of the samples can be increased and natural fibers can be used in the linings.

3.4. Surface Morphology

After the wear test of the pad samples, a Zeiss-brand SEM device was used to obtain and interpret their graphics for examining their surfaces. Looking at the SEM image of the A sample shown in ►Figure 14, the formation that occurred in the zone number 1 in the form of a scratch was considered to have occurred as a result of abrasive wear. In the zone number 2, this may have happened by that the pieces that were separated due to friction gathered on the surface again and led to adhesive wear. There was flocculation in the zone number 3. It is believed that the reason for this was barite and flocculation created border zones during wear. In the zone number 4, metal particles that actively participated in friction could be observed. There were white formations in the zone number 5 increases. Looking at the SEM image of the JF3 sample shown in ►Figure 6, the white particles seen in the zone number 1 were metal particles that took part in wear. It is known that

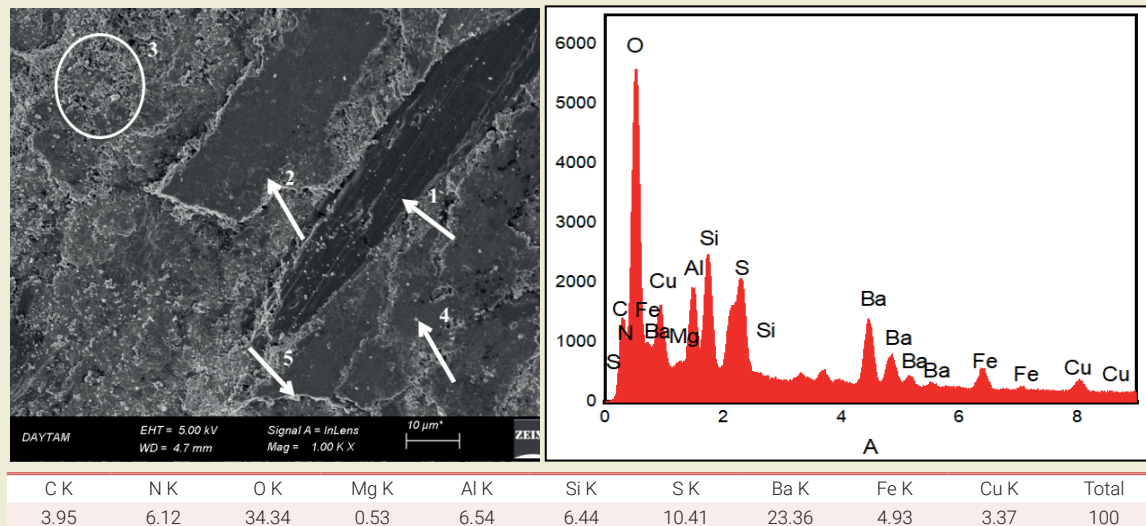
metal particles increase wear. In the zones number 2 and 3, losses of pieces due to friction led to macro and micro gaps. In the zone number 4 with a pasting-like abrasion, adhesive wear took place. It is thought that formation of multiple pasting zones increased wear by reducing the friction coefficient. Generally speaking, it was concluded that secondary plateau zones formed in many areas on the material's surface and this was caused by the abundance of real contact zones.

The components of Bataala surfaces are seen from EDX graphs. According to EDX spectra, the surfaces mainly contain sulfur (S), nitrogen (N), carbon (C), oxygen (O), iron (Fe), barium (Ba), copper (Cu), aluminum (Al), silicon (Si). When the difference between A and JF3 is examined, it is seen that the Fe ratio increases. The intensity of O, S, Si, Ba, Cu peaks increases with the addition of JF. The atomic composition of JF3 treated with silane shows that C, Si increase and the atomic composition of oxygen decreases. In a similar study by Khalili et al. and Helenka et al., when EDX analyses were compared with the pure fiber, it was observed that the silane substance in oil palm fiber had higher carbon and lower oxygen content [32,33]. Higher carbon content shows the positive effect of modification. Similarly, all these elements peaked when jute fibers were treated with silane.

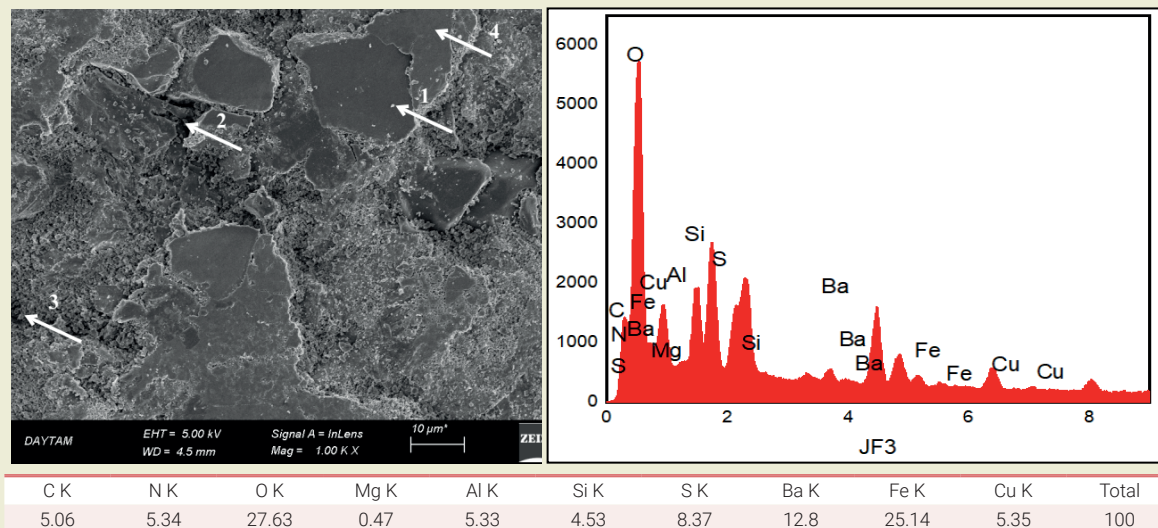
4. Conclusions

In this study, it was aimed to produce organic fiber-reinforced brake pads by minimizing the usage of metal-reinforced materials. Additionally, an environmentalist approach was displayed by avoiding usage of asbestos. The mechanical and tribological properties of the jute fiber-reinforced brake pads that were produced were studied and the following results were reached:

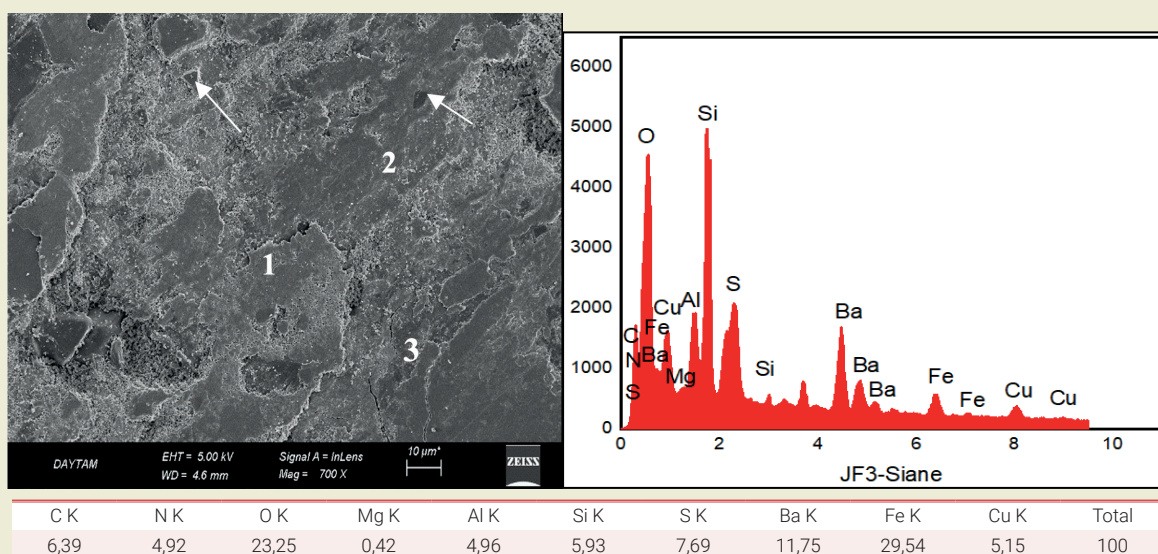
- Jute fiber reinforcement up to 5% reduced friction coefficients. From the friction coefficient time graphs, JF3 is the pad that showed the best and most stable change. Jute fiber addition at all rates positively affected the specific wear values. JF7 has



(a) A



(b) JF3



(c) JF3-Silane

Figure 14. SEM-EDX Images of the Wear Surfaces

the best wear rate but did not give a stable friction time graph.

- Adding Jute fiber to the pad mixture reduced the sample density. All samples are lower than the density value of commercial brake pads (2.0-2.3 gr/cm³).
- The shear stress and density values of all produced pads are within the reference values.
- The hardness values of JF1, JF2 and JF3 pads are within the desired values. The hardness values of other pads are outside the standards.
- Water absorption values increased as the jute fiber ratios increased. When all the results are considered, the pad sample coded JF3 has mechanical, physical and tribological properties close to the standard pad values and the pads used in the market. For this reason, silane was applied to the jute fibers of the FJ3 brake pad and the brake pads were given water-repellent properties. With the silane treatment, 30% of the brake pad's water absorption was prevented.
- When the SEM graphics of the JF3 sample were examined, it was thought that adhesive wear occurred in many areas and that the metal particles in the areas close to the surface actively participated in the wear. As a result of adhesive wear, patch areas were formed on the surface and if these areas increased, a friction film was formed.
- It is thought that this situation will reduce mass losses. It is thought that the increase in the amount of oxygen found is not only due to the oxygen found in the components, but also to the oxygen coming from the oxidation on the surface.
- Considering the test results, it can be concluded that jute fiber reinforcement has positive effects on the material.
- Natural fibers are now preferred in composite man-

ufacturing and are used in different applications in the industry. The jute fiber reinforced brake pads produced in the study comply with the standards of the brake pads used in the market. When considered from this perspective, the brake pads produced show their commercial usability. Jute fiber reinforced brake pads have good environmental performance with a green identity that can compete with commercial brake pads.

Acknowledgements

This article is the thesis of Merve Sali, who completed her master's degree at Kafkas University, Faculty of Engineering, Institute of Science.

Research ethics

Not applicable.

Author contributions

Conceptualization: [B. Hamamcı], Methodology: [All 2 authors], Formal Analysis: [All 2 authors], Investigation: [All 2 authors], Resources: [All 2 authors], Data Curation: [All 2 authors], Writing - Original Draft Preparation: [All 2 authors], Writing - Review & Editing: [All 2 authors], Visualization: [All 2 authors], Supervision: [All 2 authors], Project Administration: [All 2 authors],

Competing interests

The author(s) declare(s) no conflict of interest.

Research funding

None declared.

Data availability

Not applicable. Peer-review Externally peer-reviewed

Orcid

Benek Hamamcı  <https://orcid.org/0000-0002-5180-6798>

Merve Sali  <https://orcid.org/0000-0002-0610-7584>

References

- [1] Eriksson, M., & Jacobson, S. (2000). Tribological surfaces of organic brake pads. *Tribology International*, 33(12), 817-827. [https://doi.org/10.1016/S0301-679X\(00\)00127-4](https://doi.org/10.1016/S0301-679X(00)00127-4)
- [2] Olabisi, A. I., Adam, A. N., & Okechukwu, O. M. (2016). Development and assessment of composite brake pad using pulverized cocoa beans shells filler. *International Journal of Materials Science and Applications*, 5(2), 66-78. <https://doi.org/10.11648/j.ijmsa.20160502.16>
- [3] Tok, A., & Ateş, S. (2023). Al6061 matrisli hibrit kompozitlerin sertlik ve çekme dayanımına SiC Al2O3 ve yumurta kabuğu tozu takviyesinin etkilerinin incelenmesi. *Afyon Kocatepe Üniversitesi Fen ve Mühendislik Bilimleri Dergisi*, 23(6), 1307-1317. <https://doi.org/10.35414/akufemubid.1277913>
- [4] Kocaman, R., & Ateş, S. (2023). Al6061 matrisli SiC Al2O3 ve kömür cürufu tozu takviyeli hibrit kompozitlerin sertlik ve aşınma davranışlarının incelenmesi. *International Journal of Engineering Research and Development*, 15(2), 598-609. <https://doi.org/10.29137/umagd.1287314>
- [5] Abutu, J., Lawal, S. A., Ndalliman, M. B., Lafia-Araga, R. A., Adedipe, O., & Choudhury, I. A. (2018). Effects of process parameters on the properties of brake pad developed from seashell as reinforcement material using grey relational analysis. *Engineering Science and Technology, an International Journal*, 21(4), 787-797. <https://doi.org/10.1016/j.jestech.2018.05.014>
- [6] Singh, T., & Patnaik, A. (2015). Performance assessment of lapi-

- nus-aramid based brake pad hybrid phenolic composites in friction braking. *Archives of Civil and Mechanical Engineering*, 15(1), 151-161. <https://doi.org/10.1016/j.acme.2014.01.009>
- [7] Ikpambese, K. K., Gundu, D. T., & Tuleun, L. T. (2016). Evaluation of palm kernel fibers (PKFs) for production of asbestos-free automotive brake pads. *Journal of King Saud University - Engineering Sciences*, 28(1), 110-118. <https://doi.org/10.1016/j.jksues.2014.02.001>
- [8] Kumar, M., & Bijwe, J. (2010). NAO friction materials with various metal powders: Tribological evaluation on full-scale inertia dynamometer. *Wear*, 269(11-12), 826-837. <https://doi.org/10.1016/j.wear.2010.08.011>
- [9] Singh, T., Patnaik, A., & Chauhan, R. (2016). Optimization of tribological properties of cement kiln dust-filled brake pad using grey relation analysis. *Materials & Design*, 89, 1335-1342. <https://doi.org/10.1016/j.matdes.2015.10.045>
- [10] Hee, K. W., & Filip, P. (2005). Performance of ceramic enhanced phenolic matrix brake lining materials for automotive brake linings. *Wear*, 259(7-12), 1088-1096. <https://doi.org/10.1016/j.wear.2005.02.083>
- [11] Nagesh, S. N., Siddaraju, C., Prakash, S. V., & Ramesh, M. R. (2014). Characterization of brake pads by variation in composition of friction materials. *Procedia Materials Science*, 5, 295-302. <https://doi.org/10.1016/j.mspro.2014.07.270>
- [12] Martinez, A. M., & Echeberria, J. (2016). Towards a better understanding of the reaction between metal powders and the solid lubricant Sb₂S₃ in a low-metallic brake pad at high temperature. *Wear*, 348-349, 27-42. <https://doi.org/10.1016/j.wear.2015.11.014>
- [13] Naganathan, S., Razak, H. A., & Hamid, S. N. A. (2012). Properties of controlled low-strength material made using industrial waste incineration bottom ash and quarry dust. *Materials & Design*, 33, 56-63. <https://doi.org/10.1016/j.matdes.2011.07.014>
- [14] Dadkar, N., Tomar, B. S., & Satapathy, B. K. (2009). Evaluation of flyash-filled and aramid fibre reinforced hybrid polymer matrix composites (PMC) for friction braking applications. *Materials & Design*, 30(10), 4369-4376. <https://doi.org/10.1016/j.matdes.2009.04.007>
- [15] Matějka, V., Fu, Z., Kukutschová, J., Qi, S., Jiang, S., Zhang, X., ... et al. (2013). Jute fibers and powdered hazelnut shells as natural fillers in non-asbestos organic non-metallic friction composites. *Materials & Design*, 51, 847-853. <https://doi.org/10.1016/j.matdes.2013.04.079>
- [16] Pujari, S., & Srikanth, S. (2019). Experimental investigations on wear properties of Palm kernel reinforced composites for brake pad applications. *Defence Technology*, 15(2), 295-299. <https://doi.org/10.1016/j.dt.2018.11.006>
- [17] Omrani, E., Menezes, P. L., & Rohatgi, P. K. (2016). State of the art on tribological behavior of polymer matrix composites reinforced with natural fibers in the green materials world. *Engineering Science and Technology, an International Journal*, 19(2), 717-736. <https://doi.org/10.1016/j.jestch.2015.10.007>
- [18] Yawas, D. S., Aku, S. Y., & Amaren, S. G. (2016). Morphology and properties of periwinkle shell asbestos-free brake pad. *Journal of King Saud University - Engineering Sciences*, 28(1), 103-109. <https://doi.org/10.1016/j.jksues.2013.11.002>
- [19] Liew, K. W., & Nirmal, U. (2013). Frictional performance evaluation of newly designed brake pad materials. *Materials & Design*, 48, 25-33. <https://doi.org/10.1016/j.matdes.2012.07.055>
- [20] Chandra Verma, P., Menapace, L., Bonfanti, A., Ciudin, R., Gialanella, S., & Straffellini, G. (2015). Braking pad-disc system: Wear mechanisms and formation of wear fragments. *Wear*, 322-323, 251-258. <https://doi.org/10.1016/j.wear.2014.11.019>
- [21] Kumar, M., & Bijwe, J. (2011). Composite friction materials based on metallic fillers: Sensitivity of μ to operating variables. *Tribology International*, 44(2), 106-113. <https://doi.org/10.1016/j.triboint.2010.09.013>
- [22] Singh, T., Patnaik, A., Chauhan, R., & Rishiraj, A. (2017). Assessment of braking performance of lapinus-wollastonite fibre reinforced friction composite materials. *Journal of King Saud University - Engineering Sciences*, 29(2), 183-190. <https://doi.org/10.1016/j.jksues.2015.06.002>
- [23] Baklouti, M., Cristol, A. L., Desplanques, Y., & Elleuch, R. (2015). Impact of the glass fibers addition on tribological behavior and braking performances of organic matrix composites for brake lining. *Wear*, 330-331, 507-514. <https://doi.org/10.1016/j.wear.2014.12.015>
- [24] Erkmen, J., Yavuz, H. I., Kavci, E., & Sari, M. (2020). A new environmentally friendly insulating material designed from natural materials. *Construction and Building Materials*, 255, 119357. <https://doi.org/10.1016/j.conbuildmat.2020.119357>
- [25] Bhatt, B., Marathe, U., Kalel, N., & Bijwe, J. (2025). Efficacy of high-performance epoxy resin as a binder to replace eco-unfriendly phenolic resins in Cu-free brake pads. *Tribology International*, 202, 110359. <https://doi.org/10.1016/j.triboint.2024.110359>
- [26] Hamamcı, B., & Sali, M. (2020). Asbest içermeyen fren balata imalatında farklı sinterleme sıcaklığı ve süresinin tribolojik ve mekanik özelliklere etkisi. *Fen Bilimleri Dergisi*, 10(2), 520-531. <https://doi.org/10.21597/jist.553101>
- [27] Akıncioğlu, G., Uygur, İ., Akıncioğlu, S., & Öktem, H. (2021). Friction-wear performance in environmentally friendly brake composites: A comparison of two different test methods. *Polymer Composites*, 42(10), 4461-4477. <https://doi.org/10.1002/pc.26162>
- [28] Zhen-Yu, W., Jie, W., Feng-Hong, C., Yun-Hai, M., Singh, T., & Fekete, G. (2019). Influence of banana fiber on physicomechanical and tribological properties of phenolic based friction composites. *Materials Research Express*, 6(7), 075103. <https://doi.org/10.1088/2053-1591/ab160a>
- [29] Rajan, R., Tyagi, Y. K., & Singh, S. (2022). Waste and natural fiber based automotive brake composite materials: Influence of slag and coir on tribological performance. *Polymer Composites*, 43(3), 1508-1517. <https://doi.org/10.1002/pc.26471>
- [30] Madyan, O. A., & Fan, M. (2018). Hydrophobic clay aerogel composites through the implantation of environmentally friendly water-repellent agents. *Macromolecules*, 51(14), 5079-5087. <https://doi.org/10.1021/acs.macromol.8b02218>
- [31] Lithner, D., Larsson, Å., & Dave, G. (2011). Environmental and health hazard ranking and assessment of plastic polymers based on chemical composition. *Science of the Total Environment*, 409(18), 3309-3324. <https://doi.org/10.1016/j.scitotenv.2011.04.038>
- [32] Khalili, P., Tshai, K. Y., & Kong, I. (2018). Comparative thermal and physical investigation of chemically treated and untreated oil palm EFB fiber. *Materials Today: Proceedings*, 5(2), 3185-3192. <https://doi.org/10.1016/j.matpr.2018.01.127>
- [33] Perera, H. J., Goyal, A., & Alhassan, S. M. (2022). Morphological, structural and thermal properties of silane-treated date palm fibers. *Journal of Natural Fibers*, 19(16), 12144-12154. <https://doi.org/10.1080/15440478.2022.2051672>

Structural analysis of a rope slewing system for loads with a variable center of gravity

Sinan Duzenli¹ , Tolga Guney¹ , Mucahit Soyaslan^{2*} 

¹Yektamak Machinery Engineering Manufacturing Industry and Trade Inc., Sakarya, Türkiye

²Sakarya University of Applied Sciences, Faculty of Technology, Department of Mechatronics Engineering, Sakarya, Türkiye

Abstract: Adjustable sling cranes are specialized lifting systems equipped with adaptable sling mechanisms that enhance operational flexibility and efficiency. These systems are particularly advantageous in construction and industrial applications, where adjustable sling tension significantly affects weight distribution and safety. This study presents the design and structural analysis of a rope slewing system for loads with a variable center of gravity. First, the upper and lower lifting groups were designed, and profiles with fixing points according to the load position were mounted on the rails. A sling apparatus was used between the upper and lower groups. For structural analyses, boundary conditions and material properties were defined according to the loads to be carried in the system. Inclined conditions that may occur during transportation were taken into account in the analyses. Loading was performed under transportation conditions with a maximum inclination of 6° and accordingly, the safety of the system according to the material types was observed. According to the Finite Element Analysis (FEA) results, the maximum stress values were obtained as 267.5 MPa in the upper carrying group, 113.4 MPa in the lower carrying group and 66.1 MPa in the sling apparatus. As a result, the structural analyses performed show that the design and material selections of the rope slewing system remained within safe limits during operation. Considering loading conditions and inclined positions, the system's safety and efficiency demonstrate that it provides a practical and safe solution for industrial applications.

Keywords: Sling Cranes; Lifting Systems; Finite Element Analysis; Mechanical Design.

1. Introduction

Sling-based load lifting systems play a critical role in ensuring safety and efficiency in various sectors, particularly in construction and material handling. Adjustable sling cranes are specialized lifting systems that incorporate adjustable sling mechanisms to enhance their operational flexibility and efficiency. These systems have the ability to modify the sling tension which significantly impacts load handling and safety.

Recent studies outline key specifications, functionalities, and implications of adjustable sling cranes. One of the primary advantages of adjustable sling cranes is their ability to accommodate varying load conditions. The principle of adjustable tensioning can be applied to crane systems, where adjustable slings can be tensioned to optimize load support and stability during lifting operations.

The ability to adjust the sling tension dynamically is crucial for maintaining the center of gravity and ensur-

ing that loads are lifted safely without excessive sway or instability. In the context of tower cranes, the integration of adjustable sling systems can enhance the control of payload swing, which is a common challenge in lifting operations. Li et al. highlight the importance of accurately positioning the payload, noting that flexible steel slings can complicate this process [1]. Their research emphasizes the need for effective control strategies to minimize swing and improve operational efficiency. Similarly, Wada et al. discuss the development of a suspended-load rotation-control device that utilizes gyroscopic dampers to stabilize loads during lifting, further illustrating the potential for adjustable systems to enhance crane performance [2].

The dynamic behavior of adjustable sling cranes is also influenced by the design of the crane's structural components. Vasiljević et al. examined the parameters affecting the dynamic behavior of portal cranes, which often feature a rotating boom capable of 360° movement [3]. Their findings suggest that the configuration of the

*Corresponding author:

Email: msoyaslan@subu.edu.tr

Cite this article as:

Duzenli, S., Guney, T., Soyaslan, M. (2025). Structural analysis of a rope slewing system for loads with a variable center of gravity. *European Mechanical Science*, 9(1): 78-86. <https://doi.org/10.26701/ems.1629942>

History dates:

Received: 30.01.2025, Revision Request: 02.03.2025, Last Revision Received: 13.03.2025, Accepted: 13.03.2025



© Author(s) 2025. This work is distributed under <https://creativecommons.org/licenses/by/4.0/>



sling and boom attachment points plays a critical role in the crane's stability and load handling capabilities. This highlights the need for careful engineering and design considerations when implementing adjustable sling systems in cranes. Moreover, the cost-effectiveness of adjustable sling systems has been analyzed in various studies.

Onur, Devaraj and Krishnaveni et al. investigated the effects of sling angle and size on the reliability of lifting hooks using with stress analyses [4-7]. The researchers utilized computer-aided modeling and finite element analysis to assess the stress on hooks under different sling configurations. The findings indicated that variations in sling size and angle significantly affect the safety factor of lifting hooks, emphasizing the importance of proper rigging techniques to prevent accidents during lifting operations. These studies provided a comprehensive understanding of the mechanical properties and limitations of lifting hooks, which are crucial for material handling systems. The results underscored the necessity of stress testing and modeling to ensure that lifting hooks can withstand the demands of heavy loads without failure. Additionally, mechanical analysis has highlighted the importance of material selection in designing lifting equipment to maintain operational efficiency and load safety [8].

Sydora et al. explored the application of simulation technologies in heavy industrial construction, specifically focusing on lifting processes [9]. Their research developed a real-time interactive simulation that allows users to visualize and understand the complexities of lifting operations. This approach not only enhances training and operational planning but also aids in identifying potential risks associated with sling-based lifting systems. Li analyzed various parameters, including sling length and counterweight position. The research demonstrated how careful design adjustments can enhance the performance of lifting systems [10]. The development of innovative detection methods, such as the anti-lifting detection system based on neural networks used during train loading operations, highlights the ongoing evolution towards intelligent detection and safety mechanisms within crane operations [11]. This reflects a broader trend recognizing the importance of predictive technologies in enhancing the safety and efficiency of crane operations. In the sector of adjustable sling cranes, recent research has shown a trend toward enhancing operational productivity through advanced control systems and ergonomics. A study on the synchronous control of multi-lift overhead cranes highlights the complexities associated with potential loads in crane operations, advocating for robust control mechanisms that adapt to dynamic load conditions [12]. The integration of advanced stability and control systems, such as pulse-width modulation (PWM) technology for lifting platform speed control, showcases innovation in maintaining safety and efficiency during operations [13].

In conclusion, adjustable sling cranes represent a significant advancement in lifting technology, offering enhanced flexibility, safety, and efficiency in load handling. The ability to adjust sling tension dynamically allows for better control of payloads, minimizes swing, and improves operational outcomes. As the literature indicates, careful consideration of design, dynamic behavior, and cost-effectiveness is essential for optimizing the performance of these advanced crane systems. Also the integration of simulation tools in engineering practices represents a significant advancement in ensuring the safety and efficiency of lifting operations.

This study presents a comprehensive structural analysis of a rope slewing system designed to accommodate variations in load center of gravity under transport conditions with a maximum inclination of 6°. Using Finite Element Analysis (FEA), it determines stress values in both the upper and lower carrying groups, evaluating system durability based on material types. Unlike previous studies, this research provides detailed dynamic and static analysis results specifically related to the rope slewing system and inclined loading conditions. Consequently, this study demonstrates that adjustable sling crane systems offer a safe solution under dynamic and inclined loading conditions, making a significant contribution to the existing literature.

2. Materials and Methods

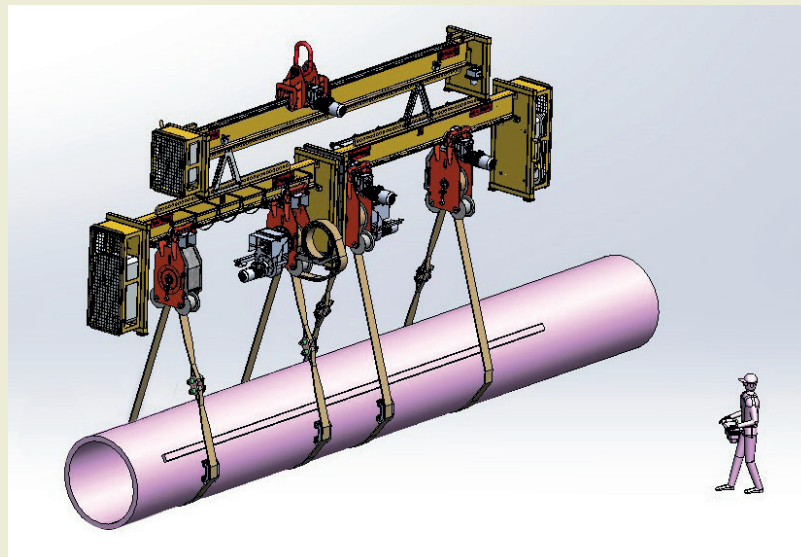
2.1. Design of the System

In sling-based load rotation systems used for handling large and heavy workpieces, sling sideslip during the rotation process can lead to various operational issues. To eliminate these problems and ensure a safer application of the process from both technical and occupational safety perspectives, the sling-centering mechanism must be designed accordingly.

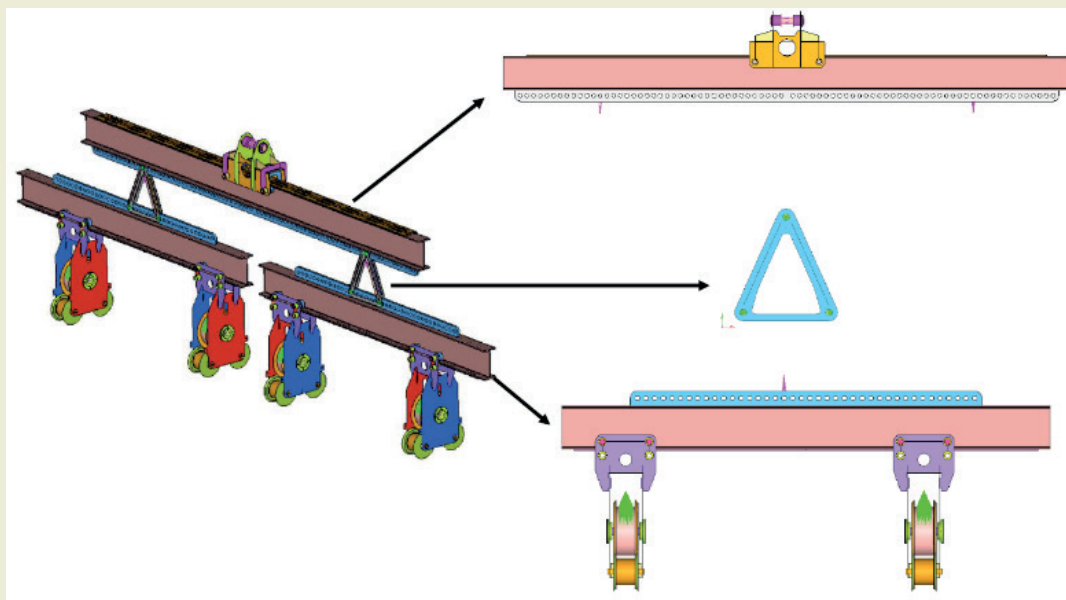
In current systems, the fabric sling may shift laterally along the X-axis across the main drum during load rotation. This slippage causes the sling to climb over the edge flanges of the main drum or, in cases where it cannot, to sag. Such slippage and sagging result in issues during load rotation, causing deformation of the sling and reducing its service life. The proposed design aims to deliver an innovative solution that enhances efficiency, reduces operational costs, and complies with safety standards. ► **Figure 1** shows the overall system design and exploded view of its components. There are upper and lower lifting groups, and profiles with fixing points according to the load position were mounted on the rails. Two triangle sling apparatuses were used between upper and lower lifting profiles.

2.2. Structural Analyses

Defining boundary conditions such as fixed supports,



a)



b)

Figure 1. a) Complete system design, b) The design of the rope slewing system.

symmetry conditions, and any constraints that restrict movement in specific directions is critical in structural analysis [14]. Inertia relief analysis is a method used to simulate static loading conditions on a structure that is not fully constrained. By balancing external forces with inertial forces, inertia relief allows for static analysis of systems without fixed boundary conditions. The analyses of the system in ►Figure 1 were done according to inertia relief method.

The analyses were done separately for the upper lifting group, lower lifting group and triangle sling apparatus. Since the inertia relief method was used in the analyses, fixing points were not used for the parts. The applied loads for three different analyses are shown in ►Figure 2. Changes in the center of gravity of transported products can cause imbalances in the system, affect-

ing stability during the transport process. To evaluate these potential issues, analyses were conducted to examine how the carrier system behaves at different tilt angles. This approach enables an understanding of the system's performance under inclined operating conditions and provides insights into how imbalances can be minimized.

Loading was performed under transportation conditions with a maximum inclination of 6° . This is the maximum inclination angle that can occur during load transportation, and the boundary conditions were applied based on the worst-case working conditions. All analyses also were done according to maximum loading conditions. For balancing, the loads were applied vertically in opposite directions along the +Y and -Y axes from connection points. RBE2 and RBE3 elements were

used to define the connections between the apparatus. While RBE2 creates a fully rigid connection between multiple nodes, constraining all degrees of freedom, RBE3 element distributes loads across the connected nodes, allowing for a more realistic load transfer on the structure.

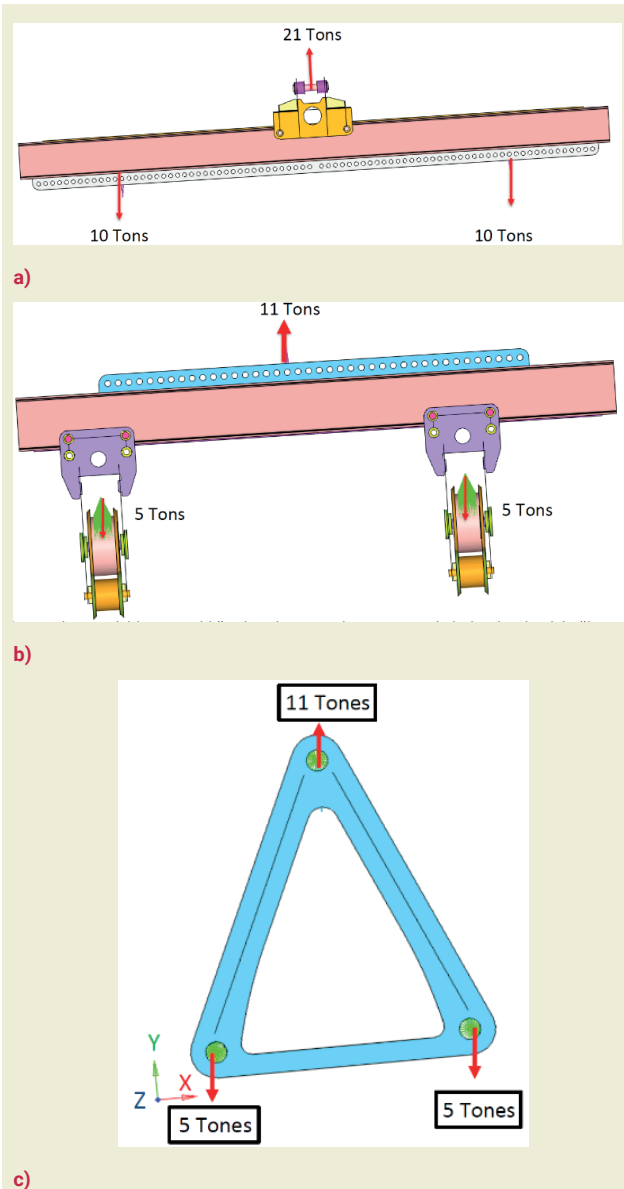


Figure 2. Applied loads with inclination of 6° for three different analyses a) Upper lifting group, b) Lower lifting group, c) Triangle sling apparatus.

Before proceeding with the analysis, the properties of the materials used in the system must be defined. Various materials are used in the production of the system's rails, profiles, connecting pins, and sling apparatus. ►Table 1 defines the material types used in the analyses. In the analyses conducted, certain sections exhibited high stress values; therefore, AISI 1050 steel, which has a higher yield strength, was preferred in these areas. In contrast, in sections with lower stress values, St37 steel was selected to reduce the overall system cost.

Table 1. The material types used in analyses.

Connection pins	AISI 1050
Rails, profiles	St37
Sling apparatus	ALU6061-T6

The geometric details of the structure significantly influence the mesh structure selection. Regions with complex or intricate details may require a finer mesh, while simpler, flat regions may be adequately represented with larger elements. Convergence studies were conducted to verify mesh accuracy. By repeating analyses with varying mesh densities, changes in results were observed. Once results stabilized to a certain precision, the mesh density was considered adequate. Mesh convergence for 9 mm, 10.5 mm and 13.5 mm mesh dimensions are shown in ►Figure 3. The maximum stress values obtained according to the mesh numbers and sizes are presented in ►Table 2. As shown in the ►Figure 3 and ►Table 2, even though the number of elements was increased and the mesh size was reduced, the difference in stress values decreased. The difference in stress values between the 9 mm and 10 mm mesh sizes is less than 1%. The mesh convergence processes, shown on the suspension apparatus, were applied throughout all the analysis processes.

Table 2. Mesh convergence values.

Mesh Size	Stress Value	Total Elements
13.5 mm	62.4 MPa	2117
10.5 mm	65.8 MPa	2412
9 mm	66.1 MPa	2576

The structural finite element model of the sling apparatus was developed using shell elements, with welds and assembly connections arranged to accurately represent the physical boundary conditions. ►Figure 4 illustrates the mesh structures of the system components.

3. Results and Discussions

3.1. Analyses Results

The analysis results for the upper carrying group, lower carrying group, and sling apparatus based on the material, load, and boundary condition definitions are provided in ►Figures 5-10. For the upper carrying group, the maximum Von Mises stress under applied loads is obtained to be 267.5 MPa, which is below the yield strength of the specified connection pin material (550 MPa). Accordingly, the safety factor for the connection pin is calculated as 2.056. Furthermore, the stress levels in the rails and profiles are considerably low, indicating that these components operate well within safe limits. ►Figure 5 displays the stress analysis results on the left side and the filtered regions above 155 MPa on

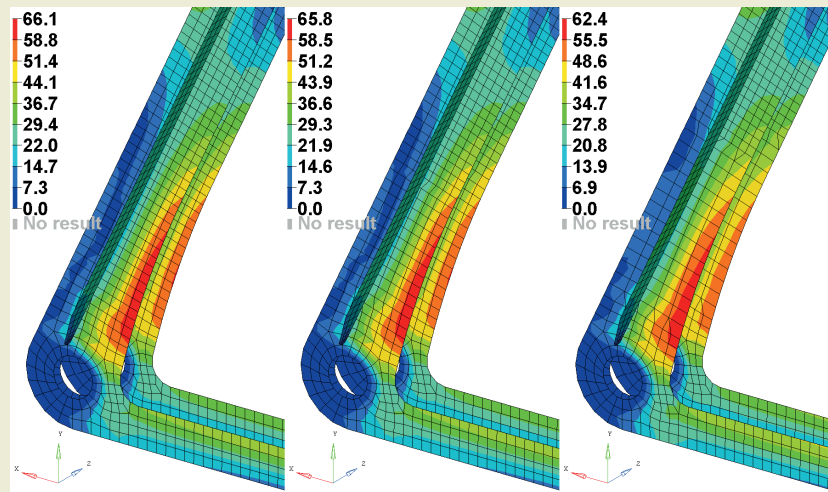


Figure 3. Mesh convergence stress values for 9 mm, 10.5 mm and 13.5 mm mesh sizes.

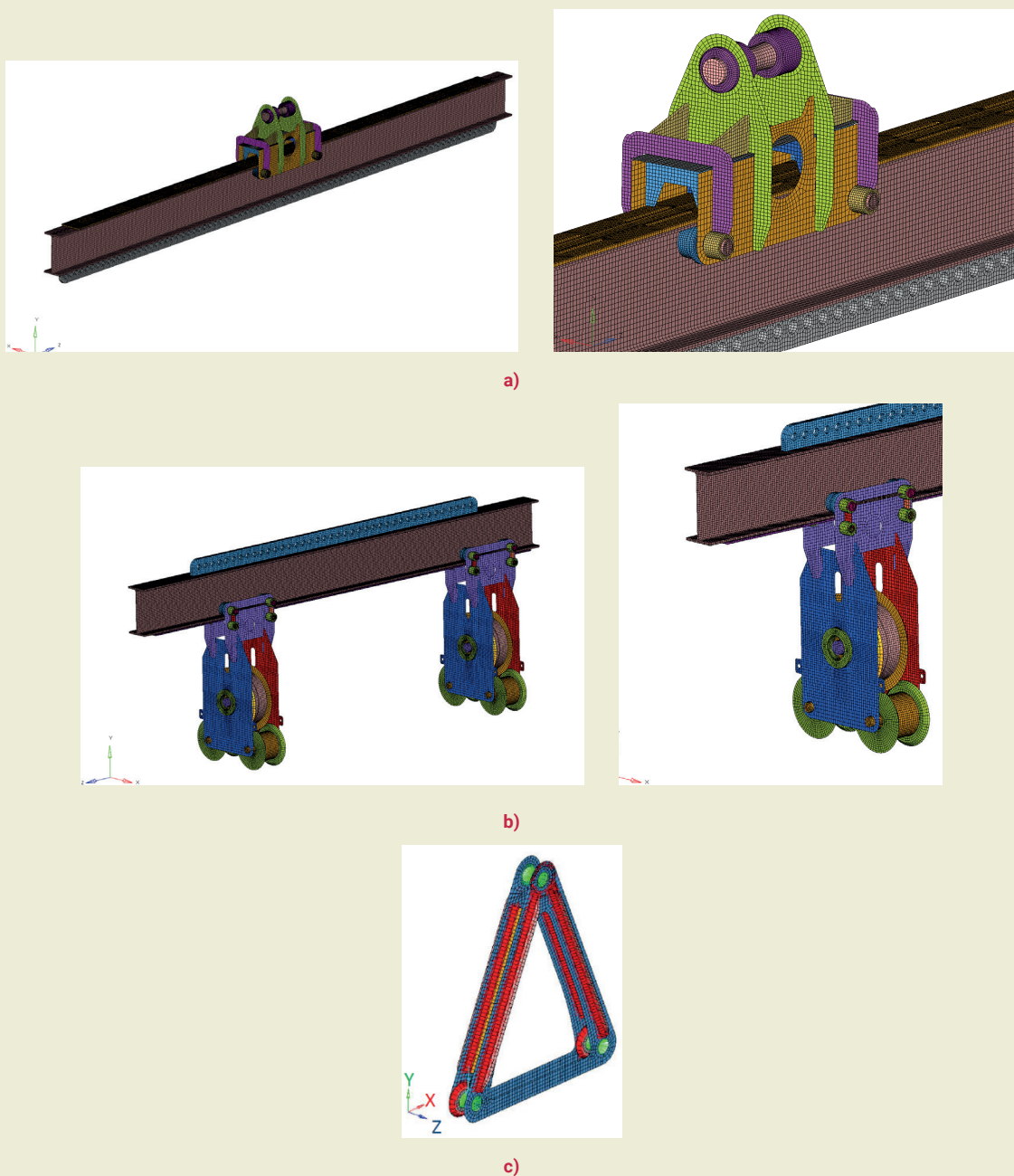


Figure 4. Mesh structures of the system components a) Upper lifting group, b) Lower lifting group, c) Triangle sling apparatus.

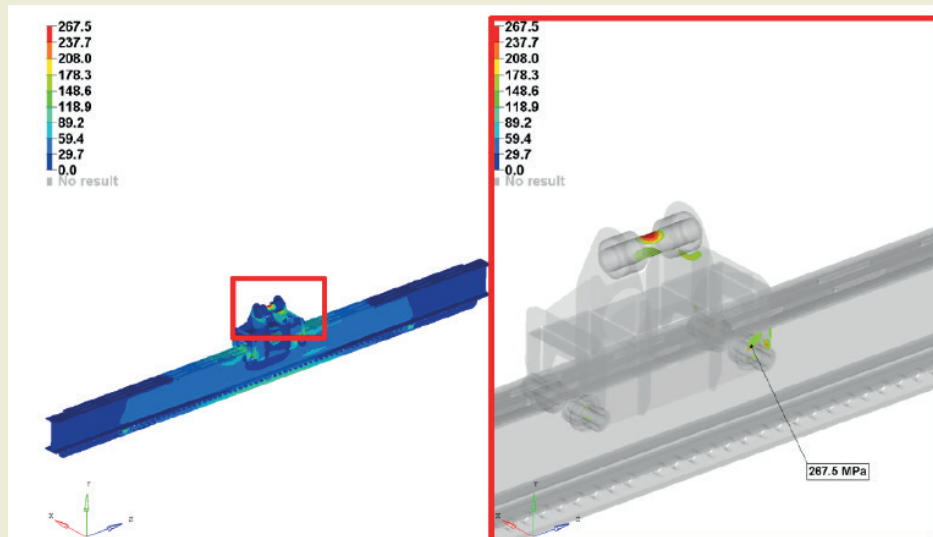


Figure 5. Stress analysis results for upper carrying group.

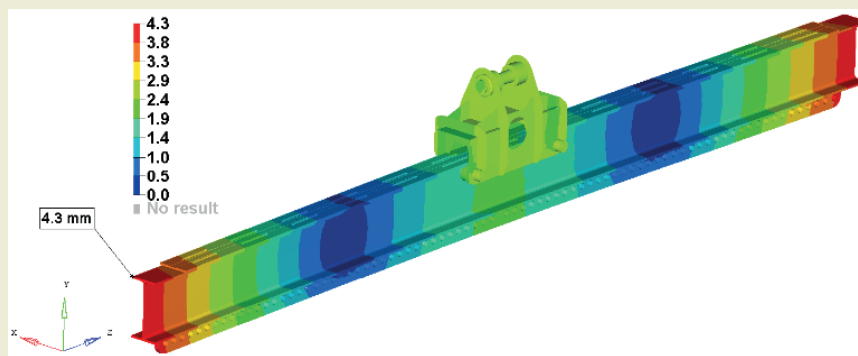


Figure 6. Displacement results for upper carrying group.

the right. Maximum displacement was obtained as 4.3 mm at the end regions of the rails and profiles, as shown in ►Figure 6. Considering the applied boundary conditions and load distributions, it is understandable that maximum displacement occurs at the rail and profile ends.

For the lower carrying group, the maximum Von Mises stress under applied loads is 113.4 MPa, which is less than the specified rail and profile material's yield strength (235 MPa). Thus, the safety factor for the lower carrying group is 2.072. ►Figure 7 shows the stress analysis results on the left and the filtered regions greater than 50 MPa on the right. ►Figure 8 shows the maximum displacement of 1 mm at the rope connection pulleys.

The maximum Von Mises stress for the sling apparatus under applied loads is 66.1 MPa, which is significantly lower than the yield strength of the specified sling apparatus material (240 MPa). As a result, the safety factor for the sling apparatus is calculated as 3.63. According to the Machinery Safety Regulation (2006/42/EC), the safety factor value in strength calculations for manually operated machines and lifting accessories is 1.5, and this value has been used as a reference in the analyses.

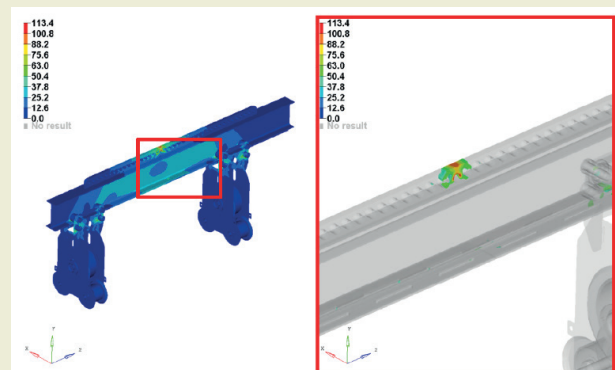


Figure 7. Stress analysis results for lower carrying group

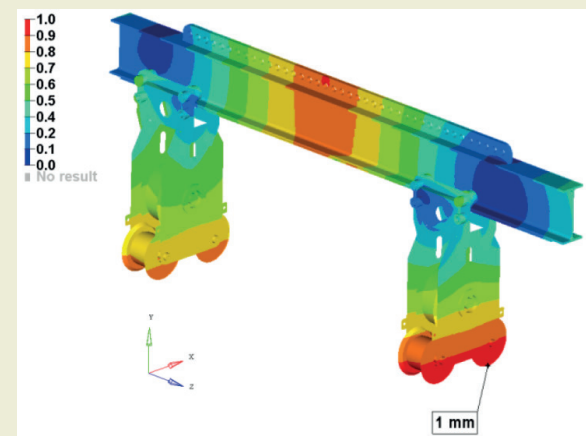


Figure 8. Displacement results for lower carrying group.

► **Figure 9** shows the stress analysis results on the left and the filtered regions greater than 30 MPa on the right. The maximum displacement was 0.4 mm in the middle of the connection pins, as shown in ► **Figure 10**.

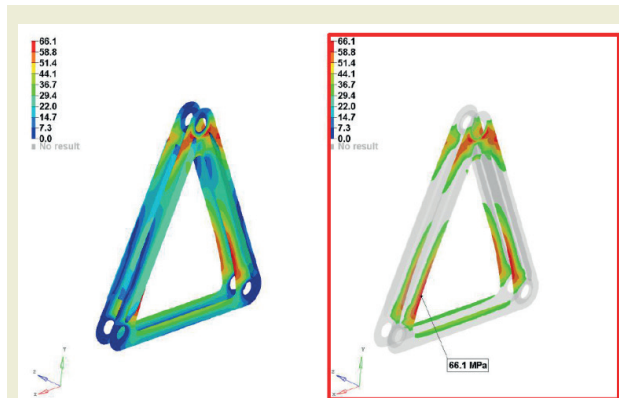


Figure 9. Stress analysis results for sling apparatus.

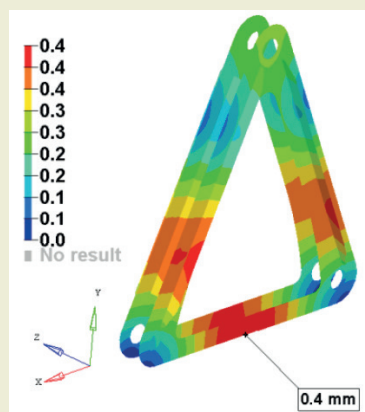


Figure 10. Displacement results for sling apparatus.

3.2. Production of the System

Following the comprehensive design and structural analysis, the adjustable sling crane system was successfully produced, incorporating all the necessary components and ensuring they met the design specifications. The manufacturing process involved precise machining and fabrication of each component, ensuring accurate dimensions and quality standards. The upper and lower lifting groups, as well as the sling apparatus, were fabricated according to the design specifications. Special attention was given to the connection points and the assembly of the profiles to ensure that they would align correctly under operational loads.

The key components were then assembled and tested to verify their functionality. The sling apparatus, which connects the upper and lower lifting groups, was carefully positioned, and the necessary adjustments were made to ensure smooth operation. ► **Figure 11** depicts that the produced system was tested under varying load conditions and inclinations, as predicted in the analysis. During testing, the system demonstrated its ability to function efficiently and safely, with minimal displacement and stress levels within the safe limits.

4. Conclusions

This study presents the design and structural analysis of an adjustable sling crane system, specifically focusing on a rope slewing mechanism that accounts for the varying center of gravity of loads. Through the use of FEA, the system was evaluated under realistic loading conditions, including a maximum inclination of 6°. The results indicate that the designed system remains



Figure 11. Load tests of the produced system

within safe operational limits, with stress values significantly lower than the yield strengths of the selected materials.

The maximum Von Mises stress for the upper lifting group was found to be 267.5 MPa, which is well below the yield strength of the AISI 1050 material (550 MPa), yielding a safety factor of 2.056. Similarly, the lower lifting group and the sling apparatus both demonstrated stress values far below the yield strengths of their respective materials (St37 and ALU6061-T6), with safety factors of 2.072 and 3.63, respectively. These findings confirm the structural integrity of the system, ensuring its durability and reliability under dynamic and inclined loading conditions.

Additionally, the system has been successfully produced, with the final design tested in real-world conditions. The manufactured system demonstrated its ability to safely and efficiently handle loads with varying centers of gravity, validating the analysis results. The successful production and validation of the system further confirm its practical applicability in industrial lifting operations.

This study distinguishes itself from previous research by specifically addressing the effects of inclined loading conditions on a rope slewing system, providing detailed dynamic and static analysis results, and integrating real-world production and testing phases. This research also contributes to the ongoing development of more advanced and reliable lifting systems by offering valuable insights into the performance of adjustable sling cranes under real-world conditions. The combination of appropriate material selection, detailed structural analysis, and consideration of inclined operational conditions allows for a crane system that balances both safety and operational efficiency.

Acknowledgments

This study was carried out by Yektamak Machinery Engineering Manufacturing Industry and Trade Inc. design center.

Research ethics

Not applicable.

Author contributions

Conceptualization: [S. Duzenli, T. Guney, M. Soyaslan], Methodology: [S. Duzenli, T. Guney, M. Soyaslan], Formal Analysis: [S. Duzenli, T. Guney, M. Soyaslan], Investigation: [S. Duzenli, T. Guney], Resources: [S. Duzenli, T. Guney], Data Curation: [S. Duzenli, T. Guney], Writing - Original Draft Preparation: [S. Duzenli, T. Guney, M. Soyaslan], Writing - Review & Editing: [M. Soyaslan], Visualization: [S. Duzenli, T. Guney, M. Soyaslan], Supervision: [M. Soyaslan], Project Administration: [T. Guney].

Competing interests

The author(s) state(s) no conflict of interest.

Research funding

None declared.

Data availability

Not applicable.


Peer-review

Externally peer-reviewed.

Orcid

Sinan Duzenli  <https://orcid.org/0009-0001-4230-2766>

Tolga Guney  <https://orcid.org/0009-0002-8767-3891>

Mucahit Soyaslan  <https://orcid.org/0000-0001-6658-5169>

References

- [1] Li, K., Liu, M., Yu, Z., Peng, L., & Liu, N. (2022). Multibody system dynamic analysis and payload swing control of tower crane. *Proceedings of the Institution of Mechanical Engineers Part K Journal of Multi-Body Dynamics*, 236(3), 407-421. <https://doi.org/10.1177/14644193221101994>
- [2] Wada, M., Mori, Y., & Tagawa, Y. (2020). Development of a suspended-load rotation-control device for cranes with gyroscopic damper and control by wind force (concept, modeling and experiments). *Mechanical Engineering Journal*, 7(5), 20-00268-20-00268. <https://doi.org/10.1299/mej.20-00268>
- [3] Vasiljević, R., Gašić, M., & Savković, M. (2016). Parameters influencing the dynamic behaviour of the carrying structure of a type h portal crane. *Strojniški Vestnik – Journal of Mechanical Engineering*, 62(10), 291-602. <https://doi.org/10.5545/sv-jme.2016.3553>
- [4] Onur, Y. (2017). Investigation of the effect of the sling angle and size on the reliability of lifting hooks. *Simulation*, 94(10), 931-942. <https://doi.org/10.1177/0037549717744646>
- [5] Devaraj A. (2015). Design of a crane hook of different materials and stress analysis using ANSYS workbench. *Int J Res App Sci Eng Tech*, 3: 310–314.
- [6] Krishnaveni MNV, Reddy M, Rajaroy M. (2015). Static analysis of crane hook with t-section using ANSYS. *Int J Eng Trends Tech*, 25: 53–58.
- [7] Onur, Y. (2018). Computer aided lifting hook modeling and stress analysis. *Erzincan Üniversitesi Fen Bilimleri Enstitüsü Dergisi*, 11(2), 231-236. <https://doi.org/10.18185/erzifbed.371751>
- [8] Sanches, L. V., Goulart, C. A., Bustos MacLean, P. A., & Villas-Boras, L. A. (2024). Mechanical analysis and materials selection of a scissor lift system for pig transportation. *Acta Scientiarum Technology*, 46(1). <https://doi.org/10.4025/actascitech.v46i1.65406>
- [9] Sydora, C., Lei, Z., Siu, M., Han, S., & Hermann, U. (2020). Critical lifting simulation of heavy industrial construction in gaming environment. *Facilities*, 39(1/2), 113-131. <https://doi.org/10.1108/f-08-2019-0088>

- [10] Li, W. (2023). Optimization of hoisting attitude in non-standard steel structures via adjustable counterweight balance beam technology. *J. Civ. Hydraul. Eng.*, 1(1), 11-22. <https://doi.org/10.56578/jche010102>
- [11] Jiang, J. (2024). A train f-tr lock anti-lifting detection method based on improved bp neural network. *Journal of Measurements in Engineering*, 12(1), 149-161. <https://doi.org/10.21595/jme.2023.23638>
- [12] Jin, X., & Xu, W. (2024). Finite-time model-free robust synchronous control of multi-lift overhead cranes based on iterative learning. *Transactions of the Institute of Measurement and Control*, 46(13), 2570-2584. <https://doi.org/10.1177/01423312241231282>
- [13] Ouyang, Z., Zhang, M., & Zeng, W. (2024). Lifting platform pwm control system design combining distance detection. *Journal of Physics Conference Series*, 2787(1), 012017. <https://doi.org/10.1088/1742-6596/2787/1/012017>
- [14] Kozkurt, C., Fenercioglu, A., & Soyaslan, M. (2012). Structural Analysis of Warehouse Rack Construction for Heavy Loads. *International Journal of Civil and Environmental Engineering*, 6(7), 414-418.

Analysis of the pressure resistance of mini valve used in drip irrigation with finite elements

Yavuz Turan¹ , Murat Kuru¹ , Beyza Gizem Duman¹ , Hülya Alaca¹ , İbrahim Keleş^{2*} 

¹ Poelsan Plastic Industry and Trade Inc., 55139, Tekkeköy/Samsun, Türkiye

² Samsun University, Faculty of Engineering and Natural Sciences, Department of Mechanical Engineering, 55420, Samsun, Türkiye

Abstract: Different types of valves are used in irrigation systems to transport water efficiently. One of these valves is mini valves, which attract attention with their ease of use and functionality. Mini valves are elements that can be quickly mounted and dismounted on the irrigation line and are generally preferred for flow control and on/off operations. In the design of valves, it is of great importance to analyze the pressure losses occurring in the irrigation system. In this study, the strength of a manually controlled, two-way mini plastic valve, which is frequently used in irrigation systems, is numerically investigated. This mini valve is an element used to control the flow direction of water in a certain direction and is especially used in drip irrigation systems. These valves, which are preferred to minimize pressure losses and manually manage the flow of the line, play a critical role in terms of system efficiency. Valves must be resistant to certain pressure values for long life and safe operation. In this study, a manually controlled bi-directional mini plastic valve with a worm mouth connection port was designed and its resistance was evaluated by numerical analysis. Tests were performed by applying 2, 4 and 6 bar pressure to the valve respectively. According to the results of the analysis, the mini valve can operate safely up to 2 bar pressure, but it is seen that the stress levels increase as the pressure increases. At 6 bar pressure, it was found that the valve approached the material strength limit. These findings provide valuable information to determine the operating limits required for the safe use of mini plastic valves in irrigation systems.

Keywords: Mini valve, Finite element analysis, Compressive strength, Stress analysis

1. Introduction

Valves are critical components used in pipelines to regulate, direct or stop the flow of fluids. Although different types of valves are used in industrial and agricultural applications, low-pressure, lightweight and durable mini plastic valves are generally preferred in drip irrigation systems. These valves provide controlled distribution of water in irrigation lines and offer advantages in terms of energy efficiency and cost. However, their structural strength is of great importance due to the pressure and mechanical loads they are exposed to during operation. The performance of mini plastic valves is affected by several hydraulic, mechanical and environmental factors. From a hydraulic point of view, pressure loss directly affects energy efficiency due to the flow resistance inside the valve, while flow and flow characteristics vary depending on the valve design. High turbulence can lead to energy loss and wear, while

cavitation in low pressure zones can threaten the structural integrity of the valve. Among mechanical factors, the strength and sealing performance of the plastic material used are critical. In long-term use, there is a risk of material fatigue and deformation under high pressure. Environmental factors are also decisive for the durability of valves; temperature changes can cause expansion and contraction of plastic materials, while fertilizers and chemicals used in agricultural irrigation can affect chemical resistance. In addition, structural weakening of plastic materials exposed to UV radiation can occur over time. In terms of installation and use, the way the valve is connected to the pipe and the sensitivity of the on-off mechanism are important for the overall efficiency of the system. Therefore, the determination of flow parameters such as pressure loss, flow coefficient, resistance coefficient and cavitation index, which are critical in the design process of valves, is necessary to understand their flow behavior.

*Corresponding author:

Email: ibrahim.keles@samsun.edu.tr

Cite this article as:

Turan, Y., et.al. (2025). Analysis of the pressure resistance of mini valve used in drip irrigation with finite elements. *European Mechanical Science*, 9(1): 87-95. <https://doi.org/10.26701/ems.1646687>

History dates:

Received: 25.02.2025, Revision Request: 17.03.2025, Last Revision Received: 18.03.2025, Accepted: 18.03.2025



© Author(s) 2025. This work is distributed under <https://creativecommons.org/licenses/by/4.0/>



Rajkumar [1] identified valve design problems encountered in industry and showed that by using finite element analysis (FEA) and computational fluid dynamics (CFD) methods, the flange weight was reduced by 50% while stress and deformation intensities remained within acceptable limits. Chem M. J. et al. [2] experimentally investigated inlet and outlet flow patterns, cavitation effects and valve performance coefficients in ball valves using Particle Tracking Visualization Method (PTVM) and showed that the proposed method provides rapid effect evaluation. Jadhav S. S. [3] determined the optimum thickness specifications for safe operation of M-Type gate valve under high pressure and showed that the stress values obtained by classical mechanical theory and FEA agree and these results can be used for further improvement of the valve. Considering that cavitation can lead to noise and vibrations due to localized under pressure, this phenomenon needs to be well understood during valve operation. Furthermore, since valves are the limiting components in any flow system, their design and performance analysis are critical [4]. Mokhtarzadeh-Dehghan et al. [5] analyzed the laminar flow in a differential angle hydraulic pressure relief valve for variable compression ratio pistons using the Finite Element Method and compared the velocity and pressure distributions, the buoyancy forces on the piston and the effect of recirculation zones on the pressure distribution with experimental and analytical data. Song X. et al. [6] proposed a meta-model for optimization of butterfly valve and used kriging model to obtain the best disc weight by FEA and CFD analysis under the constraints of pressure loss coefficient and disc safety and reduced the weight of the valve disc by 7.05% through the optimization process. Kumar S. S. et al. [7] modeled the body and seat ring of a gate valve with SolidWorks and investigated factors such as stress analysis, temperature distribution, total deformation and heat flux with ANSYS analysis tool and evaluated the effects of directed heat flux on temperature distribution and welding defects such as cracking, deformation and undercutting. Prakash et al. [8] CFD analysis supports the product development process by investigating ball and gate valves with parameters such as pressure, density, viscosity and temperature, combining pressure distribution and deformations in the valve system with finite element analysis to optimize the integration of material and product design. Song X. et al. [9] optimized the valve disc by reducing the weight of the disc by 7.05% through FEA of the mechanical properties of the disc, determination of the pressure loss coefficient by fluid analysis and interpolation of the data with the Kriging model, making the optimization process more efficient. Raut L. B. et al. [10] performed FEA analysis for weight reduction of plug valve body, used strain gauge technique for stress measurement and developed optimized models with design parameters and validated the results obtained with maximum deviations of 9.75% and minimum deviations of 6.23%. Lee et al. [11] improved the flow performance of the check valve by optimizing the flow coefficient for the pan check valve by CFD analysis, determining the length of the support

beam by pressure drop analysis and estimating the flow head loss at different flow rates, observing the pressure and velocity distribution using CFD method, and determining the optimum support beam length as 32 mm for minimum pressure drop and maximum flow coefficient. Jun-Oh K. et al. [12] emphasized the importance of topology optimization in the butterfly valve shape design process and explained how to optimize the topology of the double eccentric butterfly valve disc and how they used this optimization to define the disc shape and pressure drop was observed in the comparison between the original design and the best design.

While numerous studies have focused on the structural optimization, weight reduction, and flow behavior of industrial and metal-based valves, research specifically targeting the structural integrity and pressure resistance of mini plastic valves used in agricultural irrigation systems remains limited. Unlike previous works, this study provides a comprehensive numerical investigation of a mini plastic valve, assessing its mechanical strength under different pressure conditions using FEA. This research contributes to the field by offering new insights into the operational limits and failure mechanisms of plastic valves commonly used in drip irrigation systems.

Although various valve designs have been analyzed in previous studies, there is limited research on the structural analysis of mini plastic valves specifically used in agricultural irrigation systems. This study provides a detailed FEA of a mini plastic valve, evaluating its stress distribution, deformation, and safety limits under different pressure conditions. Unlike prior works, this research focuses on the mechanical strength and failure behavior of mini plastic valves, addressing a crucial gap in the literature. Unlike conventional mini valves, this study presents a novel valve design with several innovative features to enhance efficiency and durability in agricultural irrigation systems. The primary innovation includes the integration of a worm mouth connection port for improved sealing, optimized internal flow channels to reduce pressure losses, and a reinforced snap-fit mechanism in the handle connection for enhanced mechanical stability. Additionally, the material selection—Polyoxymethylene (POM) for strength and chemical resistance, and Polypropylene (PP) for flexibility and UV durability—ensures long-term reliability under outdoor conditions. These features collectively provide a more robust, efficient, and user-friendly solution compared to existing designs. The findings of this study not only provide a better understanding of the mechanical limitations of mini plastic valves but also offer practical insights for manufacturers to improve design durability and optimize operational performance.

In this study, the FEA analysis of a mini-valve with a water passage diameter of 10.4 mm, which has a claw structure on the on-off lever and opens and closes by rotating on these claws, was analyzed with SolidWorks simulator. The valve body material is POM an engi-

neering plastic also known as polyacetal or acetal, and the valve opening-closing handle material is polypropylene. Within the scope of this investigation, three different compressive strengths of the valve under 2, 4 and 6 bar pressure were examined, and graphs were taken to evaluate the changes.

2. Materials and Methods

POM, also known as acetal, was selected for the valve body due to its high mechanical strength, dimensional stability, and excellent resistance to moisture and chemicals. POM is widely used in fluid control applications because of its low friction coefficient and superior fatigue resistance. PP was chosen for the handle due to its lightweight nature, high impact resistance, and cost-effectiveness. PP also provides good resistance to environmental factors such as UV exposure, which is critical for outdoor agricultural applications. POM exhibits semi-crystalline behavior with a balance of strength and toughness. It is considered a ductile material under normal operating conditions but can exhibit brittle fracture when exposed to high strain rates or low temperatures. On the other hand, PP is also a ductile polymer, known for its ability to withstand impact without significant deformation. Given their ductile nature, von Mises failure criteria were used to evaluate stress distribution and structural integrity.

In this study, the mini valve shown in ►Figure 1, which has a length of 147 mm and a height of 42 mm, with a water passage diameter of 10.4 mm, has a clawed structure with an opening and closing handle and opens and closes by rotating on these claws, was examined. Three different pressure values were applied to the surface pressure of the mini valve to be analyzed in the working environment using the SolidWorks program [13]. The valve body is made of POM acetal, and the opening-closing handle is made of PP, and the mechanical properties of these plastics are given in ►Table 1. The newly designed mini valve introduces a worm mouth connection system, which enhances the sealing efficiency and ensures a more secure fit within the irrigation pipeline. The internal flow passages were redesigned

using finite element-based topology optimization to minimize turbulence and pressure drop, thus improving overall efficiency. The reinforced snap-fit mechanism in the handle connection is designed to prevent mechanical failure under repeated use, a common issue in conventional designs. These modifications provide improved structural integrity and longer service life, making the valve highly suitable for real-world agricultural applications.

Table 1. Mechanical properties of the materials that make up the mini valve for analysis

Material Feature	POM Asetal	PP
Modulus of Elasticity (N/mm ²)	2600	896
Poisson Ratio	0.3859	0.4103
Tear Modulus (N/mm ²)	932.8	315.8
Bulk Density (kg/m ³)	1390	890
Tensile Strength (N/mm ²)	71.5	27.6
Thermal Conductivity W/(m-K)	0.221	0.147
Specific Heat J/(kg-K)	1378	1881

2.1. Finite Element Modeling

In this study, a linear elastic material model was assumed for both POM and PP materials. Given that the valve operates under relatively low-pressure conditions (maximum 6 bar), nonlinearity due to plastic deformation or large deformations was not considered in the simulations. The von Mises stress criterion was used to evaluate the structural performance, assuming that both materials behave elastically within the analyzed pressure range.

The simulations were conducted using a linear static FEA in SolidWorks. The governing equation for static equilibrium in elasticity is given by:

$$\nabla \cdot \sigma + F = 0 \quad (1)$$

where σ represents the stress tensor and F is the applied force per unit volume. Since the study assumes small

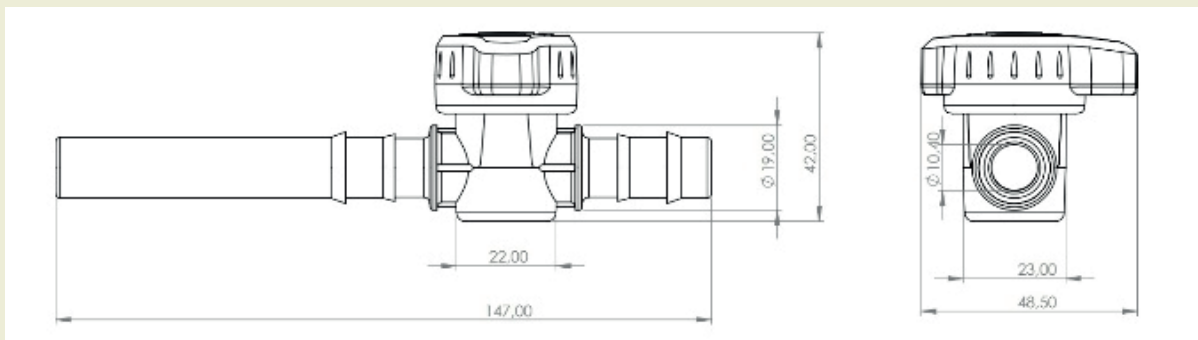


Figure 1. Mini valve used in the study

deformations and elastic behavior, the constitutive equation follows Hooke's Law:

$$\sigma = D \cdot \varepsilon \quad (2)$$

where D is the elasticity matrix and ε is the strain tensor. The von Mises yield criterion was employed to determine stress distribution and failure risk, which is defined as:

$$\sigma_V = \sqrt{\frac{1}{2}[(\sigma_1 - \sigma_2)^2 + (\sigma_2 - \sigma_3)^2 + (\sigma_3 - \sigma_1)^2]} \quad (3)$$

2.2. Consideration of Hoop Stress in the Mini Valve Design

Hoop stress (σ_h) is a critical factor in cylindrical pressure vessels and pipeline structures, where internal pressure generates circumferential stresses along the walls. The general equation for hoop stress in a thin-walled pressure vessel is given by:

$$\sigma_H = \frac{P \cdot r}{t} \quad (4)$$

where P is the internal pressure, r is the inner radius, and t is the wall thickness.

In conventional pipe systems, hoop stress dominates the stress distribution, but the geometry of the mini valve differs from a simple cylindrical shell. The mini valve contains complex features such as threaded inlet/outlet connections, a central flow regulation chamber, and varying wall thicknesses, making direct hoop stress calculations less straightforward.

To account for circumferential stress effects, the FEA model includes:

- Fine meshing in the inlet/outlet regions, where pressure-induced stresses resemble hoop stress in cylindrical structures.
- Stress distribution analysis along the valve body and internal walls, ensuring that regions experiencing circumferential loading are adequately captured.
- Von Mises stress evaluation, which inherently incorporates principal stresses, including hoop stress components.
- While hoop stress was not explicitly isolated as a separate parameter, its effects are embedded within the FEA results.

The geometry of the mini valve is given in ►Figure 2. In the simulation, the mini valve is positioned to be fully open. The boundary condition was determined by connecting the elements in contact with each other at the contact surfaces.

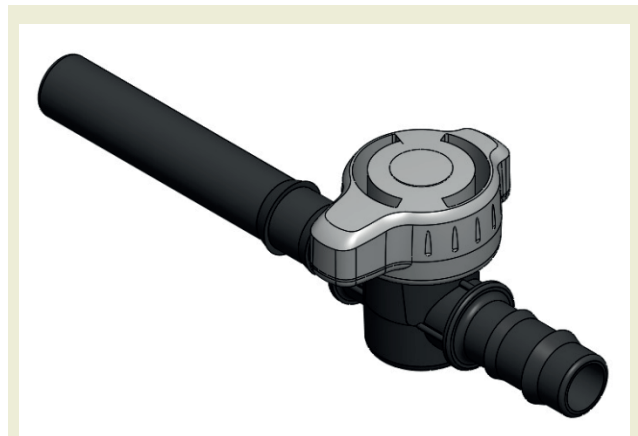


Figure 2. Geometric shape of the mini valve.

►Figure 3 shows the boundary conditions applied to the mini valve. The inlet and outlet parts of the valve have threaded structures that provide the connection. Since these parts will be connected to female fittings in practice, a fixed boundary condition is defined for the inlet and outlet regions (►Figure 3 (A)). In ►Figure 3 (B), a pressure boundary condition of 2,4,6 bar is defined for the regions shown in red color.

2.3. Justification of Boundary Conditions and Pressure Levels

The applied pressure values (2, 4, and 6 bar) were selected based on realistic operating conditions in agricultural drip irrigation systems. According to industry standards and manufacturer specifications, mini plastic valves used in such systems typically operate within a pressure range of 1.5 to 5 bar, depending on the pipeline configuration and system design.

2 bar pressure represents a common working pressure in standard drip irrigation applications, ensuring optimal water distribution. 4 bar pressure was chosen as an intermediate scenario to analyze potential mechanical responses under increased load. 6 bar pressure serves as an upper limit test, allowing us to evaluate the structural integrity of the valve under extreme but possible conditions, particularly during unexpected pressure surges or water hammer effects.

2.4. Boundary Condition Application in FEA

Fixed constraints were applied at the inlet and outlet to represent real-world installation, where the valve is secured within the pipeline. A uniform internal pressure was applied to the internal surfaces of the valve to simulate hydraulic loading conditions. The meshing was refined in stress-critical regions (snap-fit connection and flow chamber walls) to ensure accurate stress predictions under applied boundary conditions. These boundary conditions and pressure selections ensure that the simulation results closely represent practical operational conditions in agricultural irrigation systems.



Figure 3. Boundary conditions of the analyzed mini valve A) fixing surfaces and B) pressure application surfaces

For the numerical solution of the model shown in ►**Figure 4**, shell elements are defined via the Shell Definition feature. Specifically: Thin Shell (equivalent to SHELL181 in ANSYS) was used for thin-walled sections to account for bending and membrane effects. Also, Thick Shell (equivalent to SHELL281 in ANSYS) was applied in areas requiring improved curvature accuracy. These shell elements were subjected to curvature-based high-quality meshing due to the shape of the geometry using triangular cells with 147249 nodes and 87444 elements to ensure correct stress distribution while maintaining computational efficiency.

2.5. Mesh Convergence Analysis and Validation

To ensure that the obtained results are mesh-independent, a mesh convergence study was conducted by systematically refining the mesh and monitoring the change in maximum von Mises stress values. The analysis was performed using three different mesh densities:

Coarse Mesh: ~75,000 elements

Medium Mesh: ~87,444 elements (selected for final analysis)

Fine Mesh: ~120,000 elements

The results showed that beyond 87,000 elements, the variation in maximum von Mises stress was less than 2%, indicating that the solution had converged. Thus, the medium-density mesh was selected to balance computational efficiency and accuracy.

2.6. FEA Validation Approach

Since experimental validation was not within the scope of this study, a basic FEA validation approach was employed:

- The maximum von Mises stress values from the simulation were compared with analytical hoop

stress estimates for cylindrical sections of the valve.

- The stress distribution along the snap-fit connection and valve body was analyzed to ensure expected stress patterns were observed.
- The average stress values from mesh refinement studies were compared to verify mesh-independent results.

These validation steps confirm that the simulation results are reliable and mesh-independent, strengthening the accuracy of the presented findings.

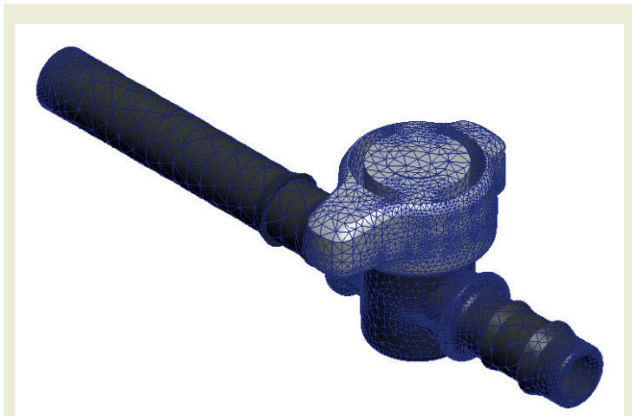


Figure 4. FEA Model meshing of the mini valve analyzed

3. Results and Discussions

To determine the compressive strength of the plastic mini valve, stresses, displacements and strains at 2, 4, 6 bar pressure values were tried to be determined. In line with this scope, Von Mises stresses, displacements and strains are shown in ►**Figure 5** by applying 2 bar pressure to the relevant surface of the mini valve.

Figure 5 (A) shows that the maximum stress in the mini valve occurs at the edges of the snap fitting between the valve body and the valve opening and closing handle. This polypropylene material is lower than the maxi-

imum flexural yield strength of 44.1 MPa. With a maximum stress value of 20 MPa obtained at 2 bar pressure, the valve has a maximum displacement of 0.16 mm as shown in ►Figure 5 (B). Again, under this pressure, the maximum strain occurs in the plug-in fastener with a value of 1.75×10^{-2} (►Figure 5 (C)).

►Figure 6 shows the Von Mises stresses, displacements and strains experienced by the mini valve under 4 bar pressure. As can be seen from ►Figure 6 (A), the highest stress occurs at the edges of the plug connection between the valve body and the on-off handle. Since the flexural yield strength of polypropylene material is 44.1

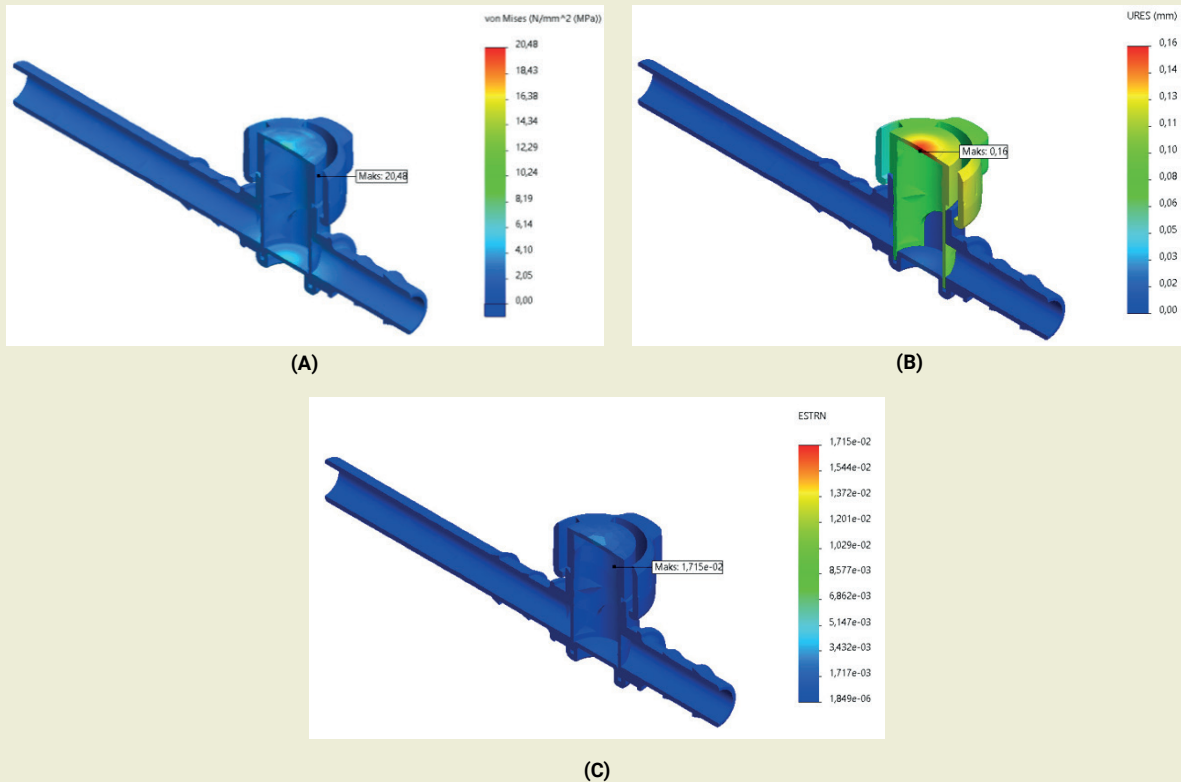


Figure 5. Pressure at mini valve with 2 bar pressure A) Von Mises Stresses B) Displacements C) Strains

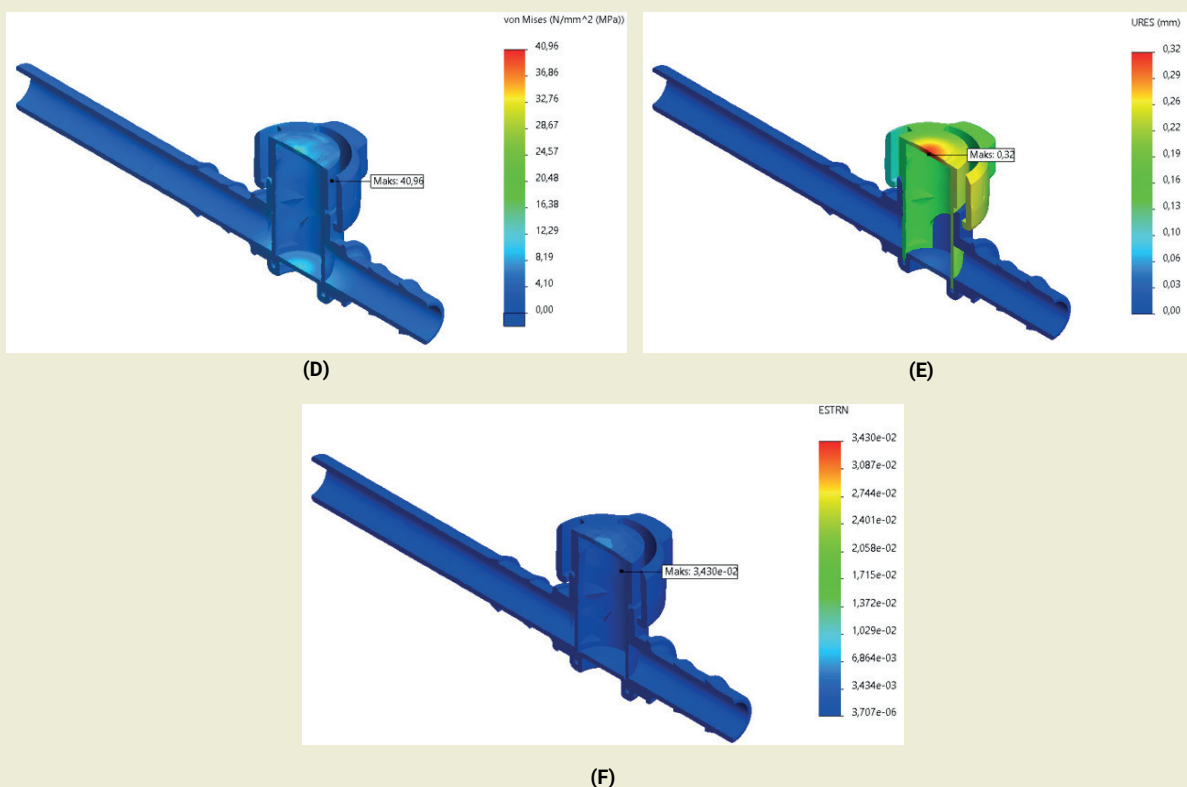


Figure 6. Formed with 4 bar pressure in the mini valve D) Stresses E) Displacements F) Strains

MPa, this stress calculated as approximately 41 MPa is below the limit value. As shown in ►Figure 6 (B), a maximum displacement of 0.32 mm was observed in the valve at this pressure level. In addition, the highest strain occurring under a pressure of 4 bar is 3.430×10^{-2} , which occurs in the snap-fit fastener (►Figure 6 (C)).

►Figure 7 shows the Von Mises stresses, displacements and strains that the mini valve is subjected to under 6 bar pressure.

►Figure 7 (A) shows that the highest stress occurs at the edges of the plug connection between the valve body and the on-off lever. This stress, calculated to be approximately 61 MPa, exceeds the flexural yield strength of the polypropylene material of 44.1 MPa. As shown in ►Figure 7 (B), a maximum displacement of 0.48 mm occurred in the mini valve at this pressure level. Furthermore, the highest strain value was determined to be 5.146×10^{-2} , which was concentrated in the plug-in fitting (►Figure 7 (C)).

A comprehensive table has been created that directly compares the yield and rupture stresses of POM (Acetal) and PP materials with the maximum Von Mises

stresses obtained in the simulation (Table 2). When ►Table 2 is examined, the stresses at 2 bar pressure are well below the yield limits of both POM and PP materials. No permanent deformation is expected in the material at this level. At 4 bar pressure, the Von Mises stress applied to the PP material approaches the yield stress. At 6 bar pressure, the yield stress in the PP material has been exceeded and is approaching the rupture stress. This indicates that the material is at risk of permanent deformation or fracture. It has also been determined from the table that the maximum deformation occurs for 6 bar.

3.1. Factor of Safety (FOS) Analysis and Engineering Implications

The Factor of Safety (FOS) is a critical parameter in structural design, defined as the ratio of material strength to the maximum applied stress:

$$FOS = \frac{\sigma_{yield}}{\sigma_{max}} \quad (5)$$

where σ_{yield} is the yield strength of the material and σ_{max}

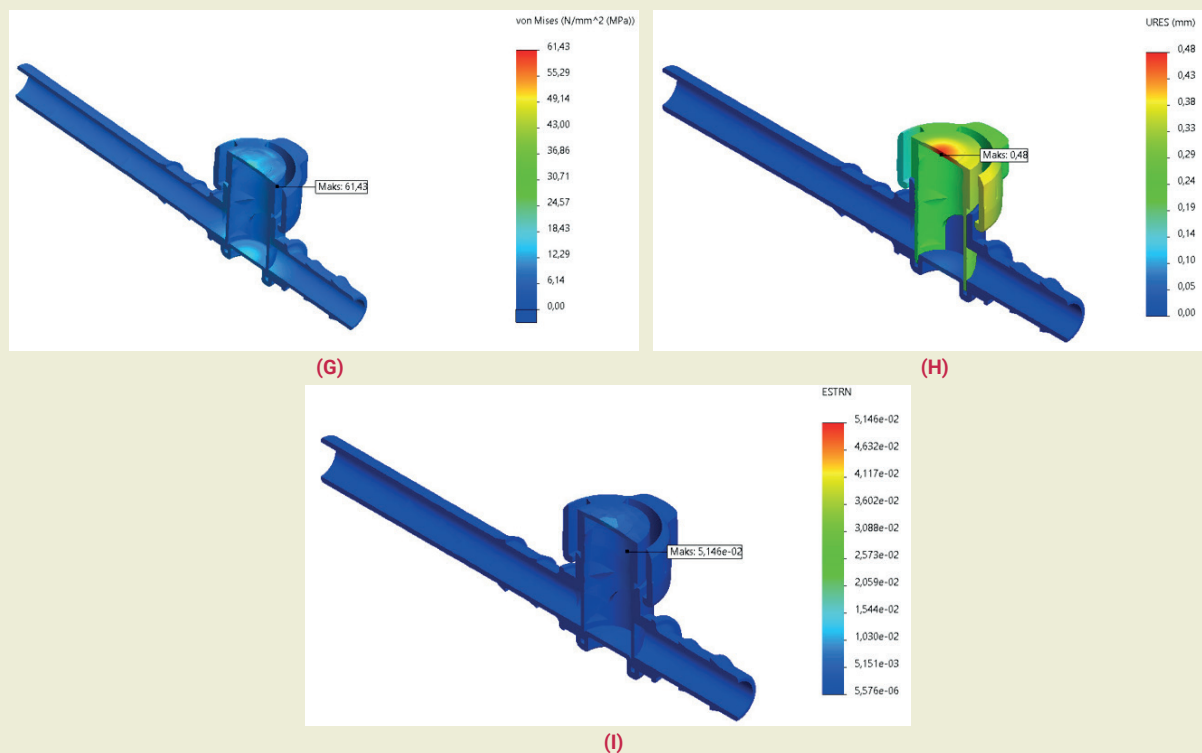


Figure 7. Formed with 6 bar pressure in the mini valve G) Stresses H) Displacements I) Strains

Table 2. Comparison of the yield and rupture stresses of POM and PP materials with the maximum Von Mises stresses obtained in the simulation.

Pressure (bar)	POM Yield Stress (MPa) [14]	POM Fracture Stress (MPa)[14]	PP Yield Stress (MPa)[15]	PP Fracture Stress (MPa)[15]	Maximum Von Mises Stress (MPa)	Maximum Displacement (mm)
2 bar	60-70	70-85	30-40	35-50	20 MPa	0.16 mm
4 bar	60-70	70-85	30-40	35-50	41 MPa	0.32 mm
6 bar	60-70	70-85	30-40	35-50	61 MPa	0.48 mm

is the maximum von Mises stress obtained from the simulation.

The results in ►Table 3 show that:

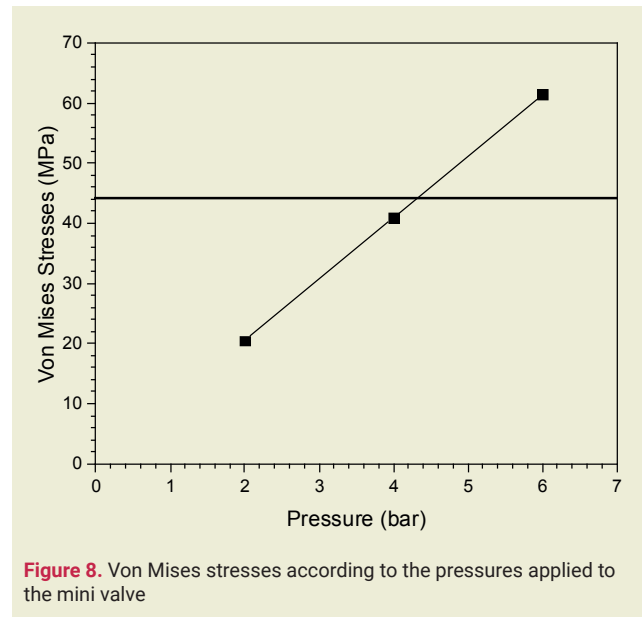
At 2 bar, the safety factors for both materials remain well above the critical threshold ($FOS > 1.5$), ensuring safe operation. At 4 bar, the PP component approaches its yield limit ($FOS = 0.73$), indicating that it is nearing structural failure. At 6 bar, PP material falls below the safe operating range ($FOS = 0.49$), confirming that it will undergo plastic deformation or failure.

This analysis reinforces the operating pressure recommendations for mini plastic valves. While the POM body remains within acceptable limits, the PP handle becomes structurally unreliable above 4 bar. Therefore, limiting the valve operation to ≤ 4 bar is essential to maintain long-term mechanical integrity.

►Figure 8 shows the Von Mises stresses in the mini valve at 2, 4 and 6 bar pressure levels.

A linear increase in Von Mises stresses is observed as the pressure increases. When 2 bar pressure is applied, the stress in the valve is well below the yield limit of the material used. However, this difference decreases as the pressure level increases and the stress value reached at 4 bar pressure is almost the same as the yield stress. At higher pressures, such as 6 bar, the stress exceeds the yield limit, straining the material strength.

►Figure 9 shows the displacements and strains occurring in the mini valve at 2, 4 and 6 bar pressure. There



is a linear increase in both displacements and strains with the increase in pressure, and the pressures are directly proportional to the amount of increase, approximately ~2 times as shown in ►Figure 8.

4. Conclusions

In this study, the pressure resistance and structural integrity of a 2-way manually controlled mini plastic valve used in drip irrigation systems were analyzed using finite element analysis (FEA) under 2, 4, and 6 bar pressure conditions. The results indicate that at 2 bar,

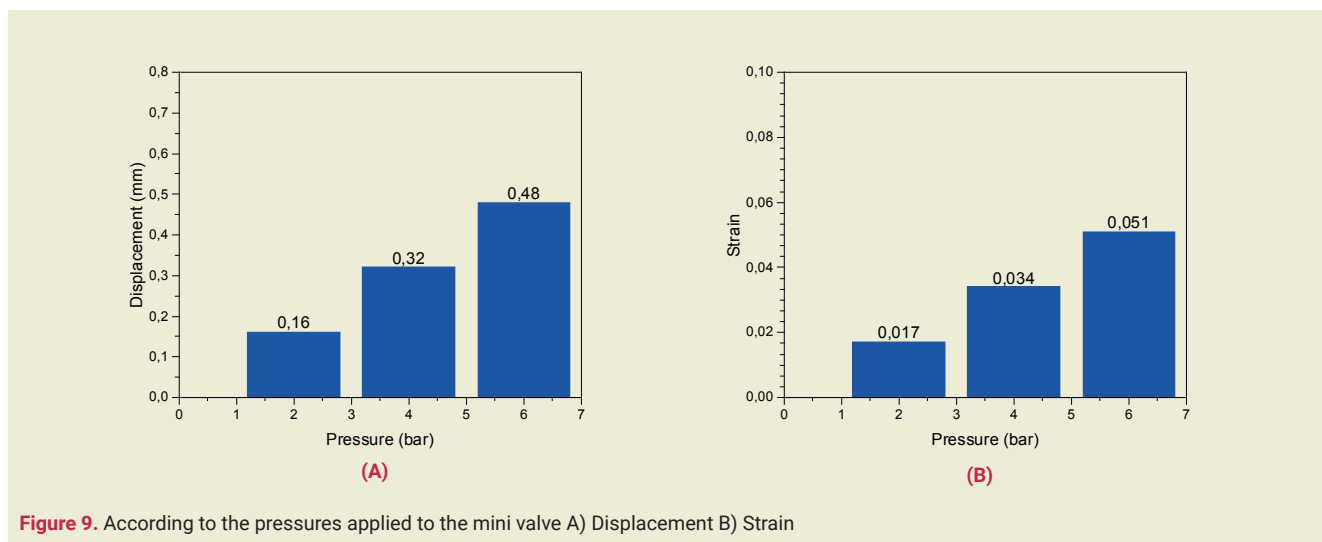


Table 3. The calculated safety factors for different pressure levels

Pressure (bar)	PP Yield Stress (MPa)	POM Yield Stress (MPa)	Max Von Mises Stress (MPa)	FOS (PP)	FOS (POM)
2 bar	30	60	20	1.50	3.00
4 bar	30	60	41	0.73	1.46
6 bar	30	60	61	0.49	0.98

the valve operates safely with a safety factor (FOS) > 1.5, while at 4 bar, the PP handle approaches its yield limit (FOS = 0.73), posing a potential structural failure risk under prolonged use. At 6 bar, the PP material exceeds its yield strength (FOS = 0.49), making it unsuitable for long-term operation due to plastic deformation or fracture risk. The study also considered hoop stress effects in inlet and outlet regions, confirming that von Mises stress evaluation inherently captures circumferential stress distribution. Based on these findings, the mini valve is recommended for safe operation at ≤ 2 bar, with 4 bar as a cautionary limit, while pressures above 4 bar should be avoided to prevent mechanical failure. It should be noted that this study only considers static pressure loading; while the results indicate that the mini valve maintains structural integrity under steady pressures, the potential impact of dynamic pressure variations, such as transient surges or cyclic loading, was not assessed. Future studies could explore these effects through transient FEA simulations, fatigue analysis, and experimental validation to provide a more comprehensive evaluation of the valve's long-term durability in real-world applications.

Research ethics

Not applicable.

Author contributions

Conceptualization: [Murat Kuru], Methodology: [Yavuz

Turan], Formal Analysis: [Beyza Gizem Duman], Investigation: [İbrahim Keleş], Resources: [Hülya Alaca], Data Curation: [İbrahim Keleş], Writing - Original Draft Preparation: [Yavuz Turan], Writing - Review & Editing: [Beyza Gizem Duman], Visualization: [Hülya Alaca], Supervision: [Murat Kuru], Project Administration: [İbrahim Keleş]

Competing interests

The author(s) state(s) no conflict of interest.

Research funding

None declared.

Data availability

The raw data can be obtained on request from the corresponding author.

Peer-review

Externally peer-reviewed.

Orcid

Yavuz Turan  <https://orcid.org/0000-0001-8537-3989>

Murat Kuru  <https://orcid.org/0009-0005-3283-3458>

Beyza Gizem Duman  <https://orcid.org/0009-0004-9045-8142>

Hülya Alaca  <https://orcid.org/0009-0004-0588-1633>

İbrahim Keleş  <https://orcid.org/0000-0001-8252-2635>

References

- [1] Rajkumar, B. (2014). Globe Valve Design Optimization & Trends. L&T Integrated Engineering Services, Fluids Handling Principles and practice, Pg. 212-234.
- [2] Chern, M. J., Wang, C. C., & Ma, C. H. (2007). Performance test and flow visualization of ball valve. *Experimental thermal and fluid science*, 31(6), 505-512. <https://doi.org/10.1016/j.expthermflusc.2006.04.019>
- [3] Jadhav, S. S. (2014). Design of M-Type Gate Valve. *International Journal of Science and Research (IJSR)*, 3(11).
- [4] Prakash, K. S., Nazirudeen, S. M., Malvinraj, M. J., & Manohar, T. (2009). Integration of Material Design and Product Design-A CFD Based Approach. *International Journal of Dynamics of Fluids*, 5(2), 199-214. <https://doi.org/10.52842/conf.ecaade.2015.1.665>
- [5] Mokhtarzadeh-Dehghan, M. R., Ladommatos, N., & Brennan, T. J. (1997). Finite element analysis of flow in a hydraulic pressure valve. *Applied Mathematical Modelling*, 21(7), 437-445. [https://doi.org/10.1016/S0307-904X\(97\)00038-3](https://doi.org/10.1016/S0307-904X(97)00038-3)
- [6] Song, X. G., Wang, L., & Park, Y. C. (2009). Analysis and optimization of a butterfly valve disc. *Proceedings of the Institution of Mechanical Engineers, Part E: Journal of Process Mechanical Engineering*, 223(2), 81-89. <https://doi.org/10.1243/09544089JPME236>
- [7] Sathishkumar, S., Hemanathan, R., Gopinath, R., & Dilipkumar, D. (2017). Design and analysis of gate valve body and seat ring. *Int. J. Mech. Eng. Technol*, 8(3), 131-141.
- [8] Prakash, K. S., Nazirudeen, S. M., Malvinraj, M. J., & Manohar, T. (2009). Integration of Material Design and Product Design-A CFD Based Approach. *International Journal of Dynamics of Fluids*, 5(2), 199-214. <https://doi.org/10.52842/conf.ecaade.2015.1.665>
- [9] Song, X., Wang, L., Kang, J., Kim, S. G., Jo, Y. J., & Park, Y. (2008, October). Optimization Of Valve Disc Using Orthogonal Array And Kriging Model. In *AIP Conference Proceedings* (Vol. 1052, No. 1, pp. 315-320). American Institute of Physics.
- [10] Raut, L. B., & Parase, P. K. (2014). Weight Reduction of 12"-150 Class Plug valve Casting Body by Finite Element Analysis and Experimental Method. *American Journal of Engineering Research*, 4(4), 108-116.
- [11] Lee, J. H., Song, X. G., Kang, S. M., & Park, Y. C. (2010, June). Optimization of flow coefficient for pan check valve by fluid dynamic analysis. In *AIP Conference Proceedings* (Vol. 1239, No. 1, pp. 337-340). American Institute of Physics.
- [12] Yang, S. M., Baek, S. H., & Kang, S. (2012). Shape design for disc of a double-eccentric butterfly valve using the topology optimization technique. *Journal of computational fluids engineering*, 17(1), 61-69.
- [13] SolidWorks Product. 2024. Nonlinear - Solution, SolidWorks Simulation Online Tutorial.
- [14] Loyer, C., Ferreira, P., Marijon, J. B., Michel, V., Regnier, G., Vera, J., ... & Richaud, E. (2022). Embrittlement of polybutylene terephthalate induced by injection molding. *Polymer Degradation and Stability*, 196, 109843.
- [15] Röscher, J., & Mülhaupt, R. (1995). Deformation behavior of polypropylene/polyamide blends. *Journal of applied polymer science*, 56(12), 1607-1613.